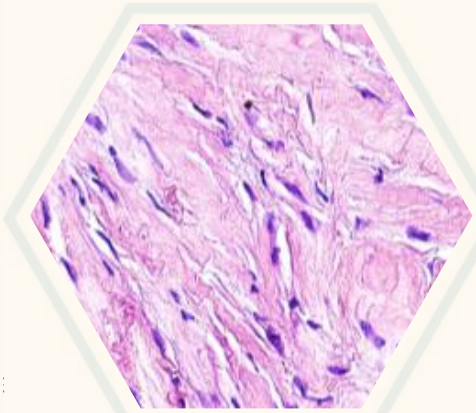
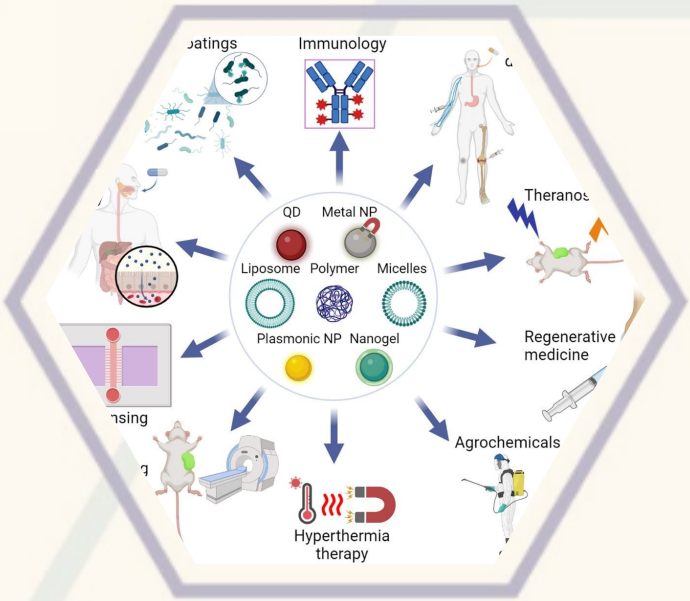
Vol 9, No 2, 2023

Journal of Biomedical Photonics & Engineering





Editor-in-Chief:
Valery Tuchin

©2023 J-BPE

Journal of Biomedical Photonics & Engineering

by Samara National Research University

Volume 9, Issue 2 (June 2023)

Editor-In-Chief

Valery V. Tuchin - Saratov National Research State University, Russian Federation;
Institute of Precision Mechanics and Control RAS, Russian Federation; a corr.-member of RAS

Deputy Editor-In-Chief

Valery P. Zakharov - Samara National Research University, Russian Federation

Postal address:
39B Lukacheva st., room #301
Samara 443086, Russian Federation

Used Figures from this issue on the Cover

Alexander Knysh et al. Dynamic Light Scattering Analysis in Biomedical Research and Applications of Nanoparticles and Polymers, 020203, Fig. 1.

Anton A. Plekhanov et al. Side-by-Side OCE-Study of Elasticity and SHG-Characterization of Collagen Fibers in Breast Cancer Tissue before and after Chemotherapy, 020305, Fig. 2 (C1).

© 2023 J-BPE

Contents

Reviews

Wearable Devices for Multimodal Optical Diagnostics of Microcirculatory-Tissue Systems: Application Experience in the Clinic and Space 020201
Andrey Dunaev

Machine Learning Algorithms for the Analysis of Age-Related Macular Degeneration Based on Optical Coherence Tomography: a Systematic Review 020202
Ekaterina A. Lopukhova, Rada R. Ibragimova, Gulnaz M. Idrisova, Irina A. Lakman, Timur R. Mukhamadeev, Elizaveta P. Grakhova, Azat R. Bilyalov, and Ruslan V. Kutluyarov

Dynamic Light Scattering Analysis in Biomedical Research and Applications of Nanoparticles and Polymers 020203
Alexander Knysh, Pavel Sokolov, and Igor Nabiev

Articles

Physical and Biological Properties of Layers with Nanoparticles Based on Metal Chalcogenides and Titanium Synthesized by Femtosecond Laser Ablation and Fragmentation in Liquid 020301
Ulyana E. Kurilova, Anton S. Chernikov, Dmitry A. Kochuev, Lidiya S. Volkova, Anna A. Voznesenskaya, Ruslan V. Chkalov, Dmitriy V. Abramov, Alexander V. Kazak, Irina A. Suetina, Marina V. Mezentseva, Leonid I. Russu, Alexander Yu. Gerasimenko, and Kirill S. Khorkov

Diagnostics of Layer-by-Layer Biotissue Evaporation in the Process of Two-Coordinate Scanning by a Laser Beam for Precision Surgery 020302
Alexander K. Dmitriev, Alexey N. Konovalov, Vladimir N. Kortunov, and Valery A. Ulyanov

Bilirubin- and Blue-Green Light-Induced Damage of Human Erythrocytes 020303
Julia V. Kruchenok, Olga N. Dudinova, and Vitaly Y. Plavskii

Lower Limb Analysis of the Biomechanical Gait Cycle at Various Phases in Real Time 020304
Zainab M. Nahi, Huda F. Jameel, and Ahmed B. Fakhri

Side-by-Side OCE-Study of Elasticity and SHG-Characterization of Collagen Fibers in Breast Cancer Tissue before and after Chemotherapy 020305
Anton A. Plekhanov, Arseniy L. Potapov, Mikhail V. Pavlov, Vadim V. Elagin, Ekaterina V. Gubarkova, Alexander A. Sovetsky, Lev A. Matveev, Dmitriy A. Vorontsov, Alexander L. Matveyev, Alexey Y. Vorontsov, Sergey V. Gamayunov, Elena V. Zagaynova, Marina A. Sirotkina, Vladimir Y. Zaitsev, and Natalia D. Gladkova

Theoretical and Experimental Study of the Hair Bonding by Continuous Laser Radiation with a Wavelength of 980 nm 020306
Andrey V. Belikov, Yulia V. Fyodorova, and Vladislav M. Ermolaev

3D Printed Modular Vein Viewing System Based on Differential Light Absorption in the Near Infrared Range 020307
Nikita V. Remizov, Elena M. Bataeva, Dmitry P. Stramousov, Anastasiya A. Shatskaya, and Dmitry N. Artemyev

Mathematical Analysis of Raman Spectra Data Arrays Using Machine Learning Algorithms 020308
Yana A. Byuchkova, Andrey Y. Zyubin, Vladimir V. Rafalskiy, Ekaterina M. Moiseeva, and Ilia G. Samusev

 © 2023 J-BPE

Wearable Devices for Multimodal Optical Diagnostics of Microcirculatory-Tissue Systems: Application Experience in the Clinic and Space

Andrey Dunaev
Research and Development Center of Biomedical Photonics, Orel State University, 95 Komsomolskaya str., Orel 302026, Russia

e-mail: dunaev@bmecenter.ru

Abstract. This work demonstrates some results of the successful experience of using wearable devices for multimodal optical diagnostics of microcirculatory-tissue systems both in clinical practice and in the conditions of a Space experiment. The multimodal approach based on simultaneously applying a minimum of 2 optical diagnostic methods, for example, laser Doppler flowmetry and fluorescence spectroscopy, allows analysing of blood flow and metabolic processes in biological tissue more systematically. Combining several wearable devices into a distributed diagnostic system allows placing them simultaneously on symmetrical parts of the body (such as opposite limbs) thus providing a possibility to study the symmetry of the measured signals. The obtained data on the state of the microcirculatory-tissue systems of the human body recorded with wearable multimodal devices make it possible to assess the relationship and dynamics of oxygen delivery and utilization by tissues more comprehensively and reliably in a variety of diagnostic tasks. © 2023 Journal of Biomedical Photonics & Engineering.

Keywords: wearable devices; microcirculatory-tissue systems; multimodal optical diagnostics; laser Doppler flowmetry; fluorescence spectroscopy; Space experiment; zero gravity.

Paper #3622 received 27 Jan 2023; revised manuscript received 17 Mar 2023; accepted for publication 22 Mar 2023; published online 1 Apr 2023. doi: 10.18287/JBPE23.09.020201.

1 Introduction

In recent decades, the knowledge about tissue optical properties in the healthy and pathological state has reached a sufficient level to develop and implement the methods of optical non-invasive diagnostics in clinical practice [1–3]. Lately, there has been a steady increase in interest in the problems of non-invasive research not only of the microcirculatory bed as the final segment of the cardiovascular system, but also of the microcirculatory-tissue systems (MTS) of the human body from the point of view of maintaining homeostasis and homeokinesis of tissues in a single holistic organism. MTS of the human body are the smallest functional unit of the vascular system, where microvessels are in close relationship with the surrounding tissue and regulatory elements. MTS is the functional element of an organ and is a structural and functional complex composed of specialized parenchyma cells, cells of the connective tissue suspended in a non-cellular matrix, blood and lymphatic microvessels, and fiber nerve endings, which are combined into a single system by regulatory mechanisms [4]. Violations in the MTS play a key role in the pathogenesis of various diseases complications (for example, rheumatological and endocrinological [5–7], dermatological [8], and otolaryngological [9] ones). Even during minimally invasive surgical operations, it is necessary to assess the state of MTS, for example, in case of organ ischemia, etc. [10]. In view of the above, timely diagnosis of MTS of the human body is a subject of extensive research.

At present, there is a surge of interest in wearable electronic diagnostic devices, because daily monitoring of parameters (for example, MTS parameters) promises a new quality of diagnostics [11–13]. Recently actively developed multimodal approach allows clinicians to obtain *in vivo* values of individual physiological and

biochemical parameters, as well as to conduct a comprehensive assessment of the viability of MTS [14–17]. One of the first developments of wearable devices for estimating MTS parameters is the analyzer "LAZMA PF" (LAZMA Ltd, Russia; in EU/UK this device is produced by Aston Medical Technology Ltd., UK as "FED-1b") [18, 19], which combines a multimodal approach, namely, consisting of 2 channels – laser Doppler flowmetry (LDF) and fluorescence spectroscopy (FS).

The LDF method is based on laser probing of biological tissues and analysis of light scattered from moving erythrocytes. The main parameter recorded by this method is called the index of microcirculation or perfusion (I_m) [20]. This method allows one to evaluate the oscillatory processes in the microvasculature in a wide range of frequencies, which are calculated using the wavelet transform [21–23]. For more than 15 years, it has been customary to use adaptive wavelet analysis to assess fluctuations in the microvasculature, which implements a continuous wavelet transform using the complex-valued Morlet wavelet as an analyzing wavelet. Previously, the fast Fourier transform and Butterworth mathematical filters were also used for this purpose, however, due to the fact that the LDF-gram (perfusion) is a non-stationary process (short-term fragmentary episodes of vasoconstriction and vasodilation of the microvascular bed are recorded in it), it is now customary to use continuous wavelet transform, which provides the optimal "time – frequency" ratio for blood flow signals and allows to trace the frequency and amplitude of oscillations [22]. At present, it is customary to distinguish several (mostly 5) main frequency ranges (oscillations) that take into account the influence of various regulatory mechanisms: endothelial 0.0095–0.02 Hz (E), neurogenic 0.02–0.06 Hz (N), myogenic 0.06–0.16 Hz (M), breathing 0.16–0.4 Hz (B) and cardiac 0.4–1.6 Hz (C) [4, 24]. However, some authors (for example, Refs. [25–27]) distinguish 2 subranges in the range of endothelial oscillations – 0.005–0.0095 Hz and 0.0095–0.02 Hz, that reflect the vascular tone regulation due to the endothelium activity, both NO-dependent and independent. In addition, some authors [28, 29] consider it reasonable to distinguish two subranges of general myogenic oscillations – 0.047–0.069 Hz (low-frequency) and 0.07–0.145 Hz. In the former, the influence of peptidergic sensory fibers can be manifested, and the second reflects the proper myogenic oscillations or vasomotions. Thus, currently, it is possible to analyze 7 different ranges of microvasculature fluctuations.

The FS method is based on laser probing of tissues and registration of fluorescence spectra of metabolic coenzymes. This method, among others, implements the registration of the normalized amplitudes of the NADH (nicotinamide adenine dinucleotide) and FAD (flavin adenine dinucleotide) fluorescence intensity depending on the excitation wavelength respectively [30]. Changes in these parameters are associated with changes in metabolic conditions due to different physiological and pathological processes, and therefore fluorescence monitoring can be used to detect cell metabolism disorders associated with the occurrence of various diseases [31].

Thus, the purpose of this work was to demonstrate the successful experience of using these wearable multimodal devices both in clinical practice and in the conditions of a Space experiment.

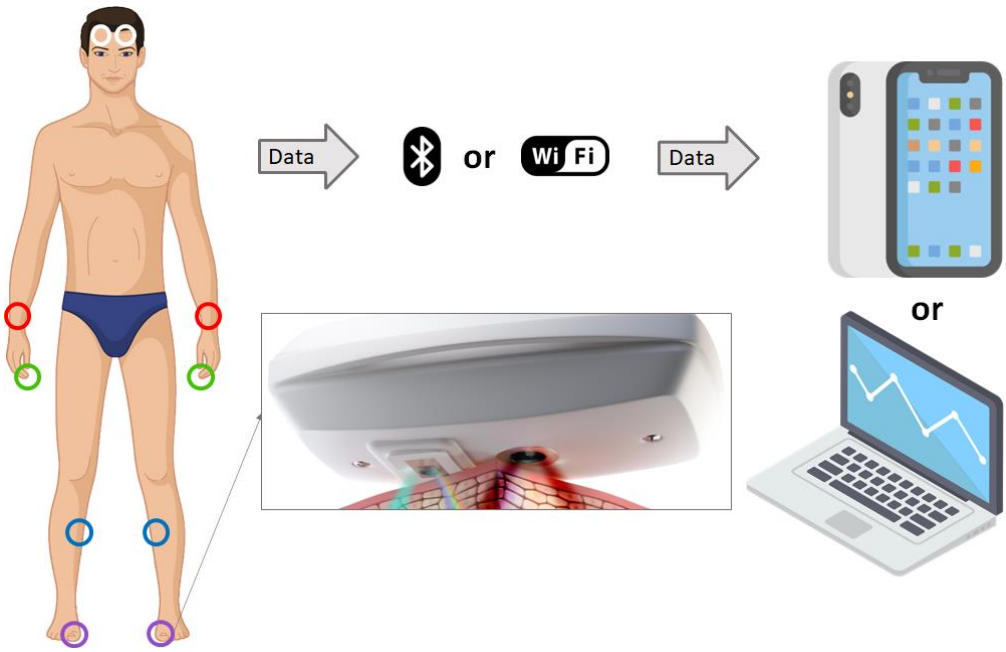


Fig. 1 Examples of location of wearable devices for diagnosing the MTS on symmetrical zones of the human body and their wireless connection to a personal computer or smartphone.

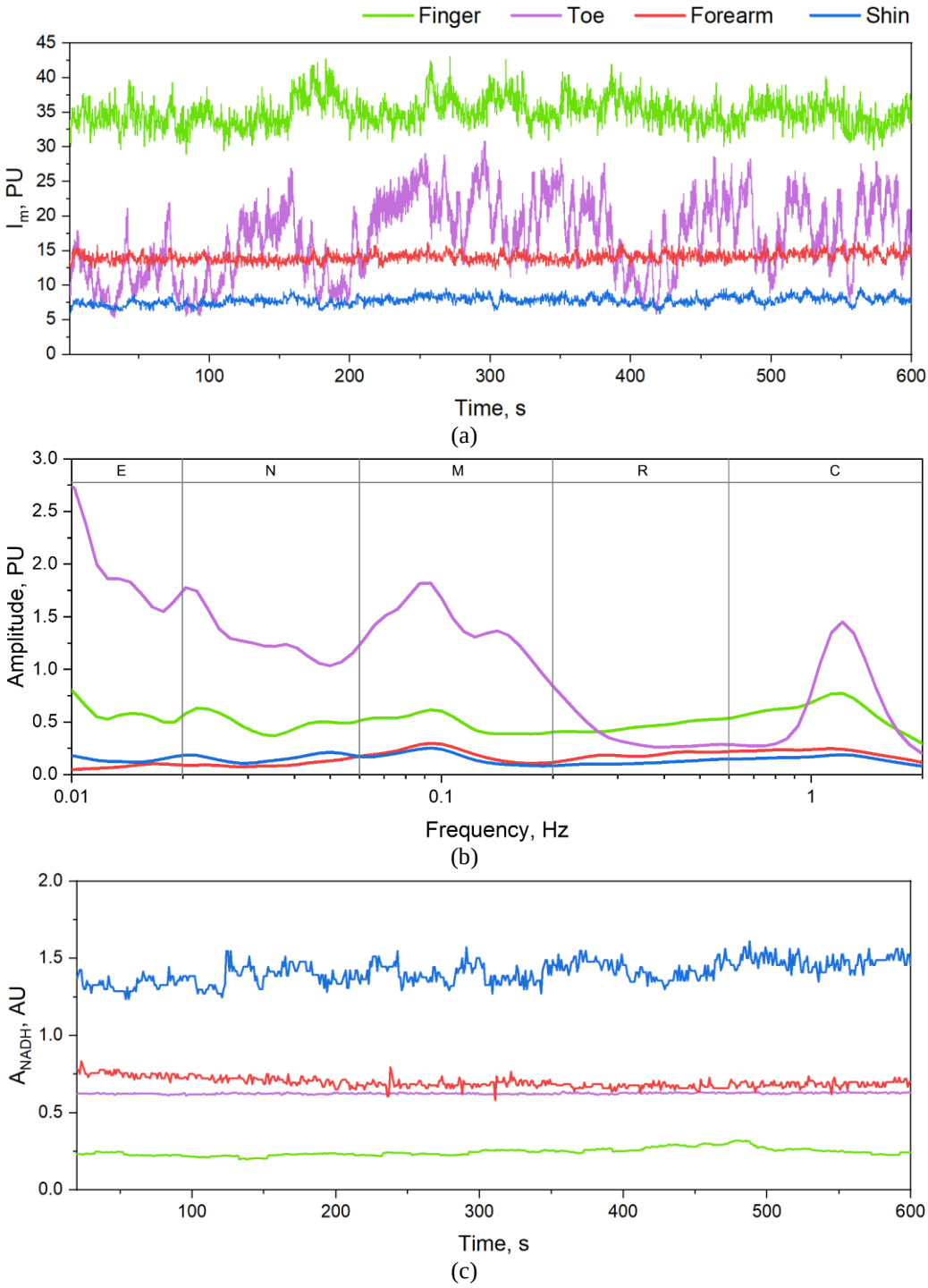


Fig. 2 A typical example of simultaneous registration from 4 skin zones of the right extremities of average perfusion (a), its wavelet analysis (b), and the normalized NADH fluorescence amplitude (c) of a conditionally healthy volunteer.

2 Design Features of a Wearable Device for Multimodal Optical Diagnostics

A distinctive feature of the wearable devices under consideration is the absence of optical fibers in their design, which allows to decrease the movement artefacts common in fibre-based LDF monitors [32]. Wearable devices are placed on the skin for direct irradiation from a window and registration of emitted (secondary) radiation from biotissue at the back of the instrument and transmitting measurement data to a PC using Bluetooth or Wi-Fi protocols (Fig. 1). Wearable device "LAZMA PF" with 2 optical diagnostic channels uses a VCSEL chip with a wavelength of 850 nm as a single-mode laser source (0.8 mW) in the LDF channel, delivering radiation directly to the skin [19]. In the FS channel it uses a 365 nm UV LED (pulse power – 1.4 mW, average power 0.35 mW with duty cycle 4) to excite endogenous fluorescence (NADH in the

wavelengths range 460–470 nm) [33]. An amplitude of NADH fluorescence intensity (A_{NADH}) is normalized to back-scattered radiation to reduce the influence of different blood filling in biotissue [30], which arises, among other reasons, due to the artifacts associated with different pressure on the skin surface [34]. The distance between the windows of 2 channels is about 1 cm (as shown in Fig. 1), the examined diagnostic volume for each of the channels is different and depends on the design features of each channel (on the so-called "measurement base" – the distance between the radiation source and detector) – on average, it does not exceed 1 mm^3. Examples of location on symmetrical zones of the limbs of wearable devices for diagnosing the MTS of the human body and their wireless connection to a personal computer or smartphone are shown in Fig. 1. This figure also shows the most common locations for wearable devices on the biotissue of the subject's body (distributed monitoring system) depending on diagnostic tasks: these are often symmetrical points on the right and left sides of the upper and lower extremities, skin areas there are rich with arteriolo-venular anastomoses (hands or toes fingers pads) and with predominant nutritive blood flow (forearms or shins), and on the forehead at areas of supraorbital arteries.

A typical example of simultaneous registration during 10 min from 4 skin zones of the right extremities of average perfusion (a), its wavelet analysis with 5 frequency ranges (b), and the normalized NADH fluorescence amplitude (c) of a conditionally healthy volunteer (men 46 years) is shown in Fig. 2 (the colors of the graphs correspond to the colors of the device's location in Fig. 1).

The software allows to calculate the average value of nutritive blood flow (I_{mn}) according to the Eq. (1), measured in perfusion units (PU). Nutritive blood flow is a characteristic of blood flow in the capillaries, that directly provides trophic and oxygenation processes (unlike blood flow through arteriolo-venular anastomoses) [18]:

$$I_{mn} = \frac{I_m \cdot A_m}{A_n + A_c}, \quad (1)$$

where is the I_{mn} – nutritive blood flow, I_m – the average value of the index of microcirculation, A_m – the amplitude of myogenic oscillations, A_n – the amplitude of neurogenic oscillations, A_c – the amplitude of cardiac oscillations.

In addition, according to the multimodal approach, as a complex parameter for a comprehensive assessment of the relationship between the state of the microvasculature and oxidative metabolism in the tissue, an oxidative metabolism index (*OMI*) has been developed (due to the use of only one fluorescence excitation with wavelength 365 nm in this device, the proposed formula is adapted) [11, 18, 35]:

$$OMI = k \frac{I_{mn}}{A_{NADH}}, \quad (2)$$

where *k* is the coefficient of proportionality (determined by the calibration of the FS channel of the device), A_{NADH} – normalized fluorescence amplitude of coenzyme NADH.

This new diagnostic parameter makes it possible to assess the relationship between the supply of oxygenated blood to the capillary bed and the utilization of oxygen in tissues.

3 Application Experience in the Clinical Practice

Despite the relatively recent invention of wearable devices in 2 versions (with one LDF channel, as well as with both LDF and FS), since 2018 they have been actively introduced into clinical practice in various fields of medicine – functional diagnostics, endocrinology (diabetes mellitus), cardiology (arterial hypertension), rehabilitation, yoga therapy, and even Space medicine. Next, we will consider several examples of the successful use (in terms of increasing the information content of diagnostics) of these wearable devices in medicine.

Before starting to implement these new wearable devices for solving various diagnostic tasks, the possibilities of using the set of them for multipoint measurements of blood perfusion were investigated [36]. These devices were used to analyze the skin blood flow synchronization in homologous regions of the contralateral limbs, both in the basal state and during various functional (occlusion or breath holding) tests. Studies have shown a high synchronization of blood flow rhythms in the contralateral limbs of healthy volunteers. Portability and low sensitivity to motion artefacts make them more mobile and capable of use even outside the clinic. Furthermore, these wearable devices demonstrate high repeatability of measurements at rest and in physiological tests, which increases the diagnostic value of measurements.

One of the first researches using new wearable devices was the study of changes in blood microcirculation for different age groups. In presented study [37] a higher level of perfusion in areas with glabrous skin of the middle finger pad in the older age group was shown and the measurements taken from the forearms skin on the dorsal wrist surface demonstrated the same tendency. A higher signal level in the older group can be explained by skin thinning during the ageing process, because of which laser radiation is less scattered, increasing the diagnostic volume. In another research [38] the LDF signal was simultaneously recorded from the 3rd fingers' pads of both hands, and amplitudes of the blood flow oscillations and wavelet coherence of the signals were used for the data analysis. Wavelet coherence shows how much the blood flow oscillations coincide in frequency and amplitude. In this case, the magnitude of the amplitudes is not taken into account, the value is the ratio of the amplitudes of the oscillations. The closer the amplitudes are to each other, the higher the coherence (approaching 1), and the closer the similar amplitudes are in the frequency range, the

higher the coherence. Thus, it was discovered that myogenic oscillations of blood perfusion in the younger group had a higher wavelet coherence parameter than in the older group. The obtained data can be considered further in the development of protocols for the studies of MTS in patients with different pathologies.

Another example of research in functional diagnostics is the study of differentiating cardiovascular parameters between healthy young non-smokers and smokers [39]. This study showed a higher level of blood perfusion in the non-smoker group compared to the smoker group and vice-versa for the variation of pulse frequency. This result can be useful to assess the sensitivity of the wearable devices in determining the effect of nicotine for smokers as compared to non-smokers and also the blood microcirculation in smokers with different pathologies.

As one of the examples of the successful use of these wearable devices in the form of a distributed system on the body of endocrinological patients can be this pilot study [40]. In this study, four wearable LDF devices for multipoint measurements of blood perfusion were utilized for microcirculatory function assessment in patients with 2 type diabetes mellitus (DM) and healthy controls of two distinct age groups. The results of the studies have shown that the average perfusion differs between healthy volunteers of distinct age groups and between healthy volunteers of the younger age group and patients with DM. It was noted that the average level of perfusion measured on the wrist in the two groups of healthy volunteers has no statistically significant differences found in similar measurements on the fingertips. This pilot study has shown that the implementation of the LDF as a fiber-free wireless wearable device is a very convenient solution to be applied as point-of-care testing. The measurements in the groups of different ages allowed for the registration of age specific changes in blood perfusion as well as changes that can be associated with the development of DM.

Another promising example of the use of these wearable devices in endocrinology may be the monitoring of the microcirculatory disorders therapy in DM during a standard course of intravenous infusions of alpha-lipoic acid solution [41]. The studies have demonstrated a tendency for a decrease in microcirculation and nutritive blood flow in patients during the course of the therapy and an increase in shunt blood flow. Since it is known that patients with DM show higher values of perfusion, these changes may be associated with a positive effect of the treatment. It was noted that after therapy, the parameters of the patients approximated their values to those of the control group. These changes are especially significantly expressed in the lower and less significantly in the upper limbs. This difference may be explained by the predominant involvement of the microvascular bed of the lower limbs in the development of diabetic complications, due to their higher susceptibility to different stress factors (more pressure due to wearing shoes and bipedalism, etc.).

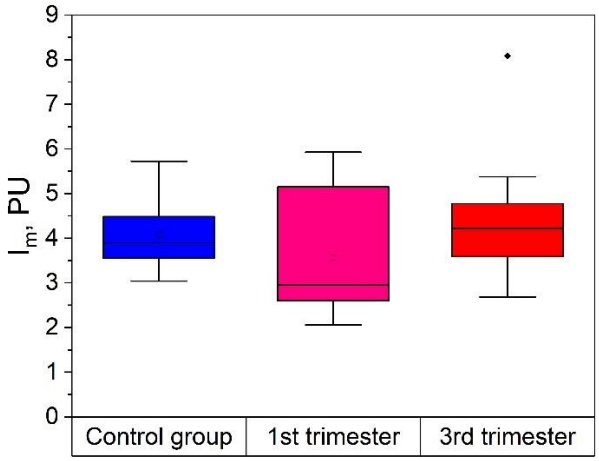
One of the first examples of the application of multimodal wearable diagnostic devices in endocrinology is the study of the effect of pregestational type 1 DM on the state of MTS in patients at different stages of pregnancy [42]. This study is the first to show the combined use of LDF and FS together with glucose variability monitoring to assess vascular function and oxidative metabolic status in 10 pregnant patients with pregestational type 1 DM (the average age of the patients was 32, and all were between 7 and 22 weeks of gestation). All patients also underwent continuous glucose monitoring with the “Libre Freestyle” system (Abbott, US), which was preinstalled subcutaneously in the forearm area. An installed system measured the values of glucose concentration in the intercellular fluid every 15 min for 10–14 days. The LDF and FS data measured at the wrists and shins were also compared with data obtained in a similar way from 7 healthy nonpregnant women with a mean age of 32 years. Fig. 3 demonstrates obtained preliminary results from 2 channels of wearable multimodal devices measured at the shins.

From the data presented in Fig. 3a, it can be seen that the average perfusion does not differ significantly in the analyzed groups. However, the analysis of perfusion frequency rhythms revealed a decrease in the oscillatory activity of the microvasculature in the legs in patients during pregnancy, which may indicate a deterioration in the functional state of microcirculation by the 3rd trimester. The data in Fig. 3b demonstrates a statistically significant increase in the amplitude of the NADH fluorescence intensity in the group of pregnant women, which may be a consequence of impaired tissue respiration. The development of this direction of using wearable multimodal devices is seen in the comparison of LDF and FS monitoring data of patients with their glucose variability monitoring data in order to analyze the possible effects of diurnal blood glucose changes on oxidative metabolism and microcirculation.

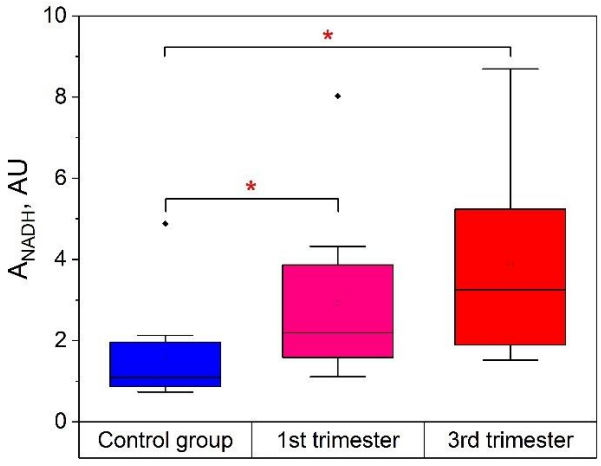
It is also worth noting that the authors [43] could demonstrate the use of peripheral blood flow oscillations analysis with wearable LDF devices to diagnose vascular disorders in patients who have undergone COVID-19 in their early and advanced stages of recovery. Obtained results show a significant increase in the amplitude of neurogenic oscillations in the upper extremities of patients undergoing COVID-19, which may be a factor preceding dilation of arterioles and venules and redirection of microcirculatory blood flow from the nutritive to the shunt pathways. But more research is needed to fully understand the changes in the mechanisms of blood flow regulation that occur after an infection.

The first successful application of wearable devices in cardiology is the study of the functional state of resistive skin microvessels in patients with newly diagnosed arterial hypertension [44]. According to the obtained LDF data, in men with arterial hypertension, there is a decrease in the amplitude (increase in the tone) of neurogenic and myogenic vasomotion, a decrease in

the amplitude of pulse oscillations of microcirculatory flow, a decrease in perfusion efficiency of endothelial, neurogenic, myogenic and pulse mechanisms of tissue perfusion regulation. Of all tone-forming mechanisms, only the myogenic mechanism had a weak negative correlation with systolic blood pressure level. The amplitude of pulse oscillations demonstrated the highest degree of correlation with blood pressure parameters. Thus, the use of wearable devices even with only an LDF channel was suggested to be a useful method for the dynamic monitoring of patients with arterial hypertension.



(a)



(b)

Fig. 3 Average perfusion (a) and normalized NADH fluorescence amplitudes (b) for groups of pregnant women with DM in the 1st and 3rd trimesters at the shins in comparison with the control group. (* – statistical significance of differences was confirmed by the Mann-Whitney test, $p \leq 0.05$).

Another interesting example of using wearable devices is the study of the dynamics of cutaneous blood perfusion and the regulatory mechanisms of blood microcirculation depending on the body position changes. It is known, that changes in hemodynamic parameters depending on the position of the body significantly assist the homeostasis in the limbs and essentially in the sufficiency of blood supply for the brain [45]. Obtained results show the importance of taking into account the position of the body in space during the monitoring of physiological parameters interrelated with blood perfusion. The results can be further implemented for the development of the methodology for the wider use of wearable devices in functional diagnostics. Presented findings of the amplitude-frequency analysis of LDF signals measured in different body positions confirm the earlier assumptions of the measurement technique for the orthostatic test and diagnostic procedures based on it, and more specifically, for the use of this particular type of wearable device together with the physiological tests. The results obtained can be of particular interest for the development of new protocols for the study of microcirculation, including those related to daily monitoring.

4 Application Experience during Space Experiment for Microcirculatory-Tissue Systems Study

A unique example of the successful application of wearable multimodal devices was a Space experiment "LAZMA" aboard the International Space Station (ISS) during the 20th visiting expedition (December 8–20, 2021) [46]. The main goal of this Space experiment was to study for the first time tissue metabolic processes (oxygen utilization by tissues) and microcirculatory blood flow in human skin under zero-gravity conditions.

The "LAZMA" experiment was carried out with a crew of astronauts (2 participated) during the ISS visiting expedition. The measurements were carried out in 3 stages: stage 1 – before spaceflight; stage 2 – during the stay of the crew on the ISS; stage 3 – after the return from spaceflight. Each stage lasted at least 7 days with daily measurements of physiological parameters. The analyzers were placed on the pads of the middle fingers and big toes, on the back of the wrists, and attached to the temples. Each measurement of one study area lasted 8 min during which the astronaut was in a state of complete physical and psychological rest. Fig. 4 shows a typical example of average perfusion and normalized NADH fluorescence amplitude on the pad of the left big toe of one of the astronauts before, during, and after the Space flight.

The obtained preliminary data show an almost complete inversion (especially during Space flight) of 2 recorded signals by different measuring channels. Moreover, in the area selected for analysis (toe), we can see an acute reaction to microgravity in the first 2–3 days of flight, both in a decrease in perfusion and in an increase in the amplitude of NADH intensity. These changes may be related to the redistribution of blood flow in the microcirculation system from the lower to the upper part of the body under the influence of zero-gravity [47–49].

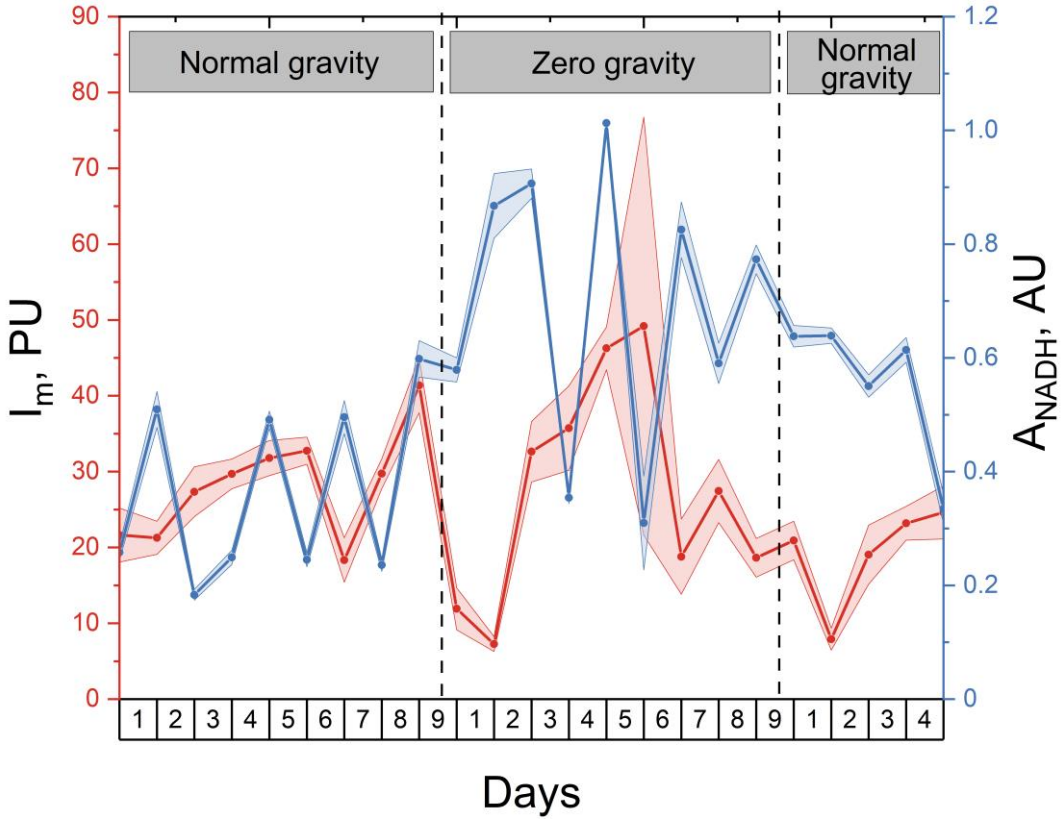


Fig. 4 Average perfusion (red) and normalized NADH fluorescence amplitude (blue) on the pad of the left big toe of one of the astronauts before, during and after Space flight.

Thus, for the first time, a technique has been developed for measuring MTS in the limbs of cosmonauts during the period of acute adaptation to microgravity conditions and readaptation after the completion of a Space flight. Obtaining the most important physiological information in real time under conditions of zero gravity will provide completely new data on the physiology of the MTS in humans under conditions of orbital flight.

5 Conclusion

Thus, in this review, the unique possibilities of using wearable devices to assess the state of the microcirculatory-tissue systems of the human body were demonstrated. In the examples presented over the past 5 years, the possibilities of their effective application in various fields of medicine – functional diagnostics, endocrinology, cardiology, and even in Space medicine have been clearly demonstrated. Moreover, in the case of using 2-channel devices based on a multimodal approach, it becomes possible to evaluate perfusion-metabolic disorders in the biological tissues of patients' limbs.

Thus, the data on the state of the MTS of the human body recorded with wearable multimodal devices make it possible to assess the relationship and dynamics of oxygen utilization more comprehensively and reliably by tissues in a variety of diagnostic tasks. In this regard, in the coming years, they are expected to be even more widely introduced into clinical practice, as well as for monitoring MTS at home, which is especially valuable during quarantine measures.

Disclosures

Author declares that there is no conflict of interests in this paper.

Acknowledgements

The author acknowledges the patients and doctors (G. I. Masalygina, E. A. Alimicheva) of the endocrinology department of the Orel Regional Clinical Hospital (Orel), as well as patients and doctors (D. Sc. A. V. Tiselko) of the gynecology and endocrinology department of the Research Institute of Obstetrics, Gynecology and Reproductology named after D. O. Ott (Saint-Petersburg). Author is very grateful to cosmonaut A. Misurkin for the opportunity to conduct "LAZMA" Space experiment and participation in it; Yu. Maezawa and Yo. Hirano for financial support and participation; SPE LAZMA Ltd. (director – Dr V. Sidorov) for the provision of wearable devices; also – Space Adventures Ltd. (M. Gubaydullin, D. Shapiro), S. P. Korolev Rocket and Space Corporation "Energia" for organizing this mission and Yu. A. Gagarin Research and Test Cosmonaut Training Center (A. Vasin, V. Dronov, P. Saburov, V. Dubinin) for assistance in organizing and conducting pre-flight and post-flight research.

References

1. V. V. Tuchin (ed.), Handbook of Optical Biomedical Diagnostics, Volume 1: Light-Tissue Interaction, 2nd ed., SPIE Press (2016). ISBN: 9781628419092.
2. T. Vo-Dinh (ed.), Biomedical photonics handbook: biomedical diagnostics, CRC press (2014). ISBN: 9780429214295.
3. A. V. Dunaev, "Optical Diagnostics in Human Diseases," Diagnostics 11(5), 873 (2021).
4. A. I. Krupatkin, "Oscillatory Processes in the Diagnosis of the State of Microvascular-Tissue Systems," Human Physiology 44(5), 581–591 (2018).
5. A. I. Zherebtsova, V. V. Dremin, I. N. Makovik, E. A. Zherebtsov, A. V. Dunaev, A. Goltsov, S. G. Sokolovski, and E. U. Rafailov, "Multimodal optical diagnostics of the microhaemodynamics in upper and lower limbs," Frontiers in Physiology 10, 416 (2019).
6. V. V. Dremin, E. A. Zherebtsov, V. V. Sidorov, A. I. Krupatkin, I. N. Makovik, A. I. Zherebtsova, E. V. Zharkikh, E. V. Potapova, A. V. Dunaev, A. A. Doronin, and A. V. Bykov, "Multimodal optical measurement for study of lower limb tissue viability in patients with diabetes mellitus," Journal of Biomedical Optics 22(8), 085003 (2017).
7. K. S. Litvinova, I. E. Rafailov, A. V. Dunaev, S. G. Sokolovski, and E. U. Rafailov, "Non-invasive biomedical research and diagnostics enabled by innovative compact lasers," Progress in Quantum Electronics 56, 1–14 (2017).
8. E. V. Potapova, M. A. Mikhailova, A. K. Koroleva, D. D. Stavtsev, V. V. Dremin, A. V. Dunaev, N. Y. Yakushkina, A. I. Krupatkin, and N. B. Margaryants, "A Multiparametric Approach to the Assessment of Cutaneous Microcirculation in Dermatological Patients (on the Example of Patients with Psoriasis)," Human Physiology 47(6), 619–627 (2021).
9. E. O. Bryanskaya, I. N. Novikova, V. V. Dremin, R. Y. Gneushev, O. A. Bibikova, A. V. Dunaev, and V. G. Artyushenko, "Optical diagnostics of the maxillary sinuses by digital diaphanoscopy technology," Diagnostics 11(1), 77 (2021).
10. E. Potapova, V. Dremin, E. Zherebtsov, and A. Mamoshin, "Multimodal Optical Diagnostic in Minimally Invasive Surgery," Multimodal Optical Diagnostics of Cancer, 397–424 (2020).
11. E. A. Zherebtsov, E. V. Zharkikh, Y. I. Loktionova, A. I. Zherebtsova, V. V. Sidorov, A. I. Krupatkin, and A. V. Dunaev, "Wearable sensors for blood perfusion monitoring in patients with diabetes mellitus," Chapter 5 in Biomedical Photonics for Diabetes Research, A. Dunaev, V. Tuchin (eds.), CRC press, 107–135 (2022).
12. J. Dunn, R. Runge, and M. Snyder, "Wearables and the medical revolution," Personalized Medicine 15(5), 429–448 (2018).
13. A. K. Yetisen, J. L. Martinez-Hurtado, B. Ünal, A. Khademhosseini, and H. Butt, "Wearables in Medicine," Advanced Materials 30(33), 1706910 (2018).
14. A. V. Dunaev, "Methodology of microcirculatory-tissue systems multimodal optical diagnostics," Proceedings of SPIE 12192, 121920T (2022).
15. A. V. Dunaev, "Multiparameter optical methods and instruments for the diagnostics of human body microcirculatory-tissue systems," Proceedings of SPIE 11845, 1184505 (2021).
16. K. Kuwabara, Y. Higuchi, T. Ogasawara, H. Koizumi, and T. Haga, "Wearable blood flowmeter appcessory with low-power laser Doppler signal processing for daily-life healthcare monitoring," in 36th Annual International Conference of the IEEE Engineering in Medicine and Biology Society, 6274–6277 (2014).
17. W. Iwasaki, H. Nogami, S. Takeuchi, M. Furue, E. Higurashi, and R. Sawada, "Detection of site-specific blood flow variation in humans during running by a wearable laser Doppler flowmeter," Sensors (Switzerland) 15, 25507–25519 (2015).
18. V. V. Sidorov, Y. L. Rybakov, V. M. Gukasov, and G. S. Evtushenko, "A System of Local Analyzers for Noninvasive Diagnostics of the General State of the Tissue Microcirculation System of Human Skin," Biomedical Engineering 55(6), 379–382 (2022).
19. E. Zherebtsov, S. Sokolovski, V. Sidorov, I. Rafailov, A. Dunaev, and E. U. Rafailov, "Novel wearable VCSEL-based blood perfusion sensor," in International Conference Laser Optics 10063, 564 (2018).
20. M. J. Leahy, F. F. M. de Mul, G. E. Nilsson, and R. Maniewski, "Principles and practice of the laser-Doppler perfusion technique," Technology and Health Care 7(2-3), 143–162 (1999).
21. A. Stefanovska, M. Bracic, and H. D. Kvernmo, "Wavelet analysis of oscillations in the peripheral blood circulation measured by laser Doppler technique," IEEE Transactions on Biomedical Engineering 46(10), 1230–1239 (1999).
22. A. Tankanag, N. Chemeris, "Application of the adaptive wavelet transform for analysis of blood flow oscillations in the human skin," Physics in Medicine & Biology 53(21), 5967 (2008).
23. E. Zherebtsov, I. Kozlov, V. Dremin, A. Bykov, A. Dunaev, and I. Meglinski, "Diagnosis of skin vascular complications revealed by time-frequency analysis and laser Doppler spectrum decomposition," IEEE Transactions on Biomedical Engineering 70(1), 3–14 (2023).

24. A. V. Dunaev, V. V. Sidorov, A. I. Krupatkin, I. E. Rafailov, S. G. Palmer, N. A. Stewart, S. G. Sokolovski, and E. U. Rafailov, "Investigating tissue respiration and skin microhaemocirculation under adaptive changes and the synchronization of blood flow and oxygen saturation rhythms," Physiological Measurement 35(4), 607–621 (2014).
25. P. Kvandal, S. A. Landsverk, A. Bernjak, A. Stefanovska, H. D. Kvernmo, and K. A. Kirkebøen, "Low-frequency oscillations of the laser Doppler perfusion signal in human skin," Microvascular Research 72(3), 120–127 (2006).
26. A. Bandrivskyy, A. Bernjak, P. McClintock, and A. Stefanovska, "Wavelet phase coherence analysis: application to skin temperature and blood flow," Cardiovascular Engineering: an International Journal 4, 89–93 (2004).
27. R. Martini, A. Bagno, "The wavelet analysis for the assessment of microvascular function with the laser Doppler fluxmetry over the last 20 years. Looking for hidden informations," Clinical Hemorheology and Microcirculation 70(2), 213–229 (2018).
28. A. I. Krupatkin, "Influence of sensory peptidergic innervation on human skin blood flow oscillations in the range 0.047–0.069 Hz," Human Physiology 33, 296–301 (2007).
29. G. J. Hodges, A. T. Del Pozzi, "Noninvasive examination of endothelial, sympathetic, and myogenic contributions to regional differences in the human cutaneous microcirculation," Microvascular Research 93, 87–91 (2014).
30. A. V. Dunaev, V. V. Dremin, E. A. Zherebtsov, I. E. Rafailov, K. S. Litvinova, S. G. Palmer, N. A. Stewart, S. G. Sokolovski, and E. U. Rafailov, "Individual variability analysis of fluorescence parameters measured in skin with different levels of nutritive blood flow," Medical Engineering & Physics 37(6), 574–583 (2015).
31. A. Mayevsky, B. Chance, "Oxidation–reduction states of NADH in vivo: From animals to clinical use," Mitochondrion 7(5), 330–339 (2007).
32. A. V. Dunaev, E. A. Zherebtsov, D. A. Rogatkin, N. A. Stewart, S. G. Sokolovski, and E. U. Rafailov, "Novel measure for the calibration of laser Doppler flowmetry devices," Proceedings of SPIE 8936, 89360D (2014).
33. E. V. Zharkikh, Y. I. Loktionova, V. V. Dremin, K. V. Podmasteryev, V. V. Sidorov, E. U. Rafailov, and A. V. Dunaev, "Comparison of wearable and bedside laser Doppler flowmetry and fluorescence spectroscopy monitors," Proceedings of SPIE 12192, 121920J (2022).
34. E. A. Zherebtsov, K. Y. Kandurova, E. S. Seryogina, I. O. Kozlov, V. V. Dremin, A. I. Zherebtsova, A. V. Dunaev, and I. Meglinski, "The influence of local pressure on evaluation parameters of skin blood perfusion and fluorescence," Proceedings of SPIE 11065, 110650R (2017).
35. E. V. Zharkikh, Y. I. Loktionova, G. I. Masalygina, A. I. Krupatkin, V. V. Sidorov, and A. V. Dunaev, "Optical noninvasive diagnostics of dynamic changes in the level of blood microcirculation and oxidative metabolism using temperature tests," Proceedings of SPIE 11363, 1136321 (2020).
36. E. A. Zherebtsov, E. V. Zharkikh, I. Kozlov, A. I. Zherebtsova, Y. I. Loktionova, N. B. Chichkov, I. E. Rafailov, V. V. Sidorov, S. G. Sokolovski, A. V. Dunaev, and E. U. Rafailov, "Novel wearable VCSEL-based sensors for multipoint measurements of blood perfusion," Proceedings of SPIE 10877, 1087708 (2019).
37. Y. I. Loktionova, E. V. Zharkikh, I. O. Kozlov, E. A. Zherebtsov, S. A. Bryanskaya, A. I. Zherebtsova, V. V. Sidorov, S. G. Sokolovski, A. V. Dunaev, and E. U. Rafailov, "Pilot studies of age-related changes in blood perfusion in two different types of skin," Proceedings of SPIE 11065, 110650S (2019).
38. Y. I. Loktionova, E. A. Zherebtsov, E. V. Zharkikh, I. O. Kozlov, A. I. Zherebtsova, V. V. Sidorov, S. G. Sokolovski, I. E. Rafailov, A. V. Dunaev, and E. U. Rafailov, "Studies of age-related changes in blood perfusion coherence using wearable blood perfusion sensor system," Proceedings of SPIE 11075, 1107507 (2019).
39. M. Saha, V. Dremin, I. Rafailov, A. Dunaev, S. Sokolovski, and E. Rafailov, "Wearable Laser Doppler Flowmetry Sensor: A Feasibility Study with Smoker and Non-Smoker Volunteers," Biosensors 10(12), 201 (2020).
40. E. A. Zherebtsov, E. V. Zharkikh, I. O. Kozlov, Y. I. Loktionova, A. I. Zherebtsova, I. E. Rafailov, S. G. Sokolovski, V. V. Sidorov, A. V. Dunaev, and E. U. Rafailov, "Wearable sensor system for multipoint measurements of blood perfusion: Pilot studies in patients with diabetes mellitus," Proceedings of SPIE 11079, 110791O (2019).
41. E. V. Zharkikh, Y. I. Loktionova, V. V. Sidorov, A. I. Krupatkin, G. I. Masalygina, and A. V. Dunaev, "Control of Blood Microcirculation Parameters in Therapy with Alpha-Lipoic Acid in Patients with Diabetes Mellitus," Human Physiology 48(4), 456–464 (2022).
42. E. Zharkikh, Y. Loktionova, A. Zherebtsova, M. Tsyganova, E. Zherebtsov, and A. Tiselko, "Skin Blood Perfusion and Fluorescence Parameters in Pregnant Women with Type 1 Diabetes Mellitus," in 2021 International Conference on Electrical Engineering and Photonics (EExPolytech), 238–240 (2021).
43. E. V. Zharkikh, Y. I. Loktionova, A. A. Fedorovich, A. Y. Gorshkov, and A. V. Dunaev, "Assessment of Blood Microcirculation Changes after COVID-19 Using Wearable Laser Doppler Flowmetry," Diagnostics 13(5), 920 (2023).

44. A. A. Fedorovich, Y. I. Loktionova, E. V. Zharkikh, A. Y. Gorshkov, A. I. Korolev, V. A. Dadaeva, O. M. Drapkina, and E. A. Zherebtsov, "Skin microcirculation in middle-aged men with newly diagnosed arterial hypertension according to remote laser Doppler flowmetry data," Microvascular Research 144, 104419 (2022).
45. A. A. Fedorovich, Y. I. Loktionova, E. V. Zharkikh, M. A. Mikhailova, J. A. Popova, A. V. Suvorov, and E. A. Zherebtsov, "Body position affects capillary blood flow regulation measured with wearable blood flow sensors," Diagnostics 11(3), 436 (2021).
46. A. V. Dunaev, E. V. Zharkikh, Y. I. Loktionova, A. A. Fedorovich, V. V. Sidorov, A. V. Vasin, A. A. Misurkin, and V. I . Dubinin, "Application of wearable multimodal devices to study microcirculatory-tissue systems under microgravity conditions," Proceedings of International Conference Laser Optics, 20–24 (2022).
47. O. G. Gazenko, E. B. Shulzhenko, V. F. Turchaninova, and A. D. Egorov, "Central and regional hemodynamics in prolonged space flights," Acta Astronautica 17(2), 173–179 (1988).
48. H. Zhu, H. Wang, and Z. Liu, "Effects of real and simulated weightlessness on the cardiac and peripheral vascular functions of humans: A review," International Journal of Occupational Medicine and Environmental Health 28(5), 793 (2015).
49. J. A. Popova, A. V. Suvorov, R. N. Zaripov, and A. I. Dyachenko, "Exposure of inspiratory negative pressure breathing on cosmonauts during spaceflight," Acta Astronautica 199, 438–444 (2022).

Machine Learning Algorithms for the Analysis of Age-Related Macular Degeneration Based on Optical Coherence Tomography: a Systematic Review

Ekaterina A. Lopukhova[1*], Rada R. Ibragimova[2,3], Gulnaz M. Idrisova[2,3], Irina A. Lakman[1,2], Timur R. Mukhamadeev[2,3], Elizaveta P. Grakhova[1], Azat R. Bilyalov[2], and Ruslan V. Kutluyarov[1]

[1] Ufa University of Science and Technology, 32 Zaki Validi str., Ufa 450076, Russia

[2] Bashkir State Medical University, 3 Lenina str., Ufa 450008, Russia

[3] CJSC "Optimedservice", 145 Khudayberdina str., Sterlitamak 453128, Russia

***e-mail:** lopuhova.ekaterina@net.ugatu.su

Abstract. Age-related macular degeneration (AMD) is one of the leading causes of irreversible blindness. Every year, there is an increase in the number of patients with AMD worldwide. To date, the primary method in diagnosing AMD is optical coherence tomography (OCT), which provides the most visual data for identifying disease biomarkers. However, a growing volume of research requires optimizing the work of an ophthalmologist to minimize diagnostic errors. In this regard, the study aimed at integrating computer vision applications into the OCT image processing system is gaining popularity since it allows not only to identify images with the most likely presence of AMD but also to determine the stages of this disease, localize biomarkers and obtain a prognosis for the dynamics of its development. The variety of such approaches is expressed in the application of various machine learning algorithms, metrics for evaluating their effectiveness, sources of input information, and work verification. This statistical review analyzes examples of works devoted to computer vision algorithms in the study of OCT images for diagnosing, staging, or predicting the dynamics of AMD and highlights the features and trends within this area. © 2023 Journal of Biomedical Photonics & Engineering.

Keywords: optical coherence tomography; age-related macular degeneration; machine learning; deep learning.

Paper #3570 received 7 Dec 2022; revised manuscript received 6 Mar 2023; accepted for publication 8 Mar 2023; published online 28 Apr 2023. doi: 10.18287/JBPE23.09.020202.

1 Introduction

Age-related macular degeneration (AMD) is a multifactorial disease, one of the leading causes of irreversible blindness worldwide [1]. According to the massive Beaver Dam Eye Study, over ten years of follow-up, the incidence of AMD in individuals aged 43–54 years increased by an average of 4.2%, and in those aged 75 years and older, by 46.2% [2]. Rising morbidity leads to decreased working capacity and disability of the population, which is a medical and social problem [3–5].

The disappointing dynamics of the disease's spread have generated many reviews on various aspects. Thus, an analysis of the AMD prevalence shows risk groups and the epidemiological situation over time [6–8], while the study of risk factors and pathogenesis provides the trend in the distribution of the patients, possible preventive measures, and method to slow down the progression [9–13]. Finally, many studies are devoted to modern advances in treating AMD [14–19].

The timely detection and staging of AMD based on already explored pathogenetic reactions is the leading assurance of successful therapy, which is the aim of various diagnostic methods.

To date, the predominant approaches for diagnosing AMD and other retinal diseases are methods of visualization of the retinal layers. These include autofluorescence photography, dilated eye examination, fundoscopy or ophthalmoscopy, visual acuity eye testing, fundus photography, fluorescein angiography, tonometry, and optical coherence tomography (OCT). The most recognized and frequently used are the non-invasive Color fundus photography (CFP) and OCT methods [20].

The advantages of the CFP are high data acquisition speed, reproducibility, high resolution, and simple image acquisition. Thanks to that, CFP is a widely used method for digital imaging of the retina. However, the quality of CFP images in the presence of macular edema without stereoscopic visualization is limited and time-consuming [21].

In turn, OCT provides three-dimensional cross-sectional *in vivo* visualization of the retina to assess the layers' thickness and the presence or absence of pathologies. Moreover, it helps monitor treatment effectiveness, necessity, and expected response [22–24]. In 1991, OCT was first described as a possible retinal imaging tool [25]. Since then, OCT has become of great importance in diagnosing diseases of the macular area, particularly AMD [26]. Drusen, hypopigmentation or hyperpigmentation of the retinal pigment epithelium, atrophy of the pigment epithelium and choriocapillaris, neovascularization, detachment of the pigment epithelium and retinal neuroepithelium, intraretinal deposits, cystic edema of the neuroepithelium, subretinal scarring are typical retinal changes that are detected using spectral domain OCT (SD-OCT) method in patients with AMD [27, 28]. Thus, in diagnosing and monitoring AMD, OCT methods are the most effective and promising for further development [29].

The possibility of storing and processing digitized archives of diagnostic images opens up vast opportunities for the development of methods for their automatic processing. Intelligent data processing methods have been widely used [30–32]. A sufficient amount of information presented in digital form makes it possible to carry out statistical analysis and intelligent data processing [33]. Modern computer vision methods based on machine learning (ML) algorithms allow the most efficient visual information processing [34]. Recent studies in integrating recommender systems based on ML algorithms into ophthalmology demonstrate impressive results in reducing the time for diagnosis and the impact of the human factor [35, 36].

There are many reviews on using ML algorithms to analyze visual information from retinal scans. CFP data analysis is represented by a rather extensive range of studies, primarily due to the prevalence of devices [37, 38]. After the introduction of SD-OCT devices with high scanning speed and sufficient visualization accuracy, an increase in the number of reviews of the use of ML for OCT data analysis [39] and both OCT and CFP began [40–42]. However, these reviews do not provide detailed information about all articles on the number of images in the dataset [39], the use of image preprocessing [39, 40], validation to assess the generalizing ability of algorithms, which demonstrates the stability of the algorithm [39–41], and the use of ML in image biomarker segmentation tasks [42]. Due to insufficient research features under consideration, it is not always possible to assess the factors that increase the likelihood of developing an effective application for analyzing OCT images with AMD. In turn, analyzing the dynamics of these research traits over time can demonstrate their "natural selection", which identifies the most viable ones.

The increase in the incidence of AMD determines the need for the introduction of productive tools for the intelligent analysis of medical images to improve the effectiveness of patient treatment, including dynamic monitoring. A convenient tool for specialists who assume the use of machine learning methods in diagnosing and treating AMD with the help of OCT would be the complete review of the proposed solutions, considering their effectiveness and maturity. To date, there is no such review to our knowledge. Therefore, the task of this work is a systematic review that aims to analyze the evolution of the ML application for diagnosing, staging, and predicting the dynamics of AMD by OCT, as well as searching and isolating biomarkers on OCT images, substantiating the specifics and conclusions that will be useful to ML users in ophthalmology.

2 Materials and Methods

2.1 Selecting Publications

In the research, we systematically reviewed papers in the international databases Pubmed, Scopus, Nature, and The Lancet, and the Russian database eLibrary. The search was focused on methods for extracting data from OCT images using ML, aimed at identifying predictors for the presence of AMD, its stage, and dynamics. To show the variety of approaches and their performance, we added to the selection studies, in which OCT data was processed with other information about the patient and, in addition to AMD, diagnosed other retinal diseases.

Thus, the search criterion was the presence in the title, abstract, and/or keywords of the terms: "optical coherence tomography", "age-related macular degeneration", "machine learning", "deep learning", "neural network", "artificial intelligence". The logical relationships of these terms were built in such a way that the first two of the above always appeared in queries with the "AND" operator, the rest with "OR": term No. 1 & term No. 2 & (term No. 3 | term No. 4 | term No. 5). Another limitation was the publication in the period from 2017 to 2022 inclusive. A link to the database or a digital DOI uploaded the full text.

After gathering the search results, we subsequently filtered them in several steps. The first step excluded duplications between databases and non-full-text articles,

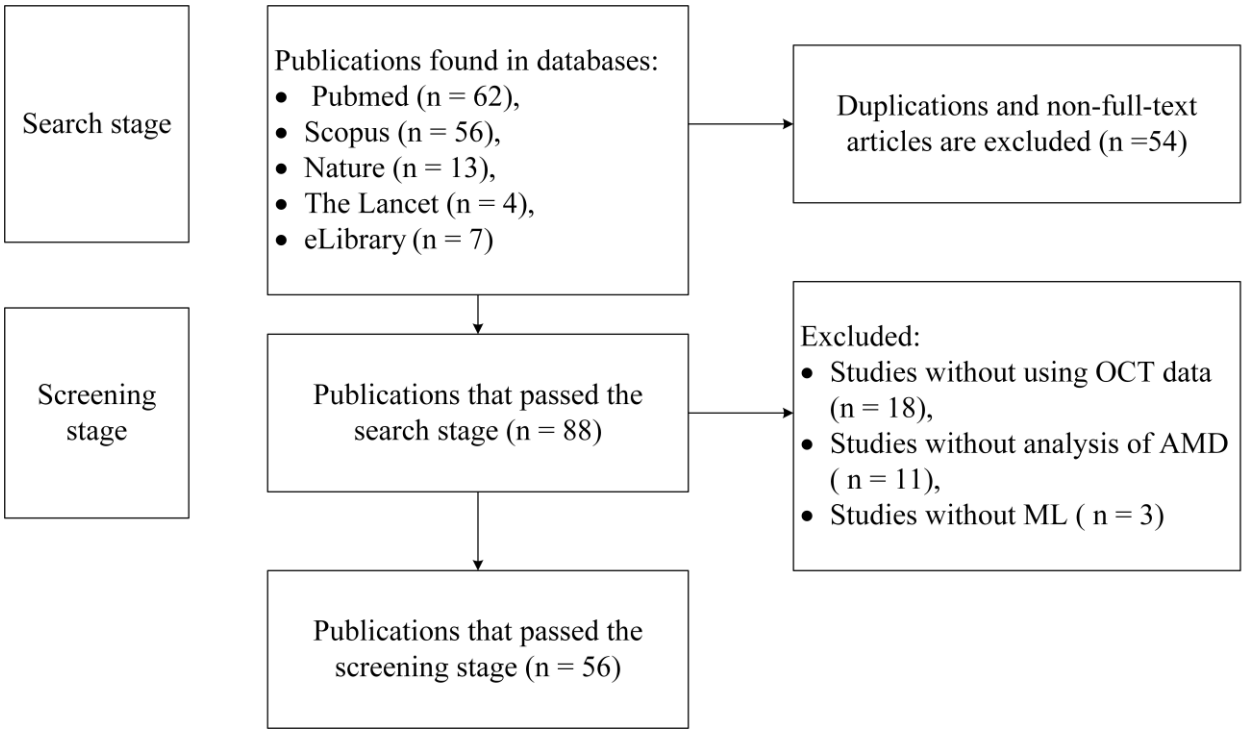


Fig. 1 Flowchart for systematic review.

and the screening step evaluated the relevance of the content to the search goal. We excluded the papers of three categories: where the retina analysis did not rely on OCT data, AMD or related pathologies were not included in the list of detected objects, or ML methods were not implied (Fig. 1). Thus, 142 studies were found, of which 54 were screened out at the search stage, including 42 duplications and 13 non-full-text articles. At the screening stage, 32 papers were removed, i.e., 18 relied on data from the fundus camera, 11 without the AMD diagnosing, and three without ML, after which 56 papers remained for inclusion in the study.

2.1 The Analysis of Publications

For the analysis, the following points were identified that characterize the features of ML performance in diagnosing AMD and other retinal diseases:

1. Date of publication, providing to track the time trend of this topic.
2. Data sources, including the existing databases of OCT images, without specifying the tomograph or other specific equipment.
3. Number of OCT images included in the dataset.
4. Tasks to be solved regarding the application of the ML algorithm:

a) classification as the problem solution for direct diagnostics;

b) segmentation to allocate the pathologies markers of a particular disease, which are the desired features of this type of image since they most fully characterize the state of the retina in the OCT image;

c) a multimodal approach using multiple sources of patient data;

d) a recommender system based on the patient data analysis and designed to accompany the diagnostician's decision.

5. Validation of the algorithm, demonstrating the degree of its generalization and the scope of its relevance.
6. The Technology Readiness Level of the proposed algorithm.

The indicators in feature 4 are not mutually exclusive since they can include each other as intermediate steps, comparable to classifying/diagnosing a disease by analyzing the selected form of pathologies achieved using segmentation. In turn, feature 5 directly influenced the assessment of feature 6, both for cross-validation of the solutions with the defined application and for solutions operating with new data aiming to increase the application area.

At the same time, the following features were identified for greater detail of the methods used:

1. pre-processing of images to facilitate the operation of the ML algorithm or extract the initial parameters;
2. research methods indicating the type of algorithm used;
3. the software for the algorithm implementation;
4. metrics used to evaluate the algorithms performance;
5. distinguished classes/features during the operation of the algorithm.

It is worth noting that features 2 and 4 were not indicated in some studies, which was especially common for those with TRL3.

3 Results

3.1 Initial Data

The papers in the final list included 11 Pubmed articles, 31 in Scopus, 10 in Nature, 2 in The Lancet, and 2 in eLibrary. Of all the papers, one was in Russian, and all the rest were in English. We used only Russian and English for the search, allowing for unaccounted articles published in other languages (Japanese, Chinese, etc.).

For a systematic analysis, the results were detailed according to the main features presented in Section 2.2 (Table 1). The detailed methods are given in the Table 2.

The trend of the publications' distribution over time makes it evident that the popularity of computer vision in AMD diagnosing by OCT images has risen dramatically.

Table 1 Initial data of research detailing.

Feature	Number	%	References
Publication year			
2017	4	7.14	[43, 49, 55, 59]
2018	5	8.93	[45, 46, 50, 53, 64]
2019	12	21.43	[44, 48, 60, 65–73]
2020	10	17.86	[47, 58, 62, 74–80]
2021	14	25.00	[51, 61, 63, 81–90]
2022	11	19.64	[52, 56, 57, 91–98]
Data sources			
Database	15	27.00	[43, 45, 48, 58, 59, 63, 65, 70, 71, 73, 76, 77, 85, 90]
Tomographs	41	73.00	[12, 20, 32, 34–36, 38–41, 44, 22, 45, 46, 48, 49, 58–63, 23, 64–73, 24, 74, 75, 25–28, 30]
Tasks to be solved			
Multimodality-classification	9	16.07	[49, 65, 68, 70, 84, 86, 89, 93, 96]
Classification	29	51.79	[43, 45, 48, 49, 55–61, 63, 67, 71–73, 79–81, 85–87, 90, 94–96, 99]
Segmentation	33	58.93	[44–47, 49–53, 57–66, 68–70, 74–77, 83, 88, 89, 91–93, 97]
Recommender system	11	19.64	[46, 49, 59, 69, 76, 78, 81, 82, 88, 93, 98]
Technology readiness level			
TRL3	26	46.43	[43–48, 55, 56, 62, 65, 66, 70, 72–74, 79, 81, 83, 85, 90, 94, 95, 99]
TRL4	25	44.64	[48–50, 53, 55, 57, 58, 61, 63, 67, 68, 75–78, 80–82, 84, 86–89, 91, 95]
TRL5	5	8.93	[51, 52, 59, 60, 97]
Number of OCT images in the dataset			
hundreds	11	19.6	[15, 44, 49, 57, 68–70, 92, 93, 96, 98]
thousands	23	41.07	[43, 47, 50–53, 55, 56, 61, 65, 66, 75, 77, 81, 83, 84, 86–89, 94, 95, 97]
tens of thousands	16	28.6	[46, 60, 63, 64, 67, 71–74, 78–80, 85, 90, 91, 99]
hundreds of thousands	5	9	[48, 58, 59, 76, 82]

Table 2 Detailing of research methods.

Characteristics of methods	Number	%	References
Image pre-processing			
Without pre-processing	36	64.29	[46, 47, 50–52, 55, 57, 61, 66, 67, 69, 70, 72–74, 77–83, 85–91, 93–99]
Normalization	8	14.29	[45, 58, 59, 63, 64, 71, 75, 76]
Augmentation	11	19.64	[21, 53, 56, 60, 63, 65, 71, 76, 79, 90, 92]
Noise suppression	4	7.14	[45, 48, 62, 84]
Salient Patch Detection	6	10.71	[43–45, 49, 62, 68]
Research methods			
Conventional ML methods	7	12.50	[43–46, 48, 49, 51]
Deep learning models	49	87.50	[46, 47, 50, 52, 53, 55, 56, 58–99]
Software			
Not specified	36	64.29	[43, 45, 46, 48, 49, 51, 53, 60–63, 67–69, 71, 72, 74, 75, 78–85, 87–89, 91, 92, 94–98]
MATLAB	4	7.14	[44, 52, 65, 76]
Python	16	28.57	[47, 50, 55–59, 64, 66, 70, 73, 77, 86, 90, 93, 99]
Metrics			
Kappa parameter	5	8.93	[60, 86, 89, 95, 96]
Intraclass correlation coefficient (ICC)	6	10.71	[53, 61, 64, 70, 83, 92]
Pearson's correlation coefficient (PCC)	2	3.57	[52, 74]
Jaccard index (IOU)	2	3.57	[62, 66]
Determination coefficient (R^2)	3	5.36	[47, 74, 82]
Dice similarity coefficient (DSC)	12	21.43	[44, 45, 53, 61, 62, 64, 68, 83, 88, 89, 91, 97]
F1-score	11	19.64	[51, 55, 61, 79, 80, 84–86, 93, 99]
Quadratic error (RMSE)	1	1,79	[44]
Point of interest (POI)	1	1.79	[57]
CAMs	6	10.71	[57, 58, 85, 87, 90, 95]
AUS	21	37.50	[43, 46, 48, 49, 57, 58, 65, 67–69, 75, 76, 78, 80–83, 85, 87, 96, 98]
precision/recall	12	21.43	[48, 57, 62, 65, 67, 68, 79, 81, 85, 91, 97, 99]
Regression coefficient	3	5.36	[51, 59, 82]
Sensitivity/specificity	21	37.50	[43, 49, 51, 55, 57, 59, 61, 63, 65, 67, 71–73, 77, 79, 81, 86, 87, 89, 93, 98]
Accuracy, %	25	44.64	[48, 50, 51, 55–57, 59–61, 63, 65, 67, 71–73, 81, 84, 85, 87, 90, 93–95, 98, 99]
Validation	31	55.36	[46, 48–50, 52, 55, 57–59, 61, 63, 65, 67–69, 73, 75, 76, 78–82, 86, 89, 91, 92, 95, 96, 99]
Distinguishable classes/features			
Binary classification (absence/presence of AMD)	4	7.14	[55, 62, 73, 87]
AMD and other diseases	12	21.43	[45, 56, 60, 63, 72, 76, 87, 90, 92, 95, 96, 99]
Stages of AMD	15	26.79	[43, 46, 48, 57, 65, 67, 69, 71, 77–79, 84, 86, 93, 94]
AMD biomarkers	28	50.00	[44, 47, 49–53, 58, 61–64, 66, 68–70, 74, 75, 83–85, 88, 89, 91–93, 97]
Prognosis of the disease dynamics	11	19.64	[49, 51, 59, 67, 69, 75, 77, 78, 81, 82, 98]

ML algorithms used in computer vision can be divided into standard (without using multilayer neural networks) and deep learning methods. The standard ML methods include classification based on the visual dictionary [43], pathology detection based on clustering of retinal layers [44, 45], layer and pathology segmentation based on graphs [46, 47] and disease markers identification based on support vectors for finding clusters of superpixels extracted with a shallow autoencoder [48] and voxel clusters for 3D-OCT [49]. Also, standard methods are used in ophthalmological devices' software for automatic retinal layers segmentation, where graph-based methods have become very popular [50–52].

Over the past few years, deep learning methods have become more prevalent than standard ML methods. Firstly, the reason is that standard methods have a greater tendency to operate on the "ad-hoc" principle, which, on average, increases their performance with the data sources considered in the study, however limiting their generalizing abilities [53, 54]. Secondly, the evolution of deep learning possibilities is promoted by accumulating a large amount of OCT data and improving its quality by enhancing the visualizing mechanisms of optical equipment [55–57]. As part of the growing popularity of deep learning in diagnosing/classifying AMD and other retinal diseases, there is a trend towards using segmented biomarkers on OCT images as predictors [45, 49, 57–63]. That is due to the previously stated conclusions, coupled with improving the elaborateness of deep learning methods without a high risk of overfitting.

Many studies have demonstrated the high efficiency of OCT image analysis. However, the results can significantly change in natural experiments with data from sources not represented in the training set. Therefore, in the application's design, it is essential to understand the generalizing ability of the algorithm, carrying out verification using cross-validation and other data sets from different sources, e.g., ophthalmic equipment from various manufacturers and/or various patient samples.

The division of the proposed solutions by TRL relied on the results' maturity, the size of the training and test datasets, and the procedure of verification. For TRL3, the idea was typically experimentally confirmed with data from the training set provided by a single database or one type of commercial tomograph. TRL4 included the concept validation on data from various sources, while for TRL5, the proposed ideas were tested during the diagnostics in natural conditions. The most significant results with TRL5 have been published over the past year, demonstrated in Table 1, indicating the relevance of these methods in OCT diagnostics.

The algorithm's generalizing ability strongly depends on the training dataset's size when operating with actual data. At the same time, the relevance of performance indicators for the entire variety of input data depends on the test dataset. In studies using several hundred examples obtained from one or two brands of tomographs, the applicability of the results is severely limited. However, such an approach can be practical for testing the concepts of AMD data processing at low dataset costs [44, 45, 69, 70, 92, 93, 96, 98].

In most papers, a dataset contained thousands of OCT image examples obtained by the collaboration of several institutions that provided their databases of OCT images, which made it possible to bring more hardware and racial diversity into the dataset. In addition to direct data collection, many studies use publicly available datasets to generate tens of thousands of images, including the most popular OCT2017 [100]. For example, this dataset was used both for training and testing the algorithm [71, 72, 90] and only for training in Refs. [63, 79], while for testing, researchers assembled a separate small set (hundreds of images).

The most extensive datasets of hundreds of thousands of OCT images were created by using large databases accumulated over a long period [59, 76, 82], or by merging several databases into one dataset [48, 58]. The ML algorithm trained on such a dataset will potentially have the highest generalizing ability, as well as adequate behavior on the entire variety of input data. It should be noted that regardless of the size of the dataset, the distribution of standard and non-standard ML algorithms applied in the studies has minimal differences.

Finally, several papers on the analysis of the AMD progression over time do not indicate the exact number of images in the dataset [49, 52, 67, 69, 70, 73, 75]. In such cases, we calculated the number of samples based on the provided information on the study's duration, the number of eyes examined, and the frequency of scanning patients.

Several studies have used image augmentation and Generative Adversarial Networks (GAN) [60, 64, 68, 70], synthesizing OCT images with AMD to move up to the larger category regarding the number of scans. However, in the case of GAN, the generated dataset must be peer-reviewed to filter out the most outliers from the real picture, in addition to using methods to measure the similarity between two images like the Structural Similarity Index Measure (SSIM) [70]. The usefulness of augmentation, in turn, is limited by the fact that the images obtained on its basis have a certain tilt of the retina. However, in most modern tomographs, the presentation of OCT images of the retina occurs with layer alignment.

Regarding the sources of OCT data, the public databases were typical for studies of image classification with TRL3 [43, 45, 48, 56, 58, 65, 70, 71, 73, 90]. At the same time, studies identified as TRL4 [63, 76, 77, 87] indicated the data on institutions and other sources that provided databases for compiling the dataset. However, they did not provide specific equipment brands for obtaining OCT images. In turn, for pathologies segmentation, in which the features of visualization and OCT images' resolution play a significant role, the optical devices were specified in most studies.

Most of the papers that mentioned the brand of the tomograph used SD-OCT technology, as it has become very popular in research and medical institutions due to its high scanning speed. The prevalence of this

technology among images in datasets was also noted in a review paper devoted to the direct diagnosis of AMD [42]. Along with SD-OCT, the Swept Source OCT (SS-OCT) technology is employed [52, 66, 81, 92], which allows to achieve of higher scanning speeds with high resolution [101]. All studies based on SS-OCT used convolutional neural networks (CNN) for biomarker extraction [52, 66, 92] and analysis of disease dynamics [81]. At the same time, the performance indicators of the algorithm for SS-OCT are at the level of similar works for SD-OCT. To isolate biomarkers in three dimensions, 3D-OCT is typically used, which potentially provides more information about their actual shape [44, 47, 66, 76, 83, 88, 93] and dynamics of changing [69, 77, 82].

As already noted, the classification primarily relied not only on the preliminary visual data processing when extracting features for ML algorithms [43, 48] or arbitrary parameter selection by deep learning algorithms [43, 48, 55, 56, 67, 71–73, 79–81, 86, 87, 90, 95,96, 99], but rather on selected image segments associated with the pathologies of diseases [45, 49, 58, 61–63, 84, 85]. Such solutions, in some cases, demonstrate a more remarkable generalizing ability and easier verifiability of the algorithm.

The multimodal approach was performed for pathologies segmentation on OCT and images from the fundus camera, where the correlated appearance of disturbances helped to estimate the probability of their presence [49, 65, 70, 84, 86, 89], or when processing images of several OCT modes together [68, 93, 96].

Existing recommender systems use the above methods with the application of risk models based on the information received. Examples of such systems are predictive models for evaluating AMD treatment strategies through intravitreal injection of a blocking vascular endothelial growth factor. That is especially true since such treatment is expensive. Therefore, methods have been proposed to predict the injection response based on an OCT image before the procedure [55, 61, 78, 81, 98] or identify accumulation areas of fluid and its type in the macula [46, 52, 53, 59, 76]. Other forms of recommender systems allowed the prediction of AMD progression by biomarkers [49, 69, 75, 88, 93].

3.2 Research Methods

Since the form of retinal disease biomarkers varies depending on patients' race [102], there is a need to increase the generalizing ability of OCT image analysis algorithms. At the same time, a high generalizing ability is necessary for processing data from several types of tomographs since they have different visualization features of OCT images. A more detailed specification of the methods used showed the predominant advantage of neural network approaches due to the potentially high generalizing ability for various characteristics of input data [54]. Accordingly, using neural network approaches, combined with training on an extensive data set, can significantly increase the efficiency of allocating biomarkers for diseases. [49, 66, 76] and allow you to create an application designed to work with data from several types of tomographs [44, 52, 53].

Another feature of deep learning is the transfer learning ability, which uses neural networks pre-trained on a large data set. That enables efficiently detecting of objects with just a priori data about their boundaries and textures, which in some cases demonstrated a boost in performance indicators in comparison with similar architectures without transfer learning [55, 63, 67, 73, 76, 85, 95]. However, due to the specificity of OCT images and pathologies, as well as the relatively large number of parameters in pre-trained models, some studies deliberately did not use transfer learning [57, 90]. Regarding the last argument, a real-time OCT data analysis based on deep learning methods requires a limited number of free parameters to reduce the computational complexity that affects the maximum system response time [56].

Convolutional neural networks have demonstrated their significance in a variety of computer vision applications and, as expected, have been used in the majority of works that use deep learning for processing OCT images [46, 47, 52, 53, 55–99]. However, in some cases, recurrent neural networks are preferable since they have shown high efficiency in assessing the dynamics of various processes over time. In conjunction with convolutional networks, recurrent neural networks can obtain potentially highly accurate predictions regarding the dynamics of the disease and the likelihood of progression of AMD [78, 80].

Image pre-processing can be used for pre-feature extraction for traditional ML methods [43–45, 49], dataset extension using augmentation [21, 53, 56, 60, 63, 65, 71, 76, 79, 90, 92] and to reduce the shortcomings of visualization and normalization, which in most cases speeds up the training of intelligent algorithms [45, 48, 58, 59, 62–64, 71, 75, 76].

Predominantly, the platform for developing the ML algorithm was not specified. Most of the studies in which this information was provided used Python, which has more flexible functionality than Matlab.

The applicability of the metrics depended mainly on the nature of the output information and the task at hand. To assess the classification efficiency, it is essential to evaluate the errors of the "first" and "second" kinds for each distinguished class is essential. From the given compilation devoted to classification, the following were used as metrics:

– accuracy in terms of the percentage of correct answers, which was most often used in research;

– F1 is a harmonic mean of accuracy and recall;

– sensitivity and specificity, reflecting the proportion of positive and negative results, respectively;

– AUC-ROC (Area Under Curve-Receiver Operating Characteristic) representing the area under the curve of errors, which is more resistant to class imbalance, which is relevant for stages and pathologies of AMD with a varying frequency of detection during an examination of patients.

An additional verifying method for the classifier is the visualization of the attention areas on the image, relying on which it is possible to understand which information supports the decision. For this purpose, several works used class activation maps [57, 58, 90, 95] and the selection of points of interest [57].

In the problems of pathologies segmentation, the rules for evaluating the result are more manageable. To assess the accuracy of area selection, it is possible to represent the sets of segmented pixels of the example and the impact of the algorithm as two compared sets. That enables using the Pearson correlation coefficient, representing a measure of the correlation between two data sets [52, 74]. By limiting the selected areas as an image segment, it is also possible to estimate the overlap area of the original mask, chosen by experts, and the image segmented by the algorithm based on the Jaccard index [66]. The Dice similarity coefficient is a more commonly used analog for the Jaccard index applicable in cases with significant class imbalance [44, 53, 61, 88].

It is also essential to evaluate the degree of consistency between the experts and the ML algorithm, especially when developing a recommender system. Examples of metrics suitable for this assessment are Cohen's Kappa coefficient when measuring interregional agreement, which is more typical for classification/diagnosing problems [60, 95]. An expert's activity in analyzing AMD data is based on background information about the shape and size of biomarkers and professional experience. Therefore, the generally accepted statistical approach is to correlate the found form of pathology with tabular data. The ability of an intelligent algorithm to reproduce this activity can be assessed by parallel testing of experts unfamiliar with the test dataset and the algorithm itself. Numerically, the results of the comparative test are evaluated using the intraclass correlation coefficient (ICC) [53, 61, 64, 83, 92].

Distinguished classes or features represent the results of the algorithm operation. Classes in most works personified the diagnoses of either the presence or absence of AMD in the case of binary classification, the stages of AMD, or various retinal diseases. For the OCT image segmentation tasks, the algorithm's output data was the selected biomarkers, which act either as the final goal or as an intermediate one, based on which a diagnosis, recommendation, or prediction of the disease dynamics was made. Such approaches most reliably reflect an expert's diagnosing process and are easier to analyze the decision-making process using deep learning algorithms.

With a dataset size of hundreds of examples, Unet architectures showed the highest ICC, primarily due to the mechanism for refining the edges of an object based on the concatenation of parallel layers. In turn, Resnet networks showed an accuracy of 86% on average. At the same time, the OptiNet architecture [57], whose structure consists of serial convolution instead of parallel convolution in Resnet, demonstrated an accuracy of 98% that the highest binary classification accuracy.

For datasets of thousands of examples, the VGG network has become the most commonly used model. She also presented the highest numerical performance indicators values, up to 97.7% accuracy. The sensitivity and specificity of the model reach 0.91 and 0.896, respectively [65]. However, Unet networks showed the best specificity at 0.98 [61]. In addition, VGG has demonstrated its potential in optimizing its structure for real-time operation.

For datasets of tens of thousands of images, the highest performance indicators of deep algorithms were demonstrated by pre-trained Resnet networks, where parallel convolutions of different sizes helped to highlight standard features of the same biomarkers that are displayed with differences depending on different tomographs and augmentations. The achieved values of accuracy of 99% and sensitivity and specificity of 0.99 were performed on test data obtained from tomographs not included in the training set [63]. The results obtained on a reasonably large data set show the prospects for pre-training the model on a data bank like the OCT2017.

For several hundred thousand OCT images, parallel network convolutions in the GoogLeNet structure have also shown their effectiveness. Thanks to them, an accuracy of up to 95.5% was obtained, with specificity and sensitivity of 0.9 and 0.96, respectively [59].

4 Discussions

According to the collected data, the application of ML methods for OCT data analysis in diagnostics, staging, search and isolation of biomarkers, and prediction of AMD dynamics, is gaining more and more popularity. An increasing number of publications over the past five years confirm this conclusion. This trend (Fig. 2) is primarily due to the transition from standard ML to deep learning. One of the prerequisites for this transition is extending capabilities to generate large datasets from hundreds to hundreds of thousands of OCT scan samples, which directly affects the efficiency of deep neural network models [40]. The importance of this requirement for datasets in ophthalmology is consistent with the review's conclusions [39]. The availability of large datasets is due to the increasing spread of OCT devices, a collaboration between research and medical institutions, and the improvement of algorithms for the synthetic generation of OCT images. However, synthetic generation, along with augmentation, requires additional expert guidance. In all the analyzed works, ML methods were applied correctly concerning the processed information and methods for evaluating the results obtained.

It is worth noting that at the time of writing the systematic review, not all studies conducted in 2022 have been published, affecting the shape of the bar graphs that display the indicators mentioned below.

The efficiency of deep learning is due to the potentially high generalization ability compared to ML methods and the ability to extract algorithm predictors automatically, simplifying application development.

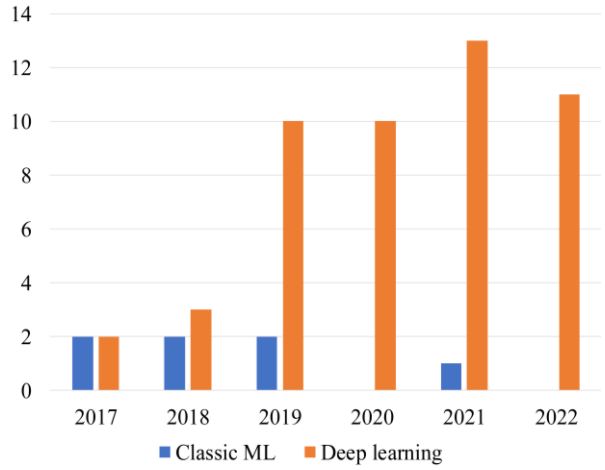


Fig. 2 Distribution of standard and deep ML approaches by years.

The approach to working with AMD data is also changing. Advanced intelligent systems make it possible to bring the classification of OCT images, similar to direct diagnostics requiring additional sufficiency verification of computer vision logic, to the progressive level equal to an expert's visual assessment. The latter relates to segmentation algorithms for retinal pathologies, based on the analysis of which the doctor and an additional classification algorithm carry out diagnostics or staging. Methods for analyzing pathologies and biomarkers have also found wide application in recommender systems and multimodal diagnostic techniques.

This transition from direct diagnosis to the analysis of the retina's segmented areas influenced the quality metrics of ML algorithms used. For direct classification (classic for medical diagnostic mechanisms), the parameters of accuracy, sensitivity, and specificity, i.e., AUS and F1, are evaluated. In turn, various studies differ in the methods used to assess the accuracy of segment boundary detection for segmentation mechanisms. However, recent studies show a greater preference for DSC and IOU due to the calculation simplicity and the relative accuracy of matching with natural segment boundaries.

The specifics of the transition from classical ML to deep learning also influenced the need for pre-processing of images since primary processing, which is extremely important for the self-selection of predictors, does not always make a significant contribution to processing by deep neural networks.

Among the structures used in deep neural network approaches, in connection with the above trends, auto-encoders are distinguished by type: Unet, Resnet, VGG, and a specially designed structure OptiNet. They are applied as the basis for classifiers, clusterers, and predictive models of diseases. Each dimension category of the dataset contains a different variety of data on the nationality of patients. Consistent with the conclusions in Ref. [41], the analysis confirmed the influence of nationality on the shape of biomarkers with the same diagnosis, which imposes additional requirements on the generalizing ability of intelligent algorithms for applications positioned as universal.

Since the dataset's size significantly affects the algorithm's relevance limitations, different deep learning architectures and numerical indicators of their effectiveness should be compared only within the same category It should also be noted that it is difficult to compare research results in many cases due to using different indicators. Therefore, examples of comparisons with only the same indicators are presented below.

Fig. 3 shows the average accuracy of deep learning models. On the given histogram, they are arranged in descending order of their use in the OCT data analysis. The selected most effective deep learning models are included in the selection of basic models for classifiers and segmenters given in Ref. [37] which is devoted to working with CFP data.

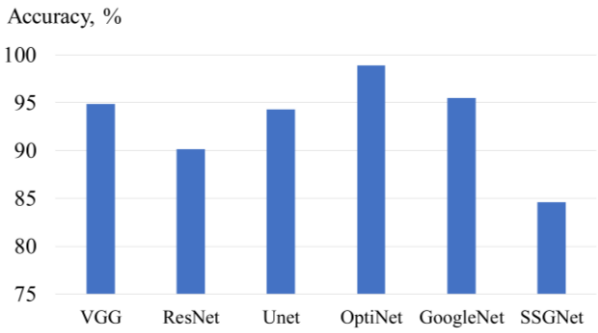


Fig. 3 Average achievable accuracy of deep learning models in disease classification tasks.

According to the results of the metrics used, such as AUS, F1, and sensitivity and specificity, for direct diagnostic methods, the highest indicators were demonstrated by: VGG and ResNet. The same and GoogLeNet with a sufficient data set for segmentation of pathologies.

Based on the papers reviewed in this work and paying particular attention to those studies in which the greatest TRL was obtained, it is possible to identify the key components that characterize the most effective approaches. These approaches included a data set of at least a thousand images, deep learning methods, and operations of both cross-validation and validation on data from other sources (different brands of tomographs or groups of people with different parameters). When solving the problem of diagnosing and staging AMD, approaches with the allocation of biomarkers have the greatest informativeness and explainability, which most clearly reflects the visual analysis of the expert. These circumstances may increase the likelihood of successfully developing an OCT image processing application with a high generalization capability.

5 Conclusions

Due to the trend of increasing the number of integrations of intelligent systems in ophthalmology, the dynamics of the use of various ML applications to solve problems in

this area will inevitably correlate with the dynamics of the development of intelligent technologies. This statistical review evaluated this correlation by analyzing 56 studies on the use of ML methods in OCT image analysis tasks with AMD, according to a variety of features. Among the highlighted features were: Publication year, Data sources, Tasks to be solved, Technology readiness level, Number of OCT images in the dataset, Image pre-processing, Research methods, Software, Metrics, Validation, and Distinguishable classes/features. Analyzing feature data in the time domain allowed us to identify the most important and viable factors for creating an up-to-date intelligent OCT image analysis application with AMD. These effective artificial intelligence programs provide us with a unique opportunity to analyze visual information about the state of the retina and help make clinical decisions in the field of ophthalmology, in particular, in diagnosing the disease, automatically identifying biomarkers, and forming and correcting treatment strategies.

Disclosures

The authors declare that they have no conflict of interest.

Acknowledgments

The research is partly supported by the Ministry of Science and Higher Education of the Russian Federation within the state assignment for the FSBEI HE "USATU" (#FEUE-2021-0013, agreement No. 075-03-2021-014) and conducted in the research laboratory "Sensor systems based on integrated photonics devices" (Sections "Introduction", "Materials and Methods"), and partly by subsidy in the field of science from the budget of the Republic of Bashkortostan for state support of scientific research conducted under the guidance of leading scientists (REC-RMG-2021, agreement with the Federal State Budgetary Educational Institution of Higher Education "USATU") (section "Results").

References

1. World Health Organisation, "World report on vision," World Health Organisation, Switzerland (2019) (accessed 14 November 2022). [https://www.who.int/publications-detail/world-report-on-vision]. ISBN 978-92-4-151657-0.
2. R. Klein, B. E. K. Klein, S. C. Tomany, S. M. Meuer, and G.-H. Huang, "Ten-year incidence and progression of age-related maculopathy: The Beaver Dam eye study," Ophthalmology 109(10), 1767–1779 (2002).
3. T. A. C. D. Guimaraes, M. D. Varela, M. Georgiou, and M. Michaelides, "Treatments for dry age-related macular degeneration: therapeutic avenues, clinical trials and future directions," British Journal of Ophthalmology 106(3), 297–304 (2021).
4. N. M. Schultz, S. Bhardwaj, C. Barclay, L. Gaspar, and J. Schwartz, "Global Burden of Dry Age-Related Macular Degeneration: A Targeted Literature Review," Clinical Therapeutics 43(10), 1792–1818 (2021).
5. B. Swenor, V. Varadaraj, M. J. Lee, H. Whitson, and P. Ramulu, "World Health Report on Vision: Aging Implications for Global Vision and Eye Health," Innovation in Aging 4(1), 807–808 (2020).
6. L. S. Lim, P. Mitchell, J. M. Seddon, F. G. Holz, and T. Y. Wong, "Age-related macular degeneration," The Lancet 379(9827), 1728–1738 (2012).
7. N. M. Bressler, S. B. Bressler, and S. L. Fine, "Age-related macular degeneration," Survey of Ophthalmology 32(6), 375–413 (1988).
8. J. R. Evans, "Risk Factors for Age-related Macular Degeneration," Progress in Retinal and Eye Research 20(2), 227–253 (2001).
9. P. Mitchell, G. Liew, B. Gopinath, and T. Y. Wong, "Age-related macular degeneration," The Lancet 392(10153), 1147–1159 (2018).
10. J. Ambati, B. J. Fowler, "Mechanisms of Age-Related Macular Degeneration," Neuron 75(1), 26–39 (2012).
11. R. Klein, T. Peto, A. Bird, and M. R. Vannewkirk, "The epidemiology of age-related macular degeneration," American Journal of Ophthalmology 137(3), 486–495 (2004).
12. T. J. Heesterbeek, L. Lorés-Motta, C. B. Hoyng, Y. T. E. Lechanteur, and A. I. den Hollander, "Risk factors for progression of age-related macular degeneration," Ophthalmic and Physiological Optics 40(2), 140–170 (2020).
13. M. P. Rozing, J. A. Durhuus, M. K. Nielsen, Y. Subhi, T. B. Kirkwood, R. G. Westendorp, and T. L. Sorensen, "Age-related macular degeneration: A two-level model hypothesis," Progress in Retinal and Eye Research 76, 100825 (2020).
14. C. T. Supuran, "Agents for the prevention and treatment of age-related macular degeneration and macular edema: a literature and patent review," Expert Opinion on Therapeutic Patents 29(10), 761–767 (2019).
15. D. W. Lem, P. G. Davey, D. L. Gierhart, and R. B. Rosen, "A Systematic Review of Carotenoids in the Management of Age-Related Macular Degeneration," Antioxidants 10(8), 1255 (2021).
16. M. Gil-Martínez, P. Santos-Ramos, M. Fernández-Rodríguez, M. J. Abraldes, M. J. Rodríguez-Cid, M. Santiago-Varela, A. Fernández-Ferreiro, and F. Gómez-Ulla, "Pharmacological advances in the treatment of age-related macular degeneration," Current Medicinal Chemistry 27(4), 583–598(2020).

17. S. K. Dubey, R. Pradhan, S. Hejmady, G. Singhvi, H. Choudhury, B. Gorain, and P. Kesharwani, "Emerging innovations in nano-enabled therapy against age-related macular degeneration: A paradigm shift," International Journal of Pharmaceutics 600, 120499 (2021).
18. Y. P. Yang, Y. J. Hsiao, K. J. Chang, S. Foustine, Y. K. Ko, Y. C. Tsai, H. Y. Tai, Y. C. Ko, S. H. Chiou, T. C. Lin, S. J. Chen, Y. Chien, and D. K.Hwang, "Pluripotent Stem Cells in Clinical Cell Transplantation: Focusing on Induced Pluripotent Stem Cell-Derived RPE Cell Therapy in Age-Related Macular Degeneration," International Journal of Molecular Sciences 23(22), 13794 (2022).
19. T. A. C. De Guimaraes, M. V. Daich, M. Georgiou, and M. Michaelides, "Treatments for dry age-related macular degeneration: therapeutic avenues, clinical trials and future directions," British Journal of Ophthalmology 106(3), 297–304 (2022).
20. A. Sarkar, S. Dyawanapelly, "Nanodiagnostics and Nanotherapeutics for age-related macular degeneration," Journal of Controlled Release 329, 1262–1282 (2021).
21. K. W. Graham, U. Chakravarthy, R. E. Hogg, K. A. Muldrew, I. S. Young, and F. Kee, "Identifying features of early and late age-related macular degeneration: A comparison of multicolor versus traditional color fundus photography," Retina 38(9), 1751–1758 (2018).
22. B. Lumbroso and M. Rispoli, Practical handbook of OCT (Retina, Choroid, Glaucoma), Jaypee Brothers Medical Publishers, New Delhi, India (2012). ISBN: 978-93-5025-758-6.
23. B. M. Aznabaev, T. R. Mukhamadeev, and T. I. Dibaev, Optical coherence tomoghraphy + angiography of the eye in the diagnosis, therapy and surgery of eye diseases, August Borg, Moscow (2019). [in Russian]. ISBN: 978-5-901053-71-3.
24. A. V. Arus, "The Role of Imaging in Age-Related Macular Degeneration," in Visual Impairment and Blindness-What We Know and What We Have to Know, G. L. Giudice, A. Catalá(Eds.), IntechOpen, UK (2020).
25. D. Huang, E. A. Swanson, C. P. Lin, J. S. Schuman, W. G. Stinson, W. Chang, M. R. Hee, T. Flotte, K. Gregory, C. A. Puliafito, and J. G. Fujimoto, "Optical coherence tomography," Science 254(5035), 1178–1181 (1991).
26. C. V. Regatieri, L. Branchini, and J. S. Duker, "The role of spectral-domain OCT in the diagnosis and management of neovascular age-related macular degeneration," Ophthalmic Surgery, Lasers and Imaging Retina 42(4), S56–S66 (2011).
27. E. H. Lim, J. I. Han, C. G. Kim, S. W. Cho, and T. G. Lee, "Characteristic Findings of Optical Coherence Tomography in Retinal Angiomatous Proliferation," Korean Journal of Ophthalmology 27(5), 351–360 (2013).
28. E. Corbelli, R. Sacconi, A. Rabiolo, S. Mercuri, A. Carnevali, L. Querques, F. Bandello, and G. Querques, "Optical Coherence Tomography Angiography in the Evaluation of Geographic Atrophy Area Extension," Investigative Ophthalmology and Visual 58(12), 5201–5208 (2017).
29. J. Walther, M. Gaertner, P. Cimalla, A. Burkhardt, L. Kirsten, S. Meissner, and E. Koch, "Optical coherence tomography in biomedical research," Analytical and Bioanalytical Chemistry 400, 2721–2743 (2011).
30. L. Rampasek, A. Goldenberg, "TensorFlow: Biology's Gateway to Deep Learning?" Cell Systems 2(1), 12–14 (2016).
31. M. M. Najafabadi, F. Villanustre, T. M. Khoshgoftaar, N. Seliya, R. Wald, and E. Muharemagic, "Deep learning applications and challenges in big data analytics," Journal of Big Data 2(1), 1–21 (2015).
32. D. Shen, G. Wu, and H. I. Suk, "Deep Learning in Medical Image Analysis," Annual Review of Biomedical Engineering 19, 221–248 (2017).
33. B. Juba, H. S. Le, "Precision-Recall versus accuracy and the role of large data sets," Proceedings of the AAAI Conference on Artificial Intelligence 33(1), 4039–4048 (2019).
34. J. Latif, C. Xiao, A. Imran, and S. Tu, "Medical imaging using machine learning and deep learning algorithms: A review," in 2019 2nd International Conference on Computing, Mathematics and Engineering Technologies (iCoMET), 1–5 (2019).
35. B. Lee, M. D'Souza, E. L. Singman, J. Wang, F. A. Woreta, M. V. Boland, and D. Srikumaran, "Integration of a Physician Assistant Into an Ophthalmology Consult Service in an Academic Setting," American Journal of Ophthalmology 190, 125–133 (2018).
36. S. Pandey, V. Sharma, "Robotics and ophthalmology: Are we there yet?" Indian Journal of Ophthalmology 67(7), 988 (2019).
37. B. Goutam, M. F. Hashmi, Z. W. Geem, and N. D. Bokde, "A Comprehensive Review of Deep Learning Strategies in Retinal Disease Diagnosis Using Fundus Images," IEEE Access 10, 57796–57823 (2022).
38. L. Dong, Q. Yang, R. H. Zhang, and W. B. Wei, "Artificial intelligence for the detection of age-related macular degeneration in color fundus photographs: A systematic review and meta-analysis," EclinicalMedicine 35, 100875 (2021).
39. R. Kapoor, B. T. Whigham, and L. A. Al-Aswad, "Artificial Intelligence and Optical Coherence Tomography Imaging," The Asia-Pacific Journal of Ophthalmology 8(2), 187–194 (2019).
40. K. Jin, J. Ye, "Artificial intelligence and deep learning in ophthalmology: Current status and future perspectives," Advances in Ophthalmology Practice and Research 100078, (2022).

41. M. H. Sarhan, M. A. Nasseri, and D. Zapp, "Machine Learning Techniques for Ophthalmic Data Processing: A Review," IEEE Journal of Biomedical and Health Informatics 24(12), 3338–3350 (2020).
42. R. Cheung, J. Chun, T. Sheidow, M. Motolko, and M. S. Malvankar-Mehta, "Diagnostic accuracy of current machine learning classifiers for age-related macular degeneration: a systematic review and meta-analysis," Eye 36(5), 994–1004 (2022).
43. F. G. Venhuizen, B.V. Ginneken, F. V. Asten, M. J. J. P. V. Grinsven, S. Fauser, C. B. Hoyng, T. Theelen, and C. I. Sánchez, "Automated staging of age-related macular degeneration using optical coherence tomography," Investigative Ophthalmology and Visual Science 58(4), 2318–2328 (2017).
44. B. I. Dodo, Y. Li, D. Kaba, and X. Liu, "Retinal Layer Segmentation in Optical Coherence Tomography Images," IEEE Access 7, 152388–152398 (2019).
45. A. Chakravarty, J. Sivaswamy, "A supervised joint multi-layer segmentation framework for retinal optical coherence tomography images using conditional random field," Computer Methods and Programs in Biomedicine 165, 235–250 (2018).
46. U. Schmidt-Erfurth, S. M. Waldstein, S. Klimscha, A. Sadeghipour, X. Hu, B. S. Gerendas, A. Osborne, and H. Bogunović, "Prediction of Individual Disease Conversion in Early AMD Using Artificial Intelligence," Investigative Ophthalmology Visual Science 59(8), 3199–3208 (2018).
47. G. Moraes, D. J. Fu, M. Wilson, H. Khalid, S. K. Wagner, E. Korot, D. Ferraz, L. Faes, C. J. Kelly, T. Spitz, P. J. Patel, K. Balaskas, T. D. L. Keenan, P. A. Keane, and R. Chopra,"Quantitative Analysis of OCT for Neovascular Age-Related Macular Degeneration Using Deep Learning," Ophthalmology 128(5), 693–705 (2021).
48. P. Seeböck, S. M. Waldstein, S. Klimscha, H. Bogunovic, T. Schlegl, B. S. Gerendas, R. Donner, U. Schmidt-Erfurth, and G. Langs, "Unsupervised Identification of Disease Marker Candidates in Retinal OCT Imaging Data," IEEE Transactions on Medical Imaging 38(4), 1037–1047 (2019).
49. H. Bogunović, A. Montuoro, M. Baratsits, M. G. Karantonis, S. M. Waldstein, F. Schlanitz, and U. Schmidt-Erfurth, "Machine Learning of the Progression of Intermediate Age-Related Macular Degeneration Based on OCT Imaging," Investigative Ophthalmology & Visual Science 58(6), BIO141-BIO150 (2017).
50. J. Kugelman, D. Alonso-Caneiro, S. A. Read, S. J. Vincent, and M. J. Collins, "Automatic segmentation of OCT retinal boundaries using recurrent neural networks and graph search," Biomedical Optics Express 9(11), 5759–5777 (2018).
51. T. D. L. Keenan, T. E. Clemons, A. Domalpally, M. J. Elman, M. Havilio, E. Agrón, G. Benyamini, and E .Y. Chew, "Retinal specialist versus artificial intelligence detection of retinal fluid from OCT: age-related eye disease study 2: 10-year follow-on study," Ophthalmology 128(1), 100–109 (2021).
52. S. K. Sodhi, A. Pereira, J. D. Oakley, J. Golding, C. Trimboli, D. B. Russakoff, and N. Choudhry, "Utilization of deep learning to quantify fluid volume of neovascular age-related macular degeneration patients based on swept-source OCT imaging: The ONTARIO study," PLoS One 17(2), e0262111 (2022).
53. F. G. Venhuizen, B. V. Ginneken, B. Liefers, F. V. Asten, V. Schreur, S. Fauser, C. Hoyng, T. Theelen, and C. I. Sánchez, "Deep learning approach for the detection and quantification of intraretinal cystoid fluid in multivendor optical coherence tomography," Biomedical Optics Express 9(4), 1545–1569 (2018).
54. Z. Akkus, A. Galimzianova, A. Hoogi, D. L. Rubin, and B. J. Erickson, "Deep Learning for Brain MRI Segmentation: State of the Art and Future Directions," Journal of Digital Imaging 30, 449–459 (2017).
55. M. Treder, J. L. Lauermann, and N. Eter, "Automated detection of exudative age-related macular degeneration in spectral domain optical coherence tomography using deep learning," Graefe's Archive for Clinical and Experimental Ophthalmology 260(6), 1941–1946 (2017).
56. P. K. Upadhyay, S. Rastogi, and K. V. Kumar, "Coherent convolution neural network based retinal disease detection using optical coherence tomographic images," Journal of King Saud University-Computer and Information Sciences 34(10), 9688–9695 (2022).
57. A. O. Tvenning, S. R. Hanssen, D. Austeng, and T. S. Morken, "Deep learning identify retinal nerve fibre and choroid layers as markers of age-related macular degeneration in the classification of macular spectral-domain optical coherence tomography volumes," Acta Ophthalmologica 100(8), 937–945 (2022).
58. T. H. Rim, A. Y. Lee, D. S. Ting, K. Teo, B. K. Berzler, Z. L. Teo, T. K. Yoo, G. Lee, Y. Kim, A. C. Lin, S. E. Kim, Y. C. Tham, S. S. Kim, C. Cheng, T. Y. Wong, and C. M. G. Cheung, "Detection of features associated with neovascular age-related macular degeneration in ethnically distinct data sets by an optical coherence tomography: trained deep learning algorithm," British Journal of Ophthalmology 105(8), 1133–1139 (2020).
59. P. Prahs, V. Radeck, C. Mayer, Y. Cvetkov, N. Cvetkova, H. Helbig, and D. Märker, "OCT-based deep learning algorithm for the evaluation of treatment indication with anti-vascular endothelial growth factor medications," Graefe's Archive for Clinical and Experimental Ophthalmology 256(1), 91–98 (2017).
60. S. Kuwayama, Y. Ayatsuka, D. Yanagisono, T. Uta, H. Usui, A. Kato, N. Takase, Y. Ogura, and T. Yasukawa, "Automated Detection of Macular Diseases by Optical Coherence Tomography and Artificial Intelligence Machine Learning of Optical Coherence Tomography Images," Journal of Ophthalmology 2019, 6319581 (2019).
61. G. Zhang, D. J. Fu, B. Liefers, L. Faes, S. Glinton, S. Wagner, R. Struyven, N. Pontikos, P. A. Keane, and K. Balaskas, "Clinically relevant deep learning for detection and quantification of geographic atrophy from optical coherence

tomography: a model development and external validation study," The Lancet Digital Health 3(10), e665–e675 (2021).
62. Z. Chen, D. Li, H. Shen, H. Mo, Z. Zeng, and H. Wei, "Automated segmentation of fluid regions in optical coherence tomography B-scan images of age-related macular degeneration," Optics and Laser Technology 122, 105830 (2020).
63. A. Haq, A. Fariza, and N. Ramadijanti, "Development of vulnerable web application based on owasp api security risks," in 2021 International Electronics Symposium (IES), Surabaya, Indonesia, 343–348 (2021).
64. H. Lee, K. E. Kang, H. Chung, and H. C. Kim, "Automated Segmentation of Lesions Including Subretinal Hyperreflective Material in Neovascular Age-related Macular Degeneration," American Journal of Ophthalmology 191, 64–75 (2018).
65. T. K. Yoo, J. Y. Choi, J. G. Seo, B. Ramasubramanian, S. Selvaperumal, and D. W. Kim, "The possibility of the combination of OCT and fundus images for improving the diagnostic accuracy of deep learning for age-related macular degeneration: a preliminary experiment," Medical and Biological Engineering and Computing 57, 677–687 (2018).
66. P. M. Maloca, A. Y. Lee, E. R. de Carvalho, M. Okada, K. Fasler, I. Leung, B. Hormann, P. Kaiser, S. Suter, P. W. Hasler, J. Zarranz-Ventura, C. Egan, T. C. Heeren, and H. P. N. Scholl, "Validation of automated artificial intelligence segmentation of optical coherence tomography images," PLoS One 14(8), e0220063 (2019).
67. S. Saha, M. Nassisi, M. Wang, S. Lindenberg, Y. kanagasingam, S. Sadda, and Z. J. Hu, "Automated detection and classification of early AMD biomarkers using deep learning," Scientific Reports 9(1), 10990 (2019).
68. L. Varga, A. Kovács, T. Grósz, G. Thury, F. Hadarits, R. Dégi, and J. Dombi, "Automatic segmentation of hyperreflective foci in OCT images," Computer Methods and Programs in Biomedicine 178, 91–103 (2019).
69. D. B. Russakoff, A. Lamin, J. D. Oakley, A. M. Dubis, and S. Sivaprasad, "Deep Learning for Prediction of AMD Progression: A Pilot Study," Investigative Ophthalmology and Visual Science 60(2), 712–722 (2019).
70. M. Wu, X. Cai, Q. Chen, Z. Ji, S. Niu, T. Leng, D. L. Rubin, and H. Park, "Geographic atrophy segmentation in SD-OCT images using synthesized fundus autofluorescence imaging," Computer Methods and Programs in Biomedicine 182, 105101 (2019).
71. V. Das, S. Dandapat, and P. K. Bora, "Multi-scale deep feature fusion for automated classification of macular pathologies from OCT images," Biomedical Signal Processing and Control 54, 101605 (2019).
72. L. Fang, Y. Jin, L. Huang, S. Guo, G. Zhao, and X. Chen, "Iterative fusion convolutional neural networks for classification of optical coherence tomography images," Journal of Visual Communication and Image Representation 59, 327–333 (2019).
73. J. Qiu, Y. Sun, "Self-supervised iterative refinement learning for macular OCT volumetric data classification," Computers in Biology and Medicine 111, 103327 (2019).
74. U. Schmidt-Erfurth, W. D. Vogl, L. M. Jampol, and H. Bogunović, "Application of Automated Quantification of Fluid Volumes to Anti-VEGF Therapy of Neovascular Age-Related Macular Degeneration," Ophthalmology 127(9), 1211–1219 (2020).
75. S. M. Waldstein, W. D. Vogl, H. Bogunovic, A. Sadeghipour, S. Riedl, and U. Schmidt-Erfurth, "Characterization of Drusen and Hyperreflective Foci as Biomarkers for Disease Progression in Age-Related Macular Degeneration Using Artificial Intelligence in Optical Coherence Tomography," JAMA Ophthalmology 138(7), 740–747 (2020).
76. K. K. Bhatia, M. S. Graham, L. Terry, A. Wood, P. Tranos, S. Trikha, and N. Jaccard, "Disease classification of macular Optical Coherence Tomography scans using deep learning software: validation on independent, multi-centre data," Retina 40(8), 1549–1557 (2019).
77. J. Yim, R. Chopra, T. Spitz, J. Winkens, A. Obika, C. Kelly, H. Askham, M. Lukic, J. Huemer, K. Fasler, G. Moraes, C. Meyer, M. Wilson, J. Dixon, C. Hughes, G. Rees, P. T. Khaw, A. Karthikesalingam, D. King, D. Hassabis, M. Suleyman, T. Back, J. R. Ledsam, P. A. Keane, and J. D. Fauw,"Predicting conversion to wet age-related macular degeneration using deep learning," Nature Medicine 26(6), 892–899 (2020).
78. I. Banerjee, L. de Sisternes, J. A. Hallak, T. Leng, A. Osborne, P. J. Rosenfeld, G. Gregori, M. Durbin, and D. Rubin, "Prediction of age-related macular degeneration disease using a sequential deep learning approach on longitudinal SD-OCT imaging biomarkers," Scientific Reports 10(1), 15434 (2020).
79. X. He, L. Fang, H. Rabbani, X. Chen, and Z. Liu, "Retinal optical coherence tomography image classification with label smoothing generative adversarial network," Neurocomputing 405, 37–47 (2020).
80. X. Wang, F. Tang, H. Chen, L. Luo, Z. Tang, An-Ran Ran, C. Y. Cheung, and P. A. Heng, "UD-MIL: Uncertainty-Driven Deep Multiple Instance Learning for OCT Image Classification," IEEE Journal of Biomedical and Health Informatics 24(12), 3431–3442 (2020).
81. X. Zhao, X. Zhang, B. Lv, L. Meng, C. Zhang, Y. Liu, C. Lv, G. Xie, and Y. Chen, "Optical coherence tomography-based short-term effect prediction of anti-vascular endothelial growth factor treatment in neovascular age-related macular degeneration using sensitive structure guided network," Graefe's Archive for Clinical and Experimental Ophthalmology 259(11), 3261–3269 (2021).
82. D. J. Fu, L. Faes, S. K. Wagner, G. Moraes, R. Chopra, P. J. Patel, K. Balaskas, T. D. L. Keenan, L. M. Bachmann, and P. A. Keane,"Predicting Incremental and Future Visual Change in Neovascular Age-Related Macular Degeneration Using Deep Learning," Ophthalmology Retina 5(11), 1074–1084 (2021).

83. B. Liefers, P. Taylor, A. Alsaedi, C. Bailey, K. Balaskas, N. Dhingra, C. A. Egan, F. G. Rodrigues, C. G. Gonzalo, T. F. C. Heeren, A. Lotery, P. L. Müller, A. Olvera-Barrios, B. Paul, R. Schwartz, D. S. Thomas, A. N. Warwick, A. Tufail, and C. I. Sánchez, "Quantification of Key Retinal Features in Early and Late Age-Related Macular Degeneration Using Deep Learning," American Journal of Ophthalmology 226, 1–12 (2021).
84. A. Szeskin, R. Yehuda, O. Shmueli, J. Levy, and L. Joskowicz, "A column-based deep learning method for the detection and quantification of atrophy associated with AMD in OCT scans," Medical Image Analysis 63, 101693 (2021).
85. Y. Yan, K. Jin, Z. Gao, X. Huang, F. Wang, Y. Wang, and J. Ye, "Attention Based Deep Learning System for Automated Diagnoses of Age-Related Macular Degeneration in Optical Coherence Tomography Images," Medical Physics 48(9), 4926–4934 (2021).
86. Z. Xu, W. Wang, J. Yang, J. Zhao, D. Ding, D. Chen, Z. Yang, X. Li,W. Yu, and Y. Chen, "Automated diagnoses of age-related macular degeneration and polypoidal choroidal vasculopathy using bi-modal deep convolutional neural networks," British Journal of Ophthalmology 105(4), 561–566 (2021).
87. D. D. J. Hwang, S. Choi, J. Ko, J. Yoon, J. I. Park, J. S. Hwang, J. M. Han, H. J. Lee, J. Sohn, K. H. Park, and J. Han, "Distinguishing retinal angiomatous proliferation from polypoidal choroidal vasculopathy with a deep neural network based on optical coherence tomography," Scientific Reports 11(1), 9275 (2021).
88. F. G. Holz, R. Abreu-Gonzalez, F. Bandello, R. Duval, L. O'toole, D. Pauleikhoff, G. Staurenghi, A. Wolf, D. Lorand, A. Clemens, and B. Gmeiner, "Does real-time artificial intelligence-based visual pathology enhancement of three-dimensional optical coherence tomography scans optimise treatment decision in patients with nAMD? Rationale and design of the RAZORBILL study," British Journal of Ophthalmology 107(1), 96–101 (2021).
89. Y. Derradji, A. Mosinska, S. Apostolopoulos, C. Ciller, S. De Zanet, and I. Mantel, "Fully-automated atrophy segmentation in dry age-related macular degeneration in optical coherence tomography," Scientific Reports 11(1), 21893 (2021).
90. Sunija, S. Kar, Gayathri, V. P. Gopi, and P. Palanisamy, "OctNET: A Lightweight CNN for Retinal Disease Classification from Optical Coherence Tomography Images," Computer Methods and Programs in Biomedicine 200, 105877 (2021).
91. S. Riedl, V. Wolf-Dieter, J. Mai, G. S. Reiter, D. Lachinov, C. Grechenig, A. McKeown, L. Scheibler, H. Bogunović, and U. Schmidt-Erfurth, "The Effect of Pegcetacoplan Treatment on Photoreceptor Maintenance in Geographic Atrophy Monitored by Artificial Intelligence–Based OCT Analysis," Ophthalmology Retina 6(11), 1009–1018 (2022).
92. V. Pramil, L. de Sisternes, L. Omlor, W. Lewis, H. Sheikh, Z. Chu, N. Manivannan, M. Durbin, R. Wang, P. Rosenfeld, M. Shen, R. Guymer, M. Liang, G. Gregori, and N. K Waheed, "A Deep Learning Model for Automated Segmentation of Geographic Atrophy Imaged Using Swept-Source OCT," Ophthalmology Retina 7(2), 127–141 (2022).
93. K. A. Thakoor, J. Yao, D. Bordbar, O. Moussa, W. Lin, P. Sajda, and R. W. S. Chen, "A multimodal deep learning system to distinguish late stages of AMD and to compare expert vs. AI ocular biomarkers," Scientific Reports 12(1), 2585 (2022).
94. T. G. Kamenskikh, O. N. Dolinina, I. O. Kolbenev, and E. V. Veselova, "An intelligent decision-making system for early diagnosis of macular pathology," Rossiiskii Oftal'mologicheskii Zhurnal 15(2), 69–74 (2022). [in Russian].
95. J. Han, S. Choi, J. I. Park, J. S. Hwang, J. M. Han, H. J. Lee, J. Ko, J. Yoon, and D. Duck-Jin Hwang, "Classifying neovascular age-related macular degeneration with a deep convolutional neural network based on optical coherence tomography images," Scientific Reports 12(1), 1–10 (2022).
96. P. Zang, T. T. Hormel, T. S. Hwang, S. T. Bailey, D. Huang, and Y. Jia, "Deep-learning-aided Diagnosis of DR, AMD, and Glaucoma based on Structural and Angiographic Optical Coherence Tomography," Ophthalmology Science 3(1), 100245 (2022).
97. E. Parra-Mora, L. A. da Silva Cruz, "LOCTseg: A lightweight fully convolutional network for end-to-end optical coherence tomography segmentation," Computers in Biology and Medicine 150, 106174 (2022).
98. T. C. Yeh, A.C. Luo, Y. S. Deng, Y. H. Lee, S. J. Chen, P. H. Chang, C. J. Lin, M. C. Tai, and Y. B. Chou, "Prediction of treatment outcome in neovascular age-related macular degeneration using a novel convolutional neural network," Scientific Reports 12(1), 5871 (2022).
99. A. Thomas, P. M. Harikrishnan, R. Ramachandran, S. Ramachandran, R. Manoj, P. Palanisamy, and V. P. Gopi, "A novel multiscale and multipath convolutional neural network based age-related macular degeneration detection using OCT images," Computer Methods and Programs in Biomedicine 209, 106294 (2021).
100. D. S. Kermany, M. Goldbaum, W. Cai, C. C. S. Valentim, H. Liang, S. L. Baxter, A. McKeown, G. Yang, X. Wu, F. Yan, J. Dong, M. K. Prasadha, J. Pei, M. Y. L. Ting, J. Zhu, C. Li, S. Hewett, J. Dong, I. Ziyar, A. Shi, and K. Zhang, "Identifying Medical Diagnoses and Treatable Diseases by Image-Based Deep Learning," Cell 172(5), 1122–1113 (2018).
101. M. Adhi, J. S. Duker, "Optical coherence tomography-current and future applications," Current Opinion in Ophthalmology 24(3), 213 (2013).

102. S. Laotaweerungsawat, C. Psaras, Z. Haq, X. Liu, and J. M. Stewart, "Racial and ethnic differences in foveal avascular zone in diabetic and nondiabetic eyes revealed by optical coherence tomography angiography," PLoS One 16(10), e0258848 (2021).

Dynamic Light Scattering Analysis in Biomedical Research and Applications of Nanoparticles and Polymers

Alexander Knysh[1]*, Pavel Sokolov[1], and Igor Nabiev[1,2+]

[1] National Research Nuclear University MEPhI (Moscow Engineering Physics Institute), 31 Kashirskoe shosse, Moscow 115409, Russian Federation

[2] Université de Reims Champagne-Ardenne, 51 rue Cognacq Jay, Reims 51100, France

e-mail: *knyshkikai@mail.ru,+igor.nabiev@gmail.com

Abstract. Dynamic light scattering (DLS) is one of the most commonly used photonic methods for estimating the hydrodynamic radius, ζ-potential, polydispersity, and concentrations of nanoparticles (NPs), polymers, and cells, as well as for studying changes in these parameters upon interaction or aggregation of molecules and particles. NPs and polymers are components of numerous drugs, cosmetics, and food industry products. Hence, the monitoring of their physical, chemical, and morphological properties, often related to their functional characteristics and toxicity, are of vital importance. This review deals with the specifics of the DLS method as applied to the analysis of samples of different types and the modifications of this method depending on the characteristics of the samples. The theoretical basis of the DLS method and its applications to the study of NPs, polymers, and their interactions are presented, with the focus on biomedical applications. The last section of the review considers the advantages and limitations of DLS analysis as compared with other photonic analytical methods, as well as future trends in the development of this approach. © 2023 Journal of Biomedical Photonics & Engineering.

Keywords: dynamic light scattering; nanoparticles; polymers; hybrid materials; ζ-potential; hydrodynamic diameter.

Paper #8681 received 2 Mar 2023; revised manuscript received 13 Apr 2023; accepted for publication 17 Apr 2023; published online 30 May 2023. doi: 10.18287/JBPE23.09.020203.

1 Introduction

Photonic methods of analysis based on various principles of light–matter interaction are widely used to analyze both organic (including biological) and inorganic objects. Light can be absorbed, refracted, or reflected upon its interaction with molecules, or change its plane of polarization or wavelength. These effects have been employed in a variety of methods of analysis in medicine, biology, biosensing, detection and analysis of mineral resources, and many other fields of science and technology. For example, Raman spectroscopy is used to study chemical bonds, to identify molecules, and to study their structure, which allows the detection of various microorganisms [1] or to use this approach in the diagnosis of cancer [2] and many other diseases. Specific light absorption by protein molecules at 280 nm, and the maximum absorption of radiation by nucleotides at 260 nm are used to determine the concentrations of proteins and nucleic acids, respectively [3, 4]. Estimation of light polarization and measurement of circular dichroism spectra can be used to study the chirality of compounds, such as amino acids, monosaccharides, or drugs [5, 6]. In refractometry, the measurement of the refractive index is used to determine the concentrations of chemical compounds in solutions [7], which is used in cell biology, hematology [8], and other fields. Thus, optical methods make it possible to study the composition and structure of biological objects at the atomic and molecular levels. These optical methods are also successfully used for identifying organic molecules and determining the concentration and purity of biopolymers.

Unlike the approaches mentioned above, the dynamic light scattering (DLS) method is suitable for estimating macroscopic parameters of objects, such as the size of

nanoparticles (NPs), microparticles, and polymers and the ζ-potential of their surface, as well as for studying the interaction of polymers, cells, NPs, and microparticles of various types. It is especially important that DLS can be used to study biological polymers in liquid phase, in their natural environment, whereas many other methods of determining macroscopic parameters, such as electron and atomic force microscopies, require the sample to be transferred to the dry or partly dehydrated phase.

Liposomes, polymers, and NPs of various compositions are examples of advanced drug delivery systems that have proved to be promising in delivering drugs effectively and selectively to target cells or tissues. Liposomes are spherical vesicles composed of a phospholipid bilayer that can encapsulate both hydrophilic and hydrophobic drugs. These vesicles can be made in different sizes and can be functionalized with specific ligands to target specific cells or tissues. The use of liposomes as a drug delivery system has several advantages, including improved drug solubility, increased drug stability, prolonged drug circulation time, and reduced toxicity [9]. Several liposomal formulations have been approved by regulatory agencies for clinical use, such as Doxil for ovarian and breast cancer and AmBisome for fungal infections [10]. Polymer-based drug delivery systems offer several advantages, including their biocompatibility, biodegradability, and ease of functionalization. Polymers can be synthesized in different forms, such as micelles, dendrimers, and NPs, and can be functionalized with specific ligands to target specific cells or tissues. The use of polymers in drug delivery has been shown to enhance drug solubility, stability, and bioavailability. For example, polymeric nanoparticles have been used to deliver anticancer drugs, such as paclitaxel, and have proved to be more efficacious than traditional chemotherapy [11]. Nanoparticles are submicron-sized particles made from different materials, such as metals, polymers, and lipids. Nanoparticles can also be functionalized with ligands targeting specific cells or tissues and can be used to encapsulate drugs to improve their solubility and stability. The advantages of using NPs in drug delivery are an improved drug bioavailability, a reduced toxicity, and the capability of crossing biological barriers, such as the blood–brain barrier. Several NP-based drug delivery systems have been approved for clinical use, such as Abraxane for breast cancer and Onpattro for hereditary transthyretin-mediated amyloidosis [12].

Nanoparticle size is an important parameter for many applications of NPs, including imaging, catalysis, and development of advanced drug delivery systems, and has been a subject of research in the field of medical NP applications for many years [13]. The main areas of the use of nanoparticles are shown in Fig. 1.

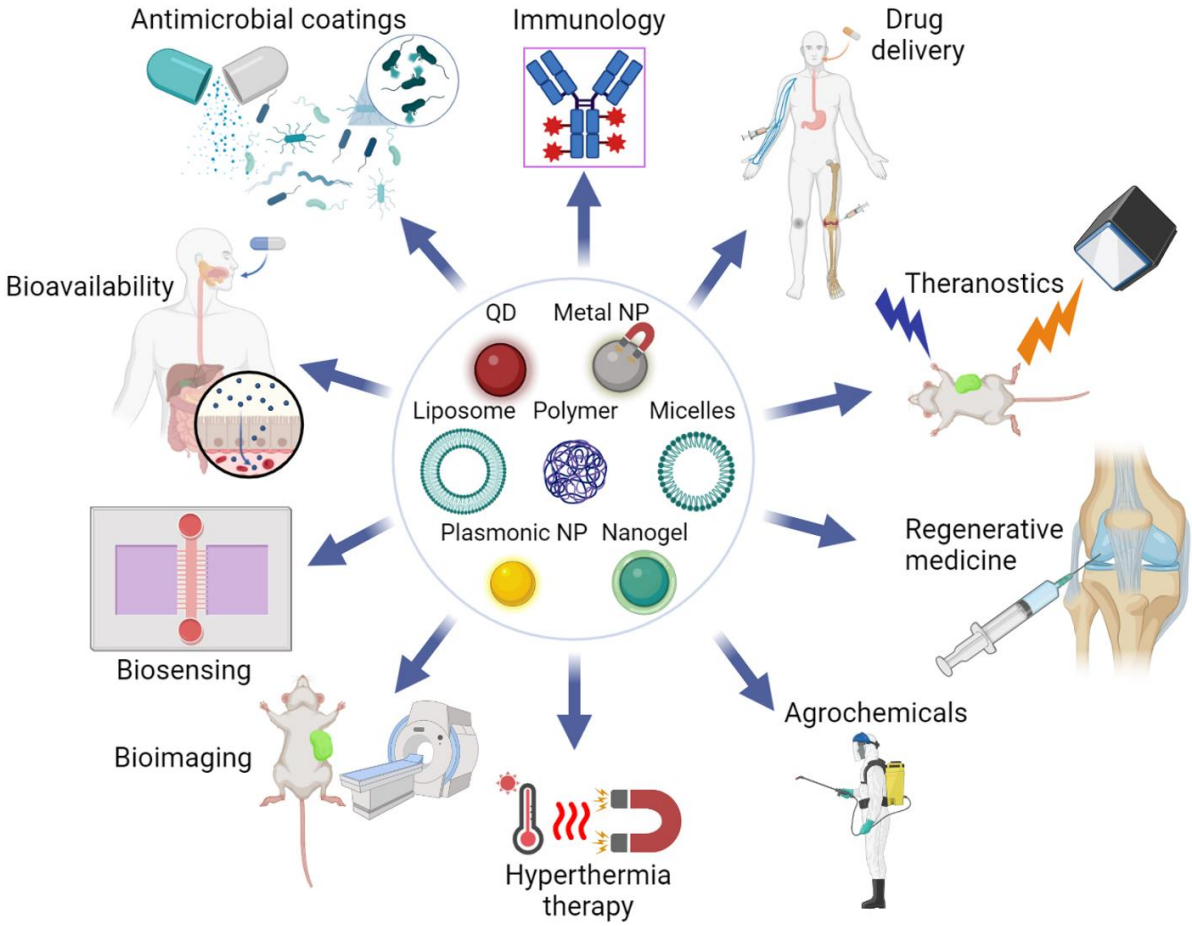


Fig. 1 Applications of nanoparticles in biomedicine sphere.

The size of NPs can affect their physical, chemical, and biological properties, which can, in turn, affect their behavior and performance in different applications. In drug delivery, e.g., the size of NPs can affect their capacities for circulating in the bloodstream, penetrating biological barriers, and interacting with target cells or tissues. Smaller NPs usually have longer circulation times, they better penetrate barriers but may also be more susceptible to clearance by the immune system. Larger NPs usually have longer circulation times, but they may be less capable of penetrating biological barriers or interact with target cells or tissues. In imaging, the size of NPs may affect their contrast properties, such as brightness and resolution [14]. Overall, understanding the size-dependent properties of NPs, ζ-potential, polydispersity, and concentrations is crucial for their effective use in various applications and can help in designing more efficient and effective NP-based systems.

The DLS method employs the interaction of monochromatic coherent radiation with light-scattering particles in the solution studied. Analysis of scattered radiation spectra in the DLS method is based on the Rayleigh scattering theory, Fraunhofer theory and the Mie theory. In the general case, the interaction of the light with a particle in the solution may lead to diffraction, refraction, reflection, and absorption. If the characteristic particle size is larger than the incident light wavelength, the diffraction process described by the Fraunhofer theory is predominant, and if the characteristic particle size is smaller than the wavelength of the scattered light, elastic light scattering without wavelength change occurs, which is described by the Rayleigh scattering theory [15]. Radiation scattered by particles whose size is comparable to the wavelength is detected at large angles (more than 90°) and is described in terms of the Mie theory. The DLS technique is implemented in various devices differing in optical configuration, signal modulation and analysis, detection system, and sensor geometry. The differences in design do not so much affect the calculated data or intensities of the measured signal, but rather determine the differences in operating concentration ranges, sensitivity of devices to certain sizes of objects, achievable resolutions of size distributions, and methods of data processing and signal analysis, which directly affects the measurement error and the results of measurements.

This review considers examples of using the DLS method in recent studies of biopolymers, NPs, and microparticles of various types, as well as interactions between them, to establish the relationships between the detected parameters and the properties of the objects studied. The concluding section of the review provides details on the application areas of the DLS method, its advantages and inherent limitations, and comparison with other optical methods of biomolecule analysis.

2 Theoretical Basis of the Dynamic Light Scattering Method

The DLS method is based on analysis of changes in incident radiation parameters, including the frequency and intensity, as well as the directional diagram, which changes or fluctuates when light passes through a layer of Brownian particles [16]. In this case, interference of individual scattering waves (signals) may lead to signal fluctuations on the radiation detector. The principle of DLS method is schematically shown in Fig. 2.

In the standard implementation of the DLS method, the sample or system studied is laser-irradiated, and the scattered light is detected at a certain scattering angle θ.

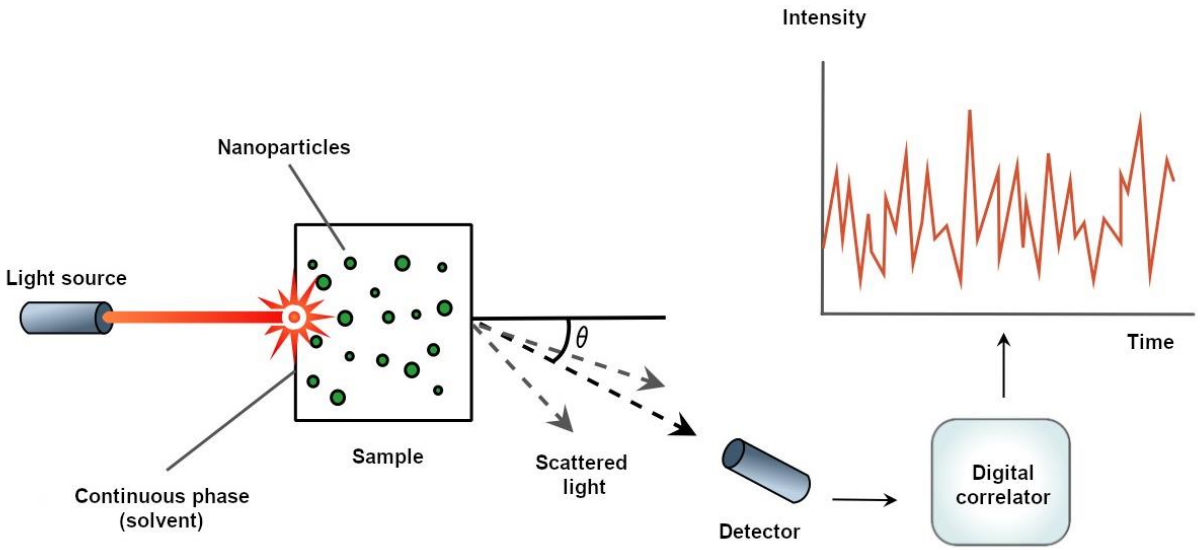


Fig. 2 The principle of the dynamic light scattering method. Light scattered by nanoparticles irradiated by a laser is measured with a high time resolution at a certain angle θ; the scattering signal fluctuation reflects the dynamics of microstructural processes, such as the Brownian motion of the particles.

The scattered radiation is either directly received by the detector or is superimposed or "mixed" with the reference signal reflected from the sample surface with an unshifted frequency. The power of the resultant signal is proportional to the product of the intensities of the scattered and reference signals. This makes it possible to detect low-power scattered radiation, which is important in studying nanometer-sized particles. The measured size of particles should not depend on the concentration of the sample. The use of backscatter detection allows a wider range of concentrations to be measured accurately compared with the standard operating procedures with the detection angle $\theta = 90°$ [17]. According to the first approximation of the classical theory of radiation, a pair of interacting molecules or NPs can be considered as a time-varying dipole that emits electromagnetic radiation. As such, the NP behaves like a secondary light source and scatters light. This scattered light is fully polarized at 90° to the incident beam, and its intensity (I_0) is proportional to the diameter (d) of the analyte ($I_0 \propto d^6$) and its polarizability [18]. The polarization of light scattered from particles with various shapes was described by Damaschke et al. [19]. Thus, the DLS method requires the use of colloidal suspensions with low concentrations to avoid the effects of secondary scattering and destructive interference.

Typical dynamic light scattering instruments use a detection angle of 90°, which may be not sensitive enough to measure small particles or molecules even with the use of a high-powered laser at a small wavelength. Backscatter detection is an optical configuration that can measure samples with smaller sizes and lower concentrations. At $\theta = 173°$, the scattering volume detected at the detector is about eight times greater than in the case of the traditional 90° optics [20]. This leads to an eightfold increase in the detected count rate, which is directly related to the instrument sensitivity to small particles at lower concentrations. Depending on the experiment, the angle θ can vary and reach, e.g., 175° [21]. The use of fiber optics in combination with this optical setup ensures that the signal-to-background ratio or the intercept of the correlation function is not degraded at high detection volumes, in contrast to the traditional geometric optics ($\theta = 90°$). Maintaining the count rate while reducing the intercept of the correlation function is crucial. This optical configuration provides the exceptional sensitivity necessary for measuring the size of NPs and molecules at low concentrations.

Regardless of the version of the DLS method, the general principle is that the analysis of the detected signals takes into account their fluctuations, whose duration is determined by the Brownian motion of particles and lies in the range from nano- to milliseconds. Analysis of the DLS signals assumes that the scattered light is coherent, but the classical DLS setup cannot distinguish between coherent and incoherent signals, which are mainly caused by multiple scattering. This calls for alternative analytical methods, e.g., cross-correlation techniques [22].

In this review, we consider the main uses of the classical DLS method in various fields. The use of the dynamic light backscattering method and new DLS approaches have been described by Malm et al. [23] and Hou et al. [24].

In addition, the laser self-mixing interferometry (SMI) and laser feedback interferometry (LFI) methods [25, 26] should be mentioned. The interferometric technique enables a laser to act as both a source and a detector. The operating principle of the laser techniques is the interference of light waves that are emitted and then reflected back to the laser cavity by an external target. The resulting frequency shift, which is proportional to the displacement of the target, is detected as a phase shift in the laser output signal. This signal can be used to determine the position, velocity, and acceleration of the target [27].

There are also various speckle-based methods. This is a class of optical methods that use the speckle structure formed by coherent light scattered by a rough or dynamic surface to extract information about the object or system under study. One of the most commonly used speckle-based techniques is speckle pattern correlation, which measures the displacement of speckle patterns obtained upon two separate measurements of the same object or system [28]. However, this class of optical research methods requires the development of time-consuming algorithms for data analysis [29]. All these methods have been used in various biomedical applications, including measuring the thickness and mechanical properties of biological tissues and detecting blood flow in blood vessels. Although some optical techniques share similarities with the DLS method, we do not discuss them in detail here, because they are not commonly used for characterizing microparticles, NPs, or polymers.

2.1 Light Absorption and Scattering by an Arbitrary Particle

All media except for vacuum can be considered, in a sense, heterogeneous. Even the media that are regarded homogeneous, such as pure gases, contain some local inhomogeneities – these are atoms and molecules. Consequently, all media will scatter light due to these local inhomogeneities. When an electromagnetic wave passes a system, each particle in the system is affected not only by the incident wave, but also by the sum of secondary fields generated by all other molecules in the medium. Under nonideal conditions, the average number of molecules in a given area of the system at any moment of time differs from that at the preceding moment. Precisely these density fluctuations lead to scattering in dense media. There are also concentration fluctuations, which also lead to scattering. If molecules have an irregular (nonspherical) shape, then orientation fluctuations occur. With clusters of particles, the situation is more complicated, because each particle is excited by an external field and resultant field scattered by all the other particles. In this case, the field scattered by the particle directly depends on the field in which it

is placed. When dealing with a cluster of charged NPs, we should bear in mind that this group of particles may display specific optical properties, which may drastically differ from the optical properties of NPs measured in a classical colloidal solution. For example, a spiral arrangement of gold NPs (GNPs) results in circular dichroism [30]. Interacting metal NPs exposed to an external electromagnetic wave exhibit a greater amplification of the electric field compared to isolated metal NPs, as well as a shift of the resonance peak and a change in scattering direction with changing distance between the particles [30].

When a particle is irradiated by a light beam with given characteristics (wavelength, incident angle, and temporal and spatial coherences), the amount of scattered light and its angular distribution, as well as the amount of absorbed radiation, directly depend on the particle shape, size, and composition. Light scattered by a single particle or a set of particles with the same shape, composition, size, and orientation is completely polarized. In this case, the intensity of scattered light is maximal if the wavelength of incident radiation is of the same order as the size of the examined object. If the inhomogeneities are small-sized compared to the wavelength of light, the intensity of the scattered light is proportional to the fourth power of the frequency or inversely proportional to the fourth power of the wavelength [31]. This relationship is called Rayleigh's law:

$$I \sim \omega^4 \sim \frac{1}{\lambda^4}, \tag{1}$$

$$I = I_0 \frac{9\pi^2 \varepsilon_0^2 N \tilde{V}^2}{2\lambda^4 L^2} \left(\frac{\varepsilon - \varepsilon_0}{\varepsilon + \varepsilon_0}\right)^2 (1 + \cos^2\theta), \tag{2}$$

where I and I_0 are the intensities of the scattered and incident radiations, N is the number of particles in the light-scattering volume, $\tilde{V}$ is the particle volume, ε is the dielectric constant of the particles, ε_0 is the dielectric constant of the medium where the particles are suspended, θ is the scattering angle, L is the distance between the scattering volume and the observation point, and λ is the wavelength of nonpolarized incident light.

Thus, Rayleigh scattering is coherent scattering of light which does not change the incident wavelength on particles or inhomogeneities. This type of scattering is termed elastic scattering. The vibrational electric field of incident light induces an oscillatory dipole moment in the particle, which subsequently emits light in the characteristic zone described by the dipole radiation pattern. For example, in the case of a spherically symmetric particle and linearly polarized light, the induced dipole moment is parallel to the direction of incident light polarization and is proportional to the polarizability of the particle.

2.2 Light Absorption and Scattering by a Spherical Particle

The Mie scattering theory is a complete solution of Maxwell's equations for scattering of electromagnetic waves on spherical particles and predicts the intensity of scattering induced by all particles in the measurement range [32]. It can be used to analyze the characteristic intensity distributions for small particles (in this case particle size is comparable with wavelength of the scattered light), which, in contrast to those predicted by the Fraunhofer theory, are not limited to scattering angles smaller than 90° (forward direction) but can be also calculated for scattering angles larger than 90° (backward direction). For calculating the particle size on the basis of the intensity distribution determined in this way, the Mie theory, in contrast to the Fraunhofer theory, requires that the refractive index and the absorption coefficient of the material studied be known. It is worth clarifying that for particles (with size a) that are significantly greater than the wavelength (λ) of the scattered light ($a \gg \lambda$), and with refractive indices that are substantially different from the unity, the scattering light can be accurately describe by Fraunhofer diffraction theory [33]. This theory valid for particles of size greater than several μm when analyzed with visible light [34]. When not all the optical properties of the nanoparticles are known, Fraunhofer is used since it is an approximation to the Mie theory. However, in the case of small or transparent particles, the use of the Fraunhofer approximation leads to an error in the size measurement [35].

The cross section of electromagnetic wave scattering on a particle depends on the ratio between the particle size and the incident wavelength, as well as the change in the light wavelength upon interacting with the particle material [36]. Rayleigh scattering is a special case of Mie scattering when the particle is much smaller than the wavelength. In this case, the external electromagnetic wave polarizes the particle, exciting an oscillating dipole moment in it. The dipole moment, whose oscillation is synchronous with the frequency of the external wave, re-emits light with a radiation pattern characteristic of the dipole moment. The Mie theory and Mie coefficients are described in more detail in Ref. [37]. As an electromagnetic wave effect is an external perturbation, we can use physical formalism to analyze the forces and moments acting on the object. If the size of this object is between the Rayleigh and geometric optics limits, its original form considers the scattering of a plane wave by a spherical particle and generalization of the Lorentz–Mie scattering is required. Whereas the Mie theory is more suitable for analyzing charged NPs in a solution [38], the generalized Lorentz–Mie theory describes the scattering of arbitrary fields [39] and makes it possible to find exact solutions for the scattering of plane waves by individual dielectric spheres in arbitrary frequency modes [40]. The differences between Rayleigh scattering and Mie scattering are shown in Table 1 and Fig. 3.

Table 1 Differences between Rayleigh scattering and Mie scattering.

Rayleigh scattering	Mie scattering
Fluctuation of the concentration may affect the refractive index.	The suspension is strongly diluted, and light can be considered to be scattered by a single particle and detected before it has interacted with other particles.
The scattering strongly depends on the incident wavelength.	The scattering weakly depends on the incident wavelength.
The particle size (a) is smaller than the incident wavelength [41]: $a \le \frac{\lambda}{10}$ The scattered light carries the same energy (elastic scattering) as the incident light and is independent on the angle.	The particle size (a) is about the same as, or larger than, the incident wavelength [41]: $a > \frac{\lambda}{10}$ Rayleigh scattering is replaced by the anisotropic Mie scattering, with the scattered light energy unequal to the incident light energy (inelastic scattering) and depending on the angle; i.e., the scattered light is more intense along the direction of the incident light.

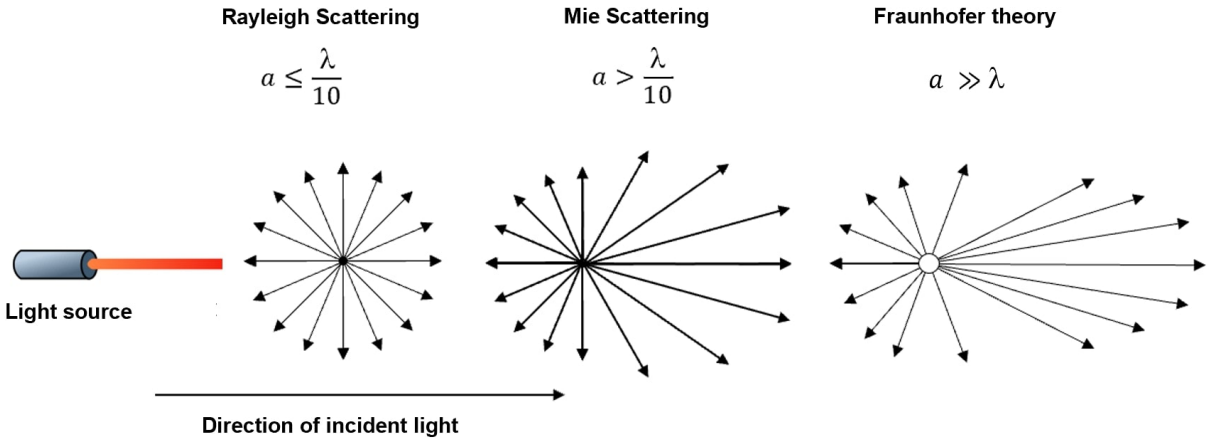


Fig. 3 Differences between Rayleigh scattering and Mie scattering; a is the characteristic size of the particles studied.

According to Yue et al. [42], disperse NPs scatter incident light proportionally to the sixth power of their radius ($I \propto d^6$). In this case, the intensity distribution has the form:

$$I = I_0 \frac{1+\cos^2\theta}{2R^2}\left(\frac{2\pi}{\lambda}\right)^4\left(\frac{n^2-1}{n^2+2}\right)^2\left(\frac{d}{2}\right)^6, \quad (3)$$

where I and I_0 are the intensities of the scattered and incident radiations, R is the distance between the scattering volume and the observation point, θ is the scattering angle, λ is the wavelength of nonpolarized incident light, d is the particle diameter, and n is the absolute refractive index of the medium.

2.3 Brownian Motion

The behavior of colloidal particles is described by the kinetic molecular theory, which assumes that spherical particles diffuse in a liquid phase consisting of molecules small enough for this phase to be considered as a continuous medium. Then, Brownian motion of particles results in self-diffusion of molecules in the liquid medium, whose coefficient is estimated using the Stokes–Einstein equation [43]:

$$D_p = \frac{k_B T}{3\pi\eta r_{h,t}}, \quad (4)$$

where D_p is the diffusion coefficient of the particles, η is the dynamic viscosity of the liquid, $r_{h,t}$ is the hydrodynamic radius (HR) of translationally moving particles, T is the temperature of the colloidal solution, and k_B is Boltzmann's constant.

The HR (Stokes radius) is the size of an object that is calculated from its diffusion coefficient in a liquid, on the assumption of its spherical shape. For spherical particles, such as components of sols and latexes, the real size is almost the same as the HR. For nonspherical particles, such as ellipsoids, cubes, rods, or particles with through holes, the HR is a conditional or effective parameter.

Brownian motion is a continuous chaotic motion of particles of the dispersed phase caused by hits from the molecules of the solvent (dispersion medium), which are in the state of intense thermal motion. The particles of the dispersed system, repeatedly hit by fluid molecules from different sides, can translationally move in different

directions. The Einstein–Smoluchowski equation shows [44] that the mean squared displacement of a particle in the case of one-dimensional Brownian motion during the time (t) is equal to following:

$$\overline{\Delta x^2} = 2D_p t, \tag{5}$$

where D_p is defined by Eq. (4).

The chaotic Brownian motion of dispersed particles leads to microscopic fluctuations of the particle concentration in local points of space and the corresponding local inhomogeneities of the refractive index of the medium. When a laser beam passes through the medium with local inhomogeneities, part of the light will be scattered on these inhomogeneities. The fluctuations of the intensity of scattered light will correspond to the fluctuations of the local concentration of dispersed particles. Information about the diffusion coefficient of particles is contained in the time-dependent correlation function of the intensity fluctuations detected by the detector, and it depends on the fluctuations of the particle coordinate in the solution (see Fig. 4).

Frequency analysis or correlation spectroscopy can be used for qualitative and quantitative estimation of scattering signal fluctuations. Frequency analysis decomposes the signal into its frequency components to obtain the frequency distribution or the spectrum of the power $P(\omega)$ [45]:

$$P(\omega) = \lim_{T\to\infty} \frac{2}{T} \left\langle \left| \int_0^{\frac{T}{2}} I_{det}(t) \cdot e^{-i\omega t}\, dt \right|^2 \right\rangle, \tag{6}$$

$$P(\omega) = \int_0^{\infty} \langle I_{det}(t) \cdot I_{det}(t + \tau) \rangle e^{i\omega t}\, dt,$$

where $I_{det}(t)$ is the detected light intensity, τ is the delay time between two scattering signals, ω is the carrying frequency, and i is the imaginary unit.

By definition, the time autocorrelation function has the following form [46]:

$$g_2(q,\tau) = \frac{\langle I_{det}(t) \cdot I_{det}(t+\tau) \rangle}{\langle I_{det}(t) \rangle^2}. \tag{7}$$

The autocorrelation function $g_2(q,\tau)$ in Eq. (7) quantitatively defines the time-averaged correlation between two scattering signals measured at the time delay τ.

In a system of monodisperse particles with single scattering where Brownian motion occurs, the corresponding correlation function is represented as a sum of a constant and a damped exponential, e.g.,

$$g_2(q,\tau) = A + B \exp\left(-C \cdot D_p q^2 \tau\right), \tag{8}$$

where q is the scattering amplitude; τ is the time interval between measurements; and A, B, and C are constants.

On the other hand, the first-order correlation function of the electric field is exponentially damped in the case of Brownian motion of monodisperse particles:

$$g_1(q,\tau) = \exp(-\Gamma \cdot \tau). \tag{9}$$

For polydisperse particles, the equation takes the following form:

$$g_1(q,\tau) = \int_0^{\infty} \exp(-\Gamma \cdot \tau) dQ_{int}(\Gamma), \tag{10}$$

where Γ is the time coefficient of the decrease in particle size in the medium and $dQ_{int}(\Gamma) = A_i = const$ is the weight coefficient defining the relative contribution to the scattering intensity.

$$\Gamma = q^2 D_p. \tag{11}$$

The Euclidean norm of the scattering vector $\vec{q}$ [47] is

$$q = \|\vec{q}\| = \frac{4\pi n}{\lambda_0} sin\left(\frac{\theta}{2}\right), \tag{12}$$

where n is the refractive index of the disperse medium, λ_0 is the wavelength of incident light (a laser beam) in vacuum, and θ is the scattering angle.

Eq. (10) can be rewritten in the form:

$$g_1(q,\tau) = \int_0^{\infty} A(\Gamma) \cdot \exp(-\Gamma \cdot \tau) d\Gamma, \tag{13}$$

where $A(\Gamma) \cdot d\Gamma$ is the proportion of the correlation function damped with time of inverse relaxation between Γ and $\Gamma + d\Gamma$.

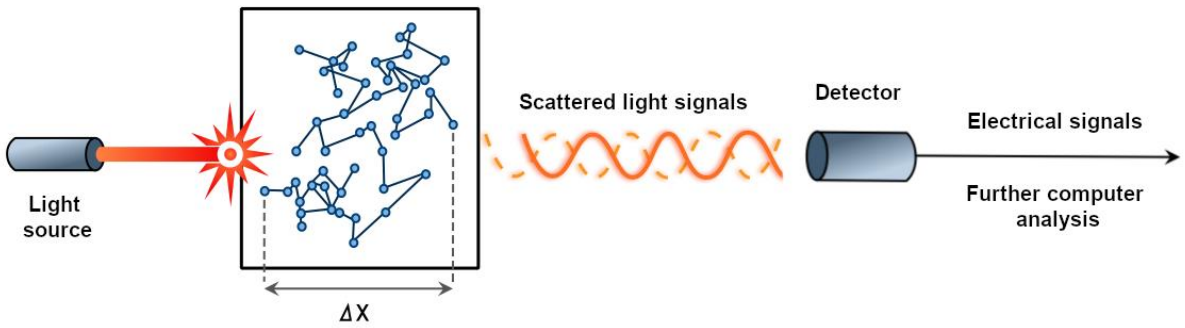


Fig. 4 Fluctuation of the particle position in a colloidal solution.

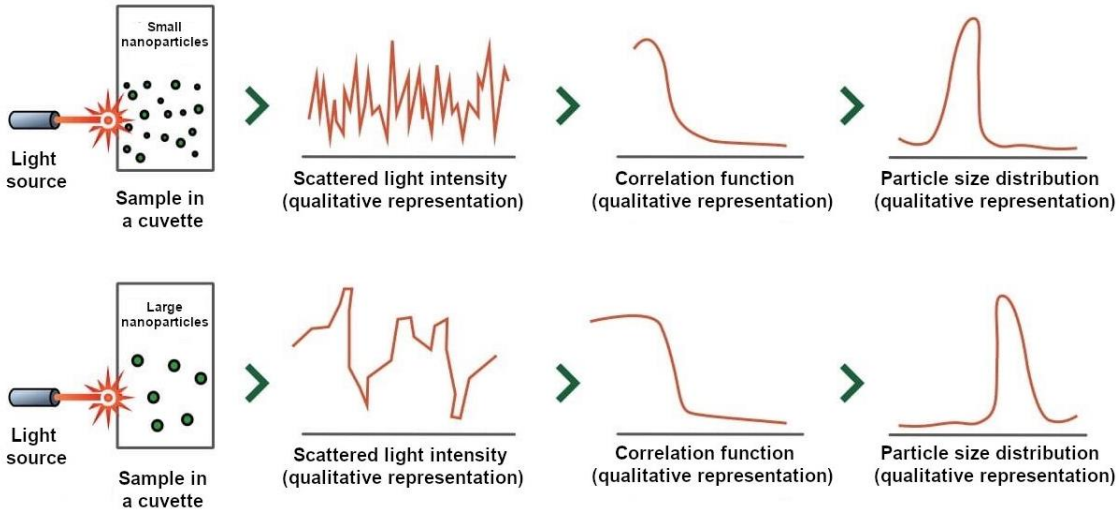


Fig. 5 The qualitative presentation of the data obtained using dynamic light scattering.

The coefficients at the exponent depend on the contribution to the total intensity of the scattered light and the intensity of the light scattered on particles of the same size. To determine the correlation times from the experimental correlation function, we need to select a set of times and coefficients in Eq. (13) so that the difference between the calculated and experimental functions tend to the minimal value. It should be noted that Eq. (13) in its general form belongs to the class of integral equations and, in our case, represents the Fredholm integral equation of the first kind. Its solution belongs to the class of incorrectly set problems [48]. This means that, if the function $g_1(q,\tau)$ is defined with a small error, the solution may differ from the true one and may not be the only one. Within the experimental error, there will be an infinite number of different solutions that fit the experimental data well. The more accurate the experimental data, the fewer solutions will fit these data. Thus, knowing the form of the correlation function, one can obtain the particle size distribution by using a software (mathematical algorithm) [49]. Fig. 5 shows the qualitative presentation of the results obtained by the DLS method.

There are also NPs whose motion does not obey the Stokes–Einstein relation. The DLS estimation of the particle size distribution assumes that the scattered light fluctuates only because the particles are continuously displaced due to Brownian motion. When DLS is used to quantify the properties of individual particles, the sample should be diluted as much as possible to exclude any influence of the particle concentration, otherwise the estimates may considerably deviate from the actual values, and the measurement error will be high.

Several factors that determine the difference between the real and the ideal experimental situations are: (i) multiple scattering within the sample; (ii) nonrandom spatial distribution of particles; (iii) viscous interaction between neighboring particles; (iv) signal fluctuation that reflects not only the Brownian motion of individual particles, but also stochastic variation of the local concentration of particles; (v) signal fluctuation determined by Brownian displacement on short- and long-time scales; (vi) possible coagulation of particles.

The results of the analysis also depend on the properties of the particles (size, shape, and optical properties) and the medium (phase boundary properties), as well as the parameters of the measuring instruments (wavelength and scattering angle). However, in the case of nonspherical particles, one more factor, Brownian rotation of the particles, inevitably contributes to the signal fluctuation. The rotation affects the spatial orientation of the particles and, hence, the scattering of light in a given direction.

It should also be borne in mind that the characteristics of the Brownian motion of particles can be influenced by surfactants. These are substances that are positively adsorbed at the phase boundary, forming an adsorption layer with an increased concentration. A surfactant may significantly affect the diffusion coefficient, which additionally alters the Stokes–Einstein relation, so that the relation does not hold for this type of systems. This effect has been observed experimentally, e.g., in a reverse micellar system containing 15 wt.% of polydisperse hexaethylene glycol monodecyl ether ($C_{10}E_6$) in cyclohexane [50]. As a result, the correction coefficients for the viscosity and self-diffusion of particles were determined to fit the experimental data to the Stokes–Einstein relation.

In the general case, the estimated hydrodynamic diameter of nonspherical particles is correlated with the scattering angle [49]. Hence, the systemic dependence of the measured size distribution on the scattering angle suggests a nonspherical shape. Note that the effects of nonspherical shape remain hidden for DLS devices with only one scattering angle.

Characterizing the motion of particles in a medium is generally a difficult task, and it is further complicated by characteristic hydrodynamic interactions (HIs) mediated by the solvent and suspended particles. Therefore, HIs affect the dynamics of the spheres and considerably

complicate the calculations. HIs are usually long-range, non-pairwise-additive forces occurring at high particle concentrations [51].

Short-term diffusion is defined as diffusion of colloidal particles investigated over a time interval t satisfying the following two inequalities [52]:

$$\tau_H \sim \tau_I \ll t \ll \tau_D, \quad (14)$$

where τ_H is the hydrodynamic time scale that quantitatively defines the interval in which shear waves of the solvent cross the characteristic distances between (larger) colloidal particles, τ_I is the time of impulse relaxation, and τ_D is the time interval of diffusion interaction described in terms of the Stokes–Einstein free translational diffusion coefficient.

Inequalities (14) define the short-term colloidal mode, which takes into account the times of impulse relaxation and diffusion interaction of the particles. At time moments $t \gg \tau_I$, many random collisions of the colloidal particle with solvent molecules occur, the particle motion is diffusive, and inertia does not play any role. During the time $t \gtrsim \tau_D$, diffusion considerably changes the spatial configuration of (smaller) particles compared to their original configuration, and, in addition to HIs, permutations of groups of neighboring particles begin to affect the dynamics of the particles in the medium. This leads to a subdiffusive particle motion at the time moment $t \gtrsim \tau_D$ preceding the finite diffusive long-term mode $t \gg \tau_D$, in which the particle can occupy many independent local regions.

The function of the scattering wavenumber q and the correlation time t is a fundamental quantity determined in DLS experiments. It represents the normalized intermediate scattering function $f_c(q,\tau)$ [51]:

$$f_c(q,\tau) \approx \exp(-q^2 \cdot D_s(q)\tau), \quad (15)$$

where $D_s(q)$ is the short-term diffusion function proportional to the hydrodynamic function $H(q)$. The hydrodynamic function serves as a generalized short-term sedimentation coefficient and directly reflects HIs. In the case of infinite dilution or (hypothetical) absence of particles, the function $H(q)$ is identically equal to unity [51].

Attempts at computer model of the process described above have been made [51, 52]. In general, the dynamic scattering functions obtained in Stokes dynamics simulations [53] agree well with the results of DLS for a range of concentrations of charged spherical silicon NPs in a mixture of organic solvents within certain experimental time range and wavenumber range. There are many approaches to determining the characteristic particle size, in particular, estimations based on the diffusion coefficient calculated from data on polydisperse samples. Most of these approaches rely on a known analytical distribution and adjust the variables so as to obtain the best fit to the experimental data. The main problem of these methods is the a priori assumption on a given form of distribution, which often leads to ambiguous results.

2.4 Variants of the Dynamic Light Scattering Method

The DLS method has some interesting variants. One of them is the multipolarization dynamic light scattering (MPDLS) method, which is based on two similar methods, multi-angle dynamic light scattering (MADLS) and depolarized dynamic light scattering (DDLS), but is essentially a new method combining the advantages of the other two. The MADLS analysis integrates information on the scattering angle from the Mie theory and analysis of the particle size distribution based on DLS measurements. Lower noise and, hence, a lesser smoothing provide a more reliable and accurate representation of the particle size distribution and better characterization of the individual components of a multicomponent sample. The MADLS method provides additional information about the sample by combining DLS measurements made from different angles. An example of comparison of the DLS and MADLS data is presented in Ref. [54]. The DDLS method provides, in addition to data on radius distributions, information on the shape of the particles. The DDLS analysis is widely used for calibrating nonspherical NPs, such as nanorods, nanowires, and nanotubes. Detailed theoretical basis of this method has been presented by Geers et al. [55]. The depolarized component of the light-scattering signal makes it possible to estimate both translational and rotational diffusions of nonspherical NPs. As a result, the DDLS method determines not only the HR of the equivalent sphere, but also the actual length and diameter of diffusing NPs [56]. By considering the Brownian motion of NPs in terms of translational and rotational diffusions, the particle sizes can be determined from the rates of damping of the scattered-light fluctuations. The damping rates are determined for light scattered with two different polarizations, one of which (co-polarization) coincides with the polarization of the excitation light and is termed the VV component (vertically polarized waves transmitted and received) and the other (cross-polarization) is perpendicular to it and is termed the VH component (horizontally polarized waves transmitted and only vertically polarized waves received) (see Fig. 6). The depolarized component, e.g., the horizontally polarized one in the case of vertically polarized incident light, results from multiple DLS and is usually weak. It disappears in the case of spherical particles in dilute suspensions. Thus, the MPDLS method differentiates between the translational Brownian motion of particles from the Brownian rotation and provides the shape parameters of the particles in addition to their sizes [49].

Diffusing wave spectroscopy (DWS) is also based on DLS. The concept behind this method is that the motion of scattering particles influences the coherence of the light scattered by them.

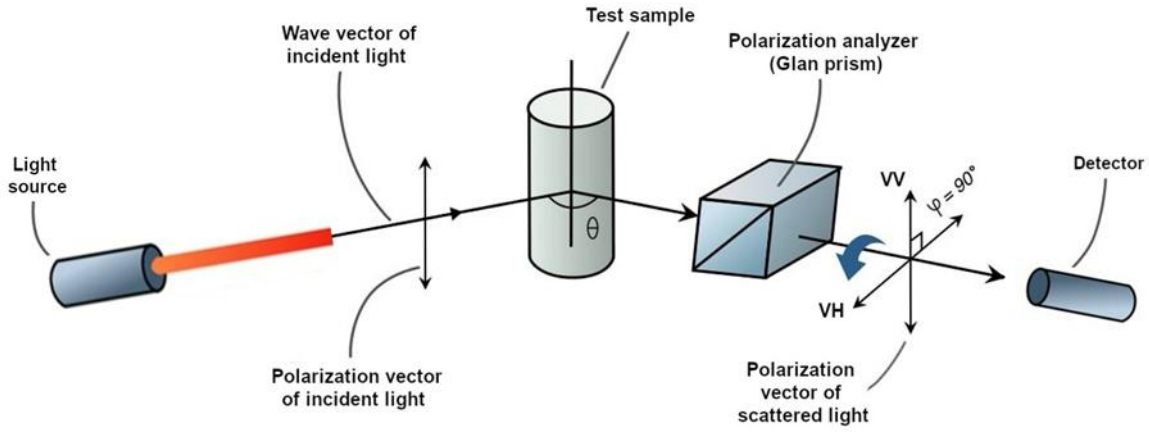


Fig. 6 A method of depolarized dynamic light scattering measurement scheme.

By analyzing the temporal fluctuations of scattered light, the diffusion properties of the particles can be determined. In contrast to the DLS method, which measures the intensity fluctuations of scattered light, the DWS method measures the temporal fluctuations of the speckle pattern of the scattered light, which ensures more robust measurements. One of the primary applications of DWS in biomedicine is the measurement of the size and shape of NPs and molecules [57].

3 Specifics of the Dynamic Light Scattering Analysis of Nanoparticles and Polymers

This section describes examples of the use of DLS in biochemistry, with the focus on important specifics of studying samples of different types and some guidelines to these studies.

3.1 Measurement of Nanoparticle and Polymer Sizes

DLS size measurements are based on measuring the time parameters of light fluctuations on the detector caused by random diffusion or motion of suspended particles in a small "scattering volume". The scattering volume is defined as the volume inside the sample illuminated by the laser beam from which the light scattered by particles directly goes to the detector. Small particles diffuse rapidly, leading to rapid fluctuations of intensity at the detector; large particles diffuse more slowly, causing longer fluctuations of scattered light at the detector.

The size of NPs is known to affect their distribution, sites of accumulation, and routes of elimination from the body, as well as their possible toxic effect [58]. At the same time, NPs are increasingly used in cosmetic products as sunscreens, which requires a low-cost method of controlling the size of NPs in creams. De la Calle et al. [59] have compared different analytical methods used for determining the size of NPs in cosmetic products. The DLS method quickly determined the HR of NPs and their size distribution, but the size was overestimated because of the solvation layer on the NP surface and the high viscosity of the samples. It was found that the discrepancy between the experimental data and real NP sizes in analysis of fat samples could be reduced by treating the suspensions with 0.1% sodium dodecyl sulfate or precipitating the NPs with hexane, with subsequent removal of the hexane solution and dissolution of the precipitate in distilled water. The DLS method is readily applicable to analyzing the size of dispersed liposomes and micelles intended for drug delivery. Chan et al. [60] have developed a protocol for analyzing nanoemulsions of oil in water by the DLS method, thus having shown that the DLS method is suitable for studying objects other than solid particles.

One example of an application of DLS is the study of colloidal stability of charged NPs in the presence of oppositely charged surfactants, such as cetyltrimethylammonium bromide and dodecyltrimethylammonium chloride. In this case, the DLS method can be used to determine not only the colloidal stability, but also the charge of NPs, and, hence, to infer the structure of NPs coated with charged surfactant ligands [61]. Now that a growing number of various biological imaging studies use NPs as contrast agents [62], it is important to explore the interaction of NPs with proteins. Moerz et al. [63] studied how GNPs with a citrate-functionalized surface formed stable hybrid clusters with hemoglobin. In that study, DLS analysis was used to estimate the sizes of not only GNPs, but also the hemoglobin–GNP clusters. Note that the use of DLS analysis allowed the researchers to determine minimal concentrations of clusters formed upon adding as little as 0.1 mg/L of hemoglobin, which indicates a high sensitivity of the method.

The DLS method is widely used to determine the hydrodynamic sizes of NPs of different compositions and with different surface ligands (Table 2). In addition, DLS analysis is suitable for studying changes in the size and morphology of GNPs exposed to strong laser radiation.

These studies are especially important because there are examples of using NPs for hyperthermal destruction of tumors [69], and it is essential to control the possible size of the NPs after their heating with laser irradiation.

Table 2 Hydrodynamic diameters of different nanoparticles determined by the dynamic light scattering method.

Nanoparticle type	Surface ligand	Hydrodynamic diameter, nm	Ref.
Fe_3O_4	Poly(sodium(4)-styrenesulfonate)	~200	[64]
	Poly(diallyldimethylammonium chloride)	107.4 ± 53.7	[65]
	Mercaptosuccinic acid	78.48 ± 0.91	[66]
$\varepsilon - Fe_2O_3$	Poly(4-vinylpyridine)-block-poly(methoxypolyethylenglycolacrylate-co-Rhodamine polyethylenglycolmethacrylate-co-carboxylic polyethylenglycolmethacrylate)	without coating, 18 after coating, 27	[67]
$\gamma - Fe_2O_3$		without coating, 29 after coating, 36	
Au@citrate	-	58 ± 6	[68]
Au@ pMEO$_2$MA-G1	2-(2-Methoxyethoxy)ethyl methacrylate	102	
Au@ pMEO$_2$MA-G2		177	
Au@pNIPAM-G4	N-Isopropylacrylamide	141	
Au@pNIPAM-G5		197	
Au@pMMA-G6	Methyl methacrylate	225	
Au@pMMA-G7		216	
Au@pSt-G9	Styrene	102	
Au@pSt-G10		151	
Au@pSt-G11		198	

pMEO2MA-(G1–G11) are samples differing in the molar fraction of sodium dodecyl sulfate used during sample formation and in the molar ratio of solvents (water and ethanol).

Table 3 Effect of the solvent on the detected TiO_2 nanoparticle size [73].

Organic solvent	Nanoparticle size, nm
Acetone	642
Butanol	668
Methanol	626
Isopropanol	774
Ethylene glycol	550

Cavicchi et al. [70] used the DLS, DDLS, and transmission electron microscopy (TEM) analyses to determine changes in the average size and size distribution of GNPs under laser irradiation and demonstrated a high sensitivity of DLS-based techniques and good correlation of their results with TEM data for diluted solutions of 10- to 100-nm NPs. It is also worth noting that researchers who design the experiment and select its parameters should be experienced in this field, because a minor change in the experimental parameters can significantly affect the reliability of the results. For example, Zheng et al. [71] studied the effects of GNP concentration, laser radiation power, and the multiple scattering phenomenon on the estimated HR of GNPs coated with citrate ligands with a nominal size of 100 nm. Their study has shown that the estimated HRs of GNPs strongly depend on the concentration and on the power of the incident laser radiation. The intensity of scattered light is proportional to the sixth power of the NP diameter, and the extremely intense light scattered on 80-nm or larger GNPs causes a substantial multiple scattering effect in conventional DLS instruments. This effect leads to considerable errors in the detected HR in the case of routine data analysis not taking into account the multiple scattering. Other examples of experiments with gold, silver, and alloyed gold–silver NPs in aqueous media are compiled elsewhere [72].

Zhang et al. [73] studied the effect of the medium on the measurement of NP sizes by the DLS method. As an example, the sizes of TiO_2 NPs, originally in the powder form, were determined in different solvents (Table 3).

The above examples show the importance of selecting the experimental parameters in DLS studies and demonstrate the effects of the laser flux density and medium composition on the estimated NP size. The composition of the NPs may also influence the size estimates. For example, a strong surface plasmon resonance (SPR) on GNPs significantly increases the intensity of scattered light compared to particles of the same size and shape made from materials that do not display SPR. This is of particular importance given the widespread use of the SPR effect in the imaging of malignant neoplasms, in theranostics, and in bioimaging [74]. Lehmann et al. [75] used DLS to measure the photoinduced size changes of hybrid particles, GNPs coated with a thermosensitive polymer. They used the setup for the MADLS analysis where the particle size was determined by irradiation with a helium–neon laser (633 nm), and an additional sapphire laser (532 nm) was used to irradiate GNPs in the SPR wavelength range. The use of MADLS made it possible to obtain absolute values of the HRs of bare GNPs and GNPs coated with thermosensitive polymer and to correct the data by excluding the light scattered by the GNPs. In contrast, in a single-angle DLS experiment, the light scattered by the GNPs would dominate the signal, especially at large angles, and only relative HR values would be available. This example shows the effect of SPR on the measurement process. A similar setup could be used for studying vesicles, microgels, and other hybrid systems, e.g., in developing drug carriers that would degrade in response to irradiation. Table 4 summarizes data on the sizes of different types of NPs as estimated by the DLS, TEM, and small-angle X-ray scattering (SAXS) methods.

However, it should be remembered that direct comparison of NP sizes estimated using different techniques is not entirely correct. For example, DLS measures the HR of particles that actually consist, apart from the particles per se, of the layers of ions and solutes adsorbed from the solution, depending on the measurement conditions. We will consider the comparative advantages and drawbacks of the DLS method in more detail in the conclusion to this review.

The DLS measurement of NPs size is used in many test systems. For example, Liu et al. [79] have described a test system for detecting picomolar concentrations of free prostate-specific antigen (f-PSA), a prostate cancer biomarker, that identifies immunocomplexes of GNPs, f-PSA, and gold nanorods by the DLS method. Dai et al. [80] have reported a DLS-based method for detecting specific DNA sequences. This method uses two types of GNPs about 30 nm in size conjugated with oligonucleotides complementary to the 5' and 3' ends of the detected DNA. Here, DLS is used to detect the complex formed by two GNPs with DNA. The detection sensitivity is 1 pM, which is four orders of magnitude more sensitive compared with the methods based on light absorption measurement. At the same time, in developing DLS test systems, it is necessary to take into account inherent limitations of the DLS method. Specifically, the mean HR of an NP or a globular polymer remains constant, within the margin of error, as the concentration increases to a certain threshold, but further increase in concentration leads to a considerable decrease in the mean HR. Zheng et al. [71] analyzed the effect of the concentration of GNPs coated with citrate ligands on their HR estimated by the DLS method. With increasing GNP concentration, their estimated HR decreased from the nominal size of ~100 nm at a concentration of 5.6×10^8 GNPs/ml to ~50 nm at 5.6×10^9 GNPs/ml and further to ~3 nm in the most concentrated samples. Such a high measurement error is explained by the aforementioned effect of multiple scattering in concentrated solutions.

DLS measurement of the size of fluorescent quantum dots (QDs), which are widely used as fluorescent tags for *in vivo* and *in vitro* imaging [81], also has some peculiarities. The reason is that DLS analysis often involves laser radiation with a wavelength of about 630 nm, and CdSe QDs about 15 nm in size fluoresce in this wavelength range.

Table 4 Sizes of nanoparticles of different types estimated using the dynamic light scattering, transmission electron microscopy, and small-angle X-ray scattering.

Nanoparticles		**Actual size, nm**	**Estimated size, nm**			**Ref.**
Type	Sample		DLS	SAXS	TEM	
Hollow SiO_2/TiO_2 nanoparticles	HNP25	25	28 ± 2	30.0 ± 0.5	26 ± 5	[76]
	HNP50	50	57 ± 2	62.8 ± 0.5	59 ± 5	
	HNP100	100	108 ± 2	101.4 ± 0.5	105 ± 5	
Polystyrene nanoparticles	PS1	–	33.5	43.2	40.5	[77]
	PS2	–	25.0	29.6	25.5	
Gold nanoparticles	Au1	15	50.7	-	13.7	[78]
	Au2	60	50.8	-	59.1	
Silicon nanoparticles	Si1	50	153.7	-	43.8	
	Si2	80	121.6	-	57.7	

This can distort the correlation function and lead to incorrect results. Therefore, the researcher has to prevent the overlap between the QD fluorescence spectrum and the laser radiation spectrum by using narrow-band optical filters or a laser with a different radiation wavelength [82]. Modlitbová et al. [83] studied the growth of the QD silicon shell as a function of time using the DLS and SEM methods. The authors observed only a minor discrepancy between the sizes of the shelled QDs estimated by the two methods at the initial stage of shell growth, but this discrepancy increased as the shell grew. Specifically, the difference between the estimates obtained by these methods was only about 8% before the start of shell growth and increased to 20% when the shell was formed. The explanation is simple: in the course of shell growth, the QD shape gradually deviated from spherical and the QD size became more variable, which led to incorrect results of the DLS measurements. It is important to correctly estimate the size of $CsPbBr_3$ semiconductor crystals with a perovskite structure. Due to their unique properties, perovskite nanocrystals are actively used in the production of solar cells, as well as scintillation detectors for biological imaging [84]. In determining their size by the DLS method, recommendations developed for quantum dots would be useful. Below, we will consider how the size of nonspherical NPs can be nevertheless determined.

3.1.1 Measurement of the Sizes of Nonspherical Nanoparticles

If the particles are considered as homogeneous spheres, then all angular scattering data must satisfy the Mie theory. In all other cases, the Rayleigh–Gans approximation yields the best results, with root-mean-square radii calculated for the model selected on the basis of all previously known or assumed particle structures. For all interpretations based on the Mie theory or Rayleigh–Gans approximation [85], the particle samples should be fractionated before the measurement to ensure that the measurements are made in monodisperse samples. Nanomaterials of various shapes are widely used in biomedical research. The shape of NPs affects, e.g., their distribution in the bloodstream, circulation time in the body, and efficiency of cellular uptake, which is important when they are used for targeted drug delivery [86]. As mentioned above, the DLS method is the most suitable for measuring the sizes of NPs and microparticles (more precisely, their HRs) under the assumption that they are spherical. Therefore, the estimation of the HR of nonspherical NPs [87–90] is more difficult in both theoretical and practical terms. Two-dimensional materials have unique light-dynamic properties, a high heat conversion coefficient, and a large effective area-to-volume ratio. Therefore, they are of particular interest for various medical applications [91], including highly efficient drug loading [92]. Therefore, these materials are promising potential components of smart drug-delivery systems [93]. For example, Y_2O_3 NPs inhibit the growth of both Gram-positive and Gram-negative bacteria, and flake-like Y_2O_3 NPs exhibit anticancer activity [94]. For qualitative analysis of the shape of NPs under study, it is necessary to develop mathematical models and introduce correction factors determining the HR of NPs of different shapes [42]. Thus, when dealing with nonspherical structures, a correction factor should be taken into account. In the given example, this coefficient was so selected that the transverse size of a square-shaped NP and a circular nanoplate was 1.96 and 2.667 times the HR of their equivalent sphere [42]. With these correction factors, the DLS method can be used to accurately measure the lateral sizes of two-dimensional or nonspherical NPs. The following equation for calculating the HR of cylindrical particles is an example of the use of a correction factor:

$$R_h = \frac{3}{4}d^2\left[\begin{array}{c}\sqrt{d^2+L^2}+\frac{d^2}{L}\times \\ \times \ln\left(\frac{L}{d}-\frac{1}{d}\sqrt{d^2+L^2}\right)-L\end{array}\right]^{-1}, \quad (16)$$

where L is the thickness and d is the diameter of the particle.

However, complex mathematical calculations are not always necessary. For example, Lotya et al. [95] studied solutions of graphene, MoS_2, and WS_2 nanoplates with sizes ranging from 40 nm to 1 μm. They have shown that good calibration curves can be plotted with an error between the DLS (in the backscatter mode, at an angle of 173°) and TEM data of less than 40%. Thus, it sometimes suffices to plot calibration curves for NPs of different shapes and sizes in different solutions and use them to determine the size of nonspherical NPs and microparticles by the DLS method.

It should be taken into account that even small hollows and non-uniformity of shapes lead to significant divergence of DLS results from actual values. Experiments with nonspherical silver NPs with a nominal diameter of about 50 nm have shown that DLS significantly overestimates the size distribution, and primary study of unknown samples should always combine DLS with electron microscopy or a similar method [96]. Alternative methods for estimating the size of nonspherical silver NPs are summarized in Ref. [97].

Gold nanorods are a convenient biomedical material because they bind amino and thiol groups of biomolecules, thus facilitating functionalization and bioconjugation involved in the fabrication of hybrid imaging and therapeutic systems [98]. In addition, gold nanorods, due to their effective radiation absorption in the near-infrared spectral range, are ideal candidates for photothermal destruction of tumor cells [99]. The optical properties of gold nanorods and their distribution in the body depend on their size and length-to-diameter ratio, which makes the measurement of their sizes a topical task. Levin et al. [56] used the MPDLS method to determine the size of gold nanorods. Their technique was based on time-resolved measurements of the intensity of light scattered by the NPs for different angles between the directions of incident and scattered light

polarizations. Experiments with gold and iron oxide nanorods were performed. The lengths and diameters of gold nanorods estimated from diffusion coefficients using the simple Kirkwood diffusion model agreed with the TEM data. However, this was not the case for iron oxide nanorods, most likely because their shape was far from cylindrical. To determine the size of axisymmetric nonspherical NPs, these authors suggested the concept of an equivalent cylinder with the same translational and rotational diffusion coefficients as those of the real particle. This concept can be useful for monitoring the stability of NPs in liquid media and the changes in their size with time, which has been demonstrated using the example of gold nanorods subjected to selective etching.

The DDLS method was used to estimate the parameters of several suspensions of gold nanorods and a suspension of hematite (Fe_2O_3) rods, as well the changes in the size of gold nanorods upon selective etching [100]. For evaluating the DDLS data, all samples were also examined by TEM, and, for gold nanorods, the extinction spectra were measured in the spectral range around the localized surface plasmon resonance (LSPR) peak. The studies have shown that the method described in Ref. [100] can be used to calibrate nonspherical particles in liquid media. A study on citrate-coated gold nanorods [55] provides another example of the difference between the estimates of the nanorod sizes obtained by the DLS and DDLS methods.

Other structures, including tubes, disks, thin layers, ellipsoids of rotation, rings, hollow balls, and spherical shells with specified radius and thickness, have been considered [101]. Here, the DLS method could not be used in its classical form, because ensembles of NPs of irregular shape were studied. Therefore, the MADLS method was used for more accurate estimation of sizes. Equations have been derived for NPs of individual types, whose root-mean-square radii are defined, e.g. nanotubes (Eq. (17)), nanorods (Eq. (18)), nanolayers (Eq. (19)) and nanorings (Eq. (20)).

$$\langle r_g^2 \rangle = \frac{L}{12} + a^2 + \frac{t^2}{2} - at, \tag{17}$$

$$\langle r_g^2 \rangle = \frac{L^2}{12} + \frac{a^2}{2}, \tag{18}$$

$$\langle r_g^2 \rangle = \frac{1}{12}(L^2 + t^2 + \omega^2), \tag{19}$$

$$\langle r_g^2 \rangle = a^2 - at + \frac{7}{12}t^2, \tag{20}$$

where the nanotube has a length L, thickness t, and radius a; the uniform nanorod has a length L and radius a; the nanolayer has a length L, width w, and thickness t; and the nanoring has an external radius a and a square cross-section thickness t.

In conclusion, note that the DLS method in the classical form yields size estimates substantially differing from the actual ones when applied to asymmetrical particles.

Of no less interest are Janus particles, a subclass of anisotropic particles considered to be among the most complex colloidal particles available [102]. Janus particles have two sides with different surface features, structures, and compositions [103]. This asymmetric structure allows combining different and even incompatible physical, chemical, and mechanical properties within a single particle. A new class of Janus photonic particles based on poly(4-vinylpyridine)-r-polystyrene has been reported [104], capable of re-emitting light in a dynamically tunable range by varying the size of the particle and the molecular weights of dendronized block copolymers and poly(4-vinylpyridine)-r-polystyrene, as well as the mass ratio of these last two components. This material is promising for biomedical imaging. Much effort has been made to obtain Janus particles with a high homogeneity, tunable size and shape, combined functionalities, and scalable synthesis. An approach to the synthesis of such particles has been proposed [105]. Due to their unique properties, Janus particles have attracted attention in a wide range of applications, such as optics, catalysis, and biomedicine [102]. For example, several materials or combinations of materials can be incorporated into a single particle to provide controlled release of several drugs with independent release kinetics. This can be used to obtain synergistic effects of combination therapy and multilevel targeting that are impossible in the case of isotropic systems. Silicon-based Janus particles are known to be a promising material for biomedical imaging. In addition, anti-cancer effect of dual-loaded Janus particles against HeLa cells has been demonstrated, with doxorubicin (DOX) release monitored using the Förster energy transfer between DOX and 7-hydroxycoumarin-3-carboxylate [106]. Therefore, correct estimation of the size of Janus particles will allow the monitoring of drug release, and the estimation of the diffusion coefficient can be used to calculate the kinetics of Janus particle distribution in the human body. Onajite Shemi et al. [107] studied the behavior of spherical and elliptical Janus particles in water and in 8% hydrogen peroxide. The Janus spheres in hydrogen peroxide solution had a diffusion coefficient of $D = 0.60$ μm²s⁻¹ and an average velocity of $v = 1.9$ μm²s⁻¹. For comparison, 1.0-μm spherical Janus particles with a 5-nm platinum layer in 10% hydrogen peroxide had $D = 0.31$ μm²s⁻¹ and $v = 3.1$ μm²s⁻¹.

The DLS method has been used directly for estimating the Janus NP sizes [108]. Four types of polymeric NPs were synthesized: TCD1, TCD2, TCD3, and TCD4. TCD1 Janus NPs had a "snowman" morphology, and the other three types were spherical. According to the DLS data, the mean HR of TCD1 Janus NPs was 40 nm, which corresponded to the axial length of the "snowman"-like structure of TCD1 Janus NPs. The estimated mean HRs of TCD2, TCD3, and TCD4 NPs were 27.5, 34.5, and 79.5 nm, respectively.

Silicon Janus NPs doped with rhodamine and functionalized with 1,2-distearoyl-sn-glycero-3-phosphoethanolamine (DSPE) on one hemisphere of the

NP surface and a high-molecular-weight, long-chain poly(ethylene glycol) on another hemisphere were synthesized [109]. The size of the NPs as estimated by the DLS method was 50.5 ± 6 nm.

Because blood and water are similar in their physical characteristics, such experiments allow using DLS for qualitative estimation of the distribution of Janus NPs in the bloodstream, as well as their size, in order to implement flexible control of the release of the loaded drugs.

3.2 Measurement of Nanoparticle ζ-Potential

In disperse systems, an electrical double layer (EDL) emerges on the surface of particles (at the particle–medium interface). EDL is a layer of ions formed on the particle surface as a result of adsorption of ions from solution or dissociation of surface compounds. The surface of the particle acquires a layer of ions of a certain sign evenly distributed over the surface and creating a charge on it. These ions are called potential-determining ions (PDIs). Ions of the opposite sign or counter-ions (CIs) are attracted to the particle surface from the liquid medium. Thus, the EDL consists of the PDI layer, and the CI layer located in the dispersion medium. The CI layer, in turn, also consists of two layers. The first layer is the adsorption layer (dense layer) adjacent to the interphase surface. This layer results from electrostatic interaction with PDIs and specific adsorption. The second layer is the diffusion layer, which contains CIs attracted to the particle due to electrostatic forces. The diffusion layer may be very thick, depending on the properties of the system.

When the particle moves, the EDL is disrupted. The place of disruption upon the movement of the solid and liquid phases relative to each other is called the slip plane. The slip plane lies at the boundary between the diffusion and adsorption layers, or in the diffusion layer near this boundary. The potential at the slip plane is called the electrokinetic potential or ζ-potential. It is calculated from the electrophoretic mobility of charged particles under the action of an applied electric field. The electrophoretic mobility of particles is equal to

$$U_p = \frac{V}{E}, \tag{21}$$

where V is the speed of the particles (nm/s) and E is the linear electric field intensity (V/cm).

The Helmholtz–Smoluchowski equation defines the relationship between the electrokinetic potential and the electrophoretic (electroosmotic) mobility:

$$\zeta \sim \frac{\eta \cdot U_p}{\varepsilon_r \varepsilon_0} = A \cdot \frac{\eta \cdot U_p}{\varepsilon_r \varepsilon_0}, \tag{22}$$

where A is a coefficient depending on the size and concentration of the particles, η is the viscosity at the experimental temperature, ε_r is the dielectric constant of the medium, and ε_0 is the electric constant (dielectric constant of the vacuum). More details on the calculation of the ζ-potential in practical applications are presented in Ref. [110].

The ζ-potential can be understood as the electric potential formed between the charged groups associated with the surface of the particle and the suspension medium. From the known value of ζ-potential, the surface charge of the particle can be deduced.

Laser Doppler velocimetry (LDV) uses the Doppler effect to measure the velocity of fluids or particles. LDVs have been used to estimate particle sizes [111]. However, the sizes of some NPs, such as micelles and liposomes [112], do not directly affect their velocities and, hence, cannot be directly measured using LDV. However, LDV can be used in conjunction with other techniques, such as DLS, to indirectly estimate the NP size from the velocity of NPs in a fluid. This information can then be used to correct the DLS measurements of the NP hydrodynamic diameter and obtain a more accurate estimation. The combination of the two methods has been used to measure the ζ-potentials of Ag, Cu, Ag/Cu [113], Al_2O_3, Al, HC-Ag, SiO_2, and TiO_2 NPs [114].

The DLS method can be used to determine the surface charges of lipid exosomes, polymeric microcapsules or particles, QDs, and other microparticles and NPs. For example, lysosomes are used as a biomarker of diseases, including Alzheimer's disease and cancer, estimation of the liposome surface charge being an essential diagnostic step [115]. Determination of the surface charge is a step in obtaining polymeric microcapsules whose shell consists of oppositely charged electrolytes. Such microcapsules can be used for encapsulation and targeted delivery of anticancer drugs [116], for biological imaging [117], and for engineering of multiplexed diagnostic systems based on suspension microarrays [118]. The fabrication of all these diverse nanosystems involves layer-by-layer deposition of oppositely charged electrolytes, fluorescent tags, and sometimes drugs, and precisely the electrostatic interaction between adjacent layers determines the assembly and stabilization of the layers.

Estimating the charge of microparticles and NPs is also important from a toxicological point of view. For example, the NP charge largely determines the mechanisms of NP entry into cells and their toxic effect. Specifically, positively charged NPs interact better with the negatively charged cell membrane or DNA and, hence, are more toxic than neutral or negatively charged NPs [58]. This tendency of microparticles and NPs of different charges to accumulate differently in different tissues is also used in designing delivery vehicles for anticancer drugs [119]. In addition, NPs can serve as centers of self-association or fibrillation of proteins and peptides, provoking amyloid-like proteinopathies, or, conversely, inhibitors of protein self-association. For example, Sukhanova et al. [120] have shown that only certain combinations of NP size and surface charge induce insulin fibrillation, and even minor changes in these parameters significantly reduce its rate.

Estimating the ζ-potential of QDs is an equally demanding task. QDs are characterized by a number of optical properties, including a high quantum yield, high brightness, high extinction coefficient, high resistance to photobleaching, as well as intermittent fluorescence signals (blinking), that have determined the wide use of QDs in medicine, particularly in medical imaging [121]. At the same time, QDs are potentially toxic, their characteristic size and the composition of their surface ligands and protein corona directly affecting the toxicity of QDs [122]. Nifontova et al. [123] used QDs as fluorescent nanolabels for hollow polyelectrolyte microcapsules. The microcapsules were assembled of several layers formed over calcium carbonate cores through successive precipitation from polystyrene sulfonate, peracetic acid, and polycyclic aromatic hydrocarbon solutions, and DLS estimation of the ζ-potential upon the formation of each layer is essential because it determines the success of the microcapsule synthesis. The size of the original calcium carbonate particles should be known for selecting the concentrations of the initial solutions used for layer-by-layer adsorption of polyelectrolyte polymers and the colloidal suspensions of hydrophilic magnetic NPs of iron (II, III) oxide with a carboxylated surface loaded into some microcapsules.

3.3 Designing Theranostic Agents for in Vitro/in Vivo Fluorescence Imaging, Magnetic Resonance Imaging, and Magnetically Controlled Drug Delivery and Release

Correct estimation of QD sizes is necessary in some immunostaining techniques where antigen–antibody interaction is accompanied by the Förster resonance energy transfer from QDs to reference fluorophores. This approach is relevant if, e.g., CdSe/ZnS core/shell QDs surrounded with a specific protein corona are used to detect free tumor biomarkers, such as prostate-specific antigen (PSA), in human serum samples [124]. In a study on improving the aforementioned microcapsule technology, Nifontova et al. [117] reported the mean HRs and ζ-potentials of the main building blocks of the microcapsules measured by the DLS method. The sizes of different building blocks ranged from about 31 nm to about 4137 nm, and their ζ-potentials ranged from –41.8 mV for the smallest block to –8.86 mV for the largest one. These parameters affect the photoluminescence of polyelectrolyte microcapsules with opposite surface charges in multicomponent media and, hence, the possibility of using this platform as an imaging agent.

3.4 Estimation of the Molecular Weight of Polymers

Molecular weight is one of the most important properties of a molecule. Comparison of the reference molecular weights of proteins or nucleic acids with experimentally determined values can provide useful information on, e.g., the oligomeric state of the biomolecules, their degradation, and interactions between binding partners. For example, estimation of the molecular weight for confirming the absence of aggregates is a mandatory step in the testing of antibodies used for therapy [125]. Molecular weight estimation is also a convenient test for detecting interactions between molecules. Two approaches can be used for molecular weight estimation by the DLS method. The first is based on the calibration of the instrument using particles with a known molecular weight, such as ovalbumin (44 kDa, HR = 2.98 nm), aldolase (158 kDa, HR = 4.98), and other proteins. The second approach is based on combining data on the sedimentation coefficient obtained using an analytical ultracentrifuge and the HR measured by the DLS method, using the Svedberg equation [126]:

$$M_\omega = \frac{6\pi\eta_0 R_h N_A s^0_{20,\omega}}{1-\bar{\nu}\rho_0}, \quad (23)$$

where $s^0_{20,\omega}$ is the sedimentation coefficient converted to standard conditions (in water at 20°C) , $\bar{\nu}$ is the partial specific volume of the molecule, η_0 is the viscosity of the solvent at the experimental temperature T(°C), ρ_0 is the density of the solvent at the given temperature T(°C), N_A is the Avogadro number, and R_h the universal gas constant. This approach is widely used for estimating the molecular weights of proteins and nucleic acids [127, 128].

Another example of molecular weight estimation by the DLS method is reported by Badasyan et al. [129]. In order to correctly evaluate the results, identical solutions of dendritic molecules and polycarbosilane were analyzed by the DLS method and gel filtration chromatography (GFC) under the same conditions. By heating the diluted solutions, the agglomerates were broken up to obtain a molecular dispersion, i.e., the solution of individual dendrimer molecules, where the molecule size could be measured by the DLS method. The obtained HR value was used to measure the molecular weight of the globular structure of the dendrimer using the equation:

$$M_w = V\rho N_A = \frac{4\pi D^3}{6}\rho N_A, \quad (24)$$

where N_A is the Avogadro number, D is the particle diameter, V is hydrodynamic particle volume, and the density ρ = 1.54 g/ml is assumed as a calculated one. In conclusion, it has to be noted that the measurement of the molecular weight by the DLS method is used for solving routine tasks, most commonly for the detection of dimers or other aggregations of protein molecules.

3.5 Dynamic Light Scattering in Dealing with Biopolymers

The most common examples of using the DLS method for studying biological molecules are studies on protein aggregation and assembly of nucleic acid complexes,

formation of protein–protein and protein–nucleic acid complexes, and interactions between proteins and small molecules. Complex formation is detected by measuring the HRs of microparticles and NPs in solutions. For example, Patel et al. [130] used DLS analysis to study the interaction between the nidogen-1 membrane protein and the laminin γ-1 extracellular matrix glycoprotein, which plays a key role in cell membrane formation. The DLS method makes it possible to promptly study the formation of this complex and its degradation by various chemical agents. DLS can also be used to determine the equilibrium and dissociation constants, as shown by Sharma et al. [131] in experiments on the interaction of the fibroblast growth factor with its receptor. Similarly, the DLS method allows quick and high-throughput screening of molecules inhibiting the interaction of two proteins [132]. Test systems for DLS detection of viruses have also been developed. For example, Driskell et al. [133] used conjugates of antibodies against the influenza virus with GNPs and detected the formation of aggregates by the DLS method. The detection limit of this technique was less than 100 $TCID_{50}$ per milliliter (tissue culture infectious doses ($TCID_{50}$) is the number of infectious virus particles required to infect 50% of a given cell culture).

It is known that single-stranded nucleic acid molecules, particularly RNA, tend to form various secondary structures, e.g., hairpins and pseudoknots. The formation of one or another structure is determined by the nucleotide sequence of RNA, which makes it possible to search for single-nucleotide substitutions in the RNA sequence by estimating its size using the DLS method [134]. In addition, complementary nucleic acid strands may form dimers, which can be used for detecting viral or other specific RNA sequences. Finally, in 2020 Gao et al. [135] proposed a DLS method for ultrasensitive detection of microRNA in the rolling circle replication reaction. Further development of this approach could provide a simple, inexpensive method of cancer diagnosis based on DLS detection of microRNAs.

Applications of DLS to the analysis of biological molecules and polymers are practically unlimited and depend only on the design of the experiment. The use of DLS is still one of the easiest and least expensive approaches to high-throughput analysis of the properties of biological molecules; therefore, its applications for diagnosis and study of molecular interactions are rapidly widening.

4 Conclusions

The examples presented in this review article clearly demonstrate that DLS analysis has a number of unique advantages over other analytical methods, notwithstanding some challenges in the experimental techniques and data processing. The DLS method estimates parameters indispensable for characterization of biological molecules, microparticles and NPs, such as HR, surface charge, and molecular weight. Unlike transmission, scanning, and atomic force microscopies, DLS analysis is performed in the liquid phase, which is a natural medium for biological molecules. Furthermore, the HRs of protein globules, microparticles, and NPs coated with components of biological fluids are more natural parameters than the physical sizes of denatured protein molecules or solid shells of particles. The range of research and applied tasks solved by the DLS method includes testing of protein- and antibody-based drugs for stability and aggregability; study of the interaction between receptors and their ligands (proteins, nucleic acids, and small biomolecules); fabrication of multilayer polymeric functional microcapsules stabilized by electrostatic interaction forces to be used for drug delivery and imaging of lesions; characterization of nanomaterials for biological research, medicine, and electrical engineering; development of diagnostic test systems; and many others. The DLS analysis is advantageous over other analytical techniques due to its higher technical availability, ease of performing, and high throughput. In contrast to many microscopy techniques, the DLS method can be used to study dynamic processes, which is extremely important for biological and medical research. At the same time, the DLS method has a number of limitations and difficulties related to the selection of experimental conditions, such as the concentration range of solutions and the types of solvents, as well as additional mathematical calculations if the analyzed objects are not spherical. The DLS method dovetails with other analytical techniques, such as GFC and various types of microscopy, supplementing the results and simplifying the analysis of large amounts of samples, and it is also suitable for the study of dynamic processes.

Thus, having considered the physical principles of DLS necessary for understanding the DLS method and planning experiments with proper account of its strengths and limitations, as well as the examples of the use of this approach for solving specific research and applied problems, we can conclude that DLS analysis is promising for a variety of research areas.

Disclosures

The authors have no relevant financial interest in this article and no conflict of interest to disclose.

Acknowledgments

The research was carried out with financial support of the Russian Science Foundation, grant no. 21-79-30048.

References

1. K. Rebrosova, O. Samek, M. Kizovsky, S. Bernatova, V. Hola, and F. Ruzicka, "Raman Spectroscopy – A Novel Method for Identification and Characterization of Microbes on a Single-Cell Level in Clinical Settings," Frontiers in Cellular and Infection Microbiology 12, 866463 (2022).
2. M. A. Kouri, E. Spyratou, M. Karnachoriti, Dimitris Kalatzis, N. Danias, N. Arkadopoulos, I. Seimenis, Y. S. Raptis, A. G. Kontos, and E. P. Efstathopoulos, "Raman Spectroscopy: A Personalized Decision-Making Tool on Clinicians' Hands for In Situ Cancer Diagnosis and Surgery Guidance," Cancers 14(5), 1144 (2022).
3. M. H. Simonian, "Spectrophotometric Determination of Protein Concentration," Current Protocols in Toxicology 21(1), A.3G.1–A.3G.7 (2004).
4. A. M. García-Alegría, I. Anduro-Corona, C. J. Pérez-Martínez, M. A. G. Corella-Madueño, M. L. Rascón-Durán, and H. Astiazaran-Garcia, "Quantification of DNA through the NanoDrop Spectrophotometer: Methodological Validation Using Standard Reference Material and Sprague Dawley Rat and Human DNA," International Journal of Analytical Chemistry 2020, 8896738 (2020).
5. W. H. Brooks, W. C. Guida, and K. G. Daniel, "The Significance of Chirality in Drug Design and Development," Current Topics in Medicinal Chemistry 11(7), 760–770 (2011).
6. R. Ding, J. Ying, and Y. Zhao, "An electronic circular dichroism spectroscopy method for the quantification of L – and D – amino acids in enantiomeric mixtures," Royal Society Open Science 8(3), 201963 (2021).
7. H. S. Son, Y. S. Hong, W. M. Park, M. A. Yu, and C. H. Lee, "A Novel Approach for Estimating Sugar and Alcohol Concentrations in Wines Using Refractometer and Hydrometer," Journal of Food Science 74(2), C106– C111 (2009).
8. P. Y. Liu, L. K. Chin, W. Ser, H. F. Chen, C.-M. Hsieh, C.-H. Lee, K.-B. Sung, T. C. Ayi, P. H. Yap, B. Liedberg, K. Wang, T. Bourouina, and Y. Leprince-Wang, "Cell refractive index for cell biology and disease diagnosis: past, present and future," Lab on a Chip 16(4), 634–644 (2016).
9. U. Bulbake, S. Doppalapudi, N. Kommineni, and W. Khan, "Liposomal Formulations in Clinical Use: An Updated Review," Pharmaceutics 9(2), 12 (2017).
10. Y. Jia, Y. Jiang, Y. He, W. Zhang, J. Zou, K. T. Magar, H. Boucetta, C. Teng, and W. He, "Approved Nanomedicine against Diseases," Pharmaceutics 15(3) 774 (2023).
11. Y. Yao, Y. Zhou, L. Liu, Y. Xu, Q. Chen, Y. Wang, S. Wu, Y. Deng, J. Zang, and A. Shao, "Nanoparticle-Based Drug Delivery in Cancer Therapy and Its Role in Overcoming Drug Resistance," Frontiers in Molecular Biosciences 7, 193 (2020).
12. A. C. Anselmo, and S. Mitragotri, "Nanoparticles in the clinic: An update," Bioengineering & Translational Medicine 4(3), e10143 (2019).
13. R. Raliya, T. Singh Chadha, K. Haddad, and P. Biswas, "Perspective on Nanoparticle Technology for Biomedical Use," Current Pharmaceutical Design 22(17), 2481–2490 (2016).
14. J. J. Giner-Casares, M. Henriksen-Lacey, M. Coronado-Puchau, and L. M. Liz-Marzán, "Inorganic nanoparticles for biomedicine: where materials scientists meet medical research," Materials Today 19(1), 19–28 (2016).
15. H. Moosmüller, W. P. Arnott, "Particle Optics in the Rayleigh Regime," Journal of the Air & Waste Management Association 59(9), 1028–1031(2009).
16. J. Jeevanandam, A. Barhoum, Y. S. Chan, A. Dufresne, and M. K. Danquah, "Review on nanoparticles and nanostructured materials: history, sources, toxicity and regulations," Beilstein Journal of Nanotechnology 9(1), 1050–1074 (2018).
17. M. Kaszuba, M. T. Connah, "Protein and Nanoparticle Characterisation Using Light Scattering Techniques," Particle & Particle Systems Characterization 23(2), 193–196 (2006).
18. A. Wishard, B. C. Gibb, "Dynamic light scattering – an all-purpose guide for the supramolecular chemist," Supramolecular Chemistry 31(9), 608–615 (2019).
19. N. Damaschke, H. Nobach, N. Semidetnov, and C. Tropea, "Optical particle sizing in backscatter," Applied Optics 41(27), 5713–5727 (2002).
20. M. Kaszuba, D. McKnight, M. T. Connah, F. K. McNeil-Watson, and U. Nobbmann, "Measuring sub nanometre sizes using dynamic light scattering," Journal of Nanoparticle Research 10, 823–829 (2008).
21. A. Kurzhals, K. Wulf, V. Senz, T. Eickner, N. Grabow, and W. Schmidt, "Determination of Infusion Filter Efficiency applying Dynamic Light Scattering," Current Directions in Biomedical Engineering 8(2), 485–488 (2022).
22. J. K. G. Dhont, C. G. de Kruif, "Scattered light intensity cross correlation. I. Theory," The Journal of Chemical Physics 79(4), 1658–1663 (1983).
23. A. V. Malm, J. C. W. Corbett, "Improved Dynamic Light Scattering using an adaptive and statistically driven time resolved treatment of correlation data," Scientific Reports 9, 13519 (2019).
24. K. Hou, C. Wang, and X. Liu, "Study on Backward Scattering Characteristics of Submicron Particles," Optics and Photonics Journal 10(5), 79–87 (2020).
25. C. Wang, K. Kou, and J. Yan, "Frequency-shifted nano-particle sizing using laser self-mixing interferometry under linear current tuning," Laser Physics Letters 19(6), 066202 (2022).

26. J. Herbert, K. Bertling, T. Taimre, A. D. Rakić, and S. Wilson, "Microparticle discrimination using laser feedback interferometry," Optics Express 26(20), 25778–25792 (2018).
27. K. Zhu, H. Chen, S. Zhang, Z. Shi, Y. Wang, and Y. Tan, "Frequency-Shifted Optical Feedback Measurement Technologies Using a Solid-State Microchip Laser," Applied Sciences 9(1), 109 (2018).
28. M. Draijer, E. Hondebrink, T. van Leeuwen, and W. Steenbergen, "Review of laser speckle contrast techniques for visualizing tissue perfusion," Lasers in Medical Science 24, 639–651 (2009).
29. Q. Zhang, J. C. Gamekkanda, A. Pandit, W. Tang, C. Papageorgiou, C. Mitchell, Y. Yang, M. Schwaerzler, T. Oyetunde, R. D. Braatz, A. S. Myerson, and G. Barbastathis, "Extracting particle size distribution from laser speckle with a physics-enhanced autocorrelation-based estimator (PEACE)," Nature Communications 14, 1159 (2023).
30. M. Sadrara, M. Miri, "Scattering of electromagnetic waves by a cluster of charged spherical nanoparticles," Journal of the Optical Society of America B 33(12), 2552 (2016).
31. J. C. Dyre, "Rayleigh scattering revisited," Nature Materials 15(11), 1150–1151 (2016).
32. X. Yu, Y. Shi, T. Wang, and X. Sun, "Dust-Concentration Measurement Based on Mie Scattering of a Laser Beam," PLoS ONE 12(8), e0181575 (2017).
33. Z. Cao, L. Xu, and J. Ding, "Integral inversion to Fraunhofer diffraction for particle sizing," Applied Optics 48(25), 4842–4850 (2009).
34. J. Vargas-Ubera, J. F. Aguilar, and D. M. Gale, "Reconstruction of particle-size distributions from light-scattering patterns using three inversion methods," Applied Optics 46(1), 124–132 (2007).
35. C. M. Keck, R. H. Müller, "Size analysis of submicron particles by laser diffractometry - 90% of the published measurements are false," International Journal of Pharmaceutic 355(1-2), 150–163 (2008).
36. G. Brodie, "Energy Transfer from Electromagnetic Fields to Materials," Chapter 4 in Electromagnetic Fields and Waves, H. Yeap, and K. Hirasawa (Eds.), IntechOpen, Rijeka, (2019).
37. A. Rahimzadegan, R. Alaee, C. Rockstuhl, and R. W. Boyd, "Minimalist Mie Coefficient Model," Optics Express 28(11), 16511 (2020).
38. X. Li, L. Xie, and X. Zheng, "The Comparison between the Mie Theory and the Rayleigh Approximation to Calculate the EM Scattering by Partially Charged Sand," Journal of Quantitative Spectroscopy and Radiative Transfer 113(3), 251–258 (2012).
39. R. Gutiérrez-Cuevas, N. J. Moore, and M. A. Alonso, "Lorenz-Mie Scattering of Focused Light via Complex Focus Fields: An Analytic Treatment," Physical Review A 97(5), 053848 (2018).
40. L. André Ambrosio, "Symmetry relations in the generalized Lorenz–Mie theory for lossless negative refractive index media," Journal of Quantitative Spectroscopy and Radiative Transfer 180, 147–153 (2016).
41. D. J. Lockwood, Encyclopedia of Color Science and Technology, Springer, Heidelberg (2016).
42. Y. Yue, Y. Kan, H. Choi, A. Clearfield, and H. Liang, "Correlating hydrodynamic radii with that of two-dimensional nanoparticles," Applied Physics Letters 107(25), 253103 (2015).
43. J. Zmpitas, J. Gross, "Modified Stokes–Einstein Equation for Molecular Self-Diffusion Based on Entropy Scaling," Industrial & Engineering Chemistry Research 60(11), 4453–4459 (2021).
44. M. A. Islam, "Einstein – Smoluchowski Diffusion Equation: A Discussion," Physica Scripta 70(2–3), 120–125 (2004).
45. K. Ishii, T. Iwai, "Theoretical Analysis of Path-Length-Resolved Power Spectrum Measurement Using Low-Coherence Dynamic Light Scattering," Japanese Journal of Applied Physics 47(11), 8397–8401 (2008).
46. D. Ferreira, R. Bachelard, W. Guerin, R. Kaiser, and M. Fouché, "Connecting field and intensity correlations: The Siegert relation and how to test it," American Journal of Physics 88(10), 831–837 (2020).
47. G. Derkachov, D. Jakubczyk, K. Kolwas, K. Piekarski, Y. Shopa, and M. Woźniaket, "Dynamic Light Scattering Investigation of Single Levitated Micrometre-Sized Droplets Containing Spherical Nanoparticles," Measurement 158, 107681 (2020).
48. S. C. Buranay, M. A. Özarslan, and S. S. Falahhesar, "Numerical Solution of the Fredholm and Volterra Integral Equations by Using Modified Bernstein–Kantorovich Operators," Mathematics 9(11), 1193 (2021).
49. R. Xu, Particle Characterization: Light Scattering Methods, Springer, Dordrecht (2000).
50. M. M. Hoffmann, M. D. Too, M. Vogel, T. Gutmann, and G. Buntkowsky, "Breakdown of the Stokes–Einstein Equation for Solutions of Water in Oil Reverse Micelles," The Journal of Physical Chemistry B 124(41), 9115–9125 (2020).
51. A. J. Banchio, M. Heinen, P. Holmqvist, and G. Nägeleet, "Short- and Long-Time Diffusion and Dynamic Scaling in Suspensions of Charged Colloidal Particles," The Journal of Chemical Physics 148(13), 134902 (2018).
52. M. Wang, M. Heinen, and J. F. Brady, "Short-Time Diffusion in Concentrated Bidisperse Hard-Sphere Suspensions," The Journal of Chemical Physics 142(6), 064905 (2015).
53. A. M. Fiore, J. W. Swan, "Fast Stokesian Dynamics," Journal of Fluid Mechanics 878, 544–597 (2019).
54. M. Naiim, A. Boualem, C. Ferre, M. Jabloun, A. Jalochaa, and P. Ravier, "Multiangle Dynamic Light Scattering for the Improvement of Multimodal Particle Size Distribution Measurements," Soft Matter 11(1), 28–32 (2015).

55. C. Geers, L. Rodriguez-Lorenzo, D. A. Urban, C. Kinnear, A. Petri-Fink, and S. Balog, "A New Angle on Dynamic Depolarized Light Scattering: Number-Averaged Size Distribution of Nanoparticles in Focus," Nanoscale 8(34), 15813–15821 (2016).
56. A. D. Levin, E. A. Shmytkova, and B. N. Khlebtsov, "Multipolarization Dynamic Light Scattering of Nonspherical Nanoparticles in Solution," The Journal of Physical Chemistry C 121(5), 3070–3077 (2017).
57. M. Alexander, D. G. Dalgleish, "Dynamic Light Scattering Techniques and Their Applications in Food Science," Food Biophysics 1, 2–13 (2006).
58. A. Sukhanova, S. Bozrova, P. Sokolov, M. Berestovoy, A. Karaulov, and I. Nabiev, "Dependence of Nanoparticle Toxicity on Their Physical and Chemical Properties," Nanoscale Research Letters 13(1), 44 (2018).
59. I. de la Calle, M. Menta, M. Klein, and F. Séby, "Screening of TiO2 and Au Nanoparticles in Cosmetics and Determination of Elemental Impurities by Multiple Techniques (DLS, SP-ICP-MS, ICP-MS and ICP-OES)," Talanta 171, 291–306 (2017).
60. M. Y. Chan, Q. M. Dowling, S. J. Sivananthan, and R. M. Kramer, "Particle Sizing of Nanoparticle Adjuvant Formulations by Dynamic Light Scattering (DLS) and Nanoparticle Tracking Analysis (NTA)," in Vaccine Adjuvants. Methods and Protokols, C. B. Fox (Eds.), Humana Press, New York, 239–252 (2017).
61. S. Skoglund, E. Blomberg, I. O. Wallinder, I. Grillo, J. S. Pedersen, and L. M. Bergström, "A Novel Explanation for the Enhanced Colloidal Stability of Silver Nanoparticles in the Presence of an Oppositely Charged Surfactant," Physical Chemistry Chemical Physics 19(41), 28037–28043 (2017).
62. G. Almeida, O. J. Ashton, L. Goldoni, D, Maggioni, U. Petralanda, N. Mishra, Q. A. Akkerman, I. Infante, H. J. Snaith, and L. Manna, "The Phosphine Oxide Route toward Lead Halide Perovskite Nanocrystals," Journal of the American Chemical Society 140(44), 14878–14886 (2018).
63. S. T. Moerz, A. Kraegeloh, M. Chanana, and T. Kraus, "Formation Mechanism for Stable Hybrid Clusters of Proteins and Nanoparticles," ACS Nano 9(7), 6696–6705 (2015).
64. S. P. Yeap, A. L. Ahmad, B. S. Ooi, and J. Lim, "Electrosteric Stabilization and Its Role in Cooperative Magnetophoresis of Colloidal Magnetic Nanoparticles," Langmuir 28(42), 14878–14891 (2012).
65. J. K. Lim, D. C. J. Chieh, S. A. Jalak, P. Y. Toh, N. H. M. Yasin, B. W. Ng, and A. L. Ahmad, "Rapid Magnetophoretic Separation of Microalgae," Small 8(11), 1683–1692 (2012).
66. L. C. Gonçalves, A. B. Seabra, M. T. Pelegrino, D. R. de Araujo, J. S. Bernardes, and P. S. Haddad, "Superparamagnetic Iron Oxide Nanoparticles Dispersed in Pluronic F127 Hydrogel: Potential Uses in Topical Applications," RSC Advances 7(24), 14496–14503 (2017).
67. Y. Gu, M. Yoshikiyo, A. Namai, D. Bonvin, A. Martinez, R. Piñol, P. Téllez, N. J. O. Silva, F. Ahrentorp, C. Johansson, J. Marco-Brualla, R. Moreno-Loshuertos, P. Fernández-Silva, Y. Cui, S. Ohkoshi, and A. Millán, "Magnetic Hyperthermia with ε- Fe2O3 Nanoparticles," RSC Advances 10(48), 28786–28797 (2020).
68. N. Guarrotxena, O. García, and I. Quijada-Garrido, "Synthesis of Au@polymer Nanohybrids with Transited Core-Shell Morphology from Concentric to Eccentric Emoji-N or Janus Nanoparticles," Scientific Reports 8(1), 5721 (2018).
69. J. B. Vines, J.-H. Yoon, N.-E. Ryu, D.-J. Lim, and H. Park, "Gold Nanoparticles for Photothermal Cancer Therapy," Frontiers in Chemistry 7, 167 (2019).
70. R. E. Cavicchi, D. C. Meier, C. Presser, V. M. Prabhu, and S. Guha, "Single Laser Pulse Effects on Suspended-Au-Nanoparticle Size Distributions and Morphology," The Journal of Physical Chemistry C 117(20), 10866–10875 (2013).
71. T. Zheng, S. Bott, and Q. Huo, "Techniques for Accurate Sizing of Gold Nanoparticles Using Dynamic Light Scattering with Particular Application to Chemical and Biological Sensing Based on Aggregate Formation," ACS Applied Materials & Interfaces 8(33), 21585–21594 (2016).
72. R. Fathima, A. Mujeeb, "Nonlinear Optical Investigations of Laser Generated Gold, Silver and Gold-Silver Alloy Nanoparticles and Optical Limiting Applications," Journal of Alloys and Compounds 858, 157667 (2021).
73. Y. Zhang, Y. Chen, P. Westerhoff, K. Hristovski, and J. C Crittenden, "Stability of Commercial Metal Oxide Nanoparticles in Water," Water Research 42(8–9), 2204–2212 (2008).
74. S. Rajkumar, M. Prabaharan, "Theranostics Based on Iron Oxide and Gold Nanoparticles for Imaging- Guided Photothermal and Photodynamic Therapy of Cancer," Current Topics in Medicinal Chemistry 17(16), 1858–1871 (2017).
75. M. Lehmann, W. Tabaka, T. Möller, A. Oppermann, D. Wöll, D. Volodkin, S. Wellert, and R. von Klitzing, "DLS Setup for in Situ Measurements of Photoinduced Size Changes of Microgel-Based Hybrid Particles," Langmuir 34(12), 3597–3603 (2018).
76. Z. H. Chen, C. Kim, X. Zeng, S. H. Hwang, J. Jang, and G. Ungar, "Characterizing Size and Porosity of Hollow Nanoparticles: SAXS, SANS, TEM, DLS, and Adsorption Isotherms Compared," Langmuir 28(43), 15350–15361 (2012).
77. J. C. Wong, L. Xiang, K. H. Ngoi, C. H. Chia, K. S. Jin, and M. Ree, "Quantitative Structural Analysis of Polystyrene Nanoparticles Using Synchrotron X-Ray Scattering and Dynamic Light Scattering," Polymers 12(2), 477 (2020).

78. P. Eaton, P. Quaresma, C. Soares, C. Neves, M.P. de Almeida, E. Pereira, and P. West, "A direct Comparison of Experimental Methods to Measure Dimensions of Synthetic Nanoparticles," Ultramicroscopy 182, 179–190 (2017).
79. X. Liu, Q. Dai, L. Austin, J. Coutts, G. Knowles, J. Zou, H. Chen, and Q. Huo, "A One-Step Homogeneous Immunoassay for Cancer Biomarker Detection Using Gold Nanoparticle Probes Coupled with Dynamic Light Scattering," Journal of the American Chemical Society 130(9), 2780–2782 (2008).
80. Q. Dai, X. Liu, J. Coutts, L. Austin, and Q. Huo, "A One-Step Highly Sensitive Method for DNA Detection Using Dynamic Light Scattering," Journal of the American Chemical Society 130(26), 8138–8139 (2008).
81. C. T. Matea, T. Mocan, F. Tabaran, T. Pop, O. Mosteanu, C. Puia, C. Iancu and L. Mocan, "Quantum Dots in Imaging, Drug Delivery and Sensor Applications," International Journal of Nanomedicine 12, 5421–5431 (2017).
82. D. Geißler, C. Gollwitzer, A. Sikora, C. Minelli, M. Krumrey, and U. Resch-Genger, "Effect of fluorescent staining on size measurements of polymeric nanoparticles using DLS and SAXS," Analytical Methods 7(23), 9785–9790 (2015).
83. P. Modlitbová, K. Klepárník, Z. Farka, P. Pořízka, P. Skládal, K. Novotný, and J. Kaiser, "Time-Dependent Growth of Silica Shells on CdTe Quantum Dots," Nanomaterials 8(6), 439 (2018).
84. F. Cao, D. Yu, W. Ma, X. Xu, B. Cai, Y. M. Yang, S. Liu, L. He, Y. Ke, S. Lan, K.-L. Choy, and H. Zeng, "Shining Emitter in a Stable Host: Design of Halide Perovskite Scintillators for X-Ray Imaging from Commercial Concept," ACS Nano 14(5), 5183–5193 (2020).
85. J. Leinonen, S. Kneifel, and R. J. Hogan, "Evaluation of the Rayleigh–Gans Approximation for Microwave Scattering by Rimed Snowflakes," Quarterly Journal of the Royal Meteorological Society 144(S1), 77–88 (2018).
86. B. Ankamwar, "Size and Shape Effect on Biomedical Applications of Nanomaterials," Chapter 4 in Biomedical Engineering – Technical Applications in Medicine, R. Hudak (Ed.), InTechOpen, Rijeka (2012).
87. Y. Chen, Z. Fan, Z. Zhang, W. Niu, C. Li, N. Yang, B. Chen, and H. Zhang, "Two-Dimensional Metal Nanomaterials: Synthesis, Properties, and Applications," Chemical Reviews 118(13), 6409–6455 (2018).
88. J. Yang, Z. Zeng, J. Kang, S. Betzler, C. Czarnik, X. Zhang, C. Ophus, C. Yu, K. Bustillo, M. Pan, J. Qiu, L.-W. Wang, and H. Zheng, "Formation of Two-Dimensional Transition Metal Oxide Nanosheets with Nanoparticles as Intermediates," Nature Materials 18(9), 970–976 (2019).
89. H. Zhao, X. Chen, G. Wang, Y. Qiu, and L. Guo, "Two-Dimensional Amorphous Nanomaterials: Synthesis and Applications," 2D Materials 6(3), 032002 (2019).
90. F. Yang, P. Song, M. Ruan, and W. Xu, "Recent Progress in Two-Dimensional Nanomaterials: Synthesis, Engineering, and Applications," FlatChem 18, 100133 (2019).
91. Z. Liu, H. Chen, Y. Jia, W. Zhang, H. Zhao, W. Fan, W. Zhang, H. Zhong, Y. Nia, and Z. Guo, "A Two-Dimensional Fingerprint Nanoprobe Based on Black Phosphorus for Bio-SERS Analysis and Chemo-Photothermal Therapy," Nanoscale 10(39), 18795–18804 (2018).
92. Z. Xie, D. Wang, T. Fan, C. Xing, Z. Li, W. Tao, L. Liu, S. Bao, D. Fan, and H. Zhang, "Black phosphorus Analogue Tin Sulfide Nanosheets: Synthesis and Application as near-Infrared Photothermal Agents and Drug Delivery Platforms for Cancer Therapy," Journal of Materials Chemistry B 6(29), 4747–4755 (2018).
93. H. Zhang, T. Fan, W. Chen, Y. Li, and B. Wang, "Recent Advances of Two-Dimensional Materials in Smart Drug Delivery Nano-Systems," Bioactive Materials 5(4), 1071–1086 (2020).
94. J. A. Mariano-Torres, A. López-Marure, M. García-Hernández, G. Basurto-Islas, and M. Á. Domínguez-Sánchez, "Synthesis and characterization of glycerol citrate polymer and yttrium oxide nanoparticles as a potential antibacterial material," Materials Transactions 59(12), 1915–1919 (2018).
95. M. Lotya, A. Rakovich, J. F. Donegan, and J. N. Coleman, "Measuring the Lateral Size of Liquid-Exfoliated Nanosheets with Dynamic Light Scattering," Nanotechnology 24(26), 265703 (2013).
96. C. A. Little, C. Batchelor-McAuley, N. P. Young, and R. G. Compton, "Shape and Size of Non-Spherical Silver Nanoparticles: Implications for Calculating Nanoparticle Number Concentrations," Nanoscale 10(34), 15943–15947 (2018).
97. O. I. Sukharevsky, G. S. Zalevsky, "3-D Electromagnetic Scattering by Ellipsoidal Silver Nanoparticles in Optical Band," In 2018 IEEE 17th International Conference on Mathematical Methods in Electromagnetic Theory (MMET), Kyiv, UKraine, 152–155 (2018).
98. F. Gao, L. Bai, S. Liu, R. Zhang, J. Zhang, X. Feng, Y. Zheng, and Y. Zhao, "Rationally Encapsulated Gold Nanorods Improving Both Linear and Nonlinear Photoacoustic Imaging Contrast in Vivo," Nanoscale 9(1), 79–86 (2017).
99. S. Liao, W. Yue, S. Cai, Q. Tang, W. Lu, L. Huang, T. Qi, and J. Liao, "Improvement of Gold Nanorods in Photothermal Therapy: Recent Progress and Perspective," Frontiers in Pharmacology 12, 664123 (2021).
100. A. D. Levin, E. A. Shmytkova, "Nonspherical Nanoparticles Characterization by Partially Depolarized Dynamic Light Scattering," Proceedings of SPIE 9526, 95260P (2015).
101. P. J. Wyatt, "Measurement of Special Nanoparticle Structures by Light Scattering," Analytical Chemistry 86(15), 7171–7183 (2014).
102. H. Su, C.-A. H. Price, L. Jing, Q. Tian, J. Liu, and K. Qian, "Janus Particles: Design, Preparation, and Biomedical Applications," Materials Today Bio 4, 100033 (2019).

103. G. Agrawal, R. Agrawal, "Janus Nanoparticles: Recent Advances in Their Interfacial and Biomedical Applications," ACS Applied Nano Materials 2(4), 1738–1757 (2019).
104. Q. He, H. Vijayamohanan, J. Li, and T. M. Swager, "Multifunctional Photonic Janus Particles," Journal of the American Chemical Society 144(12), 5661–5667 (2022).
105. J. Wang, X. Chen, F. Lang, L. Yang, D. Qiu, and Z. Yang, "Large Scale Synthesis of Single-Chain/Colloid Janus Nanoparticles with Tunable Composition," Chemical Communications 56(27), 3875–3878 (2020).
106. H. Cao, Y. Yang, X. Chen, and Z. Shao, "Intelligent Janus nanoparticles for intracellular real-time monitoring of dual drug release," Nanoscale 8, 6754–6760 (2016).
107. O. Shemi, M. J. Solomon, "Self-Propulsion and Active Motion of Janus Ellipsoids," The Journal of Physical Chemistry B 122(44), 10247–10255 (2018).
108. W. Zhang, J. He, and X. Dong, "Controlled Fabrication of Polymeric Janus Nanoparticles and Their Solution Behaviors," RSC Advances 6(107), 105070–105075 (2016).
109. R. Kadam, J. Ghawali, M. Waespy, M. Maas, and K. Rezwan, "Janus Nanoparticles Designed for Extended Cell Surface Attachment," Nanoscale 12(36), 18938–18949 (2020).
110. S. Bhattacharjee, "DLS and Zeta Potential – What They Are and What They Are Not?" Journal of Controlled Release 235, 337–351 (2016).
111. J. C. Wilson, B. Y. H. Liu, "Aerodynamic particle size measurement by laser-doppler velocimetry," Journal of Aerosol Science 11(2), 139–150 (1980).
112. S. Dattani, X. Li, C. Lampa, D. Lechuga-Ballesteros, A. Barriscale, B. Damadzadeh, and B. R. Jasti, "A comparative study on micelles, liposomes and solid lipid nanoparticles for paclitaxel delivery," International Journal of Pharmaceutics 631, 122464 (2023).
113. D. Gonzalez-Mendoza, B. Valdez-Salas, E. Bernardo-Mazariegos, O. Tzintzun-Camacho, F. Gutiérrez-Miceli, V. Ruíz-Valdiviezo, L. Rodríguez-Hernández, and G. Sanchez-Viveros, "Influence of monometallic and bimetallic phytonanoparticles on physiological status of mezquite," Open Life Sciences 14(1), 62–68 (2019).
114. R. C. Murdock, L. Braydich-Stolle, A. M. Schrand, J. J. Schlager, and S. M. Hussain, "Characterization of Nanomaterial Dispersion in Solution Prior to In Vitro Exposure Using Dynamic Light Scattering Technique," Toxicological Sciences 101(2), 239–253 (2008).
115. M. K. Rasmussen, J. N. Pedersen, and R. Marie, "Size and Surface Charge Characterization of Nanoparticles with a Salt Gradient," Nature Communications 11(1), 2337 (2020).
116. G. Nifontova, T. Tsoi, A. Karaulov, I. Nabiev, and A. Sukhanova, "Structure–Function Relationships in Polymeric Multilayer Capsules Designed for Cancer Drug Delivery," Biomaterials Science 10(18), 5092–5115 (2022).
117. G. Nifontova, V. Krivenkov, M. Zvaigzne, A. Efimov, E. Korostylev, S. Zarubin, A. Karaulov, I. Nabiev, and A. Sukhanova, "Nanoparticle-Doped Hybrid Polyelectrolyte Microcapsules with Controlled Photoluminescence for Potential Bioimaging Applications," Polymers 13(23), 4076 (2021).
118. R. Bilan, A. Ametzazurra, K. Brazhnik, S. Escorza, D. Fernández, M. Uríbarri, I. Nabiev, and A. Sukhanova, "Quantum-Dot-Based Suspension Microarray for Multiplex Detection of Lung Cancer Markers: Preclinical Validation and Comparison with the Luminex XMAP® System," Scientific Reports 7(1), 44668 (2017).
119. H.-X. Wang, Z.-Q. Zuo, J.-Z. Du, Y.-C. Wang, R. Sun, Z.-T. Cao, X.-D. Ye, J.-L. Wang, K. W. Leong, and J. Wang, "Surface Charge Critically Affects Tumor Penetration and Therapeutic Efficacy of Cancer Nanomedicines," Nano Today 11(2), 133–144 (2016).
120. A. Sukhanova, S. Poly, S. Bozrova, É. Lambert, M. Ewald, A. Karaulov, M. Molinari, and I. Nabiev, "Nanoparticles With a Specific Size and Surface Charge Promote Disruption of the Secondary Structure and Amyloid-Like Fibrillation of Human Insulin Under Physiological Conditions," Frontiers in Chemistry 7, 480 (2019).
121. A. A. Abdellatif, M. A. Younis, M. Alsharidah, O. A. Rugaie, and H. M. Tawfeek, "Biomedical Applications of Quantum Dots: Overview, Challenges, and Clinical Potential," International Journal of Nanomedicine 17, 1951–1970 (2022).
122. 1A. Sukhanova, S. Bozrova, E. Gerasimovich, M. Baryshnikova, Z. Sokolova, P. Samokhvalov, C. Guhrenz, N. Gaponik, A. Karaulov, and I. Nabiev, "Dependence of Quantum Dot Toxicity In Vitro on Their Size, Chemical Composition, and Surface Charge," Nanomaterials 12(16), 2734 (2022).
123. G. Nifontova, F. Ramos-Gomes, F. Alves, I. Nabiev, and A. Sukhanova, "Stimulus-Sensitive Theranostic Delivery Systems Based on Microcapsules Encoded with Quantum Dots and Magnetic Nanoparticles," in Quantum Dots: Applications in Biology, A. Fontes, B. Santos (Eds.), Humana, New York, 199–212 (2020).
124. T. Tsoy, A. Karaulov, I. Nabiev, and A. Sukhanova, "Multiplexed Detection of Cancer Serum Antigens with a Quantum Dot-Based Lab-on-Bead System," in Quantum Dots: Applications in Biology, A. Fontes, B. Santos (Eds.), Humana, New York, 225–236 (2020).
125. C. G. Conner, J. McAndrew, S. Menegatti, and O. D. Velev, "An Accelerated Antibody Aggregation Test Based on Time Sequenced Dynamic Light Scattering," Colloids and Surfaces A: Physicochemical and Engineering Aspects 653, 129833 (2022).
126. W. A. Lindner, J. M. Brand, "A Coherent Approach to the Svedberg Equation," Biochemical Education 15(2), 71–72 (1987).

127. E. Dzananovic, T. R. Patel, G. Chojnowski, M. J. Boniecki, S. Deo, K. McEleney, S. E. Harding, J. M. Bujnicki, and S. A. McKenna, "Solution Conformation of Adenovirus Virus Associated RNA-I and Its Interaction with PKR," Journal of Structural Biology 185(1), 48–57 (2014).
128. T. R. Patel, M. Meier, J. Li, G. Morris, A. J. Rowe, and J. Stetefeld, "T-shaped Arrangement of the Recombinant Agrin G3 - IgG Fc Protein," Protein Science 20(6), 931–940 (2011).
129. A. Badasyan, A. Mavrič, I. K. Cigić, T. Bencik, and M. Valant, "Polymer Nanoparticle Sizes from Dynamic Light Scattering and Size Exclusion Chromatography: The Case Study of Polysilanes," Soft Matter 14(23), 4735–4740 (2018).
130. T. R. Patel, C. Bernards, M. Meier, K. McEleney, D. J. Winzor, M. Koch, and J. Stetefeld, "Structural Elucidation of Full-Length Nidogen and the Laminin–Nidogen Complex in Solution," Matrix Biology 33, 60–67 (2014).
131. P. Sharma, D. Rajalingam, T. K. S. Kumar, and S. Singh, "A Light Scattering Study of the Interaction of Fibroblast Growth Factor (FGF) with Its Receptor," Biophysical Journal 94(9), L71–L73 (2008).
132. A. D. Hanlon, M. I. Larkin, and R. M. Reddick, "Free-Solution, Label-Free Protein-Protein Interactions Characterized by Dynamic Light Scattering," Biophysical Journal 98(2), 297–304 (2010).
133. J. D. Driskell, C. A. Jones, S. M. Tompkins, and R. A. Tripp, "One-Step Assay for Detecting Influenza Virus Using Dynamic Light Scattering and Gold Nanoparticles," The Analyst 136(15), 3083 (2011).
134. E. Dzananovic, Astha, G. Chojnowski, S. Deo, E. P. Booy, P. Padilla-Meier, K. McEleney, J. M. Bujnicki, T. R. Patel, and S. A. McKenna, "Impact of the Structural Integrity of the Three-Way Junction of Adenovirus VAI RNA on PKR Inhibition," PLoS ONE 12(10), e0186849 (2017).
135. Y. Gao, S. Xu, T. He, J. Li, L. Liu, Y. Zhang, S. Ge, M. Yan, H. Liu, and J. Yu, "Ultrasensitive and Specific MicroRNA Detection via Dynamic Light Scattering of DNA Network Based on Rolling Circle Amplification," Sensors and Actuators B: Chemical 324, 128693 (2020).

Physical and Biological Properties of Layers with Nanoparticles Based on Metal Chalcogenides and Titanium Synthesized by Femtosecond Laser Ablation and Fragmentation in Liquid

Ulyana E. Kurilova[1,2,3], Anton S. Chernikov[1], Dmitry A. Kochuev[1], Lidiya S. Volkova[4], Anna A. Voznesenskaya[1], Ruslan V. Chkalov[1], Dmitriy V. Abramov[1], Alexander V. Kazak[1,5], Irina A. Suetina[6], Marina V. Mezentseva[6], Leonid I. Russu[6], Alexander Yu. Gerasimenko[3,7], and Kirill S. Khorkov[1*]

[1] Institute of Applied Mathematics, Physics and Computer Science, Vladimir State University, 87 Gorky str., Vladimir 600000, Russia

[2] World-Class Research Center "Digital Biodesign and Personalized Healthcare", I. M. Sechenov First Moscow State Medical University, 2–4 Bolshaya Pirogovskaya str., Moscow 119991, Russia

[3] Institute of Biomedical Systems, National Research University of Electronic Technology MIET, 1 Shokin sq., Zelenograd, Moscow 124498, Russia

[4] Department of Structural Analysis and Metrology, Institute of Nanotechnology of Microelectronics of the Russian Academy of Sciences, 16A (bld. 11) Nagatinskaya str., Moscow 115487, Russia

[5] Department of Physics, Moscow Polytechnic University, 38 Bolshaya Semenovskaya str., Moscow 107023, Russia

[6] Ivanovsky Institute of Virology, National Research Center for Epidemiology and Microbiology Named after the Honorary Academician N.F. Gamaleya, 18 Gamaleya str., Moscow 123098, Russia

[7] Institute for Bionic Technologies and Engineering, I. M. Sechenov First Moscow State Medical University, 2–4 Bolshaya Pirogovskaya str., Moscow 119991, Russia

***e-mail:** khorkov@vlsu.ru

Abstract. In this paper, we present the physical properties and toxicological assessment of layers with nanoparticles based on metal chalcogenides and titanium on human fibroblast cells. Nanoparticles layers based on metal chalcogenides (MoS_2, WS_2, ZnS) and titanium were applied onto substrate by spray deposition method. Nanoparticles and flakes were synthesized by laser ablation and fragmentation in liquid by femtosecond pulses. We investigated the size and morphology of the synthesized nanoparticles: WS_2-based flakes have a polygonal shape with dimensions up to 600 nm, other types of nanoparticles have a shape closer to spherical with sizes from 50 to 150 nm. Interaction of ultrafast laser radiation with materials in liquid is accompanied by the dissociation of water molecules leads to formation of hydrogen sulfide and oxides. To assess the biocompatibility of layers with synthesized nanoparticles, the MTT assay was performed with fibroblast cells. According to *in vitro* studies, Ti-based nanoparticles have the largest biocompatibility, and WS_2-based flakes have the smallest ones. Thus, synthesized Ti-based nanoparticles can be used in biomedical applications to support tissue regeneration without additional modification. Due to their properties, metal sulfides-based nanoparticles can be used in the photodynamic therapy of oncological diseases to destroy cancer cells. © 2023 Journal of Biomedical Photonics & Engineering.

Keywords: metal chalcogenides; pulsed laser ablation in liquid; pulsed laser fragmentation; nanoparticles; toxicity; theranostics; targeted drug delivery; biological markers.

Paper #3587 received 21 Jan 2023; revised manuscript received 24 Mar 2023; accepted for publication 10 Apr 2023; published online 3 May 2023. doi: 10.18287/JBPE23.09.020301.

1 Introduction

Currently, various nanoparticles based on metals and their compounds for biomedical applications are widely used due to new synthesis methods development and the need to find innovative solutions for the therapy of socially significant diseases [1–2]. Immobilization on the surface or nanocapsulation of medicinal substances and receptor molecules in such nanoparticles, their high thermal and electrical conductivity, which facilitates the detection of nanoparticles, will allow combining therapy and diagnostics within the concept framework of theranostics [3–5].

For each new synthesis method of nanoparticles, deeper physicochemical studies to assess their biocompatibility depending on their size, shape, and surface features are required [6–8].

Laser ablation in a liquid medium is a complex and multifactorial process. The main criteria that determine the performance of this operation is the energy expended and the yield of the target product. The use of laser systems with subpicosecond duration makes it possible to fine-tune the synthesis of nanoparticles with desired properties and dispersion, but clearly loses in terms of the mass yield of the ablated material [9]. The advantages of femto- and picosecond laser ablation processing for micro- and nanotechnologies are also due to non-thermal interaction with solid target materials, which is especially important when processing in liquid media.

According to the review [10], the fundamental difference between laser ablation using femto- and picosecond laser pulses and nanosecond ones lies in the sequence and cumulative interaction of such processes as absorption of laser radiation, emission of nanoparticles, plasma interaction with the medium, a gas bubble formation.

With femtosecond laser ablation in a liquid, it is possible to differentiate these processes by controlling the energy in the pulse and the environmental conditions. It is possible to fine-tune the process of laser ablation and, as a result, obtain predictable results. Femto- and picosecond laser processing is also accompanied by the phenomenon of multiphoton ionization, which improves the efficiency of laser beam energy transfer to the ablation process; the effects of the dependence of the absorption spectrum of the processed material on the wavelength of the acting radiation are not dominant.

The defining fact in liquid media processing is the achievement of conditions that facilitate precise processing of the material with a minimum thermal load [11]. The mechanism of production of nanoparticles and the sequence of processes of interaction of laser radiation with matter is presented as follows: within a few femtoseconds, multiphoton and tunneling ionization takes place; after about 50 fs, avalanche ionization will occur; and after 100 fs, the thermalization of the electrons of the metal target will occur; after 1 ps, the transfer of electron energy to the lattice is observed; then, after 10 ps, some thermodynamic processes are possible, such as thermal diffusion, synthesis of nanoparticles, and explosion [12]. Photochemical processes and phase transformations take place in time intervals from 1 ns [13]. The question arises about the effective difference between femto- and picosecond laser systems, since during ablation the phenomena occurring in the impact zone in the energy and time intervals are comparable. In Ref. [14], the authors note a 20% performance advantage under the ablation effect of femtosecond laser pulses.

The size distribution and formation rate of laser-generated nanoparticles depend on the power density of laser radiation, the overlap of zones of influence of laser pulses, and the properties of the medium [15–16]. Therefore, the irradiated area at a certain pulse energy and the ratio of scan rate to repetition rate must be kept constant in order to obtain predictable and reproducible size distribution results. The use of F-Theta scanning system allows to control these parameters in a wide range of speeds. The linear mechanical scanning systems are often limited to beam travel speeds of up to 20 mm/s. If the task is to obtain nanopowders of a given dispersion, stoichiometric composition, and particle shape, the validity of the low cost of nanosecond systems and the complexity of using F-theta scanners are not taken into account. It is also noted that the size and dispersion of nanoparticles can be controlled by changing the wavelength [12, 17].

High fluence densities make it possible to create conditions for rapid heating of the material structure and rapid fixation of the crystalline structure. These properties are achieved due to local action and rapid cooling of the flow of ablated particles in the volume of the liquid medium. With femto- and picosecond laser ablation, a higher temperature and pressure in the local volume can be achieved. These conditions favor the synthesis of materials corresponding to the high-temperature phases of the crystal lattice; smaller nanocrystals with a narrow size distribution can be obtained [18–19]. Such results are unattainable for laser processing using long pulses (longer than ns duration) in view of the possible relaxation of structural changes during prolonged exposure to temperature. The absence of volumetric heating of the surface in the environment allows ablation even in temperature-sensitive liquids such as organic solvents or biomolecular solutions [20–21]. In addition, nanoparticles after ultrashort pulsed laser ablation retain the stoichiometric composition of the target material better than nanoparticles after nanosecond pulsed ablation, which is confirmed by the results of EDX analysis of nanoparticles [22]. Nevertheless, laser ablation with

femto- and picosecond laser pulses also has a negative side associated with propagation through liquid media and the development of a number of nonlinear effects. These effects lead to the development of a laser-induced plasma channel in the focal plane and lead, among other things, to beam filamentation [23–24]. Volumetric boiling up of the liquid and difficulty in the propagation of laser radiation through a layer of microbubbles in the caustic zone can be observed, which is less pronounced with nanosecond processing, but can be eliminated with ablation with high-speed beam scanning over the surface. Under the action of nanosecond laser pulses, the processes leading to the ablation of nanoparticles occur almost simultaneously, which makes it difficult to fine-tune the properties of the resulting nanomaterials (of course, if it is necessary to obtain compositions consisting of target materials – a liquid medium, when the liquid medium is used as a reaction medium). The nanosecond ablation effect is characterized by the transition of the ablated material through the melting stage. The generation of large nanoparticles in a liquid medium at a laser pulse duration of nanoseconds or more is due to the significant melting of the target material and the interaction of the laser pulse, including with cavitation bubbles, which are then formed in the liquid medium [25]. Nanosecond laser ablation ejects a stream of ablated particles, gas bubbles, intense hydrodynamic flows, which creates a kind of screen that prevents the energy of the laser beam from reaching the treated surface. Chemical reactions of the material, cumulative changes in the surface texture and morphology of the target material will occur due to surface melting and a combination of ablation and thermal activation processes [26]. A further increase in the pulse duration, on time scales from microseconds to milliseconds, triggers the mechanisms for the production of nanoparticles through plasma plume condensation [27]. Processing with longer pulses does not lead to productive synthesis due to the significant influence of hydrodynamic processes in a liquid medium. Intense boiling prevents effective transfer of laser radiation energy to the surface of the material being processed.

Thus, features of femtosecond laser ablation and fragmentation in liquid are the possibility of synthesizing a wide range of nanomaterials, including both the source material and new compounds formed during laser irradiation and depend on the environment [28–30].

For example, laser processing in water leads to the dissociation of water molecules, the formation of oxygen, and further oxidation of metal sulfides [31].

One of the nanoparticles groups can be successfully used in biomedicine are nanoparticles based on metal chalcogenides [32]. They are used, for example, in bioimaging, biosensing, drug delivery, photothermal therapy due to their excellent characteristics, antibacterial activity and high biocompatibility [33–34]. WS_2 nanoparticles have high antitumor activity, actively absorbing near-infrared radiation and converting it into thermal energy during photothermal therapy [35]. WS_2 nanoparticles accession with various molecules, it becomes possible to use the obtained complexes for visualization and destruction of tumor lesions *in vivo* [36].

MoS_2 nanoparticles are also of great interest for basic research and applications in biomedicine, such as the development of functional nanoagents for biosensors, drug delivery, bioimaging, cancer therapy, and other biomedical applications [37–39]. There are a number of studies claiming that MoS_2 nanostructures, especially those with appropriate surface functionalization, do not have noticeable toxicity *in vitro* and *in vivo* [40]. Complexes with MoS_2 nanoparticles are used for tissue repair and antibacterial therapy [41].

ZnS nanoparticles are promising materials in the therapy of oncological diseases, since their introduction into tumor cells leads to the generation of reactive oxygen species that trigger cell destruction [42]. Complexes with ZnS nanoparticles can be used in magnetic hyperthermia [43], *in vivo* imaging [44], and skin regeneration [45].

ZnO is a semiconductor material with high biological stability and good exciton response, these properties make it a popular material for biosensors. Doping of ZnO with metals makes it possible to significantly change its sensor and catalytic properties [46–48]. ZnO nanoparticles production by laser ablation and subsequent fragmentation is a flexible method for tune the properties of described properties of zinc oxide.

Titanium and its alloys have a unique combination of strength and biocompatibility, which allows them to be used for medical purposes and explains their widespread use as materials for implants [49]. Compounds with TiO nanoparticles are also used in biomedicine to suppress tumor growth and have an antibacterial effect [50].

TiO_2 nanoparticles are widely used in the phototherapy of cancer cells, bacteria and are potential photosensitizing agents for photodynamic therapy due to their high stability and unique phototoxic effects upon irradiation [51–52].

All these nanoparticles can be obtained using method of laser ablation and fragmentation. Its advantages are simplicity, versatility, high purity of nanoparticles and absence of toxic products during synthesis [53]. Femtosecond regime gives an opportunity to control precisely nanoparticle structure [54].

In this work, we have considered the possibilities of using various dichalcogenides as starting materials for the formation of nanoparticles using the femtosecond laser ablation and fragmentation in water. The article considers the physicochemical characteristics and biocompatibility of nanoparticles synthesized by laser ablation and fragmentation in deionized water with femtosecond pulses of WS_2, MoS_2, ZnS and Ti targets. The sizes and morphology of nanoparticles were analyzed by dynamic light scattering (DLS) and scanning electron microscopy (SEM), and the features of the elemental composition were analyzed by energy dispersive spectroscopy (EDS). *In vitro* biocompatibility studies indicate the most suitable application for each of the types of synthesized nanoparticles.

2 Materials and Methods

2.1 Synthesis of Nanoparticles

For the synthesis of nanoparticles, the techniques of laser ablation and fragmentation in liquid with femtosecond pulses were used. Schemes, as well as images of the processes are presented in Fig. 1.

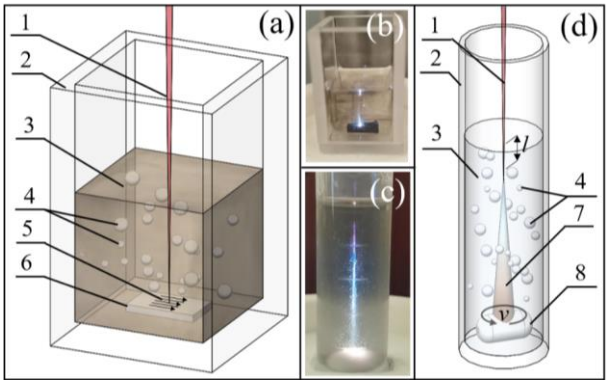


Fig. 1 Schemes and images of the processes of laser ablation of the target (a, b) and fragmentation (c, d) in liquid.

In our experiments, we used a Yb:KGW femtosecond laser system (Avesta Ltd., Russia) generating 280 fs pulses at 1030 nm wavelength of with 10 kHz repetition rate and maximum pulse energy of 150 μJ. In Fig. 1 the following positions are indicated: 1 – laser radiation; 2 – cuvette/tube; 3 – liquid medium; 4 – nanoparticles; 5 – trajectory of laser beam scanning; 6 – target; 7 – supercontinuum; 8 – magnetic anchor.

In the process of laser ablation and fragmentation, scanning with laser beam over the target surface, as well as scanning in the volume of the liquid, was carried out using a two-coordinate X-Y scanner system Raylase RLA-1504, equipped with a F-Theta lens with a working distance of 200 mm. Focused beam diameter according to the intensity level $1/e^2$ was 50 μm. Deionized water was used as the liquid medium. In laser ablation, the targets were a synthetically grown molybdenum disulfide (MoS_2) crystal, a bulk sample of polycrystalline CVD zinc sulfide (ZnS MS), and high-purity titanium.

In experiments on laser fragmentation in liquid, in addition to colloidal solutions prepared by laser ablation in liquid, suspensions of monolayer tungsten disulfide (WS_2) of various concentrations were also used. The starting material consisted of flakes with lateral sizes of 0.1–4 μm and a thickness of ~1 nm. Suspensions of monolayer tungsten disulfide were prepared by adding WS_2 powder to test tubes with deionized water and then placed in an ultrasonic bath. Suspensions of WS_2 were prepared at concentrations of 0.2 and 1 mg/ml then irradiated with femtosecond laser pulses.

During the laser ablation synthesis of MoS_2 nanoparticles, the crystal was located at the bottom of a cuvette filled with 5 ml of deionized water, the processing area was a square with a side of 5 mm, the scanning density was 20 lines/mm, the scanning speed was 100 mm/s, the number of processing iterations was 60. This regime made it possible to achieve the required concentration of nanoparticles (0.2 mg/ml). Synthesis of ZnS nanoparticles was carried out at the same parameters. In the case of laser ablation of a titanium plate, the processing area was a square with a side of 1.5 mm with scanning density was 20 lines/mm and scanning speed was 100 mm/s, time of laser ablation was 10 min (total number of pulses $6 \cdot 10^6$, energy per pulse 100 μJ).

A test tube with a prepared suspension/colloidal solution, including those containing large particles in the form of shatter of ablated materials, was subjected to laser fragmentation. The solution was continuously stirred during laser fragmentation. The mixing of the solution during laser processing was carried out as follows: test tube was filled with a solution of 5 ml in volume; at the bottom, a magnetic anchor was located, and a torque was transmitted to the magnetic anchor by means of a magnetic stirrer. The waist region of the laser beam was located 10 mm below the air/liquid interface (in Fig. 1d distance is marked with *l*), while the rotation speed of the magnetic anchor was 400 rpm. The speed was chosen to ensure efficient mixing and to prevent the formation of a funnel on the solution surface. The beam scanning trajectory during the laser fragmentation of the solution was a 4 mm diameter circle with a linear filling density of 20 lines/mm and a scanning speed of 100 mm/s, while the scanning direction was changed by 90º, so the processing area was a grid.

Laser fragmentation of ZnS and MoS_2 colloidal solutions obtained by laser ablation in liquid was for 20 min (total number of pulses $12 \cdot 10^6$), pulse energy 100 μJ, energy fluence 10.2 J/cm^2.

During laser fragmentation of WS_2 suspension with concentration of 0.2 mg/ml, the pulse energy was set at the level of 30 μJ, energy fluence was 3 J/cm^2, and the laser irradiation duration was 2 min. In the case of WS_2 suspension with a concentration of 1 mg/ml, the pulse energy was 100 μJ, energy fluence was 10.2 J/cm^2, and the duration of the laser fragmentation process was 20 min.

2.2 DLS

To determine the sizes of the obtained nanoparticles, DLS measurements were performed using a Photocor setup (Photocor Ltd., Russia). The measurements were carried out at a temperature of 23 ºC. The autocorrelation function was processed with the DynaLS software. Based on the measurement results, the hydrodynamic diameter of nanoparticles was calculated.

2.3 Layers Deposition on Substrates

Each of the solutions was applied by spray deposition onto sterile clean 1 × 1 cm silicon substrates. The substrates were fixed in a special holder and placed in an E2V dispensing system for deposition (Nordson EFD, Westlake, OH, USA). The setup was a deposition system that can be positioned relative to three axes with high

accuracy. The diameter of the nozzle was 0.5 mm, the solutions were supplied under a pressure of 0.05 bar at air pressure 20 bar. To form a layer, 1.5 ml of solution was applied to each of the substrates. During the deposition process, the substrates were heated using a heating table to ensure faster drying of the solution and formation of a layer. For physical studies, WS_2 nanoparticles with lower concentration were deposited on the substrate for the convenience of analyzing individual nanoparticles. In biological studies, for the most complete coverage of the substrate and the maximum consideration of the effect of nanoparticles on cells, WS_2 nanoparticles with higher concentration were applied.

2.4 Microscopy

The surface features of the deposited layers of nanoparticles on silicon were studied using an FEI Helios NanoLab 650 scanning electron microscope (FEI Ltd., Hillsboro, OR, USA) equipped with an attachment for energy-dispersive X-ray spectroscopy (EDS). The samples were attached to the holder with carbon tape. Accelerating voltage of the electron beam was 5 kV, electron probe current was 21 pA. Images were obtained both in frontal projection and with the substrates tilted by 52°.

2.5 Layer Studies In Vitro

For a comparative assessment of the cytotoxicity of the synthesized nanoparticles, the surfaces of the silicon substrates were completely covered with a layer of each type of nanoparticles according to the method described in Section 2.3. Thus, the layer on the substrate was a sample with the highest possible concentration of nanoparticles that affect the vital activity of cells. This method makes it possible to make a choice of the type of nanoparticles for further research, depending on the specific application. After fabrication, the samples were sterilized with ultraviolet for 20 min. Cellular experiments were carried out with FH-T cell line – human fibroblasts, which was acquired at the National Research Center for Epidemiology and Microbiology of the Ministry of Health of the Russian Federation. Protocol for incubation of nanoparticles with cells was as follows. The samples with layers of nanoparticles were placed to the bottom of the wells of a 12-well culture plate (the area of the well bottom was 3.8 cm^2) and filled with a cell suspension in a DMEM culture medium supplemented with 10% calf serum in an amount of 2×10^5 cells/ml. 1 ml of cells was added to each well. The plates were placed in a CO_2 thermostat and kept there for 48 h.

To quantify the cells on the samples, the MTT (3-(4,5-dimethylthiazol-2-yl)-2,5-diphenyl-2H-tetrazolium bromide) assay was performed according to the standard method [55]. At the end of the incubation period, the culture medium was removed. 100 µl of pure culture medium was added to each well with 20 µl of MTT at a concentration of 5 mg/ml. MTT is a tetrazole-based dye that interacts with the mitochondria of living cells to form formazan crystals. MTT remained in the wells for 2 h, after which the culture medium was removed. Further, dimethyl sulfoxide was added to dissolve the formazan crystals and obtain a purple color of the solution, the cell pellet was resuspended for 10 min. Staining intensity is proportional to the number of living cells, a microplate photometer Immunochem 2100 (High Technology Inc., North Attleboro, MA, USA) was used to quantify staining intensity.

3 Results and Discussion

3.2 Nanoparticles Fabrication and Determining Their Size in a Colloidal Solution

Nanoparticles solutions and samples obtained after solutions deposition to the substrate are presented in Fig. 2. The average hydrodynamic diameters of nanoparticles in a colloidal solution after synthesis were obtained by the DLS method. The calculated nanoparticle sizes are given in Table 1.

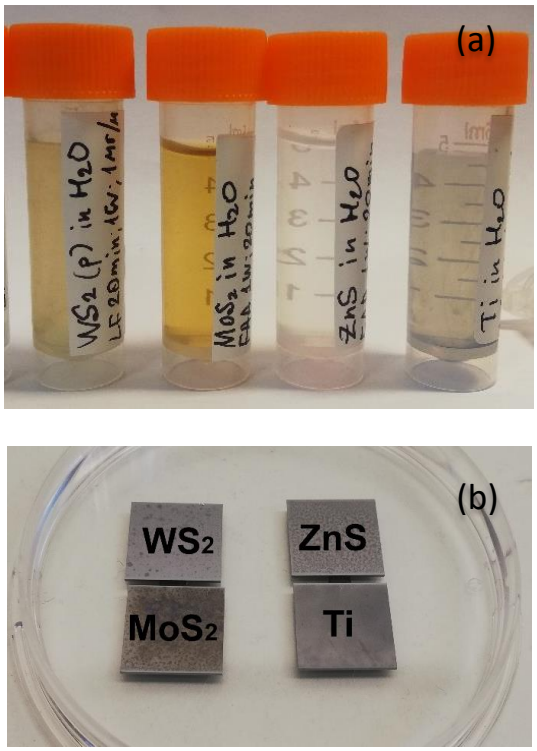


Fig. 2 Appearance of colloidal solutions of synthesized nanoparticles (a) and layers of nanoparticles applied to silicon (b).

Despite the possibility of studying nanoparticles directly in a liquid medium, the DLS method is inferior in accuracy to microscopic methods in determining the size of nonspherical particles, as well as nanoparticles with a large size spread in one solution [56]. In addition, various surface non-homogeneities, such as porosity or the presence of smaller particles on the surface, also cannot be assessed by the DLS method [57].

Table 1 Results of DLS measurements.

Types of nanoparticles from starting materials	Average hydrodynamic diameter, nm
WS_2	226
MoS_2	92
ZnS	106
Ti	166

3.3 Morphology and Composition of Layers

The surface features of the deposited layers were analyzed by SEM (Fig. 3). According to microscopy data, WS_2-based nanoparticles are polygonal sheets 120 to 600 nm in size (Fig. 3 a, b). In addition, accumulation of agglomerates of nanoparticles is found in some areas, which indicates the requirements for their longer processing to break the agglomerates before application. MoS_2-based nanoparticles are more uniformly distributed over the silicon surface, have a shape close to spherical, and sizes from 50 to 100 nm (Fig. 3 c, d).

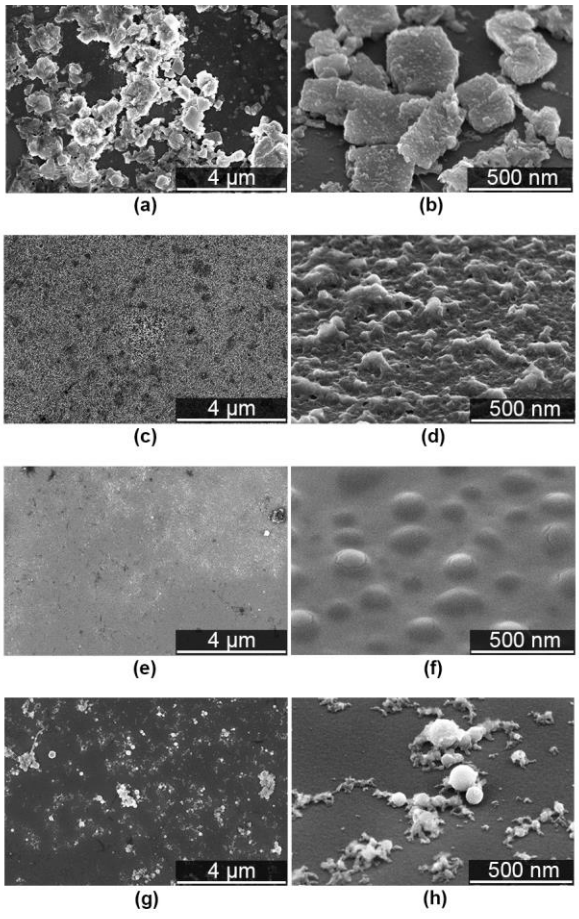


Fig. 3 SEM images of the surface of layers of deposited WS_2-based (a, b), MoS_2-based (c, d), ZnS-based (e, f), and Ti-based (g, h) nanoparticles obtained by passing an electron beam at a right angle to the surface (a, c, e, g) and at a surface tilt of 52° (b, d, f, h).

ZnS-based nanoparticles have a spherical shape and sizes from 60 to 130 nm, distributed mostly uniformly, occasionally there are agglomerates of 2–3 connected particles (Fig. 3 e, f). Ti-based nanoparticles are individual spheres with sizes from 60 to 140 nm (Fig. 3 g, h), distributed over the surface less uniformly compared to ZnS-based nanoparticles. The sizes of nanoparticles measured by the SEM method approximately correspond to the DLS estimate, except for WS_2-based nanoparticles, which have a nonspherical shape and a large size spread.

Thus, according to the DLS and microscopy data, among the synthesized nanoparticles, MoS_2-based nanoparticles have the smallest sizes, while WS_2-based nanoparticles are the largest sizes. Large flat nanoparticles can be efficiently absorbed by cells and accumulate in tumors, which is an advantage in cancer therapy [58]. Non-spherical nanoparticles also have a large surface area for attaching different molecules. WS_2-based and Ti-based nanoparticles are deposited on substrates less uniformly and tend to aggregate; therefore, when using them *in vivo*, special attention should be paid to the methods of their separation in order to avoid an uneven and hardly predictable distribution in the tissue volume.

3.4 EDS Measurements

During laser fragmentation of chalcogenides (ZnS, MoS_2, WS_2), hydrogen sulfide evolution was observed. The formation of hydrogen sulfide indicates the dissociation of water and processed chalcogenides. The conditions of irradiation during laser fragmentation promote the formation of new chemical bonds, and a partial replacement of sulfur by oxygen is observed. Laser processing of Ti in water results in the formation of oxides. The identification of the formed chemical compounds required an energy dispersive analysis of the formed nanoparticles. The results of EDS analysis are presented below in Figs. 4–7.

The oxygen content in the resulting nanoparticles can be effectively controlled during fragmentation, just as the size dispersion of nanoparticles. Energy dispersive analysis is a convenient tool for diagnosing the elemental composition of micro- and nanostructures.

During laser fragmentation of the WS_2 suspension, the presence of oxygen was established (Fig. 4). In Ref. [59], the results of the assessment of the toxicity of tungsten oxide nanoparticles are presented, it is noted that it can be controlled by changing the concentration of nanoparticles, as well as by the optical emission spectrum in view of the high photocatalytic activity of tungsten oxide, especially in the short-wavelength part of the spectrum. The pronounced dependence of toxicity on the concentration of nanoparticles was considered in Ref. [60]. There is a high sorption capacity of nanoparticles relative to microparticles by the tissues of the body of rats. In Ref. [61], the stabilization of tungsten oxide nanoparticles is noted when polyvinylpyrrolidone (PVP) is used as a coating agent. As a result of laser fragmentation, the WS_2 suspension is less susceptible to oxidation than ZnS and MoS_2 nanoparticles.

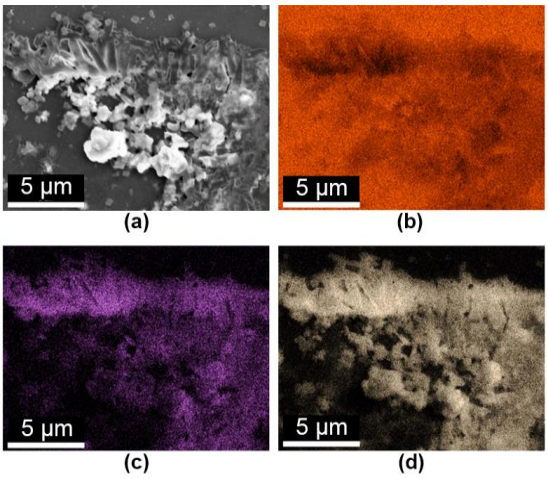


Fig. 4 SEM image of the surface of WS_2-based nanoparticles (a): distribution of tungsten (brightness + 50%) (b), sulfur (c), and oxygen (d).

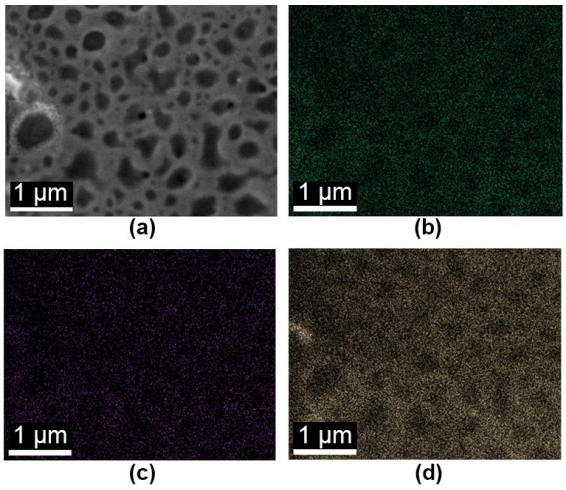


Fig. 5 SEM image of the surface of Zn-based nanoparticles (a): distribution of Zn (brightness + 50%) (b), sulfur (c), and oxygen (d).

Slight changes in the shape of the nanoparticles obtained after fragmentation may indicate an insignificant value of the laser effect, or a high stability of the tungsten oxide suspension for this type of processing. A sufficiently large size of the obtained particles may indicate the need to increase the fragmentation time in order to reduce the size.

During laser fragmentation of ablated zinc sulfide nanoparticles in water, ZnS can be destroyed and both oxygen and hydroxyl bonds can form. It is possible to violate stoichiometry, especially on the surface of nanoparticles, and, as a result, oxygen sorption from air during sample preparation. SEM image of a continuous film-like coating on the surface of the obtained samples with pronounced local elevations, while maintaining the signal of sulfur and oxygen, is shown in Fig. 5.

The prevalence of the oxygen response in fragmented ZnS nanoparticles may indicate a significant content of zinc oxide. In the process of laser ablation of ZnS in an aqueous medium, the formation of nanoparticles and flocculent deposit of the clusters are often observed [62], during the drying of which they form a continuous coating of the surface. This occurs when the concentration of particles in the solution is high.

The results obtained (Fig. 6) show the oxidative capacity of MoS_2 during laser fragmentation in an aqueous medium. This activity is due to the high catalytic capacity of water vapor for the oxidation of molybdenum [63]. During laser fragmentation, hydrogen sulfide evolution is observed. The formation of hydrogen sulfide is possible during the ionization/dissociation of water or water vapor as a result of the laser irradiation process. Laser fragmentation leads to a violation of the initial stoichiometry of molybdenum disulfide with the formation of many derivative compositions [64–66].

The results of energy dispersive analysis of nanoparticles obtained by laser ablation of titanium in deionized water showed the presence of a significant amount of oxygen (Fig. 7).

The absence of a change in the shape of particles relative to the spherical shape indicates the presence of oxygen on the surface due to some of its deficiency. An excess oxygen content leads to significant changes in the shape of nanoparticles, including intergrow and form of a single common surface. In addition, the formation of core-shell particles is possible. The presence of oxygen on the surface of titanium nanoparticles can significantly expand the area of their application in biosensorics. In Ref. [67], high biocompatibility and high stability in both acidic and alkaline media are noted.

The instability of titanium oxide can be compensated for by its deficiency in the nanoparticle. Titanium oxide in different phase states (rutile, anatase) has an ambiguous effect on biological objects. In Ref. [68], the results of the toxic effect of titanium oxide nanoparticles of various sizes and phase composition on cell cultures are presented.

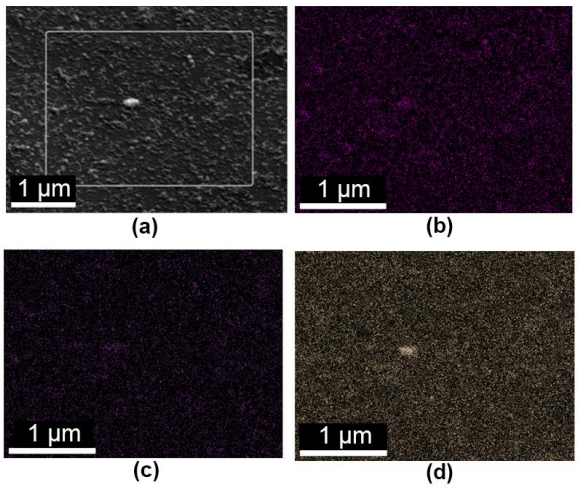


Fig. 6 SEM image of the surface of MoS_2-based nanoparticles (a): distribution of Mo (brightness + 50%) (b), sulfur (c), and oxygen (d).

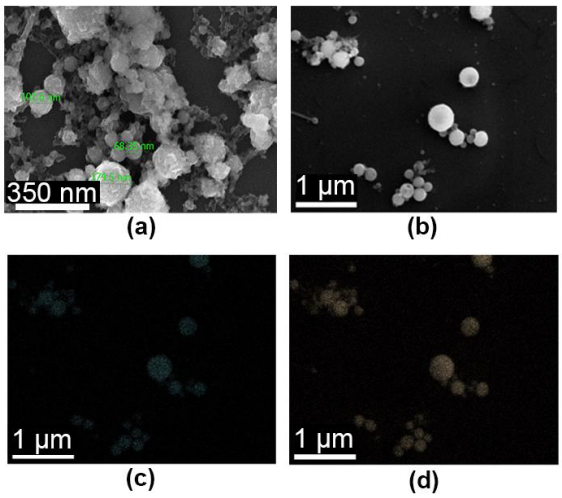


Fig. 7 SEM images of the surface of Ti-based nanoparticles (a, b): distribution of Ti (c), oxygen (d).

Localized areas of titanium oxide on the surface of the obtained titanium nanoparticles are limited by the volume of the material, which hinders its polymorphic transformations when external conditions change. These factors can be used in the production of stable sensor systems based on titanium oxide.

The results obtained allow us to conclude that water is highly reactive in the process of laser ablation and fragmentation, since significant changes in the chemistry of the obtained materials relative to the initial ones are observed. The observed changes, among other things, can be caused both by the nature of the water itself, and by significant changes in the properties of this medium in the region of the caustic of the transmitted laser radiation. The ionization energy of water is from 9.2 eV, pronounced continuum generation in the visible part of the spectrum is observed at energies of 10.5–12.5 eV [69–70] respectively, under our processing conditions, in particular fragmentation, the formation of a continuum during the laser radiation passing through water corresponds to the state ionization of the environment. Particles in a medium corresponding to the state of ionization are capable of forming chemical bonds, which was observed in Refs. [71–74].

3.5 Biological Properties of Nanoparticles

Various nanoparticles and nanostructures obtained with laser radiation can be successfully used as components for bioelectronic devices [75] and in biomedical applications, including scaffold materials for tissue engineering [76–78]. Conducting complex studies of the cytotoxicity of nanoparticles is an important step before *in vivo* and clinical studies. This section presents the results of a preliminary assessment of the cytotoxicity of the synthesized nanoparticles in the short term, which makes it possible to outline a further vector of *in vitro* studies. The method of forming layers of nanoparticles on a silicon substrate using a spray application of homogeneous colloidal solutions made it possible to achieve complete coverage of the substrate surface with a layer of nanoparticles for cell studies in order to take into account their effect on cells to the maximum. This method made it possible to determine the survival of cells on a layer with the maximum concentration of nanoparticles of various types.

One of the most common, simple and reproducible tests for determining the biocompatibility of samples is the MTT assay. The results of the MTT assay of the deposited layers of nanoparticles are presented in Fig. 8.

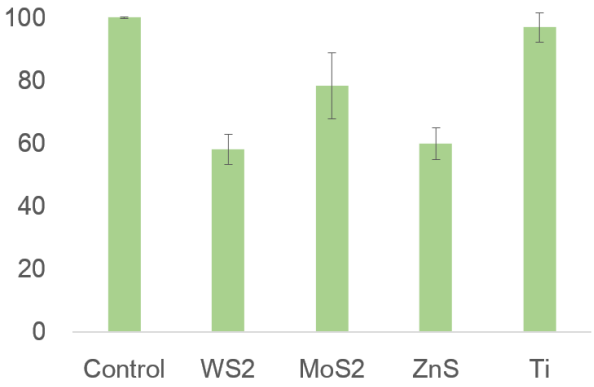


Fig. 8 The number of cells on the surface of the deposited layers of nanoparticles as a percentage of the control sample (clean substrate) according to the MTT assay.

The best biocompatibility is exhibited by layers of Ti-based nanoparticles; the layers of WS_2-based and ZnS-based nanoparticles are the least biocompatible among the studied particles. Layers of MoS_2-based nanoparticles show average biocompatibility values of ~ 80%. One of the reasons for the decrease in the biocompatibility of the layers may be the ability of metal chalcogenide nanoparticles to form reactive oxygen species, which negatively affects cells [79]. Nanoparticles, however, can be attached to molecules of photosensitizers and used at the studied concentration for an additional destructive effect on cancer cells during photodynamic therapy [80]. The toxicity of these nanoparticles for targeted drug delivery applications can be reduced by covering them with biocompatible coatings [81]. Due to the high biocompatibility, Ti nanoparticles can be used for biomedical applications in drug delivery and tissue regeneration without additional modification. The biocompatibility of synthesized nanoparticles can be affected by the concentration of nanoparticles in solution; additional binding of molecules to nanoparticles can either increase or decrease their biocompatibility.

In the case of using nanoparticles for cancer therapy, due to the characteristics of blood vessels supplying tumor tissues, it is more efficient to use large nonspherical nanoparticles [82]. In this case, the long-term presence of nanoparticles in the tumor volume is more important than their rapid removal from the body.

There is evidence that in the process of additional modification of nanoparticles (for example, addition of a polymer), it is possible to both reduce their size [83] and

change their biological properties in the required direction [84]. Modification of the surface of nanoparticles makes it possible to change the rate of their filtration by the excretory system or to minimize their absorption by the liver [85].

4 Conclusions

In this work, colloidal solutions and layers of nanoparticles of 4 types of starting materials deposited on silicon wafers were studied: WS_2, MoS_2, ZnS, Ti, obtained using the technique of laser ablation and fragmentation in liquid with femtosecond pulses. Among the considered nanoparticles, MoS_2-based nanoparticles have the smallest size, and WS_2-based nanoparticles have the largest size. WS_2-based nanoparticles have a non-spherical shape and, at the studied concentration, have an inhibitory effect on cell growth, which can be used when these nanoparticles are introduced into the tumor zone for its subsequent destruction by photodynamic therapy under the action of laser radiation. ZnS-based nanoparticles have a similar effect. It should be noted that ZnS-based nanoparticles have high antiseptic properties, including those actively used for photocatalytic antibacterial treatment. Our results demonstrate the relatively low toxicity of the structures obtained, which may be due to the presence of a shell of zinc oxide, a significant substitution of zinc sulfide, zinc oxide, which is characterized by high biological inertness. Ti-based nanoparticles are spherical and highly biocompatible, which makes them promising for targeted drug delivery and tissue regeneration. The content of titanium oxide on the surface of nanoparticles (determined using EDS) requires further research. On the one hand, the presence of titanium oxide on the surface of the obtained nanoparticles can be obtained as a result of laser fragmentation, when the nanoparticles were repeatedly exposed to laser radiation in water, as well as the formation of titanium oxide during the storage of nanoparticles, also, it is impossible to exclude a change in the phase composition of the surface of these particles due to the high chemical activity of these materials. Titanium oxide in different phase states (rutile, anatase) has an ambiguous effect on biological objects.

Disclosures

The authors have no relevant financial interest in this article and no conflict of interest to disclose.

Acknowledgments

This study was funded by the Russian Science Foundation (project no. 22-79-10348, https://rscf.ru/project/22-79-10348/).

References

1. R. Canaparo, F. Foglietta, T. Limongi, and L. Serpe, "Biomedical Applications of Reactive Oxygen Species Generation by Metal Nanoparticles," Materials (Basel) 14(1), 53 (2020).
2. K. T. Nguyen, Y. Zhao, "Engineered hybrid nanoparticles for on-demand diagnostics and therapeutics. Accounts of chemical research," Accounts of Chemical Research 48(12), 3016–3025 (2015).
3. G. Modugno, C. Ménard-Moyon, M. Prato, and A. Bianco, "Carbon nanomaterials combined with metal nanoparticles for theranostic applications," British Journal of Pharmacology 172(4), 975–991 (2015).
4. O. A. Kuchur, S. A. Tsymbal, M. V. Shestovskaya, N. S. Serov, M. S. Dukhinova, and A. A. Shtil, "Metal-derived nanoparticles in tumor theranostics: Potential and limitations," Journal of Inorganic Biochemistry 209, 111117 (2020).
5. K. Chatterjee, S. Sarkar, K. J. Rao, and S. Paria, "Core/shell nanoparticles in biomedical applications," Advances in Colloid and Interface Science 209, 8–39 (2014).
6. L. A. Dykman, N. G. Khlebtsov, "Multifunctional gold-based nanocomposites for theranostics," Biomaterials 108, 13–34 (2016).
7. X. Li, J. Wei, K. E. Aifantis, Y. Fan, Q. Feng, F. Z. Cui, and F. Watari, "Current investigations into magnetic nanoparticles for biomedical applications," Journal of Biomedical Materials Research Part A 104(5), 1285–1296 (2016).
8. C. Egbuna, V. K. Parmar, J. Jeevanandam, S. M. Ezzat, K. C. Patrick-Iwuanyanwu, C. O. Adetunji, J. Khan, E. N. Onyeike, C. Z. Uche, M. Akram, M. S. Ibrahim, M. M. El Mahdy, C. G. Awuchi, K. Saravanan, H. Tijjani, U. E. Odoh, M. Messaoudi, J. C. Ifemeje, M. C. Olisah, N. J. Ezeofor, C. J. Chikwendu, and C. G. Ibeabuchi, "Toxicity of nanoparticles in biomedical application: Nanotoxicology," Journal of Toxicology 2021, 9954443 (2021).
9. C. G. Moura, R. S. F. Pereira, M. Andritschky, A. L. B. Lopes, J. P. de Freitas Grilo, R. M. do Nascimento, and F. S. Silva, "Effects of laser fluence and liquid media on preparation of small Ag nanoparticles by laser ablation in liquid," Optics & Laser Technology 97, 20–28 (2017).
10. J. Perrière, E. Millon, and E. Fogarassy (Eds.), Recent advances in laser processing of materials, 1st ed., Elsevier, Amsterdam (2006). ISBN: 978-0-08044-727-8.
11. A. Kanitz, M. R. Kalus, E. L. Gurevich, A. Ostendorf, S. Barcikowski, and D. Amans, "Review on experimental and theoretical investigations of the early stage, femtoseconds to microseconds processes during laser ablation in liquid-phase for the synthesis of colloidal nanoparticles," Plasma Sources Science and Technology 28(10), 103001 (2019).

12. R. Viskup (Ed.), High energy and short pulse lasers, IntechOpen, London, UK (2016). ISBN: 978-953-51-2606-5.
13. A. Royon, Y. Petit, G. Papon, M. Richardson, and L. Canioni, "Femtosecond laser induced photochemistry in materials tailored with photosensitive agents," Optical Materials Express 1(5), 866–882 (2011).
14. S. Barcikowski, A. Menéndez-Manjón, B. Chichkov, M. Brikas, and G. Račiukaitis, "Generation of nanoparticle colloids by picosecond and femtosecond laser ablations in liquid flow," Applied Physics Letters 91(8), 083113, (2007)
15. A. V. Kabashin, M. Meunier, "Synthesis of colloidal nanoparticles during femtosecond laser ablation of gold in water," Journal of Applied Physics 94(12), 7941–7943 (2003).
16. S. Barcikowski, A. Hahn, A. V. Kabashin, and B. N. Chichkov, "Properties of nanoparticles generated during femtosecond laser machining in air and water," Applied Physics A 87, 47–55 (2007).
17. M. Kawasaki, N. Nishimura, "1064-nm laser fragmentation of thin Au and Ag flakes in acetone for highly productive pathway to stable metal nanoparticles," Applied Surface Science 253, 2208–2216 (2006).
18. G. W. Yang, "Laser ablation in liquids: Applications in the synthesis of nanocrystals," Progress in Materials Science 52(4), 648–698 (2007).
19. V. Amendola, M. Meneghetti, "Laser ablation synthesis in solution and size manipulation of noble metal nanoparticles," Physical Chemistry Chemical Physics 11(20), 3805–3821, (2009)
20. P. C. Vella, S. S. Dimov, E. Brousseau, and B. R. Whiteside, "A new process chain for producing bulk metallic glass replication masters with micro-and nano-scale features," The International Journal of Advanced Manufacturing Technology 76, 523–543 (2015).
21. C. G. Kuo, C. G. Chao, "A novel method of centrifugal processing for the synthesis of lead–bismuth eutectic alloy nanospheres and nanowires," The International Journal of Advanced Manufacturing Technology 32, 468–472 (2007).
22. H. Chang, C. S. Jwo, P. S. Fan, and S. H. Pai, "Process optimization and material properties for nanofluid manufacturing," The International Journal of Advanced Manufacturing Technology 34, 300–306 (2007).
23. H. Oh, M. Lee, "Laser-direct fabrication of invisible Ag nanowire electrode pattern on flexible plastic substrate," Thin Solid Films 636, 375–383 (2017).
24. M. E. Koleva, N. N. Nedyalkov, N. Fukata, W. Jevasuwan, and D. Karashanova, "Laser-assisted approach for synthesis of plasmonic Ag/ZnO nanostructures," Superlattices and Microstructures 109, 886–896 (2017).
25. R. Intartaglia, K. Bagga, and F. Brandi, "Study on the productivity of silicon nanoparticles by picosecond laser ablation in water: towards gram per hour yield," Optics Express 22(3), 3117–3127 (2014).
26. M. S. Brown, C. B. Arnold, Fundamentals of laser–material interaction and application to multiscale surface modification, in Laser Precision Microfabrication, K. Sugioka, M. Meunier, and A. Piqué (Eds.), Springer, Berlin, Heidelberg (2010). ISBN: 978-3-642-10522-7.
27. G. Lin, D. Tan, F. Luo, D. Chen, Q. Zhao, J. Qiu, and Z. Xu, "Fabrication and photocatalytic property of α-Bi2O3 nanoparticles by femtosecond laser ablation in liquid," Journal of Alloys and Compounds 507(2), L43–L46 (2010).
28. H. Zeng, X. W. Du, S. C. Singh, S. A. Kulinich, S. Yang, J. He, and W. Cai, "Nanomaterials via laser ablation/irradiation in liquid: a review," Advanced Functional Materials 22(7), 1333–1353 (2012).
29. J. Xiao, P. Liu, C. X. Wang, and G. W. Yang, "External field-assisted laser ablation in liquid: An efficient strategy for nanocrystal synthesis and nanostructure assembly," Progress in Materials Science 87, 140–220 (2017).
30. A. Subhan, A.-H. I. Mourad, and Y. Al-Douri, "Influence of Laser Process Parameters, Liquid Medium, and External Field on the Synthesis of Colloidal Metal Nanoparticles Using Pulsed Laser Ablation in Liquid: A Review," Nanomaterials 12(13), 2144 (2022).
31. V. A. Svetlichnyi, A. V. Shabalina, I. N. Lapin, and D. A. Goncharova, "Metal oxide nanoparticle preparation by pulsed laser ablation of metallic targets in liquid," Chapter 11 in Applications of Laser Ablation–Thin Film Deposition, Nanomaterial Synthesis and Surface Modification, D. Yang (Ed.), IntechOpen, London, UK, 245–263 (2016).
32. C. Senthamil, J. Hemalatha, S. Nandhabala, A. Nivetha, C. Sakthivel, and I. Prabha, "Multifunctionalized Metal Chalcogenides and Their Roles in Catalysis and Biomedical Applications," ChemistrySelect 7(46), e202203394 (2022).
33. M. Ensoylu, H. Atmaca, and A. M. Deliormanlı, "Fabrication and in vitro characterization of macroporous WS2/ bioactive glass scaffolds for biomedical applications," Journal of the Australian Ceramic Society 58(2), 397–409 (2022).
34. X. Zhou, H. Sun, and X. Bai, "Two-Dimensional Transition Metal Dichalcogenides: Synthesis, Biomedical Applications and Biosafety Evaluation," Frontiers in Bioengineering and Biotechnology 8, 236 (2020).
35. S. Wang, J. Zhao, H. Yang, C. Wu, F. Hu, H. Chang, G. Li, D. Ma, D. Zou, and M. Huang, "Bottom-up synthesis of WS2 nanosheets with synchronous surface modification for imaging guided tumor regression," Acta Biomaterialia 58, 442–454 (2017).
36. L. Cheng, J. Liu, X. Gu, H. Gong, X. Shi, T. Liu, C. Wang, X. Wang, G. Liu, H. Xing, W. Bu, B. Sun, and Z. Liu, "PEGylated WS2 Nanosheets as a Multifunctional Theranostic Agent for in vivo Dual-Modal CT/Photoacoustic Imaging Guided Photothermal Therapy," Advanced Materials 26(12), 1886–1893 (2014).

37. Z. Zohreband, M. Adeli, and A. Zebardasti, "Self-healable and flexible supramolecular gelatin/MoS2 hydrogels with molecular recognition properties," International Journal of Biological Macromolecules 182, 2048–2055 (2021).
38. K. Kasinathan, K. Marimuthu, B. Murugesan, N. Pandiyan, B. Pandi, S. Mahalingam, and B. Selvaraj, "Cyclodextrin functionalized multi-layered MoS2 nanosheets and its biocidal activity against pathogenic bacteria and MCF-7 breast cancer cells: Synthesis, characterization and in-vitro biomedical evaluation," Journal of Molecular Liquids 323, 114631 (2021).
39. M. Xie, N. Yang, J. Cheng, M. Yang, T. Deng, Y. Li, and C. Feng, "Layered MoS2 nanosheets modified by biomimetic phospholipids: Enhanced stability and its synergistic treatment of cancer with chemo-photothermal therapy," Colloids and Surfaces B: Biointerfaces 187, 110631 (2020).
40. T. Liu, Z. Liu, "2D MoS 2 Nanostructures for Biomedical Applications," Advanced Healthcare Materials 7(8), 1701158 (2018).
41. M. Liu, H. Zhu, Y. Wang, C. Sevencan, and B. L. Li, "Functionalized MoS2-Based Nanomaterials for Cancer Phototherapy and Other Biomedical Applications," ACS Materials Letters 3(5), 462–496 (2021).
42. H. Labiadh, K. Lahbib, S. Hidouri, S. Touil, and R. Ben Chaabane, "Insight of ZnS nanoparticles contribution in different biological uses," Asian Pacific Journal of Tropical Medicine 9(8), 757–762 (2016).
43. M. Stefan, C. Leostean, O. Pana, M. Suciu, A. Popa, D. Toloman, S. Macavei, C. Bele, F. Tabaran, and L. Barbu-Tudoran, "Synthesis and characterization of Fe3O4–ZnS:Mn nanocomposites for biomedical applications," Materials Chemistry and Physics 264, 124474 (2021).
44. W. Guo, N. Chen, C. Dong, Y. Tu, J. Chang, and B. Zhang, "One-pot synthesis of hydrophilic ZnCuInS/ZnS quantum dots for in vivo imaging," RSC Advances 3(24), 9470–9475 (2013).
45. B. Han, W. H. Fang, S. Zhao, Z. Yang, and B. X. Hoang, "Zinc sulfide nanoparticles improve skin regeneration," Nanomedicine: Nanotechnology, Biology and Medicine 29, 102263 (2020).
46. F. Chekin, M. Yazdaninia, "A sensor based on incorporating Ni2+ into ZnO nanoparticles-multi wall carbon nanotubes-poly methyl metacrylat nanocomposite film modified carbon paste electrode for determination of carbohydrates," Russian Journal of Electrochemistry 50(10), 967–973 (2014).
47. L. Fang, B. Liu, L. Liu, Y. Li, K. Huang, and Q. Zhang, "Direct electrochemistry of glucose oxidase immobilized on Au nanoparticles-functionalized 3D hierarchically ZnO nanostructures and its application to bioelectrochemical glucose sensor," Sensors and Actuators B: Chemical 222, 1096–1102 (2016).
48. X. Zhang, R. Zhang, A. Yang, Q. Wang, R. Kong, and F. Qu, "Aptamer based photoelectrochemical determination of tetracycline using a spindle-like ZnO-CdS@Au nanocomposite," Microchimica Acta 184(11), 4367–4374 (2017).
49. M. Kulkarni, A. Mazare, E. Gongadze, Š. Perutkova, V. Kralj-Iglič, I. Milošev, P. Schmuki, A. Iglič, and M. Mozetič, "Titanium nanostructures for biomedical applications," Nanotechnology 26(6), 062002 (2015).
50. R. Canaparo, F. Foglietta, T. Limongi, and L. Serpe, "Biomedical Applications of Reactive Oxygen Species Generation by Metal Nanoparticles," Materials 14(1), 53 (2020).
51. M. H. Nia, M. Rezaei-Tavirani, A. R. Nikoofar, H. Masoumi, R. Nasr, H. Hasanzadeh, M. Jadidi, and M. Shadnush, "Stabilizing and dispersing methods of TiO2 nanoparticles in biological studies," Journal of Paramedical Sciences 6(2), 96–105 (2015).
52. Z. Youssef, R. Vanderesse, L. Colombeau, F. Baros, T. Roques Carmes, C. Frochot, H. Wahab, J. Toufaily, T. Hamieh, S. Acherar, and A. M. Gazzali, "The application of titanium dioxide, zinc oxide, fullerene, and graphene nanoparticles in photodynamic therapy," Cancer Nanotechnology 8, 6 (2017).
53. D. Tan, S. Zhou, J. Qiu, and N. Khusro, "Preparation of functional nanomaterials with femtosecond laser ablation in solution," Journal of Photochemistry and Photobiology C: Photochemistry Reviews 17, 50–68 (2013).
54. M. S. S. Bharati, B. Chandu, and S. V. Rao, "Explosives sensing using Ag–Cu alloy nanoparticles synthesized by femtosecond laser ablation and irradiation," RSC Advances 9(3), 1517–1525 (2019).
55. T. Mosmann, "Rapid colorimetric assay for cellular growth and survival: Application to proliferation and cytotoxicity assays," Journal of Immunological Methods 65(1–2), 55–63 (1983).
56. C. M. Hoo, N. Starostin, P. West, and M. L. Mecartney, "A comparison of atomic force microscopy (AFM) and dynamic light scattering (DLS) methods to characterize nanoparticle size distributions," Journal of Nanoparticle Research 10, 89–96 (2008).
57. M. Kaasalainen, V. Aseyev, E. von Haartman, D. Ş. Karaman, E. Mäkilä, H. Tenhu, J. Rosenholm, and J. Salonen, "Size, Stability, and Porosity of Mesoporous Nanoparticles Characterized with Light Scattering," Nanoscale Research Letters 12(1), 74 (2017).
58. N. P. Truong, M. R. Whittaker, C. W. Mak, and T. P. Davis, "The importance of nanoparticle shape in cancer drug delivery," Expert Opinion on Drug Delivery 12(1), 129–142 (2015).
59. A. L. Popov, N. M. Zholobak, O. I. Balko, O. B. Balko, A. B. Shcherbakov, N. R. Popova, O. S. Ivanova-Polezhaeva, A. E. Baranchikov, and V. K. Ivanov, "Photo-induced toxicity of tungsten oxide photochromic nanoparticles," Journal of Photochemistry and Photobiology B: Biology 178, 395–403 (2018).
60. S. Chinde, N. Dumala, M. F. Rahman, S. S. K. Kamal, S. I. Kumari, M. Mahboob, and P. Grover, "Toxicological assessment of tungsten oxide nanoparticles in rats after acute oral exposure," Environmental Science and Pollution Research 24(15), 13576–13593 (2017).

61. A. L. Popov, B. Han, A. M. Ermakov, I. V. Savintseva, O. N. Ermakova, N. R. Popova, A. B. Shcherbakov, T. O. Shekunova, O. S. Ivanova-Polezhaeva, D. Kozlov, A. E. Baranchikov, and V. K. Ivanov, "PVP-stabilized tungsten oxide nanoparticles: pH sensitive anti-cancer platform with high cytotoxicity," Materials Science and Engineering: C 108, 110494 (2020).
62. Y. L. Gan, L. Wang, and R. P. Wang, "Creation of ZnS nanoparticles by laser ablation in water," Applied Physics A 122(104), 104 (2016).
63. A. J. Haltner, C. S. Oliver, "Effect of water vapor on friction of molybdenum disulfide," Industrial & Engineering Chemistry Fundamentals 5(3), 348–355 (1966).
64. F. Ye, D. Chang, A. Ayub, K. Ibrahim, A. Shahin, R. Karimi, S. Wettig, J. Sanderson, and K. P. Musselman, "Synthesis of two-dimensional plasmonic molybdenum oxide nanomaterials by femtosecond laser irradiation," Chemistry of Materials 33(12), 4510–4521 (2021).
65. F. Ye, A. Ayub, D. Chang, R. Chernikov, Q. Chen, R. Karimi, S. Wettig, J. Sanderson, and K. P. Musselman, "Molybdenum Blues with Tunable Light Absorption Synthesized by Femtosecond Laser Irradiation of Molybdenum Trioxide in Water/Ethanol Mixtures," Advanced Optical Materials 10(23), 2201304 (2022).
66. H. Wu, R. Yang, B. Song, Q. Han, J. Li, Yi. Zhang, Ya. Fang, R. Tenne, and C. Wang, "Biocompatible inorganic fullerene-like molybdenum disulfide nanoparticles produced by pulsed laser ablation in water," ACS Nano 5(2), 1276–1281 (2011).
67. J. M. George, A. Antony, and B. Mathew, "Metal oxide nanoparticles in electrochemical sensing and biosensing: a review," Microchimica Acta 185(7), 358 (2018).
68. C. Jin, Y. Tang, F. G. Yang, X. L. Li, S. Xu, X. Y. Fan, Y. Y. Huang, and Y. J. Yang, "Cellular toxicity of TiO2 nanoparticles in anatase and rutile crystal phase," Biological Trace Element Research 141(1), 3–15 (2011).
69. Y. V. Novakovskaya, "Theoretical estimation of the ionization potential of water in condensed phase. II. Superficial water layers," Protection of Metals 43(1), 22–33 (2007).
70. O. Dutuit, A. Tabche-Fouhaile, I. Nenner, H. Frohlich, and P. M. Guyon, "Photodissociation processes of water vapor below and above the ionization potential," The Journal of Chemical Physics 83(2), 584–596 (1985).
71. D. A. Kochuev, K. S. Khorkov, A. V. Ivashchenko, V. G. Prokoshev, and S. M. Arakelian, "Formation of microspheres under the action of femtosecond laser radiation on titanium samples in hydrocarbons," Journal of Physics: Conference Series 951(1), 012015 (2018).
72. D. A. Kochuev, K. S. Khorkov, D. V. Abramov, S. M. Arakelian, and V. G. Prokoshev, "Titanium-Carbide Formation in a Liquid Hydrocarbon Medium by Femtosecond Laser Irradiation," Journal of Surface Investigation: X-ray, Synchrotron and Neutron Techniques 12(6), 1220–1223 (2018).
73. D. A. Kochuev, A. S. Chernikov, R. V. Chkalov, A. V. Prokhorov, and K. S. Khorkov, "Deposition of GaN nanoparticles on the surface of a copper film under the action of electrostatic field during the femtosecond laser ablation synthesis in ammonia environment," Journal of Physics: Conference Series 2131(5), 052089 (2021).
74. A. S. Chernikov, D. A. Kochuev, R. V. Chkalov, A. V. Egorova, and D. G. Chkalova, "Ga2O3 and GaN nanoparticles synthesis by femtosecond laser ablation in ammonia environment," Proceedings of 2022 International Conference Laser Optics, 20–24 June 2022, Saint Petersburg, Russian Federation (2022).
75. A. Y. Gerasimenko, A. V. Kuksin, Y. P. Shaman, E. P. Kitsyuk, Y. O. Fedorova, A. V. Sysa, A. A. Pavlov, and O. E. Glukhova, "Electrically Conductive Networks from Hybrids of Carbon Nanotubes and Graphene Created by Laser Radiation," Nanomaterials 11(8), 1875 (2021).
76. M. S. Savelyev, A. Y. Gerasimenko, P. N. Vasilevsky, Y. O. Fedorova, T. Groth, G. N. Ten, and D. V. Telyshev, "Spectral analysis combined with nonlinear optical measurement of laser printed biopolymer composites comprising chitosan/SWCNT," Analytical Biochemistry 598, 113710 (2020).
77. A. Y. Gerasimenko, U. E. Kurilova, I. A. Suetina, M. V. Mezentseva, A. V. Zubko, M. I. Sekacheva, and O. E. Glukhova, "Laser Technology for the Formation of Bioelectronic Nanocomposites Based on Single-Walled Carbon Nanotubes and Proteins with Different Structures, Electrical Conductivity and Biocompatibility," Applied Sciences 11(17), 8036 (2021).
78. A. S. Chernikov, G. I. Tselikov, M. Y. Gubin, A. V. Shesterikov, K. S. Khorkov, A. V. Syuy, G. A. Ermolaev, I. S. Kazantsev, R. I. Romanov, A. M. Markeev, A. A. Popov, G. V. Tikhonowski, O. O. Kapitanova, D. A. Kochuev, A. Yu. Leksin, D. I. Tselikov, A. V. Arsenin, A. V. Kabashin, V. S. Volkov, and A. V. Prokhorov, "Tunable optical properties of transition metal dichalcogenide nanoparticles synthesized by femtosecond laser ablation and fragmentation," Journal of Materials Chemistry C 10 (2023).
79. L. Wang, Y. Li, L. Zhao, Z. Qi, J. Gou, S. Zhang, and J. Z. Zhang, "Recent advances in ultrathin two-dimensional materials and biomedical applications for reactive oxygen species generation and scavenging," Nanoscale 12(38), 19516–19535 (2020).
80. S. Kwiatkowski, B. Knap, D. Przystupski, J. Saczko, E. Kędzierska, K. Knap-Czop, J. Kotlińska, O. Michel, K. Kotowski, and J. Kulbacka, "Photodynamic therapy–mechanisms, photosensitizers and combinations," Biomedicine & Pharmacotherapy 106, 1098–1107 (2018).

81. J. L. Paris, A. Baeza, and M. Vallet-Regí, "Overcoming the stability, toxicity, and biodegradation challenges of tumor stimuli-responsive inorganic nanoparticles for delivery of cancer therapeutics," Expert Opinion on Drug Delivery 16(10), 1095–1112 (2019).
82. M. Sharifi, W. C. Cho, A. Ansariesfahani, R. Tarharoudi, H. Malekisarvar, S. Sari, S. H. Bloukh, Z. Edis, M. Amin, J. P. Gleghorn, T. L. M. ten Hagen, and M. Falahati, "An updated review on EPR-based solid tumor targeting nanocarriers for cancer treatment," Cancers 14(12), 2868 (2022).
83. T. Liu, C. Wang, X. Gu, H. Gong, L. Cheng, X. Shi, L. Feng, B. Sun, and Z. Liu, "Drug delivery with PEGylated MoS2 nano-sheets for combined photothermal and chemotherapy of cancer," Advanced Materials 26(21), 3433–3440 (2014).
84. I. Ocsoy, D. Tasdemir, S. Mazicioglu, C. Celik, A. Katı, and F. Ulgen, "Biomolecules incorporated metallic nanoparticles synthesis and their biomedical applications," Materials Letters 212, 45–50 (2018).
85. S. Wang, J. Zhao, H. Yang, C. Wu, F. Hu, H. Chang, G. Li, D. Ma, D. Zou, and M. Huang, "Bottom-up synthesis of WS2 nanosheets with synchronous surface modification for imaging guided tumor regression," Acta Biomaterialia 58, 442–454 (2017).

Diagnostics of Layer-by-Layer Biotissue Evaporation in the Process of Two-Coordinate Scanning by a Laser Beam for Precision Surgery

Alexander K. Dmitriev, Alexey N. Konovalov*, Vladimir N. Kortunov, and Valery A. Ulyanov
Institute of Photon Technologies of Federal Scientific Research Centre "Crystallography and Photonics" of the Russian Academy of Sciences, 2 Pionerskaya str., Moscow, Troitsk 108840, Russia

***e-mail:** ank27.ift@mail.ru

Abstract. The use of automated and robotic systems for precision low-traumatic surgery is a common trend in modern medicine. One of the promising tools for such operations is an automated laser scalpel based on a scanner with real-time diagnostics of the process of biotissue evaporation. The paper investigates the possibility of operational Doppler diagnostics of layer-by-layer laser evaporation of biomodels. A surgical CO_2 laser with a two-coordinate scanning system was used as a scalpel. The method of autodyne detection of backscattered radiation coming from the laser action zone was used to diagnose the evaporation process. Samples based on Difco agar with different water content and various tissues of pigs *in vitro* were used as biomodels. The depth of evaporation, the zone of thermal damage of the samples, and the dynamics of the autodyne signal were studied depending on the scanning modes and parameters of laser radiation. It has been shown that the autodyne signal arising from the layer-by-layer evaporation of samples is sensitive to the water content of biomodels and the structural features of the tissue. Autodyne diagnostics of layer-by-layer laser scanning makes it possible to control the evaporation process of biotissue of the same type and to determine the boundaries between tissues of different types both in the scanning plane and in the tissue depth. The obtained results can be used in the developing technologies for automated laser layer-by-layer evaporation of biological tissues in relation to the precision low-traumatic surgery tasks.
© 2023 Journal of Biomedical Photonics & Engineering.

Keywords: robotic surgery; CO_2 laser; automated feedback; autodyne diagnostics; XY scanner; automated biotissue evaporation.

Paper #3585 received 17 Jan 2023; revised manuscript received 29 May 2023; accepted for publication 29 May 2023; published online 2 Jun 2023. doi: 10.18287/JBPE23.09.020302.

1 Introduction

The use of automated and robotic systems in surgery is a modern trend in developing and improving medical technologies [1]. This approach is based on objective monitoring of the surgical intervention process in real time, which reduces the risks of the human factor and enables fast postoperative rehabilitation of patients. Currently, surgical systems of this kind are mainly based on the tactile feedback from the surgeon and various methods of visualizing the surgical field [2].

Laser radiation as a surgical manipulation instrument has such advantages as low invasiveness and traumatization of healthy tissues, high accuracy and fast removal of pathological tissues. These advantages can be fully exhibited when laser radiation is used as part of automated and robotic systems. However, one of the disadvantages that limits the surgical use of lasers is the lack of tactile feedback during laser intervention [3]. When performing laser surgery with penetration deep into the tissue, the surgeon is not able to receive

information about the actual depth of evaporation or about the underlying tissue type. In this regard, some sensors are needed that would allow the surgeon to obtain objective information about the course of laser surgical intervention in real time.

To receive feedback for single-mode surgical CO_2 lasers, we propose to use the self-mixing effect (autodyne effect) that occurs when radiation is exposed to condensed media, in particular, to biological tissues [4]. The effect is that the radiation backscattered from an external moving object enters the laser cavity and initiates modulation of the output power (autodyne signal) at the Doppler frequency. The autodyne signal is a source of operational information about the course of laser biotissue evaporation and thus serves as kind of a "sensor" for organizing feedback in intelligent surgical devices. The proposed operational diagnostics of the processes of laser evaporation of biological tissues consists in identifying differences in the amplitude-frequency characteristics of the autodyne signal that occurs when exposed to tissues of different types. We have shown the potential of this approach for monitoring and controlling the process of biotissue laser evaporation based on commercial single-mode CO_2 lasers with pulsed-periodic (PP) pumping of the active medium [5, 6].

Surgical devices based on PP single-mode CO_2 lasers with scanning systems are widely used for treating various skin lesions and high-precision removal of superficial neoplasms providing automated layered laser evaporation of the affected biological tissue [7, 8]. In general, these devices are used for laser resurfacing, removal of skin lesions and mucous membranes, which is considered the "gold standard" in dermatological surgery [9]. Currently, the quality control of laser operation with scanning systems is carried out both by setting the parameters of automated evaporation (the shape and area of the evaporated tissue, the stepwise depth of its evaporation) visually and by using video control [7, 10]. In particular, when selecting modes for precision laser cuts of a certain depth, it is proposed [11] to use an experimental database containing the results obtained from model biomaterials. Although this approach makes it possible to implement precision low-traumatic and organ-saving laser surgical interventions, at present there is no possibility to obtain objective information on the course of laser surgery in real time, in particular, to determine the boundaries and the depth of the evaporated tissue.

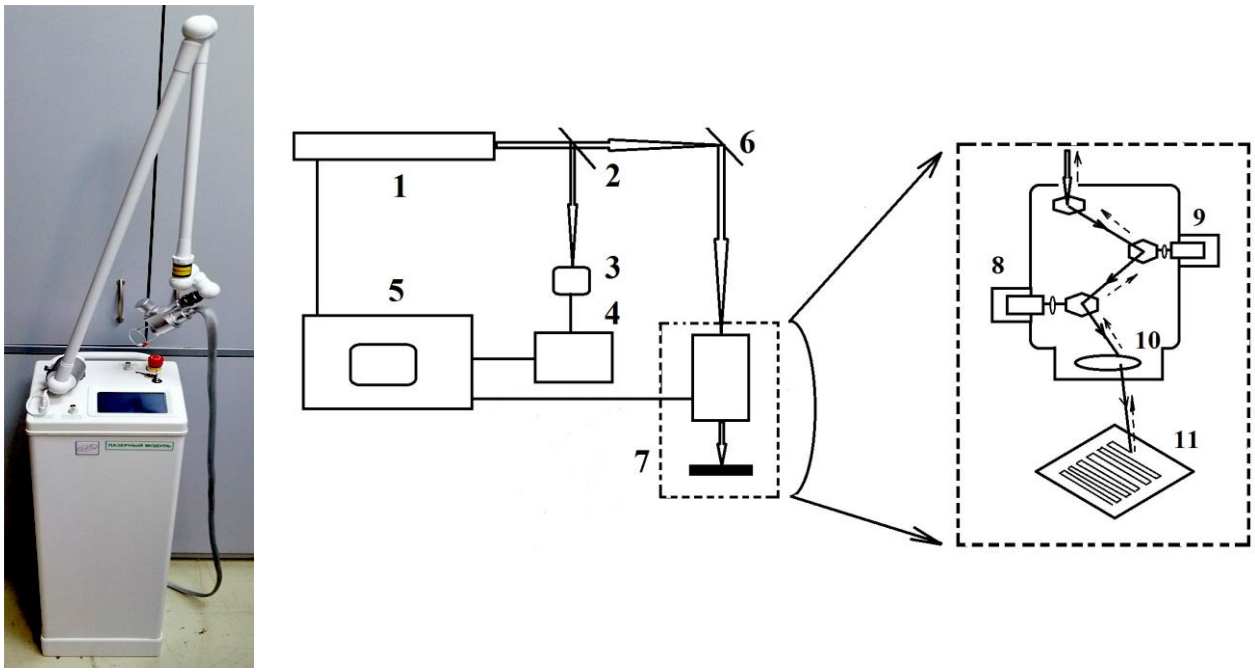
On the basis of the *in vitro* and *in vivo* experiments performed on different types of biological tissues of both animals and humans, we have revealed that the spectral characteristics of the autodyne signal change when the laser beam passes from one type of tissue to another during laser evaporation [12]. These changes are caused by a variance in the characteristics of the Doppler backscatter signal coming from the laser impact zone on different tissues. The Doppler signal is determined by a combination of laser-induced dynamic processes in the zone of laser evaporation of biotissue and depends on both the structural features of the biological tissue and on the parameters of laser action. The use of the autodyne effect makes it possible to perform real-time differential diagnostics of the evaporated biotissue type for surgical CO_2 lasers, that is, to distinguish the tissues differing from each other by the magnitude of the autodyne signal at the same parameters of laser action.

The use of scanning systems with feedback presents new opportunities for creating robotic surgical laser systems for the tasks of precision low-traumatic surgery. A peculiar characteristic of this approach lies in the fact that during the process of layer-by-layer tissue evaporation using laser beam scanning, it is necessary to identify both the boundary between the tissues in the scanning plane and the boundary between tissues by depth. In this case the laser beam repeatedly passes through the previously evaporated zone with a gradual deepening of the beam. This paper presents the results of the study of the autodyne diagnostics possibility for the process of automated laser layer-by-layer evaporation of tissues using a scanning system.

2 Methods and Materials

For automated surface laser evaporation of biomodels we used a setup consisting of a laser unit, an articulated-mirror manipulator and a JS1105 Galvo Scanner 2-coordinate galvanic scanner (Sino-Galvo Technology Co., China) docked with it (Fig. 1a) [6]. The setup is based on the C20A single-mode pulse-periodic CO_2 laser (Coherent, USA) with a power up to 20 W. It allows precision evaporation and dissection of biotissue with simultaneous real-time recording the autodyne signal generated by the CO_2 laser. The autodyne control scheme of the biotissue evaporation process is shown in Fig. 1b. The backscattered radiation from the laser evaporation zone hits the mirrors of the 2-coordinate scanner, then it is directed through the system of mirrors of the articulated-mirror manipulator to the CO_2 laser resonator and initiates modulation of the output radiation power (the autodyne signal) at the Doppler frequency. Part of laser radiation is diverted by the beam splitter to a fast IR photodetector. The signal from the photodetector routed through the ADC is fed to the computer that processes and retrieves the information component of the autodyne signal and controls the operation of the scanner.

The scanner control unit and the specially developed software make it possible to set any shape of the evaporation area within 20 mm × 20 mm, the speed of the laser beam within 1–50 mm/s, and the required filling density of the evaporated surface by laser hatching. The surface scanning area is a set of parallel lines (hereinafter, hatching lines). The width of these lines corresponds to the diameter of the focal spot. During the experiments the degree of overlap of the hatching lines was varied. To obtain a certain depth of the evaporated area, multiple laser scanning of this area of the biomodel was carried out. The dimensions of the laser beam and the distribution of the laser radiation intensity were determined with a NanoScan2s Pyro/9/5 laser beam profile analyzer (Ophir-Optronics, Israel).



(a) (b)

Fig. 1 The setup for automated surface laser evaporation of biomodels (a) and a schematic diagram of autodyne detection of backscattered radiation (b): (1) CO_2 laser, (2) beam splitter, (3) HgCdTe photodetector, (4) ADC, (5) PC, (6) mirror, (7) galvanic scanner, (8) X-axis scanning, (9) Y-axis scanning, (10) lens, and (11) biomodel.

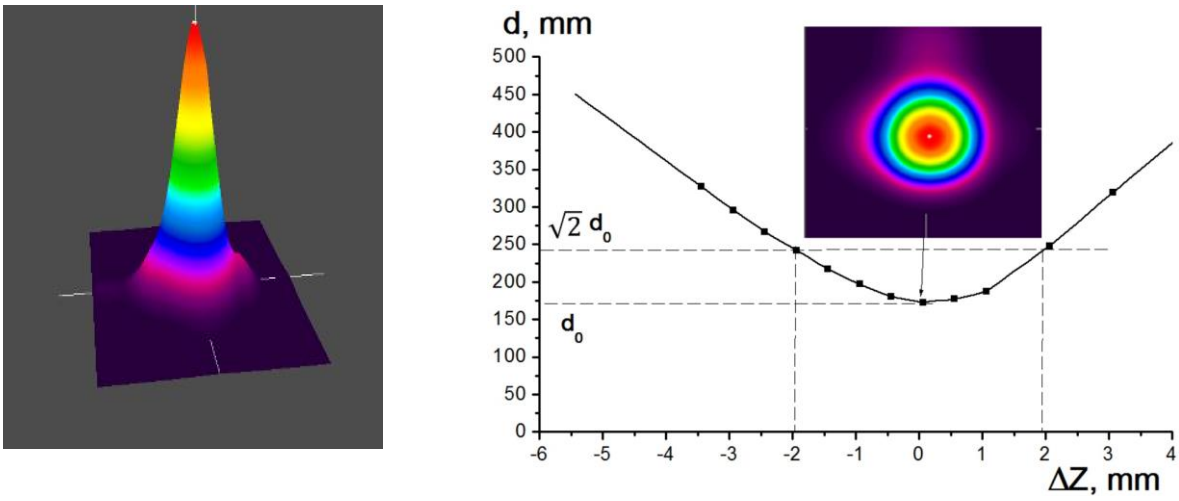
As biomodels, the samples based on Difco agar and various pig tissues *in vitro* were used: cardiac muscle, skin area with fat tissue (obtained from the abdominal part of the animal), and a fragment of the pig auricle. The cardiac muscle is a three-dimensional structure of densely packed muscle fibers [13] with water content of 79% [14]. The "skin-fat" sample consisted of the sequentially arranged skin (including epidermis and dermis) and fat tissue with water content of 69% [14]. Fat is a collection of fat cells with a central fat droplet (globule) surrounded by cytoplasm [13] with water content of 20–40% [15]. The fragment of the auricle contained a cartilaginous plate covered with skin on both sides with no fat tissue under the skin of the auricle. Cartilage is a three-dimensional structure of collagen fibers and proteoglycan molecules [13] with water content of 80% [14]. The size of the samples was 15 × 15 mm. The thicknesses of the biomodel layers are indicated in the description of the experimental results. The studies were carried out on pig tissues obtained from a butchery. Each tissue sample that was used in this study was less than 48 h *post mortem*. The samples were stored at a temperature of 0–4 °C at constant humidity. Samples for experiments utilizing agar were prepared with a mass agar fraction between 5% and 15%. Such samples simulated soft tissues with a high water content. Cross sections of biomodels after scanning were studied under a microscope, for which a sample was cut in a direction perpendicular to the direction of beam motion.

In experiments on automated evaporation of the surface of biomodels, a 8.5 mm × 11.6 mm rectangular area was scanned by means of a lens with a focal length of 50 mm. The radiation was focused on the biomodel surface. The position of the focal spot remained unchanged during multiple scanning. In the experiments, the exposure and scanning modes were changed: the power of laser radiation (3–5 W), the speed of the laser beam (from 2 mm/s to 30 mm/s), and the density of hatching lines. The evaporation depth of the biomodel surface was several millimeters.

Processing the autodyne signal during laser scanning was carried out using a special algorithm for extracting the informational Doppler component described in Ref. [16]. The signal power Ps in the selected frequency range was used as an information parameter of the autodyne signal.

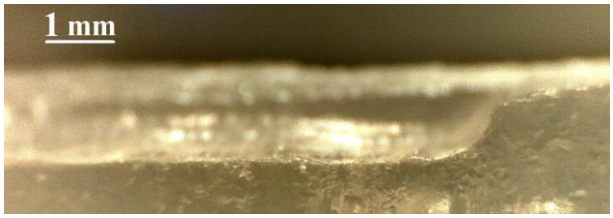
3 Results and Discussion

The use of autodyne detection of backscattered radiation imposes excessive requirements on the quality of operational laser radiation [5]. The profile of the laser beam was measured directly at the exit from the laser, whereas in the operating field it was measured in the scanning plane. The measurements show that the radiation at an output power of 3–20 W is a single spatial mode with an intensity distribution close to the Gaussian profile. Fig. 2a shows the distribution of radiation intensity at the laser exit at the radiation power of 6 W. The beam diameter (at the level of 13.5% along the X axis) was 2.3 mm, the difference from the Gaussian distribution (calculated using the Least Squares Fit method) along the X axis was 0.955. After passing through the setup optical system, the articulated-mirror manipulator, and the optical path of the scanner with a 50-mm focal length lens, the laser beam in the scanning plane retains the Gaussian profile (Fig. 2b).

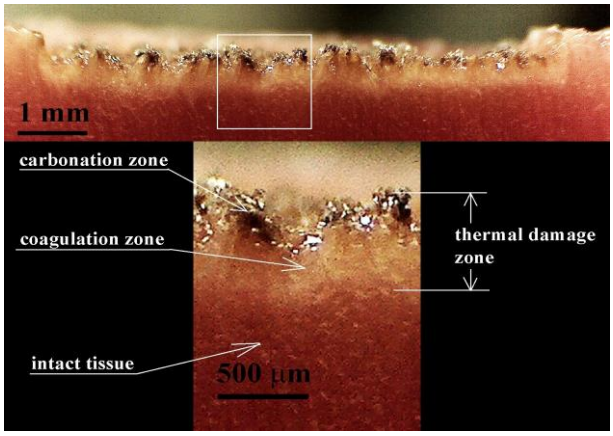


(a) (b)

Fig. 2 Distribution of laser radiation intensity in the focal spot in the scanning plane (a) and relationship between the laser beam diameter d and the ΔZ distance from the focal plane of the lens (b). The focal length of the lens is 50 mm.



(a)



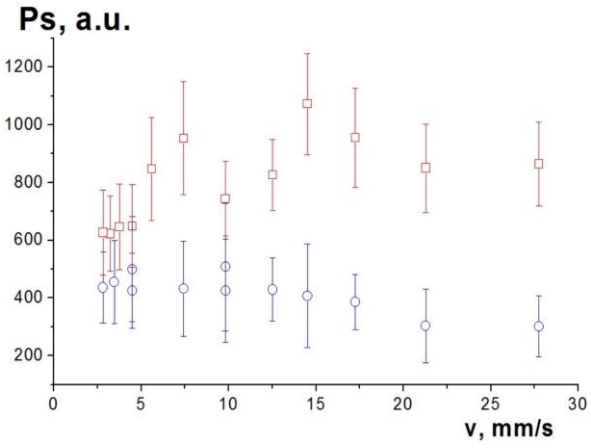
(b)

Fig. 3 Cross section of the evaporated zone of biomodels based on agar (a) and *in vitro* pig heart muscle (b) in different modes of a single scanning: a) power is 4 W, scanning speed is 18 mm/s, distance between hatching lines is 160 μm; b) power is 3.2 W, scanning speed is 12 mm/s, distance between hatching lines is 80 μm.

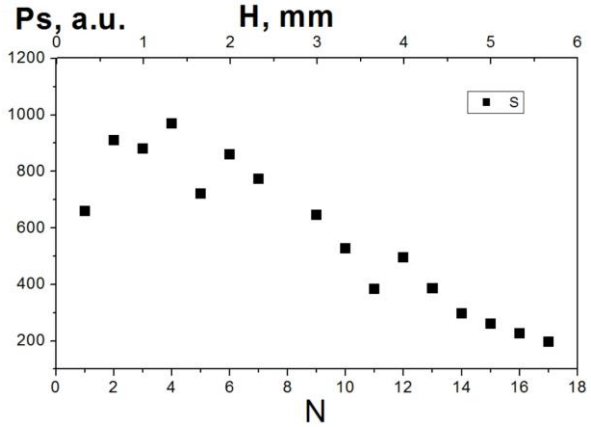
The beam diameter at the focus (along the X axis) is 175 μm, the difference from the Gaussian distribution along this axis was 0.984. Fig. 2b shows the relationship between the focused beam diameter and the distance from the focal plane of the scanner lens. The diameter of the laser beam at the distance of ±2 mm from the focal plane of the lens changes by a factor of 1.4 (correspondingly, the radiation power density changes by a factor of 2).

During laser scanning, the biomaterial evaporates to a certain depth, specified by the scanning conditions. In this case, the underlying layer of the sample is heated, which can lead to partial melting of the sample material (in the case of biomodels based on agar), or to thermal damage and changes in the properties of the underlying layer (for the case of biomodels based on the *in vitro* biotissues, see Fig. 3). The thermal damage zone (TDZ) of the tissue includes carbonization and coagulation zones (Fig. 3b). The TDZ depth was measured as the distance between the surface of the evaporated tissue and the boundary of the coagulation zone, which is visually observed as the tissue of a lighter shade. This color is the result of coagulation of tissue proteins when heated to a temperature of 70 °C [17]. With the help of a digital microscope, the TDZ depth of pig myocardial tissue was measured after single and multiple scans. It was found that at the laser radiation power of 3.5 W and the scanning speed of 10 mm/s, even a single scan leads to the tissue thermal damage to a depth of 250–300 μm. After four scans (four successive scans of the same area of the sample surface), the TDZ depth was 650–700 μm.

The peculiarities of the autodyne signal were studied in terms of the scanning speed and the number of scans of the same biomodel surface area (multiple scans). Fig. 4a shows the relationship between the power of the autodyne signal and the scanning speed for a single action to the surface of 5% and 15% agar samples. It can be seen that the power of the autodyne signal differs markedly for samples with different agar content, which allows for biotissue differential diagnostics with different water content. It is quite probable that the greater value of the signal for samples with 15% agar content is due to the fact that larger particles are formed due to microexplosions during laser exposure and are removed from the active surgery zone. During multiple laser scanning of the surface area, the sample surface is displaced relative to the focal plane of the laser beam.



(a)



(b)

Fig. 4 Relationship between the power of the autodyne signal and the scanning speed (a) and the number of scans during evaporation of the surface of agar samples; a) blue circle ○ is 5% agar; red square □ is 15% agar; b) scanning speed 10 mm/s, black filled square ■ is 15% agar. Radiation power P = 3.5 W, the distance between hatching lines is 480 μm.

Therefore, the autodyne signal may vary depending on the number of scans. Fig. 4b shows the relationship between the power of the autodyne signal, the N number of scans and evaporation of the sample surface of 15% agar. This figure also shows the distance scale H from the focal plane (or from the initial sample surface) to the sample surface after scanning. The scale was calculated assuming that a 450 μm thick layer is removed in one scan under the given action conditions. As follows from the figure, during multiple scans, a gradual decrease in the power of the autodyne signal occurs. This is due to the fact that the surface leaves the focal plane of the scanner lens. This is in agreement with the size of the caustic at the focus of the scanner lens (see Fig. 2b).

Fig. 5 shows the change in the average value of the autodyne signal power during multiple laser scans of the surface of the heart muscle sample. An increase in the autodyne signal is observed during the transition from a "fresh" tissue area (Scan 1) to subsequent scanning of the surface areas subjected to thermal effects of laser radiation and containing TDZ (see Fig. 3b).

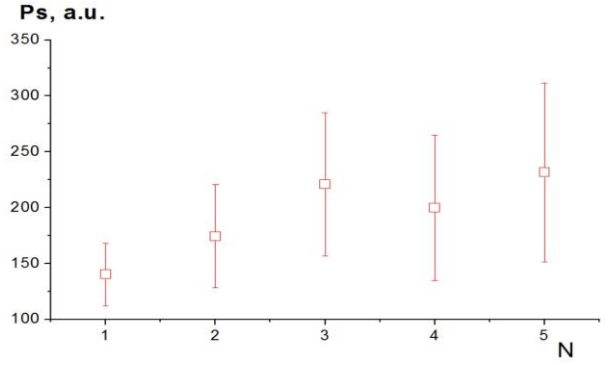


Fig. 5 The power of the autodyne signal during the evaporation of the surface of pig heart muscle *in vitro* depending on the number of scans. P = 3.5 W, v = 10 mm/s, the distance between hatching lines is 480 μm.

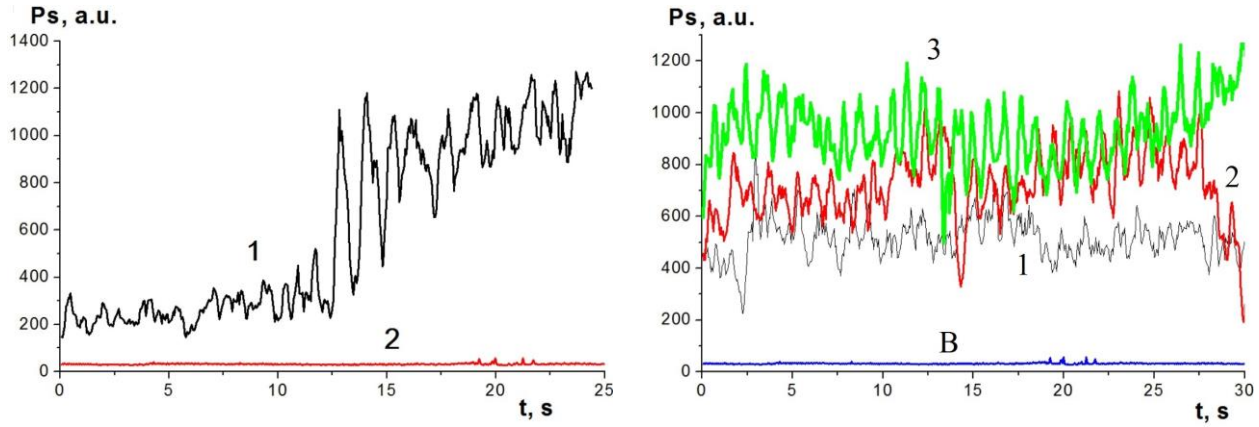
The possibility of diagnosing both the lateral boundary and the depth boundary between different tissues was investigated using two-layer biomodels based on agar. The samples with 5% and 15% agar content were used for modeling soft biotissues with different water content. In the first case, the samples connected in series were used. The samples were arranged in such a way that the direction of the hatching lines during scanning and the boundary between the samples were close to parallel. Fig. 6a shows the dynamics of the autodyne signal power during the evaporation of the combined sample.

It can be seen that when the laser radiation passes from 5% to 15% of the sample (from left to right), the signal increases. Moreover, transition from one signal level to another occurs in the form of oscillations. This is due to the fact that the direction of the hatching lines does not completely coincide with the boundary line between the samples, and the laser beam passes several times from one sample to another.

Fig. 6b shows the simulation of layer-by-layer laser evaporation of a two-layer 1.4 mm thick structure consisting of 5% agar located on a 15% agar sample. As follows from the Fig. 6b, the level of the autodyne signal in Scan 2 is greater than that in Scan 1 and smaller than that the Scan 3 because Scan 2 evaporates the remainder of the first layer and captures the underlying second layer of the sample with 15% agar content.

To simulate a situation close to a real surgical intervention, *in vitro* pig tissue samples were used. Fig. 7 shows the change of the autodyne signal during layer-by-layer scanning of a sample containing the 1–1.5 mm thick upper layer of the skin, under which the fat tissue was located. A noticeable increase in the autodyne signal occurs at the transition from the skin (Scan 1) to the layer of fat tissue (Scan 2). During Scan 1, the skin layer was not completely removed in some areas. The next pass captures both areas of exclusively fat tissue and areas with the skin remnants, which is reflected in the autodyne signal power.

Another example is layer-by-layer laser evaporation of the biomodel surface based on pig auricle.



(a) (b)

Fig. 6 Dynamics of the autodyne signal power during laser scanning of combined agar samples. P = 3.0 W, the distance between hatching lines is 325 μm. (a) Single scanning of serially connected (from left to right) 5% and 15% agar samples. Scanning speed is 12.5 mm/s. (1) Autodyne signal power, (2) noise. (b) Layered scanning of a 5% agar sample located on a 15% sample. The scanning speed is 10 mm/s. (1) – (3) are scan numbers; (B) is noise.

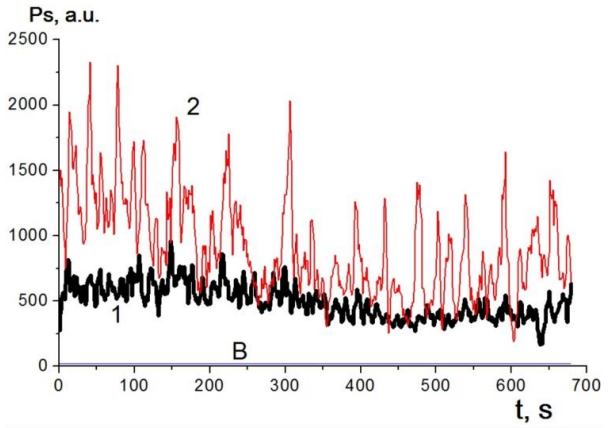


Fig. 7 Relationship between the autodyne signal power and time during layer-by-layer laser scanning of the "skin-fat tissue" biomodel. P = 4.5 W, scanning speed is 10 mm/s. Scan 1 is skin, Scan 2 is fat tissue, B is noise.

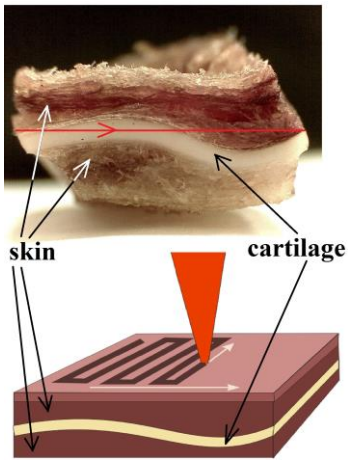


Fig. 8 Biomodel based on pig auricle. (a) Photo of pig auricle section. The red line shows the scanning plane (Scan 4, Fig. 9), the scanning direction is from left to right. (b) Schematic diagram of the process of scanning the laser beam on the biomodel surface.

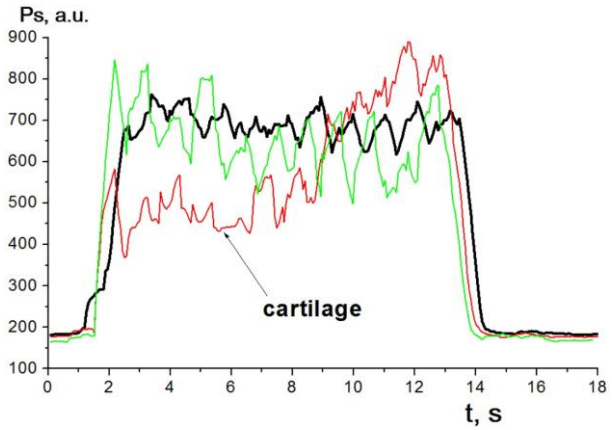


Fig. 9 Relationship between the power of the autodyne signal and the scanning time (the pig auricle segment in Fig. 8). P = 5 W, the scanning speed is 10 mm/s. Scan 1 (black) is skin, Scan 4 (red) is skin and cartilage tissue, Scan 8 (green) is skin.

The model consists of several consecutive layers (Fig. 8): skin (1.0–1.8 mm thickness), cartilage (0.7–0.8 mm) and skin (1.2–1.8 mm) The change in the autodyne signal power as a function of time during layer-by-layer scanning of this biomodel is shown in Fig. 9. This model is characterized by a curvature of the cartilage tissue layer. Scan 1 captures only the superficial area of the skin. The level of the autodyne signal determines the process of skin evaporation. Scan 4 captures both the skin and the cartilage areas. Accordingly, the area of cartilage evaporation is characterized by a significantly lower level of the autodyne signal. During Pass 8, the laser beam again vaporizes only the skin and the level of the autodyne signal becomes high as in Pass 1.

Previously [12], we showed that the differences in the nature of laser evaporation of biotissues are due to their structural peculiarities, content and distribution of interstitial water. The specificity of the Doppler spectra depends on the type of biotissue which is largely due to

the characteristics of the tissue destruction products. The size, shape, and other characteristics of the destruction products arising from the laser impact zone are largely determined by the structure features of the original biological tissue, in particular, when exposed to fat tissue, the destruction products consist of relatively large fat drops, whereas when exposed to the muscle tissue, they contain fibers. The combination of these factors and the difference in the optical and physical characteristics of different tissues lead to the differences in the Doppler backscatter signal, which makes it possible to carry out differential diagnossis of the evaporated tissue types in real time.

4 Conclusions

The study has demonstrated the possibilities of autodyne diagnosing for automated laser layer-by-layer evaporation of various biomodels based on a scanning system. The specific features of the autodyne signal were examined according to the following characteristics: the CO_2 laser radiation power, the scanning speed during single and multiple surface scans of the biomodels based on agar with different water content and biotissues of pigs *in vitro*. It has been shown that in the process of layer-by-layer laser scanning, autodyne diagnostics makes it possible to control the evaporation process of the same type of biotissue and to determine the boundaries between biotissues of different types both in the scanning plane and in the depth of the biotissue. The obtained results can be used for developing new technologies for automated laser layer-by-layer tissue evaporation as applied to the tasks of high-precision low-traumatic surgery.

This work was performed within the State assignment of Federal Scientific Research Center “Crystallography and Photonics” of Russian Academy of Sciences.

Disclosures

The authors have no relevant financial interest in this article and no conflict of interest to disclose.

References

1. G. Maza, A. Sharma, “Past, Present, and Future of Robotic Surgery,” Otolaryngologic Clinics of North America 53(6), 935–941 (2020).
2. Y.-Y. Juo, A. Abiri, J. Pensa, S. Sun, A. Tao, J. Bisley, W. Grundfest, and E. Dutson, “Center for Advanced Surgical and Interventional Technology Multimodal Haptic Feedback for Robotic Surgery,” Chapter 17 in Handbook of Robotic and Image-Guided Surgery, M. H. Abedin-Nasab (Ed.), Elsevier, 285-301 (2020). ISBN 9780128142455.
3. F. W. Neukam, F. Stelzle, “Laser tumor treatment in oral and maxillofacial surgery,” Physics Procedia 5, 91–100 (2010).
4. A. N. Konovalov, V.A. Ul’yanov, “Self-mixing detection of backscattered radiation in single-mode pulse-periodic CO_2 lasers,” Applied Optics 51(17), 3900–3906 (2012).
5. A. K. Dmitriev, A. N. Konovalov, V. N. Kortunov, and V. A. Ulyanov, “Possibilities for organizing feedback on the Doppler backscattering signal in surgical CO_2 lasers,” Journal of Laser Applications 32, 022073 (2020).
6. A. K. Dmitriev, A. N. Konovalov, V. N. Kortunov, and V. A. Ulyanov, “An Apparatus Based on a CO_2 -Laser with Feedback for Automated Precision Evaporation of Biological Tissues,” Instruments and Experimental Techniques 65, 332–335 (2022).
7. R. Colasanti, L. Giannoni, S. Dallar, V. Liverotti, D. Aiudi, A. Di Rienzo, F. Rossi, and M. Iacoangeli, “Application of a Scanner-Assisted Carbon Dioxide Laser System for Neurosurgery,” World Neurosurgery 153, e250–e258 (2021).
8. A. R. Padalhin, “Lasers and Robots: Recent Developments in Transoral Laser and Transoral Robotic Surgery,” Medical Lasers; Engineering, Basic Research, and Clinical Application 9(2), 103 (2020).
9. A. Aslam, T. S. Alster, “Evolution of Laser Skin Resurfacing: From Scanning to Fractional Technology,” Dermatologic Surgery 40(11), 1163–1172 (2014).
10. G. Dagnino, L. S. Mattos, and D. G. Caldwell, “A vision-based system for fast and accurate laser scanning in robot-assisted phonomicrosurgery,” International Journal of Computer Assisted Radiology and Surgery 10, 217–229 (2015).
11. A. Acemoglu, L. Fichera, I. E. Kepiro, D. G. Caldwell, and L. S. Mattos, “Laser Incision Depth Control in Robot-Assisted Soft Tissue Microsurgery,” Journal of Medical Robotics Research 2(03), 1740006 (2017).
12. A. K. Dmitriev, A. N. Konovalov, V. N. Kortunov, and V.A. Ulyanov, “Doppler diagnostics of laser evaporation of biological tissues,” Journal of Laser Applications 34(4), 041201 (2022).
13. D. J. Taylor, N. P. O. Green, and G. W. Stout, Biological Science, vol. 1, 2nd ed., R. Soper (Ed.), Cambridge University Press, Cambridge (1990).
14. J. T. Walsh, T. F. Deutsch, “Pulsed CO_2 laser ablation of tissue: effect of mechanical properties,” IEEE Transactions on Biomedical Engineering 36(12), 1195–1201 (1989).
15. E. V. Ross, Y. Domankevitz, and R. R. Anderson, “Effects of heterogeneous absorption of laser radiation in biotissue ablation: characterization of ablation of fat with a pulsed CO_2 laser,” Lasers in Surgery and Medicine 21(1), 59–64 (1997).

16. A. Konovalov, V. Ulyanov, "Extraction of the Information Component of the Autodyne Signal in Pulsed-periodic CO_2 Lasers for Doppler Diagnostics of the Surgical Process," Advanced Biomedical Engineering 10, 129–137 (2021).
17. G. Muller, K. Dorschel, and H. Kar, "Biophysics of photoablation process," Lasers in Medical Science 6, 241–254 (1991).

Bilirubin- and Blue-Green Light-Induced Damage of Human Erythrocytes

Julia V. Kruchenok*, Olga N. Dudinova, and Vitaly Y. Plavskii
B.I. Stepanov Institute of Physics of the National Academy of Sciences of Belarus, 68-2 Nezavisimosti ave., Minsk 220072, Republic of Belarus

***e-mail:** j.kruchenok@ifanbel.bas-net.by

Abstract. Phototherapy is widely used for neonatal hyperbilirubinemia treatment; however, the most important but not completely recognized issue is the determination of the optimal spectral range of light that provides an effective reduction of bilirubin level in the blood of a newborn with minimal adverse side effects. This study demonstrates that the exposure of radiation from LED sources of blue (emission wavelength λ_{max} = 463 nm, FWHM 20 nm) and green (λ_{max} = 517 nm, FWHM 38 nm) spectral regions to the erythrocyte suspension with the same energy dose (D = 14.4 J/cm^2) leads to approximately equally effective hemolysis of erythrocytes. It is concluded that the damage of erythrocyte membranes is caused by the excitation of endogenous porphyrin and flavin photosensitizers contained in the cells in low concentrations, but characterized by high efficiency of singlet oxygen generation. When bilirubin is added to the erythrocyte suspension, a spontaneous (dark) erythrocyte hemolysis intensifies, but the light-induced hemolysis slows down (compared to cells containing no bilirubin). Under the same conditions, the leakage of potassium ions from light-exposed erythrocytes is accelerating, with the light of green spectral region has a more pronounced effect, despite more intense absorption of blue light by bilirubin localized in cells. © 2023 Journal of Biomedical Photonics & Engineering.

Keywords: hyperbilirubinemia; phototherapy; blue LED radiation; green LED radiation; photohemolysis; potassium leakage; human erythrocyte membrane; protoporphyrin IX; Zn-protoporphyrin IX.

Paper #8188 received 28 Feb 2023; revised manuscript received 25 May 2023; accepted for publication 25 May 2023; published online 9 Jun 2023. doi: 10.18287/JBPE23.09.020303.

1 Introduction

The interest to the investigation of possible photodamage of biological systems of various structural levels treated with bilirubin is due to the widespread use of optical technologies for the treatment of hyperbilirubinemia (jaundice) in newborn children [1–6]. As it is known, this disease is caused by the excessive accumulation in the child's body of the bile pigment – Z,Z-bilirubin IXα, which at its high concentrations can effect negatively the health of the newborn. The main and in fact the only method of reduction of bilirubin levels during the jaundice is phototherapy, based on exposure of child's body surface with light of the blue-green spectral range corresponding to the pigment absorption spectrum [1–6]. On light quanta absorption, Z,Z-bilirubin IXα molecule undergoes a number of configuration and structural transformations into photoisomers, that have greater hydrophilicity compared to native bilirubin, and are characterized by a higher excretion rate.

However, despite more than 60 years of history of the use of light for the treatment of hyperbilirubinemia (despite of the use of light for hyperbilirubinemia treatment for more than 60-years), many issues related to the practical implementation of phototherapy technologies are far from being understood. One of the most important but not fully clarified issues is to determine the optimal wavelength of light for hyperbilirubinemia phototherapy. Another fundamental issue is connected to adverse side effects from

phototherapy and their dependence on the spectral range of the incident radiation. For a long time it was believed that the optimal spectral range for phototherapy should correspond to the maximum of absorption spectrum of bilirubin bound to serum albumin $\lambda_{max} \approx 460$ nm [5]. However, in recent years, quite a lot of data has appeared [6–12] that the light of green spectral region corresponding to the long-wavelength slope of the absorption band of the bilirubin-albumin complex is no less effective than blue light, or even surpasses it.

The long-time experience in using blue light for the treatment of neonatal hyperbilirubinemia has shown that no serious adverse side effects are mostly observed during phototherapy in clinical conditions. However, there is a strong opinion that phototherapy cannot be completely harmless, and it should be used carefully, not exceeding certain recommended light intensities; minimization of phototherapeutic effects is advised [1, 4]. The need to comply with certain restrictive measures during phototherapy is stipulated by some literature data [13–15] giving information that phototherapy implementation in newborns with extremely low body weight (less than 750 g) aggravates the condition of the infant and may be fatal. In addition, there is data about a higher risk of future development of cancer [16–19] and epilepsy [20] of those children who have previously had neonatal phototherapy. Sometimes there are undesirable processes in the newborn's body (bronze baby syndrome, hypocalcemia, dehydration, DNA damage, allergic reactions in the form of asthma attacks, rashes on the body), manifested directly during or after the phototherapy [1, 3, 4, 21, 22]. It is believed that some of them may be caused by the sensitizing effect of bilirubin and its photoisomers [23–26]. There are numerous data on the photocytotoxicity of bilirubin and its structural photoisomer lumirubin against cells of various body tissues [25–30] and, in particular, blood cells [31–34]. At the same time, it has been repeatedly suggested in the literature [22, 23, 27, 28, 35, 36] that the transition from light sources of the blue spectral range to sources of the green spectral range will help not only effectively reduce the level of bilirubin in the blood of newborns, but also reduce adverse side effects of phototherapy. However, there are practically no comparative studies of the adverse side effects upon exposure of blood cells treated with bilirubin to light of the blue and green spectral regions. Such studies are becoming especially relevant because of switching to LED sources of blue-green or green spectral regions in phototherapy equipment for the treatment of neonatal jaundice [1–4, 36], and also in connection with the revealed dependence of the efficiency of the formation of configuration and structural bilirubin photoisomers on the wavelength of exciting light [37–39]. The reason for the variation in the quantum yield of photoisomers formation with a change of the excitation wavelength is the bichromophoric nature of the absorption and emission of light by bilirubin molecules and the dependence of intramolecular distribution of the excitation energy between two asymmetric tetrapyrrole chromophores on the quantum energy [40, 41].

The purpose of this work is comparative *in vitro* studies of the effectiveness of human erythrocytes damage upon exposure to radiation of LED sources with the same intensity in blue and green spectral regions (promising for reduction of bilirubin levels in newborns with hyperbilirubinemia syndrome) at a bilirubin concentration suggesting phototherapy in infants. The choice of erythrocytes is specified by the known data of previous studies [31–34, 42–44], which identified the erythrocyte membrane as the main target of photocytotoxicity during sensitization with bilirubin. Moreover, in Ref. [45] we demonstrated the ability of low-intensity optical radiation of visible spectral region to have a modifying effect on erythrocyte membranes even in the absence of exogenous bilirubin.

2 Materials and Methods

Saline and buffered solutions were prepared from sodium-phosphate salts produced by Merck (Merck, extra pure, p.a.) on distilled water. Bilirubin produced by "Reakchim" SRPA Biolar high purity grade (Russia) and bilirubin produced by "Fluka" (Germany) with no additional purification were used in the work. The purity of the substances was ≥ 98.5%. The bilirubin solution was prepared according to the standard procedure: 2.5 mg of bilirubin were dissolved in 200 μl of 0.05 M NaOH (due to its very low solubility in water at physiological pH values). At calculation of bilirubin concentrations, the molar extinction coefficient $\varepsilon_{440} = 4.75 \cdot 10^4$ $M^{-1} \cdot cm^{-1}$ [41] was assumed.

For preparation of the bilirubin-albumin solution complex, human serum albumin produced by Sigma, USA, fraction V, degree of purification about 99% was used. At calculation of the components concentrations, the following values of molar extinction coefficients were used: bilirubin within the HSA complex $\varepsilon_{460} = 4.70 \cdot 10^4$ $M^{-1} \cdot cm^{-1}$, HSA $\varepsilon_{280} = 3.55 \cdot 10^4$ $M^{-1} \cdot cm^{-1}$ [41].

Flavin mononucleotide phosphate (FMN) (fluorimetric purity 76.5%) by Sigma-Aldrich, protoporphyrin IX (purity > 97%), Zn(II)-protoporphyrin IX (purity > 95%) by Frontier Scientific and dimethylsulfoxide by "Kupavnareactive" (Russia, reagent grade) with no additional purification were used.

Erythrocytes were extracted from adult donors' blood of a random group and Rh factor provided by the Republican Scientific and Practical Center of Transfusiology and Medical Biotechnologies of the Ministry of Health of the Republic of Belarus. Blood was placed into 3.8% sodium citrate. Erythrocytes were isolated from supernatant plasma by centrifugal separation at 3000 g for 15 min. Pelleted cells were resuspended in 0.155 M NaCl, centrifuged as above and a buffy coat was removed. The process was triply repeated to take away white blood cells and platelets. Finally, the washed erythrocytes were resuspended in phosphate buffered saline (PBS: 0.155 M NaCl, 1.9 mM NaH_2PO_4, 8.1 mM Na_2HPO_4, pH 7.4) to their initial concentration in the blood (hematocrit ~ 50%).

Bilirubin was added into the erythrocytes suspension in PBS to concentration of 171 μM (through 0.05 M NaOH), and such suspension samples were incubated at 37 °C for an hour in the dark simultaneously with control erythrocyte suspension samples without bilirubin. The indicated concentration of bilirubin corresponds to the level at which phototherapy is recommended for newborns with hyperbilirubinemia syndrome. For irradiation, the erythrocyte suspension was diluted to hematocrit ~ 13%. Aliquots of each suspension were exposed to blue or green light for 20 min. Forty min after irradiation, one part of the irradiated sample, as well as control unirradiated samples of identical composition, were centrifuged at 3000 g for 15 min for sedimentation and then the supernatant was analyzed. The second part of all the samples were kept for 18 h in the fridge at 8 °C, and then erythrocytes were also sedimented in them and supernatant was analyzed. The work was carried out at room temperature of 21 ± 1 °C in low light conditions.

The radiation sources were blue (the wavelength of the emission spectrum maximum λ_{max} = 463 nm, the full-width at half-maximum FWHM = 20 nm) and green (λ_{max} = 517 nm, FWHM = 38 nm) LED matrices forming a uniform intensity light spot with irradiance at the surface level of the samples $I_{LED} \approx 12$ mW/cm^2 (phototherapy device "Romashka", Institute of Physics of the National Academy of Sciences of Belarus). The light exposure was carried out for 20 min in a 10 mm thick layer with slow stirring of the suspension, excluding mechanical hemolysis of red blood cells. The energy dose during this exposure was D = 14.4 J/cm^2, which is approximately comparable to 2 h of phototherapy in the treatment of neonatal hyperbilirubinemia.

The tests indicating photodamage of the erythrocyte membrane were data on the concentrations of potassium K^+ ions and hemoglobin molecules in the solution surrounding the erythrocytes, which was extracted by centrifugation of the suspension as a supernatant. The magnitude of the photobiological effect was characterized by the ratio of optical densities at the Soret band maximum (λ_{max} = 416 nm) in the supernatant of experimental and control samples, as well as by the ratio of K^+ ion concentrations in the supernatant of experimental and control samples.

Since, during the experiments, each new part of donor material differed from the previous one due to the random choice of donors by blood type and Rh factor, as well as due to the possible presence of significantly different concentrations of antioxidants in their blood, a relative assessment of potassium ions' and hemoglobin yield in the PBS was carried out for each part of donor material. The number of measurements within one sample of donor blood was at least 3. The total amount of samples of donor blood was at least 4.

To reveal the possible contribution of singlet oxygen to photodynamic processes, sodium azide (NaN_3), a well-known quencher of this active oxygen form, in final concentration of 50 mM, was added into some samples with bilirubin before irradiation.

The analysis of the K^+ ions in the supernatant solution was carried out with an inductively coupled plasma atomic emission spectrometer (IRIS Intrepid II XDL DUO, Thermo Electron Corp., USA) with calibration by the standard sample of K^+ aqueous solution 8092-97(18K-1). The presence of hemoglobin in the solution was determined spectrophotometrically. Solutions absorption spectra were measured by Cary 500 Scan UV-Vis-NIR spectrophotometer (Varian, USA) in 1-cm quartz cuvettes.

3 Statistical Analysis

Data are expressed as mean ± error of mean. Statistical analysis was performed using Microsoft Excel. Differences between means were assessed by the Kramer-Welch criterion (applied to small independent samples) [46], based on statistics $T_{emp} = |\bar{x}-\bar{y}|/(D_x/n_x+D_y/n_y)^{0.5}$, where $\bar{x}$ and $\bar{y}$ are comparable means, D is the sample variance, n = 4. A value of $\alpha = 0.05$ was chosen as the level of statistical significance, unless otherwise specified.

4 Results

4.1 Spectral Characteristics of Bilirubin, Erythrocyte Suspension and Optical Radiation Sources

It is well known that bilirubin is a hydrophobic compound, and, in human blood, it is mainly in complex with serum albumin, which is able to bind two pigment molecules in different parts of the protein globule with association constants $k_{as} = 5.5 \cdot 10^7$ M^{-1} and $k_{as} = 4.4 \cdot 10^6$ M^{-1} [40]. Less than 10–15% of the blood total bilirubin is in a water-soluble form, being conjugated with glucuronic acid. When bilirubin concentrations in the blood exceed the albumin binding capacity, erythrocytes along with lipoproteins become the closest target for it. Human erythrocytes are capable to bind bilirubin in concentrations up to 0.93 nM/mg of protein [43] or about 1 mg per 10 ml of cells [47]. It is believed that bilirubin binding sites can be located both outside and inside of erythrocyte membrane and these sites are not formed by proteins or, at least, membrane proteins do not play a significant role in bilirubin binding [42, 43].

The absorption spectra of bilirubin in PBS (curve 1), as well as in complex with human serum albumin at 1/1 molar ratio (curve 2) are shown in Fig. 1. The absorption spectrum of bilirubin bound to erythrocyte ghosts (0.1 ml; 5 mg of ghost protein/ml, 20 μM bilirubin) is also shown here (curve 3), reproduced from Ref. [42]. A distinctive feature of bilirubin absorption spectrum in an aqueous medium is its rapid variability over time caused by the formation of aggregated forms and oxidation by air oxygen. Bilirubin complexes with albumin and erythrocyte membranes (ghosts) are significantly more stable. Note that the incorporation of bilirubin into the albumin protein globule is accompanied by a long-wave

shift of the pigment absorption spectrum from λ_{max} = 437 nm for bilirubin in the buffer solution to λ_{max} = 460 nm.

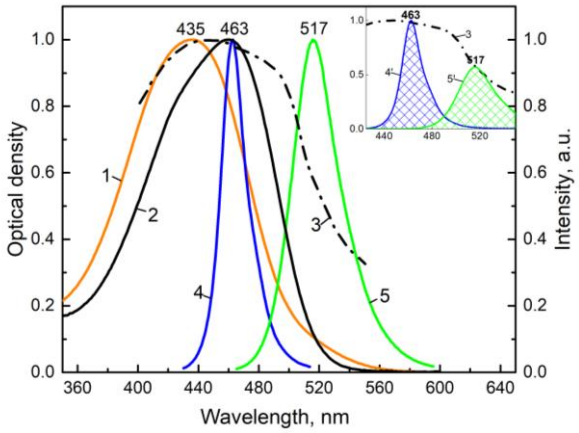


Fig. 1 The normalized absorption spectra of bilirubin in PBS (1), in complex with human serum albumin at 1/1 molar ratio (2), in erythrocyte ghosts (0.1 ml; 5 mg of ghost protein/ml, 20 μM bilirubin) from Ref. [42] (3), and normalized emission spectra of blue (4), and green (5) LEDs. The emission spectra of blue (4') and green (5') LEDs normalized to equal integral intensity are shown in the inset together with the spectrum of bilirubin in erythrocyte ghosts (3).

In contrast to the absorption spectrum of the bilirubin-albumin complex, the absorption spectrum of bilirubin bound to erythrocyte membranes is significantly broadened, its maximum is in the region of λ_{max} = 450 nm; in addition, a shoulder appears in the spectrum in the region of 490 nm. It is characteristic that those similar broadened bilirubin absorption spectra with a pronounced shoulder in the region of 500 nm are also observed when bilirubin is embedded in the synaptosomal plasma membrane vesicles isolated from rat brain [48].

Normalized emission spectra of blue (curve 4) and green (curve 5) LEDs used to irradiate the erythrocytes suspension are also shown in Fig. 1. Since the emission spectra of LEDs are characterized by quite different FWHM values, for clarity, the inset in Fig. 1 shows the emission spectra of blue (curve 4') and green (green 5') LEDs, normalized to the same integral intensities (which under identical experimental conditions means the same irradiance of blue and green light at the surface level of the samples). A fragment of the absorption spectrum of bilirubin in erythrocyte ghosts is also shown here (curve 3). It can be seen that the radiation with λ_{max} = 463 nm almost corresponds to the maximum of the absorption spectrum of free bilirubin, as well as bilirubin bound both to albumin and erythrocyte membranes (ghosts). But the radiation with λ_{max} = 517 nm corresponds to the long-wavelength slope of the pigment absorption band, where the absorption of light by bilirubin is less than in the region of the maximum of the absorption spectrum. Therefore, at the same irradiance (12 mW/cm^2) of the incident radiation of blue and green LEDs, the absorption of blue light by bilirubin bound to erythrocytes in suspensions will be greater than the absorption of green light.

Studies have shown that the radiation of LED sources in blue (λ_{max} = 463 nm) and green (λ_{max} = 517 nm) spectral regions, upon exposure of cell suspension treated with bilirubin, is to some extent shielded by hemoglobin contained in erythrocytes. At the same time, the shielding effect of hemoglobin is approximately the same for the LED sources used. This conclusion follows from the data in Fig. 2, which shows the absorption spectra of the erythrocyte suspension and the emission spectra of blue and green LEDs.

It can be seen that the absorption spectrum of the erythrocyte suspension with maxima in the region of λ_{max} = 418 nm (Soret band) and λ_{max} = 543 and 578 nm (Q-bands) corresponds to the absorption spectrum of hemoglobin. At the same time, the areas of overlap of the suspension absorption spectrum with the emission spectra of blue and green LEDs (shaded areas in Fig. 2) are approximately equal. In addition, mixing of suspensions during their irradiation almost eliminates the possible role of incident light shielding in the observed differences (see below) of the damaging effects of blue and green light on the erythrocyte membranes.

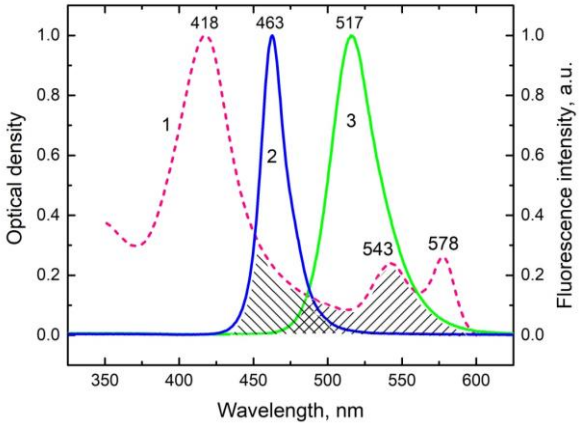


Fig. 2 The normalized absorption spectrum of the erythrocyte suspension (1) and the emission spectra of blue LED (2) and green LED (3).

4.2 The Effect of LED Sources Radiation of Blue and Green Spectral Regions to the Permeability of Erythrocyte Membranes for Potassium Ions

To quantify the change in the permeability of erythrocyte membranes for potassium K^+ ions under the influence of radiation, the ratio $[K^+_{ir}]/[K^+_{un}]$ was used, where $[K^+_{ir}]$ and $[K^+_{un}]$ are the concentrations of K^+ ions in the supernatant from irradiated and unirradiated control erythrocyte suspensions, accordingly.

The performed studies have shown that LED sources radiation of blue (λ_{max} = 463 nm) or green (λ_{max} = 517 nm) spectral regions at irradiance of $I_{LED} \approx 12$ mW/cm^2 applied to the suspension of human erythrocytes for 20 min (energy dose D = 14.4 J/cm^2)

without adding the bilirubin almost does not affect the permeability of cell membranes for potassium ions when monitoring this process both 40 min after the termination of irradiation and 18 h later. This conclusion follows from the presented in Fig. 3 arithmetic mean values of $[K^+_{ir}]/[K^+_{un}]$, determined by four independent experiments (with erythrocytes of four donors).

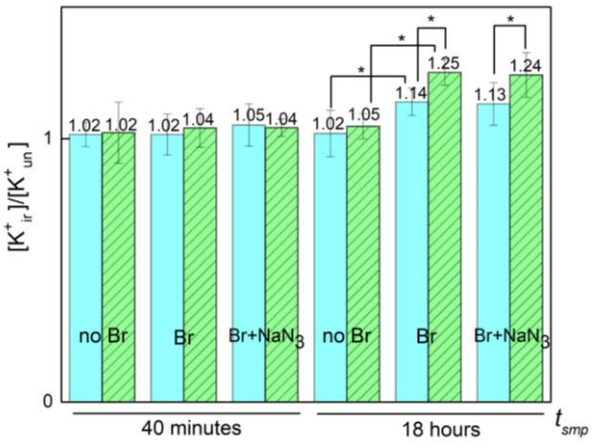


Fig. 3 The ratio of the concentration of potassium ions $[K^+_{ir}]/[K^+_{un}]$ in supernatants (irradiated relative to unirradiated suspensions) after exposure to blue LEDs radiation (λ_{max} = 463 nm, blue bars) or green LEDs radiation (λ_{max} = 517 nm, green bars) with irradiance of I_{LED} = 12 mW/cm^2 for 20 min on the suspension of human erythrocytes: without bilirubin (no Br), with 171 μM of bilirubin (Br), with 171 μM Br and 50 mM NaN_3 (Br + NaN_3), sampling time were 40 min and 18 h after the exposure. Error bars are refer to errors of $[K^+_{ir}]/[K^+_{un}]$ means. An asterisk * indicates differences in values at the significance level of 0.05.

As it follows from Fig. 3 (bars "no Br"), 40 min after irradiation, K^+ ions yield differs from the control level, taken as 100%, by no more than 2%. Eighteen hours after the light exposure to erythrocytes, the K^+ ions yield almost did not change compared to control samples, exceeding their value only by 2–5%. Note that the control unirradiated samples were incubated under the same conditions for 18 h as the irradiated ones. In this case, there were also no significant differences in the effect of green and blue LEDs.

It was found that the effect of light both from blue and green spectrum regions on the erythrocyte suspension in the presence of bilirubin also practically does not lead to an increase in the concentration of K^+ ions in the supernatant (compared to unirradiated samples) when monitoring concentrations 40 min after the termination of irradiation (Fig. 3, bars "Br", t_{smp} = 40 min).

A different situation is realized 18 h after the termination of light exposure to erythrocytes treated with bilirubin. In these conditions, potassium leakage from the erythrocytes increased on average (compared to control samples for this time period) by 14% when exposed to blue LED light and by 25% when exposed to green LED light (Fig. 3, bars "Br", t_{smp} = 18 h). In this case, there are significant differences (α < 0.05, marked with * in Fig. 3) in K^+ ions leakage between control and irradiated suspensions, as well as between suspensions irradiated by blue and green LEDs. Moreover, the radiation of green spectrum region has a more pronounced (by about 10%) damaging effect on erythrocytes, despite of weaker absorption of light in this region by bilirubin localized in the erythrocytes (Fig. 1, curve 3).

As it is known, bilirubin is a rather weak photosensitizer: the quantum yield of singlet oxygen generation sensitized by it is $\varphi_\Delta \approx 0.01$ [3]. Nevertheless, according to literature data [44], photodamage of erythrocyte membranes sensitized by bilirubin can be determined by the participation of this active oxygen form. In this regard, we investigated the possible participation of singlet oxygen in the photodamage of erythrocyte membranes by controlling the effect of sodium azide, a well-known singlet oxygen quencher, on the magnitude of the photobiological effect, estimated by the K^+ ions yield from the cells. The performed studies have shown (Fig. 3, bars "Br+NaN_3" versus "Br", t_{smp} = 18 h) that the addition of sodium azide to the bilirubin-sensitized erythrocyte suspension before irradiation reduces the value of the effect $[K^+_{ir}]/[K^+_{un}]$ (18 h after the irradiation) on average by only 1% when exposed to both blue and green light. This value is not statistically significant according to the assessment. Thus, it can be concluded that sodium azide does not actually block the light-induced yield of potassium ions, and, accordingly, singlet oxygen almost does not participate in the photochemical processes responsible for changing the permeability of cell membranes to potassium ions.

4.3 The Effect of Radiation from LED Sources in the Blue and Green Spectral Regions on the Release of Hemoglobin from Erythrocytes

The release of hemoglobin from the erythrocytes is the most frequently studied parameter characterizing the breakage of the integrity of the erythrocyte cell membrane under the influence of physical factors [31, 32, 44, 47]. It should be noted that when the erythrocyte cell membrane is damaged, along with hemoglobin, other heme derivatives (hemin, cytochromes, catalase and peroxidase enzymes, protoporphyrin, etc.) may appear in the extracellular space. However, the contribution to the recorded absorption spectrum of the supernatant, collected during the sedimentation of erythrocytes and diluted multiply with NaCl-isotonic solution is actually determined by hemoglobin. Fig. 4 shows the absorption spectra of supernatants from erythrocyte suspensions with bilirubin (curves 1, 2, 3), with bilirubin and azide (curves 4, 5, 6) in NaCl-isotonic solution, which were irradiated with blue (curves 2, 6) and green (curves 3, 5) LEDs with irradiance of $I_{LED} \approx$ 12 mW/cm^2 for 20 min, as well as from their unirradiated analogues (curves 1, 4). The supernatants were extracted from erythrocyte suspensions t_{smp} = 40 min after the light exposure.

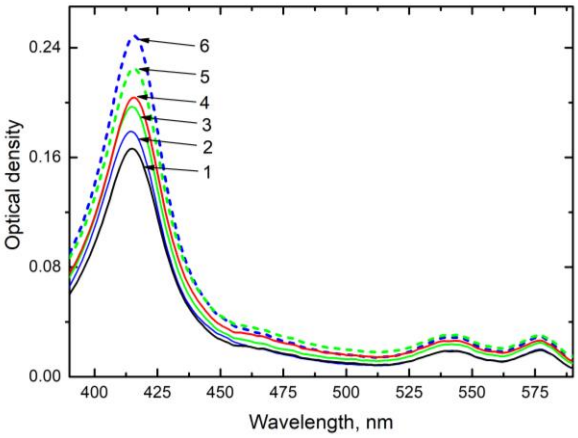


Fig. 4 Absorption spectra of supernatants from erythrocyte suspensions with bilirubin (1, 2, 3), with bilirubin and 50 mM NaN_3 (4, 5, 6) in NaCl-isotonic solution, irradiated with blue LED (2, 6), green LED (3, 5) and unirradiated (1, 4). $I_{LED} \approx 12$ mW/cm^2, exposure time is 20 min, sampling time is 40 min.

The absorption spectra of supernatants in NaCl-isotonic solution for irradiated and unirradiated erythrocyte suspensions look like typical hemoglobin absorption spectra with maxima in the region of 416 nm (Soret band), as well as in the region of 540 nm and 575 nm.

As follows from Fig. 4, the greatest dynamic range of changes upon exposure of the erythrocytes to light is observed at the maximum of the Soret band. For this reason, further, the OD_{ir}/OD_{un} value was chosen as a quantitative measure to characterize the erythrocyte hemolysis, where OD_{ir} and OD_{un} are optical densities at the maximum of the Soret band (around 416 nm) of the supernatants diluted multiply in NaCl-isotonic solution in the same proportions for irradiated and unirradiated control erythrocyte suspensions, respectively.

The performed studies showed the presence of erythrocyte hemolysis in unirradiated control samples, which is manifested in an increase in the optical density of the Soret band maximum of hemoglobin in the supernatant (Table 1) from $OD_{un} = 0.129 \pm 0.045$ when analyzed after 40 min of incubation at a room temperature to $OD_{un} = 0.147 \pm 0.049$ after 18 h of dark storage at 8 ºC. The addition of bilirubin at a concentration of 171 μM to the erythrocytes suspension (without exposure to light) increases the rate of hemolysis. This is confirmed by an increase in optical density at the maximum of the Soret band of hemoglobin in the supernatant already 40 min after incubation of cells with bilirubin ($OD_{un} = 0.152 \pm 0.019$) compared to cells without bilirubin additives ($OD_{un} = 0.129 \pm 0.045$). This tendency remains when analyzing the release of hemoglobin from erythrocytes after 18 h of dark storage: for cells with bilirubin $OD_{un} = 0.187 \pm 0.026$; for cells without addition of bilirubin $OD_{un} = 0.147 \pm 0.049$.

The results of studies of the effect of light from blue ($\lambda_{max} = 463$ nm) and green ($\lambda_{max} = 517$ nm) spectral regions on erythrocyte hemolysis during irradiation (irradiance $I_{LED} \approx 12$ mW/cm^2, exposure time 20 min) without bilirubin, as well as upon sensitization of cells with 171 μM of bilirubin, are shown in Fig. 5. The results are presented in the form of histograms reflecting the change of the optical density of OD_{ir}/OD_{un} in the supernatant of erythrocytes suspensions irradiated against unirradiated ones. Data on the effect of sodium azide, a singlet oxygen quencher, on the hemolysis process sensitized by bilirubin are also shown in Fig. 5. The data are presented as an arithmetic mean for four independent experiments.

From the data presented in Table 1 and Fig. 5, it follows that the most pronounced photodamage of erythrocytes, controlled by the release of hemoglobin, is observed upon exposure to light in the blue and green spectral regions without adding bilirubin (bars "no Br"). So, already 40 min after irradiation of erythrocyte suspensions without bilirubin with blue light, $OD_{ir}/OD_{un} = 1.41 \pm 0.30$, and when exposed to green radiation, $OD_{ir}/OD_{un} = 1.57 \pm 0.49$. 18 h after the termination of irradiation and dark storage of erythrocyte suspensions, the corresponding OD_{ir}/OD_{un} values are 1.48 ± 0.42 for blue light and 1.34 ± 0.24 for green one. Thus, irradiation of erythrocytes without bilirubin accelerates the release of hemoglobin from erythrocytes by an average of 40–50% relative to the corresponding unirradiated suspensions.

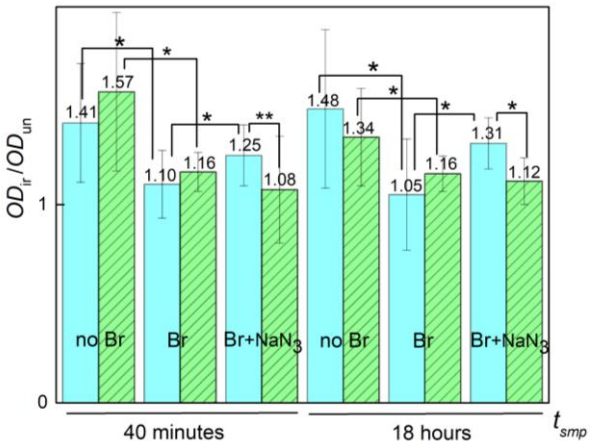


Fig. 5 Change of the optical density OD_{ir}/OD_{un} in supernatant (of the irradiated and unirradiated suspensions) after exposure to blue LED (λmax = 463 nm, blue bars) or green LED (λmax = 517 nm, green bars) at irradiance $I_{LED} \approx 12$ mW/cm^2 for 20 min to an erythrocytes suspension: without bilirubin (no Br), with 171 μM of bilirubin (BR), with 171 μM of bilirubin (BR) and 50 mM of sodium azide (Br + NaN_3), t_{smp} = 40 min and 18 h after the light exposure. Error bars refer to errors of OD_{ir}/OD_{un} means. An asterisk * indicates differences in values at the significance level of 0.05; ** – at the significance level of 0.2.

Table 1 Optical density at the maximum of the absorption spectrum of supernatant from erythrocyte suspension.

Supernatant from suspensions unirradiated or irradiated by	*OD* in "no Br" sample		*OD* in "Br" sample		*OD* in "Br + NaN_3" sample	
	t_{smp} = 40 min	t_{smp} = 18 h	t_{smp} = 40 min	t_{smp} = 18 h	t_{smp} = 40 min	t_{smp} = 18 h
Unirradiated	0.129 ± 0.045	0.147 ± 0.049	0.152 ± 0.019	0.187 ± 0.026	0.177 ± 0.025	0.229 ± 0.037
Blue LED	0.171 ± 0.046	0.202 ± 0.043	0.168 ± 0.021	0.197 ± 0.033	0.217 ± 0.025	0.298 ± 0.043
Green LED	0.185 ± 0.046	0.187 ± 0.026	0.178 ± 0.024	0.216 ± 0.030	0.185 ± 0.024	0.260 ± 0.051

* *OD* (Optical density) values are presented as an arithmetic mean ± error of mean for four independent experiments (with erythrocytes of four donors), t_{smp} (sampling time) is time interval between stopping irradiation and starting to monitor changes in erythrocytes.

During the experiments, it was found out that irradiation of the erythrocyte suspension in the presence of bilirubin not only does not enhance hemolysis, but even slightly reduces it compared to the data of irradiation without bilirubin. Thus, 40 min after the irradiation of erythrocytes sensitized by bilirubin with blue light, the average value of OD_{ir}/OD_{un} = 1.10 ± 0.17, and with green light – the average value of OD_{ir}/OD_{un} = 1.16 ± 0.10. In 18 h, the value of the blue light-photoinduced effect decreases slightly to OD_{ir}/OD_{un} = 1.05 ± 0.28. That is, the hemoglobin release from the erythrocytes irradiated in the presence of bilirubin, exceeds the corresponding value for unirradiated cells on average by 5–15%, which is significantly lower than for irradiation of erythrocytes without bilirubin (see above). Thus, the presence of 171 μM of bilirubin in the suspension and its subsequent binding to erythrocytes significantly (by ~ 20–40%) increases the resistance of cells to hemolysis initiated *in vitro* by the light exposure of blue-green spectral region. It should be noted that the mean OD_{ir}/OD_{un} values of the samples without bilirubin and those with bilirubin differ statistically significantly (according to the Kramer-Welch test applied to small independent samples) both under blue and green LEDs irradiation.

The performed studies also demonstrated (Table 1 and Fig. 5) that the addition of sodium azide to the erythrocyte suspension, at least does not block the photodamage of erythrocyte membranes initiated by exposure to light of the blue and green spectral regions in the presence of bilirubin. Moreover, when exposed to blue light in the presence of bilirubin and azide, the damaging effect exceeds the effect observed in the absence of azide (Fig. 5, blue bars "Br + NaN_3" versus "Br", t_{smp} = 40 min, 18 h): when analyzed 40 min after irradiation, the corresponding values of OD_{ir}/OD_{un} are 1.25 and 1.10, and in 18 h of incubation OD_{ir}/OD_{un} = 1.31 and 1.05, respectively. The given measures are statistically significantly different (with the significance level of 0.05).

In contrast to azide influence to the effects induced with blue light, green light irradiation of the erythrocytes suspension with bilirubin in the presence of azide leads to the decrease in hemoglobin release compared to similar samples without azide (Fig. 5, green bars "Br" versus "Br + NaN_3", t_{smp} = 40 min, 18 h). In this case, when analyzed 40 min after irradiation, the corresponding average values are: for samples with bilirubin OD_{ir}/OD_{un} = 1.16 and for samples with bilirubin and azide it is 1.08, and in 18 h OD_{ir}/OD_{un} = 1.16 and 1.12. Thus, the addition of NaN_3 before irradiation of bilirubin-containing erythrocytes with green light (contrary to exposure with blue light) somewhat reduces the release of hemoglobin through the cell membrane, which may serve as confirmation of the partial participation of singlet oxygen in the photochemical process.

5 Discussion

5.1 Effect of LEDs Radiation on Erythrocytes in the Absence of Exogenous Bilirubin

The performed study has shown that the effect of radiation from LED sources of blue (λ_{max} = 463 nm) or green (λ_{max} = 517 nm) spectral regions at irradiance of $I_{LED} \approx 12$ mW/cm^2 for 20 min (energy dose D = 14.4 J/cm^2) on the suspension of human erythrocytes without the addition of bilirubin practically does not affect the permeability of cell membranes for potassium ions (Fig. 3). The photoinduced effect assessed by this test, is practically absent when it is monitored both 40 min and 18 h after the irradiation. The results obtained correspond to the literature data, which studied the effect of blue light from special fluorescent lamps (with a maximum in the emission spectrum at 450–460 nm) on the potassium ions leakage from erythrocytes [31], and Na^+ ions leakage from the sealed erythrocyte ghosts [32]. Therefore, it can be stated that upon exposure to blue light, no endogenous compounds sensitize damage to the molecules that control the release of potassium ions from

erythrocytes (for example, the enzyme Na/K-ATPase, providing an asymmetric distribution of sodium and potassium ions on both sides of the erythrocyte membrane). Another possible explanation for this result is that the antioxidant system of the erythrocyte prevents possible damage to the molecular structures of membranes responsible for permeability to potassium ions [49]. According to Ref. [49], "Under intensive photodynamic action resulting in cell lysis directly on lighting main defence role plays membrane bound alpha-tocopherol; under erythrocyte hemolysis in dark after shot photodynamic action – decisive meaning has cytoplasm glutathione"; and in general, the nature and mechanisms of the mutually coordinated functioning of these and other antioxidants present in the cell depend on the intensity and site of application of the oxidative action.

A different situation is realized when analyzing the hemoglobin molecules release from erythrocytes under irradiation with the same parameters. According to the data obtained (Fig. 5), irradiation of the erythrocyte suspension without bilirubin accelerates the release of hemoglobin by an average of 45% relative to the corresponding unirradiated suspensions. At the same time, a significant excess of the optical density of the supernatant from the irradiated samples over the control variant is observed both when assessing hemoglobin concentrations 40 min and 18 h after the termination of irradiation. It is characteristic that, 40 min after the termination of the irradiation, a more pronounced effect is observed upon exposure to light in green spectral region: mean value $OD_{ir}/OD_{un} = 1.57$, while after irradiation with blue light, mean value $OD_{ir}/OD_{un} = 1.41$. However, 18 h after the irradiation and dark storage of erythrocyte suspensions, the corresponding mean values OD_{ir}/OD_{un} are 1.48 for blue light and 1.34 for green one. That is, the magnitude of the effect (in relation to the control unirradiated samples) upon exposure to blue light on the second day, at least, does not decrease, and, upon exposure to green light, it decreases by ~ 20%.

Based on the data obtained, it can be assumed that damage to erythrocyte membranes upon exposure to blue-green light in the absence of exogenous bilirubin is due to photochemical reactions sensitized by endogenous compounds. At the same time, it is well known that hemoglobin is not a photosensitizer and does not generate singlet oxygen upon exposure to light [50]. In our opinion, flavin compounds (riboflavin, flavin mononucleotide, FMN, and flavin adenine dinucleotide, FAD) and porphyrins (protoporphyrin IX, PPIX and zinc-protoporphyrin IX, ZnPP)) can primarily be such endogenous photosensitizers that absorb visible radiation and generate reactive oxygen species (ROS) with high efficiency. The participation of endogenous flavin and porphyrin photosensitizers in regulatory and lethal effects of optical radiation in the visible spectral region was previously established in our laboratory in relation to microbial cells and spermatozoa [51–53]. It is known that flavin and porphyrin photosensitizers are capable of generating singlet oxygen $^1O_2$ quite efficiently [53, 54]. The quantum yield of $^1O_2$ generation in an aqueous medium is $\varphi_\Delta = 0.54$ for riboflavin, $\varphi_\Delta = 0.51$ for FMN, $\varphi_\Delta = 0.07$ for FAD, $\varphi_\Delta = 0.77$ for the monomeric form of PPIX and $\varphi_\Delta = 0.91$ for the monomeric form of ZnPP (in the presence of Triton X-100 in water). Along with singlet oxygen, riboflavin and protoporphyrin IX also sensitizes the formation of other ROS: superoxide radicals, hydrogen peroxide. At the same time, flavin photosensitizers (riboflavin, FMN and FAD) have similar absorption characteristics: their long-wave maximum in the absorption spectrum is located in the region of 445 nm. PPIX and ZnPP in aqueous media are prone to aggregation and the position of the most intense band (Soret band) in their absorption spectrum strongly depends on the pH of the medium, the formation of complexes with macromolecules, etc. As a rule, the Soret band maximum for PPIX and ZnPP is in the region of 380–410 nm. Currently, the presence of porphyrin and flavin photosensitizers in human erythrocytes is beyond doubt: they are recorded by fluorescence, acetone extraction followed by fluorescence analysis, chromatographic method, etc. According to Ref. [55], the concentration of FMN and FAD in adult human erythrocytes is 44 and 469 nM, respectively; riboflavin is present only in trace amounts. As for PPIX, according to Ref. [56], its concentration in the adult healthy human erythrocytes is 0.60–0.75 μg/ml of erythrocytes and can vary significantly at various diseases. It is also known that non-heme protoporphyrins present in a healthy body in the form of approximately 85–95% ZnPP and 5–15% PPIX [57].

We should note that in the presence of several photosensitizers in the system, their relative contribution to the realization of photobiological effect depends on a number of factors: the generation efficiency of ROS, concentration, molar extinction coefficient, localization near the sensitive biologically important biosubstrate, the presence of closely located ROS quenchers, etc. Therefore, it is quite a difficult task to assess the contribution of a particular photoacceptor to the total photobiological effect, taking into account the overlap of the absorption spectra of potential endogenous photosensitizers, as well as the multiplicity of influencing factors. At the same time, certain conclusions can be made from the analysis of the absorption spectra of photosensitizers. As an example, Fig. 6 shows the absorption spectra of monomeric forms of potential endogenous photosensitizers: FMN in the PBS (curve 1), PPIX (curve 2) and ZnPP (curve 3) in dimethylsulfoxide. The arrows in Fig. 6 indicate the wavelengths of radiation from LED sources affecting the erythrocyte suspension.

As it follows from Fig. 6, LED sources of radiation both with $\lambda_{max} = 463$ nm and $\lambda_{max} = 517$ nm is able to excite each of mentioned above endogenous photosensitizers, since it is absorbed by these compounds to one degree or another. Moreover, the radiation of blue spectral region is near the maximum of the long-wave absorption band FMN ($\lambda_{max} = 447$ nm), while the radiation of green spectral region falls on the long-wavelength slope of the absorption spectrum of the specified flavin.

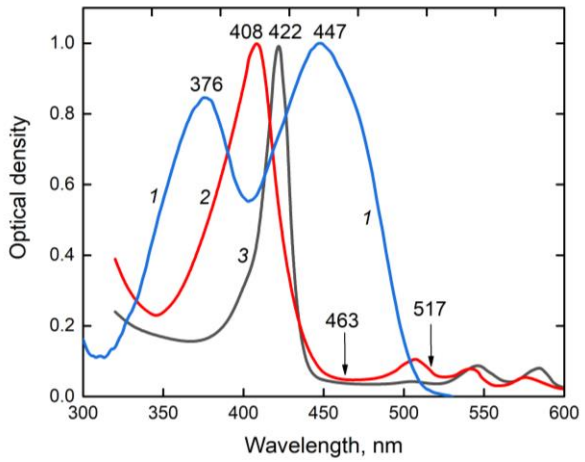


Fig. 6 Normalized absorption spectra of endogenous photosensitizers: 1 – FMN in PBS, 2 and 3 – PPIX and Zn-PPIX in dimethylsulfoxide, respectively. The concentration in solutions was 1 μM. Arrows indicate the radiation wavelengths of LED sources.

As for porphyrin photosensitizers, the radiation with both λ_{max} = 463 nm and λ_{max} = 517 nm corresponds to the minimum absorption of ZnPP, characterized by an intense Soret band ($S_2 \leftarrow S_0$ – transition) with maximum for the monomeric form in the region λ_{max} = 422 nm (B(0,0)) and two Q-bands ($S_1 \leftarrow S_0$ – transition) with maxima at λ_{max} = 547 nm (Q(1.0)) and λ_{max} = 584 nm (Q(0.0)). Light absorption by PPIX is due to the presence of an intense Soret band ($S_2 \leftarrow S_0$ – transition) in the spectrum with maximum for the monomeric form in the region of λ_{max} = 408 nm (B(0,0)) and four Q–bands ($S_1 \leftarrow S_0$ – transition) with maxima at λ_{max} = 507 nm (Q_y(1,0)), λ_{max} = 543 nm (Q_y(0,0)), λ_{max} = 575 nm (Q_x(1,0)) λ_{max} = 630 nm (Q_x(0,0)). As it can be seen from Fig. 6, the radiation of green spectral region with λ_{max} = 517 nm is absorbed by protoporphyrin IX somewhat more efficiently than the radiation of blue region with λ_{max} = 463 nm.

Analysis of the abovementioned spectral characteristics of endogenous photosensitizers allows allow us to conclude that if the light-induced release of hemoglobin molecules from the erythrocytes was stipulated by sensitizing effect of flavins, then the observed photobiological effect in the absence of exogenous bilirubin (Fig. 5) should be much more pronounced when the erythrocyte suspension is exposed to light of blue spectral region, since radiation with a wavelength of λ_{max} = 463 nm is absorbed approximately 50 times more efficiently than radiation with λ_{max} = 517 nm. At the same time, according to Fig. 5, when controlling the hemoglobin molecules release 40 min after the erythrocyte suspension irradiation in the absence of bilirubin, a more pronounced effect is observed when exposed to green region radiation. And although the situation slightly changes when monitoring the process 18 h after the irradiation (Fig. 5), the data presented cast doubt on the leading role of flavins in sensitizing photodamage to the erythrocyte membrane when exposed to radiation in blue-green spectrum region. At the same time, it is not possible to make a choice in favor of ZnPP or PPIX due to their different concentrations in the erythrocytes [56, 57], as well as overlapping absorption spectra.

Thus, we have reasons to believe that the excitation of endogenous porphyrin and flavin photosensitizers localized in erythrocytes, when exposed to radiation from blue-green spectral region and the subsequent generation of ROS (primarily singlet oxygen) by them can cause photodamage of the cell membrane, initiating the release of hemoglobin molecules – photohemolysis. The ability of optical radiation of blue spectral region (λ_{max} = 405 nm, I = 30 mW/cm^2, energy dose – 72 J/cm^2) to affect the erythrocyte suspension in the absence of exogenous photosensitizers is also evidenced by the results of studies [58], in which a significant decrease (by 0.44%) in erythrocytes volume as a result of their irradiation has been determined.

It should be noted that the noticeable effect of blue light from LED sources on the release of hemoglobin from erythrocytes during their irradiation of suspension without bilirubin does not agree with data [31, 34], according to which, irradiation of the erythrocytes suspension with the light of blue fluorescent lamp almost does not lead to an acceleration of hemolysis compared to control unirradiated samples (in the stated studies, control of hemoglobin concentrations in the supernatant was also carried out 18 h after the irradiation). At the same time, the energy parameters of the exposed radiation in our studies and in Ref. [34] (λ_{max} = 450 nm, $I \approx$ 8 mW/cm^2, dose – 14 J/cm^2) were also quite close. In our opinion, a possible reason for the observed differences in the results is the different methods of hemolysis control: in studies [34], it was initiated osmotically by adding a suspension of irradiated or non-irradiated erythrocytes into NaCl solution of low (0.35–0.45%) concentration (hypotonic solution). Besides, in study [34], not free bilirubin but its complex with albumin (ratio bilirubin/albumin = 0.8) was added into the erythrocyte suspension. The absence of data about the light energy parameters in Ref. [31] does not allow us to determine the reason for the observed differences between our results and data [31] at irradiation of the erythrocytes suspension without bilirubin.

As for green spectrum region radiation, we failed to find in the literature studies on its effect on hemolysis of human erythrocytes *in vitro*. However, in Ref. [59] it was found that against the background of experimental endotoxic shock in the membranes of rat erythrocytes, a more effective increase in lipid oxidation occurs at irradiation *in vivo* with green laser radiation of 532.5 nm (dose – 0.75 J/cm^2), than at irradiation with blue of 441.2 nm or red of 632.8 nm laser radiation at the same dose. The authors [59] also believe that this may be an indirect confirmation of the hypothesis about porphyrins as primary photoacceptors in erythrocytes.

5.2 Effect of LEDs Radiation on Erythrocytes in the Presence of Exogenous Bilirubin

As it has been already noted, the study of the sensitizing effect of bilirubin on erythrocyte membranes is of particular interest due to the importance of reducing the effectiveness of this process as a side adverse effect during phototherapy of hyperbilirubinemia in newborns. The performed studies have shown (Table 1) that the interaction of bilirubin at concentration of 171 μM (at which phototherapy of newborns with hyperbilirubinemia syndrome is prescribed) leads to molecular structural changes of the erythrocyte membrane, which is confirmed by the intensification of hemoglobin release through the membrane in dark conditions (without suspension irradiation). Evidence of this is an increase of the optical density in the Soret band maximum of hemoglobin in the supernatant both 40 min and 18 h after incubation of erythrocytes with bilirubin in comparison with cells that do not contain pigment. The effects registered by us when bilirubin binds to the erythrocyte membrane are in accordance with studies [32, 44]. According to these results, the damage of erythrocyte membranes resulting from cross-linking of membrane proteins plays a critical role in cell lysis. At the same time, peroxidation of unsaturated membrane lipids, which occurs during irradiation, also disturbs the membrane structure. However, protein modification, rather than peroxidation of unsaturated membrane lipids, is the determining factor in the initiation of cell lysis (in the photohemolytic mechanism) [44].

It could be expected that the effect of blue light corresponding to the absorption band of bilirubin on cells loaded with this pigment would contribute to their accelerated destruction due to the photodynamic effect. Moreover, the ability of bilirubin and its photoproducts to sensitize photodamage of erythrocyte membranes has been repeatedly noted in the literature [31, 32, 34, 44]. However, our studies have shown that irradiation of the erythrocyte suspension in the presence of 171 μM of bilirubin does not enhance hemolysis, moreover slightly reduces it compared to the data of irradiation without bilirubin.

The analysis 40 min after irradiation with blue light has shown that the excess of the optical density of the supernatant over the control samples was, on average, 40% in the absence of bilirubin and 10% in the case of sensitization with bilirubin; for green light the corresponding values were 57% and 16% (Fig. 5). The analysis of hemolysis 18 h after the irradiation with blue light has shown that the magnitudes of the photohemolytic effect for the erythrocyte suspensions not containing and containing bilirubin are 48 and 5%, respectively, and when exposed to green light – 34% and 16%. Thus, the binding of bilirubin to erythrocytes significantly (by ~ 20–40%) increases the resistance of cells to hemolysis initiated *in vitro* by exposure to light in blue and green spectral regions compared to the erythrocytes without bilirubin. In our opinion, the protective effect of bilirubin is connected with the antioxidant properties of bilirubin (and its photoproducts), which is one of the most powerful endogenous antioxidants [60, 61]. Thus, according to Ref. [60], 10 nM of bilirubin is enough to protect cultured cells from the destructive effects of 10,000-fold molar excess of hydrogen peroxide. Since bilirubin is a very weak photosensitizer (the quantum yield of the singlet oxygen formation sensitized by it is 0.01 [3]), then, likely, its antioxidant effect prevails over the sensitizing one in the processes controlling the release of hemoglobin through the erythrocyte membrane.

One of the reasons for the difference between our data and the results of [31, 34], having observed the acceleration of hemolysis due to the sensitizing effect of bilirubin, are different conditions for addition of the pigment to erythrocyte suspension. In studies [31, 34], bilirubin was added as part of a complex with albumin, while in our studies – in phosphate buffered saline. At the same time, according to Ref. [48, 62], the incorporation of bilirubin into biomembranes can be carried out both in the form of a monoanion and in the form of aggregates of molecules, which can affect the sensitizing and antioxidant properties of tetrapyrrol.

Studies have shown that, unlike hemolysis processes, where the antioxidant properties of bilirubin are primarily manifested, when studying the effect of light exposure on the leakage of potassium ions, the sensitizing properties of this pigment are more pronounced (Fig. 3). Moreover, the most significant light-induced structural changes of membranes (estimated by the potassium leakage) in the presence of exogenous bilirubin are observed not immediately after the light exposure of blue or green spectral regions, but 18 h after irradiation. Consequently, for the implementation of photodynamic damage to membranes when they are sensitized by bilirubin, a certain time is required. This conclusion is supported by the data of the authors [63] that the processes of peroxidation of unsaturated membrane lipids of the erythrocyte membranes during their sensitization with tetrapyrroles continue after the irradiation procedure. The authors [64] also point to the reliably registered secondary production of ROS and, above all, hydrogen peroxide hundreds of minutes after the irradiation of various cell types in the presence of a photosensitizer.

Another discovered characteristic feature of the bilirubin–sensitized leakage of potassium ions from erythrocytes is an “abnormal” dependence on the wavelength of the incident radiation. Thus, at monitoring of this process 18 h after the light exposure, potassium leakage from erythrocytes increased on average (compared to control samples for this time period) by 14% when exposed to blue LED light and by 25% when exposed to green LED light. Thus, upon sensitization of erythrocytes with bilirubin, the radiation of green spectral region has a more pronounced effect on the potassium ions leakage, despite the weaker absorption of light in this region by bilirubin localized in erythrocytes (Fig. 1, curve 3). At the same time (as it was already noted), in the absence of bilirubin, the exposure of the erythrocyte

suspension to light of blue or green spectral regions almost does not affect the potassium ions leakage, exceeding the values for control (unirradiated) samples by 2–5% ($[K^+_{ir}]/[K^+_{un}] \approx 1.02–1.05$). Consequently, the difference in the effect of blue and green light is stipulated by the different efficiency of photochemical processes affecting the potassium ions leakage during photoexcitation of bilirubin or its photoproducts with radiation wavelength of $\lambda_{max} = 463$ nm and $\lambda_{max} = 517$ nm without a noticeable contribution of endogenous photosensitizers. The reasons for observed higher photobiological effect of green light compared to blue one in the case of bilirubin-sensitized erythrocytes require a separate discussion. Literature studies of erythrocytes on this issue are unknown to us. At the same time, there are comparative data in the literature [65] on the survival of bilirubin-sensitized cultured animal cells when exposed to radiation of blue ($\lambda = 457.9$ nm) and green ($\lambda = 514.5$ nm) spectral regions. As in our studies with the potassium ions leakage from erythrocytes, the photobiological effect due to the sensitizing action of bilirubin, estimated with colorimetric MTT assay, in cultured somatic cells is more pronounced when exposed to radiation of green spectral region than blue one. Besides, our data on the photosensitizing effect of bilirubin to the potassium ions leakage from the erythrocytes under the blue radiation are in agreement with the results of studies [31].

In our opinion, the abnormal (based on the absorption spectrum of bilirubin bound to erythrocyte membranes) dependence of the light-induced potassium ions leakage from the erythrocytes on the wavelength of the incident radiation can be explained by several reasons. One of them is that along with bilirubin, its configurational and structural photoisomers can contribute to the sensitization effects, since the ability of bilirubin photoproducts to sensitize (with greater efficiency compared to bilirubin) the damage of biomolecules in solution is well known [23, 26]. At the same time, the quantum yield of photoproducts, as well as the ratio between the concentrations of individual photoproducts, strongly depend on the wavelength of the radiation due to a) bichromophoric nature of the absorption and emission of light by bilirubin molecules; b) presence of intramolecular energy transfer between two unequal chromophores forming a pigment molecule; c) dependence of the efficiency of intramolecular energy transfer of electronic excitation on the radiation wavelength [37–41, 66, 67].

Another reason for the increase in the bilirubin-sensitized potassium ions leakage during the transition from blue irradiation with $\lambda_{max} = 463$ nm to green irradiation with $\lambda_{max} = 517$ nm may be the heterogeneity (heterogeneous nature) of the microenvironment of sensitizer molecules in the erythrocyte membrane. This is indicated by the broadened absorption spectrum of bilirubin embedded in the erythrocyte membrane (Fig. 1, curve 3), as well as a strong dependence of the position of the fluorescence excitation spectrum of bilirubin bound to human erythrocyte ghosts on the registration wavelength, found in Ref. [68]. In this regard, there are reasons to believe that radiation of different wavelengths can excite bilirubin localized in different sites/regions of the erythrocyte membrane and initiate various photochemical processes (lipid peroxidation, cross-linking of proteins and damage to protein-lipid contacts in the membrane, inactivation of the Na/K-ATPase enzyme, etc.).

5.3 Involvement of ROS in Bilirubin-Sensitized Photodamage of Erythrocyte Membranes

Another characteristic feature of photochemical processes in the erythrocyte membranes initiated by exposure to light in the presence of exogenous bilirubin should be noted. It consists in a weakly pronounced effect of sodium azide, a well-known singlet oxygen quencher, on the light-induced leakage of both potassium ions (Fig. 3) and hemoglobin molecules (Fig. 5).

In our opinion, the reasons for a weak effect of this singlet oxygen quencher on photochemical processes in erythrocytes during their bilirubin – sensitization may be the following: a) low availability of singlet oxygen generation sites in the membrane for sodium azide; b) participation in damage to erythrocyte membranes of other ROS and free radicals, for which sodium azide does not act as a quencher. Moreover, unlike singlet oxygen, other reactive oxygen species (primarily hydrogen peroxide) can play a main role in the membrane damage already after the light exposure [64]. Since the lifetime of singlet oxygen in an aqueous medium is about 3 μs, its damaging effect on the erythrocyte membrane actually stops immediately after the irradiation stops, while chemical reactions mediated by hydrogen peroxide continue for a long time [63, 64]. Another reason for the weakly expressed effect of azide on the photobiological processes, estimated by the potassium ions or hemoglobin molecules leakage, may be the ability of azide ions to interact with heme iron [69], which actually reduces the concentration of free (unbound) intracellular azide capable to quench singlet oxygen generated by a photosensitizer. The spectral data obtained (Fig. 4, Table 1) also allow us to confirm the existence of such an interaction. This is manifested in a higher optical density of the supernatants (in NaCl-isotonic solution) from unirradiated erythrocytes suspensions with bilirubin and azide (curve 4 in Fig. 4) compared to the corresponding data for the erythrocyte suspension with bilirubin without NaN_3 (curve 1 in Fig. 4). Thus, for the studied biological system, there is a pronounced interaction of sodium azide with the erythrocyte membrane and erythrocyte hemoglobin under dark conditions, which can affect the photochemical and subsequent chemical reactions in cells [70].

Attention is also drawn to the seemingly abnormal effect of sodium azide on blue-light-induced release of hemoglobin molecules from the bilirubin-sensitized erythrocytes (Table 1 and Fig. 5). According to the experimental data obtained, when exposed to blue light in the presence of bilirubin and azide, the damaging

effect on membranes, estimated by the release of hemoglobin molecules from cells, exceeds the effect observed in the absence of azide (Fig. 5, blue bars "Br+NaN_3" versus "Br"). That is, the addition of the known singlet oxygen quencher sodium azide to the suspension of cells not only does not reduce the magnitude of the photobiological effect, but also increases it. In this regard, it should be noted that an increase in the photobiological effect due to the addition of sodium azide for the first time was noted in Refs. [71, 72] during the sensitization of microbial cells with methylene blue. The authors [71, 72] have shown that this effect is stipulated by the formation of azide radicals (having a high reactivity) due to electron transfer from the excited form of the sensitizer. According to Refs. [71, 72], the decrease or increase in the efficiency of photochemical reactions due to the addition of azide largely depends on the contribution to the total process of reactions of type II (occurring with the participation of singlet oxygen) or type I (due to radical processes).

Typically, that the addition of NaN_3 before irradiation of bilirubin-containing erythrocytes with green light (in contrast to exposure to blue light) slightly reduces the release of hemoglobin through the cell membrane, which may be a confirmation of the partial participation of singlet oxygen in the photochemical process. On the other hand, the multidirectional action of azide on hemolytic effects initiated in erythrocyte membranes by light of the same intensity in blue and green spectral regions indicates the different nature of the photochemical processes underlying them. In this regard, we can expect a significant role of bilirubin photoisomers in the effects of sensitized damage of erythrocyte membranes. Moreover, the contribution of various configurational and structural isomers of bilirubin to the total light absorption may differ markedly when exposed to light with wavelengths of λ_{max} = 463 nm and λ_{max} = 517 nm. The reasons for this are the different absorption spectra of bilirubin photoisomers [23], as well as the dependence of the quantum yield of the bilirubin photoisomer formation on the wavelength of the incident radiation [37–41, 65, 66].

6 Conclusions

The effect of radiation from LED sources of blue (λ_{max} = 463 nm) or green (λ_{max} = 517 nm) spectral regions at irradiance of I = 12 mW/cm^2 for 20 min (energy dose D = 14.4 J / cm^2) on the human erythrocyte suspension in the phosphate buffered saline leads to erythrocyte membrane damages, which is confirmed by an increase in the optical density of supernatant in the Soret band of hemoglobin. The values of photohemolytic effects are approximately equal when exposed to radiation from blue and green spectral regions.

Molecular-structural changes in erythrocyte membranes when exposed to light of the mentioned above parameters are most likely stipulated by the excitation of endogenous porphyrin (protoporphyrin IX, zinc-protoporphyrin) and flavin (flavin mononucleotide, flavinadenindinucleotide) photosensitizers contained in the erythrocytes in low concentrations, but characterized by high efficiency of generation of reactive oxygen species. The leading role of porphyrin compounds in the effects of sensitization is substantiated.

The effect of radiation of the same parameters on the erythrocyte suspension almost does not influence the permeability of cell membranes for potassium ions. The difference in the effect of blue-green radiation on the release of hemoglobin molecules from erythrocytes and ion transport through the membrane is consistent with the known information about the spatial separation of these processes in the membrane and the difference in the mechanisms mediating them.

Addition of exogenous bilirubin to the erythrocyte suspension at concentration of 171 μM, at which phototherapy is prescribed for newborns with hyperbilirubinemia syndrome, accelerates spontaneous (dark) hemolysis, but reduces the light-induced hemoglobin release relative to cells that do not contain bilirubin.

Bilirubin, along with weak sensitizing properties, has antioxidant functions, reducing the release of hemoglobin molecules from the erythrocytes initiated by photochemical reactions in the membrane due to the excitation of endogenous porphyrin and flavin photosensitizers localized in these cells.

Bilirubin-sensitized leakage of potassium ions is more pronounced upon exposure to radiation of green spectral region, despite the weaker absorption of light in this region by bilirubin localized in erythrocytes. The reason for the abnormal dependence of the light-induced leakage of potassium ions from the erythrocytes on the wavelength of the incident radiation may be the participation of bilirubin photoisomers in sensitization processes, the quantum yield of which depends on the exciting radiation wavelength. Another reason for the increase in the potassium ions leakage during the transition from blue to green radiation may be the heterogeneity of the microenvironment of bilirubin molecules in the erythrocyte membrane. As a result, radiation of different wavelengths can excite bilirubin localized in different membrane sites and initiate different destructive processes in the membrane.

Photochemical destructive processes in the erythrocyte membrane, initiated due to the sensitizing effect of bilirubin and its photoisomers, proceed with insignificant participation of singlet oxygen, which is confirmed by a slight decrease in the leakage of potassium ions and hemoglobin molecules when the $^1O_2$ quencher, sodium azide, is added to the suspension before irradiation.

Reliably recorded damages of the bilirubin-sensitized erythrocyte membranes upon exposure to radiation of blue-green spectral region indicates the importance of optimizing the parameters of phototherapy of hyperbilirubinemia of newborns in order to reduce effectively the level of bilirubin and ensure minimal possible adverse side effects. The presence of the damaging effect of blue-green light on erythrocyte

membranes should also be taken into account at the development of photobiomodulation methods (including those based on intravenous exposure to blue light) and photodecontamination based on the inactivation of microorganisms due to excitation of endogenous photosensitizers.

Acknowledgements

This work was financially supported by the State Program of Scientific Research of the Republic of Belarus "Photonics and electronics for innovation" (No. 1.6).

The authors are grateful to Mrs. Tatsiana Ananich for her technical assistance.

Disclosures

The authors have no relevant financial interest in this article and no conflict of interest to disclose.

References

1. T. Hansen, M. Maisels, F. Ebbesen, H. Vreman, D. Stevenson, R. Wong, and V. Bhutani, "Sixty years of phototherapy for neonatal jaundice–from serendipitous observation to standardized treatment and rescue for millions," Journal of Perinatology 40(2), 180–193 (2020).
2. A. Lamola, "A pharmacologic view of phototherapy," Clinics in Perinatology 43(2), 259–276 (2016).
3. V. Plavskiĭ, A. Tret'yakova, and G. Mostovnikova, "Phototherapeutic systems for the treatment of hyperbilirubinemia of newborns," Journal of Optical Technology 81(6), 341–348 (2014).
4. S. Itoh, H. Okada, T. Kuboi, and T. Kusaka, "Phototherapy for neonatal hyperbilirubinemia," Pediatrics International 59(9), 959–966 (2017).
5. V. Bhutani, Committee on Fetus and Newborn, "Phototherapy to prevent severe neonatal hyperbilirubinemia in the newborn infant 35 or more weeks of gestation," Pediatrics 128(4), 1046–1052 (2011).
6. D. Seidman, J. Moise, Z. Ergaz, A. Laor, H. Vreman, D. Stevenson, and R. Gale, "A prospective randomized controlled study of phototherapy using blue and blue-green light-emitting devices, and conventional halogen-quartz phototherapy," Journal of Perinatology 23(2), 123–127 (2003).
7. F. Ebbesen, P. Vandborg, P. Madsen, T. Trydal, L. Jakobsen, and H. Vreman, "Effect of phototherapy with turquoise vs. blue LED light of equal irradiance in jaundiced neonates," Pediatric Research 79(2), 308–312 (2016).
8. V. Plavskii, A. Mikulich, I. Leusenko, A. Tretyakova, L. Plavskaya, N. Serdyuchenko, J. Gao, D. Xiong, and X. Wu, "Spectral range optimization to enhance the effectiveness of phototherapy for neonatal hyperbilirubinemia," Journal of Applied Spectroscopy 84(1), 92–102 (2017).
9. T. Kuboi, T. Kusaka, H. Okada, M. Arioka, K. Nii, M. Takahashi, S. Yamato, T. Sadamura, A. Nakano, and S. Itoh, "Green light-emitting diode phototherapy for neonatal hyperbilirubinemia: Randomized controlled trial," Pediatrics International 61(5), 465–470 (2019).
10. S. Kato, O. Iwata, Y. Yamada, H. Kakita, T. Yamada, H. Nakashima, T. Sugiura, S. Suzuki, and H. Togari, "Standardization of phototherapy for neonatal hyperbilirubinemia using multiple-wavelength irradiance integration," Pediatrics & Neonatology 61(1), 100–105 (2020).
11. F. Ebbesen, P. Vandborg, and M. Donneborg, "The effectiveness of phototherapy using blue-green light for neonatal hyperbilirubinemia – Danish clinical trials," Seminars in Perinatology 45(1), 151358 (2021).
12. F. Ebbesen, M. Rodrigo-Domingo, A. Moeller, H. Vreman, and M. Donneborg, "Effect of blue LED phototherapy centered at 478 nm versus 459 nm in hyperbilirubinemic neonates: a randomized study," Pediatric Research 89(3), 598–603 (2021).
13. B. Morris, W. Oh, J. Tyson, D. Stevenson, D. Phelps, and T. O'Shea, "Aggressive vs. conservative phototherapy for infants with extremely low birth weight," New England Journal of Medicine 359(18), 1885–1896 (2008).
14. J. Tyson, C. Pedroza, J. Langer, C. Green, B. Morris, and D. Stevenson, "Does aggressive phototherapy increase mortality while decreasing profound impairment among the smallest and sickest newborns?" Journal of Perinatology 32(9), 677–684 (2012).
15. C. Arnold, C. Pedroza, and J. E. Tyson, "Phototherapy in ELBW newborns: does it work? Is it safe? The evidence from randomized clisnical trials," Seminars in Perinatology 38(7), 452–464 (2014).
16. S. Yahia, A. E. Shabaan, M. Gouida, D. El-Ghanam, H. Eldegla, A. El-Bakary, and H. Abdel-Hady, "Influence of hyperbilirubinemia and phototherapy on markers of genotoxicity and apoptosis in full-term infants," European Journal of Pediatrics 174(4), 459–464 (2015).
17. N. Auger, C. Laverdière, A. Ayoub, E. Lo, and T. M. Luu, "Neonatal phototherapy and future risk of childhood cancer," International Journal of Cancer 145(8), 2061–2069 (2019).
18. J. Oláh, E. Tóth-Molnár, L. Kemény, and Z. Csoma, "Long-term hazards of neonatal blue-light phototherapy," British Journal of Dermatology 169(2), 243–249 (2013).
19. N. Ramy, E. A. Ghany, W. Alsharany, A. Nada, R. K. Darwish, W. A. Rabie, and H. Aly, "Jaundice, phototherapy and DNA damage in full-term neonates," Journal of Perinatology 36(2), 132–136 (2016).

20. T. Newman, Y. Wu, M. Kuzniewicz, B. Grimes, and C. McCulloch, "Childhood seizures after phototherapy," Pediatrics 142(4), e20180648 (2018).
21. T. Xiong, Y. Qu, S. Cambier, and D. Mu, "The side effects of phototherapy for neonatal jaundice: what do we know? What should we do?" European Journal of Pediatrics 170(10), 1247–1255 (2011).
22. J. Wang, G. Guo, A. Li, W. Q. Cai, and X. Wang, "Challenges of phototherapy for neonatal hyperbilirubinemia," Experimental and Therapeutic Medicine 21(3), 231 (2021).
23. V. Plavskii, V. Mostovnikov, A. Tret'yakova, and G. Mostovnikova, "Sensitizing effect of Z, Z-bilirubin IXα and its photoproducts on enzymes in model solutions," Journal of Applied Spectroscopy 75(3), 407–419 (2008).
24. G. Wondrak, M. Jacobson, and E. Jacobson, "Endogenous UVA-photosensitizers: mediators of skin photodamage and novel targets for skin photoprotection," Photochemical & Photobiological Sciences 5, 215–237 (2006).
25. B. Rosenstein, J. Ducore, and S. Cummings, "The mechanism of bilirubin-photosensitized DNA strand breakage in human cells exposed to phototherapy light," Mutation Research/DNA Repair Reports 112(6), 397–406 (1983).
26. F. Bohm, F. Drygalla, P. Charlesworth, K. Bohm, T. Truscott, and K. Jokiel, "Bilirubin phototoxicity to human cells by green light phototherapy in vitro," Photochemistry and Photobiology 62(6), 980–983 (1995).
27. O. Kozlenkova, L. Plavskaya, A. Mikulich, I. Leusenko, A. Tretyakova, and V. Plavskii, "Photodamage of the cells in culture sensitized with bilirubin," Journal of Physics: Conference Series 741(1), 012063 (2016).
28. E. Bruzell Roll, T. Christensen, "Formation of photoproducts and cytotoxicity of bilirubin irradiated with turquoise and blue phototherapy light," Acta Paediatrica 94(10), 1448–1454 (2005).
29. T. Christensen, G. Kinn, T. Granli, and I. Amundsen, "Cells, bilirubin and light: formation of bilirubin photoproducts and cellular damage at defined wavelengths," Acta Pædiatrica 83(1), 7–12 (1994).
30. T. Christensen, E. B. Roll, A. Jaworska, and G. Kinn, "Bilirubin and light induced cell death in a murine lymphoma cell line," Journal of Photochemistry and Photobiology B: Biology B 58(2–3), 170–174 (2000).
31. G. Odell, R. Brown, and A. Kopelman, "The photodynamic action of bilirubin on erythrocytes," The Journal of Pediatrics 81(3), 473–483 (1972).
32. M. Deziel, A. Girotti, "Bilirubin photosensitized lysis of resealed erythrocyte membranes," Photochemistry and Photobiology 31(6), 593–596 (1980).
33. M. Tozzi-Ciancarelli, G. Amicosante, A. Menichelli, S. Di Giulio, and D. Del Principe, "Photodynamic damage induced by bilirubin on human platelets: possible relevance to newborn pathology," Neonatology 48(6), 336–340 (1985).
34. E. Bruzell Roll, T. Christensen, and O. Gederaas, "Effects of bilirubin and phototherapy on osmotic fragility and haematoporphyrin-induced photohaemolysis of normal erythrocytes and spherocytes," Acta Paediatrica 94(10), 1443–1447 (2005).
35. K. Nii, H. Okada, S. Itoh, and T. Kusaka, "Characteristics of bilirubin photochemical changes under green light-emitting diodes in humans compared with animal species," Scientific Reports 11(1), 6391 (2021).
36. V. Plavskii, "Current State and Prospects for Development of Systems for Photodynamic Therapy of Neonatal Hyperbilirubinemia," Biomedical Engineering 47, 91–95 (2013).
37. A. McDonagh, G. Agati, F. Fusi, and R. Pratesi, "Quantum yields for laser photocyclization of bilirubin in the presence of human serum albumin. Dependence of quantum yield on excitation wavelength," Photochemistry and Photobiology 50(3), 305–319 (1989).
38. J. Ennever, T. Dresing, "Quantum yields for the cyclization and configurational isomerization of 4E,15Z-bilirubin," Photochemistry and Photobiology 53(1), 25–32 (1991).
39. S. Onishi, S. Itoh, and K. Isobe, "Wavelength-dependence of the relative rate constants for the main geometric and structural photoisomerization of bilirubin IXa bound to human serum albumin: demonstration of green light at 510 nm as the most effective wavelength in photochemical changes from (ZZ)-bilirubin IXa to (EZ)-cyclobilirubin IXa via (EZ)-bilirubin," Biochemical Journal 236(1), 23–29 (1986).
40. V. Plavskii, V. Mostovnikov, G. Mostovnikova, and A. Tret'yakova, "Spectral fluorescence and polarization characteristics of Z, Z-bilirubin IXα," Journal of Applied Spectroscopy 74(1), 120–132 (2007).
41. V. Plavskiĭ, V. Mostovnikov, A. Tret'yakova, and G. Mostovnikova, "Photophysical processes that determine the photoisomerization selectivity of Z, Z-bilirubin IXα in complexes with albumins," Journal of Optical Technology 74(7), 446–454 (2007).
42. H. Sato, S. Aono, R. Semba, and S. Kashiwamata, "Interaction of bilirubin with human erythrocyte membranes. Bilirubin binding to neuraminidase-and phospholipase-treated membranes," Biochemical Journal 248(1), 21–26 (1987).
43. H. Sato, S. Kashiwamata, "Interaction of bilirubin with human erythrocyte membranes," Biochemical Journal 210(2), 489–496 (1983).
44. A. Girotti, "Bilirubin-photosensitized crosslinking of polypeptides in the isolated membrane of the human erythrocyte," Journal of Biological Chemistry 253(20), 7186–7193 (1978).
45. J. Kruchenok, A. Sobchuk, G. Kurilo, N. Nemkovich, and A. Rubinov, "Study of interference laser field action on erythrocyte membranes by fluorescent probe with intramolecular proton transfer," Proceedings of SPIE 6257, 62570W (2006).

46. S. Bondarchuk, I. Bondarchuk, Statistical processing of experimental data in MS Excel: tutorial, Tomsk State Pedagogical University Publishing, Tomsk (2018). [in Russian]
47. A. Lamola, J. Esinger, W. Blumberg, S. Patel, and J. Flore, "Fluorometric study of the partition of bilirubin among blood components: basis for rapid microassays of bilirubin and bilirubin binding capacity in whole blood," Analytical Biochemistry 100(1), 25–42 (1979).
48. J. Vazquez, M. Garcia-Calvo, F. Valdivieso, F. Mayor, and Jr. F. Mayor, "Interaction of bilirubin with the synaptosomal plasma membrane," Journal of Biological Chemistry 263(3), 1255–1265 (1988).
49. T. Vadetskaya, N. Shukanova, and A. Vorobej, "Role of α-tocopherol and glutathione in membrane defense under photodynamic action on erythrocytes," Doklady Nacional'noj akademii nauk Belarusi 42, 101–103 (1998). [in Russian]
50. S. V. Lepeshkevich, A. S. Stasheuski, M. V. Parkhats, V. A. Galievsky, and B. M. Dzhagarov, "Does photodissociation of molecular oxygen from myoglobin and hemoglobin yield singlet oxygen?" Journal of Photochemistry and Photobiology B: Biology 120, 130–141(2013).
51. V. Plavskii, A. Mikulich, A. Tretyakova, I. Leusenka, L. Plavskaya, O. Kazyuchits, I. Dobysh, and T. Krasnenkova, "Porphyrins and flavins as endogenous acceptors of optical radiation of blue spectral region determining photoinactivation of microbial cells," Journal of Photochemistry and Photobiology B: Biology 183, 172–183 (2018).
52. V. Plavskii, A. Mikulich, N. Barulin, T. Ananich, L. Plavskaya, A. Tretyakova, and I. Leusenka, "Comparative effect of low-intensity laser radiation in green and red spectral regions on functional characteristics of sturgeon sperm," Photochemistry and Photobiology 96(6), 1294–1313 (2020).
53. V. Plavskii, N. Barulin, A. Mikulich, A. Tretyakova, T. Ananich, L. Plavskaya, I. Leusenka, A. Sobchuk, V. Sysov, O. Dudinova, A. Vodchits, I. Khodasevich, and V. Orlovich, "Effect of continuous wave, quasi-continuous wave and pulsed laser radiation on functional characteristics of fish spermatozoa," Journal of Photochemistry and Photobiology B: Biology 216, 112112 (2021).
54. J. Fernandez, M. Bilgin, and L. Grossweiner, "Singlet oxygen generation by photodynamic agents," Journal of Photochemistry and Photobiology B: Biology 37(1–2), 131–140 (1997).
55. S. Hustad, M. McKinley, H. McNulty, J. Schneede, J. Strain, J. Scott, and P. Ueland, "Riboflavin, flavin mononucleotide, and flavin adenine dinucleotide in human plasma and erythrocytes at baseline and after low-dose riboflavin supplementation," Clinical Chemistry 48(9), 1571–1577 (2002).
56. W. Marsh Jr, D. Nelson, and H. Koenig, "Free erythrocyte protoporphyrin (FEP) I. Normal values for adults and evaluation of the hematofluorometer," American Journal of Clinical Pathology 79(6), 655–660 (1983).
57. G. Hennig, C. Gruber, M. Vogeser, H. Stepp, S. Dittmar, R. Sroka, and G. Brittenham, "Dual-wavelength excitation for fluorescence-based quantification of zinc protoporphyrin IX and protoporphyrin IX in whole blood," Journal of Biophotonics 7(7), 514–524 (2014).
58. M. Musawi, M. Jafar, B. Al-Gailani, N. Ahmed, F. Suhaimi, and N. Suardi, "In vitro mean red blood cell volume change induced by diode pump solid state low-level laser of 405 nm," Photomedicine and Laser Surgery 34(5), 211–214 (2016).
59. T. Machneva, N. Kosmacheva, Yu. Vladimirov, and A. Osipov, "The effects of low power laser radiation on blue, green and red ranges on free radical processes in rat blood in endotoxic shock," Biochemistry (Moscow), Supplement Series B: Biomedical Chemistry 6(3), 237–246 (2012).
60. A. McDonagh, "The biliverdin–bilirubin antioxidant cycle of cellular protection: Missing a wheel?" Free Radical Biology and Medicine 49(5), 814–820 (2010).
61. A. Dvořák, K. Pospisilova, N. Capkova, L. Muchova, M. Vecka, N. Vrzackova, J. Krízová, J. Zelenka, and L. Vítek, "The effects of bilirubin and lumirubin on metabolic and oxidative stress markers," Frontiers in Pharmacology 12, 567001 (2021).
62. M. A. Brito, R. F. Silva, and D. Brites, "Bilirubin toxicity to human erythrocytes: a review," Clinica Chimica Acta 374(1–2), 46–56 (2006) .
63. A. Frolov, G. Gurinovich, "The laws of delayed photohaemolysis sensitized by chlorin e6," Journal of Photochemistry and Photobiology B: Biology 13(1), 39–50 (1992).
64. N. Peskova, A. Brilkina, A. Gorokhova, N. Shilyagina, O. Kutova, A. Nerush, A. Orlova, L. Klapshina, V. Vodeneev, and I. Balalaeva, "The localization of the photosensitizer determines the dynamics of the secondary production of hydrogen peroxide in cell cytoplasm and mitochondria," Journal of Photochemistry and Photobiology B: Biology 219, 112208 (2021).
65. V. Plavskii, L. Plavskaya, T. Ananich, V. Katarkevich, A. Mikulich, I. Leusenko, A. Tretiakova, O. Dudinova, P. Mazmanyan, V. Karapyan, and G. Margaryan, "New approaches to improve efficacy and reduce side effects of phototherapy for neonatal hyperbilirubinemia using led and laser sources," Photobiology and Photomedicine 26, 63–72 (2019).
66. H. Vreman, S. Kourula, J. Jašprová, L. Ludvíková, P. Klán, L. Muchova, L. Vítek, B. Cline, R. Wong, and D. Stevenson, "The effect of light wavelength on in vitro bilirubin photodegradation and photoisomer production," Pediatric Research 85(6), 865–873 (2019).

67. G. Agati, F. Fusi, G. Donzelli, and R. Pratesi, "Quantum yield and skin filtering effects on the formation rate of lumirubin," Journal of Photochemistry and Photobiology B: Biology 18(2–3), 197–203 (1993).
68. V. Glushko, M, Thaler, and M. Ros, "The fluorescence of bilirubin upon interaction with human erythrocyte ghosts," Biochimica et Biophysica Acta (BBA)-General Subjects 719, 65–73 (1982).
69. R. Bormett, S. Asher, P. Larkin, W. G. Gustafson, N. Ragunathan, T. Freedman, L. Nafie, S. Balasubramanian, S. Boxer, N. Yu, K. Gersonde, R. Noble, B. Springer, and S. Sligar, "Selective examination of heme protein azide ligand-distal globin interactions by vibrational circular dichroism," Journal of the American Chemical Society 114(17), 6864–6867 (1992).
70. E. Nagababu, J. Mohanty, S. Bhamidipaty, G. Ostera, and J. Rifkind, "Role of the membrane in the formation of heme degradation products in red blood cells," Life Sciences 86(3–4), 133–138 (2010).
71. L. Huang, T. G. S. Denis, Y. Xuan, Y. Huang, M. Tanaka, A. Zadlo, T. Sarna, and M. Hamblin, "Paradoxical potentiation of methylene blue-mediated antimicrobial photodynamic inactivation by sodium azide: Role of ambient oxygen and azide radicals," Free Radical Biology and Medicine 53(11), 2062–2071 (2012).
72. M. Hamblin, H. Abrahamse, "Inorganic salts and antimicrobial photodynamic therapy: mechanistic conundrums?" Molecules 23(12), 3190 (2018).

Lower Limb Analysis of the Biomechanical Gait Cycle at Various Phases in Real Time

Zainab M. Nahi, Huda F. Jameel*, and Ahmed B. Fakhri
Department of Medical Instrumentation Techniques Engineering, Electrical Engineering Technical College, Middle Technical University, AL-Doura, AL-Masfi str., Baghdad, Iraq

***e-mail:** huda_baban@mtu.edu.iq

Abstract. Biotechnology is playing an extremely important part in medical advances. In actuality, they are the basis of pathology diagnosis, which provides doctors with the quantitative data required to choose the best treatment. This study looks at the facts of a case of weak muscular activity and devises solutions to help the disabled or very ill for the specialist to improve the patient's condition by choosing accurate treatment. This would enhance their psychological condition and make it easier for them to do their daily activities. The data are collected by surface electromyography (EMG) from the lower limb of the leg gait events (heel strike, foot flat, midstance, heel off, toe-off, and medium swing) on the right, left, and both legs are estimated. The system consists of a microcontroller, a myograph sensor, and Bluetooth. Healthy individuals utilize both legs regularly in a balanced manner and during a walk as well as stair ascending tests. On both sides of the legs (right and left), sensors are placed on the quadriceps, hamstrings, tibialis, and triceps muscles. The system was tested on 28 people (17 males and 11 females) aged 24–54 years old. The suggested method is used to analyze gait in real-time.
© 2023 Journal of Biomedical Photonics & Engineering.

Keywords: bluetooth; gait cycle; hamstrings muscle; myograph sensor; microcontroller; quadriceps muscle; surface emg; tibialis muscle; triceps muscle.

Paper #8682 received 4 Mar 2023; revised manuscript received 14 May 2023; accepted for publication 29 May 2023; published online 13 Jun 2023. doi: 10.18287/JBPE23.09.020304.

1 Introduction

Electromyography (EMG) is a method for measuring and monitoring electrical impulses in muscle contraction. An EMG examination can be used in a variety of clinical and biological circumstances. Surface EMG is employed in experimental gait analysis and for physiological diagnostics. EMG is applied to control prosthetic devices such as artificial limbs, forearms, arms, knees, and lower limbs. So, a systematic review of current publications on the EMG activity of six muscles throughout physical fitness activities in healthy individuals was proposed [1]. However, the level of proof in the included papers was mostly medium, suggesting that further high-quality research was needed to decrease the risk of distortion and make definite conclusions concerning muscle activation. Also, study of electromyography systems, control models, problems, and potential future approaches was introduced [2]. This review focuses on the potential for EMG control to enable expanded capabilities in mechanical lower limb prostheses as well as the challenges, knowledge gaps, and research possibilities in this area from the viewpoints of patient care and individual muscle control. In addition, to capture the mechanical behaviour of the lower leg, staircase ambulation was used [3] as a basis for wearable technology and control systems. This article would specifically address transitions between level walking and stair mobility, as well as transitions between bipedal walking and walking.

Biomedical technologies are becoming increasingly important in modern medicine. In reality, they were at the heart of pathology diagnosis and follow-up, providing doctors with the statistical data needed to choose the best medication. The biomedical techniques that are used in gait parameters, covering the top issues utilized in clinical practice for neurologic, musculoskeletal, and rheumatic disorders and emphasizing their usefulness in

the clinical environment [4]. In addition, electrical impedance myography (EIM) is a bioimpedance method that records the voltage produced by delivering a low or high over a muscle area without triggering myofiber or neuronal nerve impulses. The volume conduction properties (VCPs) of the muscle were measured using EIM. VCPs have the potential to be used as a standardized, measurable, and reliable electrophysiological diagnostic of muscle [5]. A classification tree gait pattern identification model effectively detected loading response, push-off, and swing for five distinct environments as well as a variety of walking speeds, using input data from the leg and knee was proposed [6]. The classifier proved resistant to a variety of simulated travel scenarios encountered in daily life and was able to generalize previously unknown data from diverse participants. Furthermore, displaying muscle activation and strength utilizing an EMG with auditory, vision, and/or motion presentation has been accomplished [7]. However, employing conductive gel to link the EMG electrode to the skin surface would generate a steady signal of muscle activity

There are many areas, which can measure the muscle activity, and there are many researches in these fields such as to examine the worker's body position during lifting and to compare the use of lower back support while lifting. It also uses EMG to study the worker's muscle function during excessive lifting and CATIA Software to replicate the worker's movement for rapid upper limb assessment (RULA) findings. The results demonstrate that workers who use lower back support have raw EMG signals with lower muscle activity than workers who do not use lower back support. When compared to not using back support, utilizing belt support can lower muscular activity by up to 67.4% [8]. Similarly, development of low back discomfort (LBD) when standing was linked to spinal muscle activation and pelvic motion. In analysis, the system looked at whether age, gender, and long-term work habits modified the LBD. However, given the relatively minor changes discovered, the therapeutic significance of this discovery in the chosen difference requires further investigation [9]. Although, a surface electromyography (sEMG) electrodes were used to measure muscle activity in the bilateral and trapezius muscles during the continuous farmland preparation procedure. Objective preference findings suggest that the bilateral, tracked by the trapezius left muscle, were the most uncomfortable during earthwork [10]. Based on machine learning, a unique approach for classifying gait phases in power gait exoskeleton users was proposed [11]. A period camera mounted on the crutches used for assisted walking was employed to capture the depth information. The machine learning approach predicts the first stage of data collection and processing throughout which the 3D points related to the foot and those related to the surface are established.

On the other hand, there are many research measured the muscle activity for arm, forearm, upper arm, and wrist as well as arm like an electrical device that can estimate the activity of any muscle in the human body was generate. The contraction in the normal case, with athletic body muscles, as well as in the situation of neuromuscular disorder was designed [12]. The initial concept was based on a biosensor on the biceps muscle. Muscle activity was monitored using different hand-loaded weights and varied ranges of action of the elbow joint. In addition, a surface EMG signal based joint torque estimate technique was provided to quantify the motion intention. To improve the accuracy of the calculated torque, a neural network was employed to learn the ideal factor of muscular strength. However, it should focus on creating a control technique based on this torque estimation method to operate rehabilitative exoskeleton robots [13]. Moreover, examines the effectiveness of stroke survivors in terms of detecting weak muscle activity and reaction by involuntary amplitude variation of EMG signals was illustrated. Using surface EMG data obtained from six hemiparesis stroke patients and six healthy participants, according to the findings, the amplitude-independent algorithm performed better in terms of recognizing weaker muscle activity and avoiding false alarms. However, this may be done by utilizing surface EMG data from individuals with various kinds of damage to validate the effectiveness of amplitude-independent approaches for detecting muscle activation [14]. Besides, a compare EMG for handstands done on three different pieces of equipment (ground, circles, and parallel bars), as well as the variation between juvenile and highly-trained senior gymnasts was presented. The study included ten adults and fifteen young gymnasts. Researchers looked at the magnitude of EMG signals in thirteen muscles that were standardized by the arbitrary angle of maximal exercise voluntary movement [15].

A new force myography (FMG) sensor has been developed to identify physical muscle contractions in lost limbs [16]. FMG is an approach for registering limb muscle activity utilizing accelerometer sensors and movement observation applications. Notwithstanding its recent recognition among investigators, many of its essential properties are right now unclear. The FMG consists of one or maybe more sensors for obtaining muscle contraction data from missing limbs and an embedded system that receives input data from the sensors as well as produces control instructions. Also, techniques for converting FMG signals from the sensing element to control instructions have been developed. Moreover, a muscular activity visualization system was developed to investigate the mapping link between hand gestures and activated upper arm-specific muscles. The graphics system's human-computer interaction showed that this approach could visually depict the relationship between multiple channels in the image space, allowing users to intuitively recognize the activity intensity of different muscles in hand movements [17]. To determine the lowest sample frequency required for capturing upper-limb FMG responses without compromising signal quality. Twelve participants took part in the test in which they were taught to perform quick hand motions while

FMG responses from the wrist and the bulk area of the arm were monitored [18].

In the same way, a muscle activity for the lower limbs and knee is clarified like postural control, as well as trunk independence, increased considerably after multi-muscle stimulation of the lower limbs was proposed. The aforementioned lower body part multi-muscle stimulator training strategy, using standard parameters at sub-maximal rates, is therefore expected to benefit trunk functional status. To test the generalizability of the findings and the motor patterns in assisted stepping, the number of musculoskeletal electrical events, stand training routines, and a larger sample size of studies were required [19]. Along with, to examine the effects of hippotherapy on lower-body activation and gross motor performance in participants with cerebral palsy in a population with appropriate motor development. It is possible to infer that hippotherapy offered a sequence of muscular stimulation that resulted in gains in capability and lower limb activation, and this treatment practice could contribute to the active recovery and better motor ability of people with cerebral palsy [20]. Four short pieces of training of submaximal attempt in eccentric (ECC) cycling resulted in lower activities of the rectus femoris (RF), biceps femoris (BF), soleus (SOL), and vastus lateralis (VL) muscles. Also, an impression of mostly less effort in ECC than in Concentric (CON) cycling across a variety of power outputs – despite the fact that most different factors were not different between exercise methodologies prior to the event. Subdivisions in muscular activity and heart rate decreased following the cycling events but were generally larger with ECC cycling. However, before doing any muscular activity or sensory tests, future studies should consider undertaking numerous periods of ECC cycling [21]. In spite of, to examine hip and knee muscular activation during single-limb standing and single-limb squat in men having patellofemoral pain (PFP) as well as a control group, which thus did not have PFP was proposed. Furthermore, muscle activation patterns differed between the PFP and healthy individuals. As a result, the findings confirm the idea that any impairment in the intermediate muscles involved in the leg might have an impact on the patellofemoral joint [22].

Inertial motion detectors are essential components of today's intelligent devices. They have the ability to be a component of future technologies like intelligent buildings, the internet of things (IoT), and the internet of everything (IoE). A two-stage sensor fusion technique that produces joint angle in real-time was proposed, implemented, and verified [23]. In the first stage, the drifts in each inertial sensor combined gyroscope data were estimated using the method designated gradient declivity. To provide a real-time evaluation of the angular position, the inclination data from both inertial sensors were combined in the second stage using a gradient declivity approach. Examines and develops a mobile gait detection method for patients depending on an inertial measurement unit, including the hardware and software design of the data collection module, were presented [24]. Control performance of the musculoskeletal systems is used to determine gait kinematics and reaction mechanisms [25]. Inertial sensor information proposes a methodology for immediately estimating gait from inertial sensors using a single dynamic algorithm. Furthermore, the muscular effort was reduced to ensure a one-of-a-kind response. A seven-inertial measurement was used to collect data from 10 people walking and jogging at six different speeds. Create practical and reliable approaches for detecting gait movements in people with gait abnormalities in real-time. In addition, a collection of methods for online identification of gait patterns and actions was presented. Furthermore, they created an upgraded version of an IMU-based portable device that enables gait data monitoring and recording [26].

Typical gait analysis approaches were carried out under controlled conditions in a costly motion-capture laboratory. Although the technique produces reliable findings, it does not allow for continual monitoring and evaluation. Wearable systems with inertial measurement units are an option. However, inertial sensor suffers from drift as a result of the double processing used to obtain position information. However, ultrasonic sensors can be used to counteract this drift. A simple, reliable measure of the ankle angle (AA) utilizing ultrasonic sensors and triangulation methods without using sophisticated inertial sensor techniques was proposed [27]. Furthermore, the suggested technique detects the minimal toe clearance (MTC), which was another significant gait parameter. The suggested system analyzes a person's gait for long durations for a day scenario and assesses essential gait characteristics that were utilized for gait problem therapy and fall detection in the older adult population. Finally, a novel approach for measuring knee joint angle was proposed. The technique used force myogram responses from thigh muscles as individuals walked on a machine at various speeds, including slow, moderate, high, and run. The method has been validated on both able-bodied people and a transfemoral prosthesis. However, research might look at expanding the current technique to a more diverse patient group [28]. The actions of the multifidus, internal oblique, quadriceps, and tibialis anterior muscles in inactive adults were identical to those observed with walking and hippotherapy employing various methods and elements. The results of this controlled research may be compared to those of patients with various clinical illnesses who appear to have independent walking impairment in order to truly comprehend the alterations that happen in their trunks [29].

The drawback from the previous works is that they have used only one sensor location and one to five muscle types, so to get effective results in collecting data and analyzing it, this paper uses heel-strike, foot flat, midstance, heel-off, toe-off, and medium swing of the right leg, left leg, and both legs. This paper has been classified several related studies based on sensor location, sensor type, muscle test, and gender and

compared with proposed method as illustrated in (Table 1).

The purpose of this study is to get a more thorough understanding of the challenges posed by weak muscular activity and to propose options to assist the disabled by enabling the specialist to assist patients, improve their situation and stimulate the weak muscles. The aforementioned would improve their psychological state and enable them to do their everyday tasks more naturally. The system components include a Bluetooth module, a myograph sensor, and a microcontroller. It was established during a walking and stair climbing test that healthy participants use both legs equally and in a balanced way.

The research contributes:

1. A review of the use of muscle activity systems in previous works.
2. To collect surface EMG data from the lower limb of the leg.
3. To predict gait events (heel-strike, foot flat, midstance, heel off, toe-off, and Medium swing) of the right leg, left leg, and both legs.

2 Methodology

The suggested system consists of a myograph put on the limb of the user, the data (muscle activity) is wirelessly transmissible to a computer or phone for analysis, and a microcontroller processes the data. The sensors were placed on the legs of the chosen muscles, namely quadriceps, hamstrings, tibialis, and triceps on both sides (right and left). The suggested method can be used for real-time motion analysis. The system is simple to wear, practical for outdoor usage, lightweight, and commercially feasible. Fig. 1 represents the block diagram of the system with all components.

Table 1 Comparison of sensor location, sensor type, muscle test, and gender in previous works.

Year, Ref.	Sensor location	Sensor type	Muscle test	Gender
2020, [8]	back	myograph	low back	7 male
2020, [12]	arm	myograph	biceps	4 persons
2021, [13]	arm	myograph	elbow joint angle	not available
2020, [14]	arm	myograph	not available	6 healthy and 6 hand impairment (4 female)
2019, [19]	lower limbs	myograph		
2019, [9]	back	myograph	erector spinae and medio-lateral pelvic	15 young females, 15 young males, 15 older males, and 15 young males
2019, [20]	lower limbs	myograph		7 individuals
2019, [22]	hip and knee muscles	myograph	not available	18 males
2020, [16]	forearm	force myography sensor	forearm	1 male
2020, [17]	arm	sEMG	upper arm muscle	not available
2019, [15]	arm	EMG	anterior deltoid, pectoralis major, latissimus dorsi, biceps brachii, and trapezius descendent muscles	10 adult and 15 young
2021, [10]	bellies	sEMG	trapezius and biceps brachii	10 volunteers
2019, [18]	wrist and forearm	force myography (FMG)	not available	12 volunteers
2020, [28]	knee	FMG	thigh muscles	8 men
Proposed method	lower limbs	myograph	quadriceps, hamstrings, tibialis, and triceps on both sides (right and left).	28 persons (17 males and 11 females)

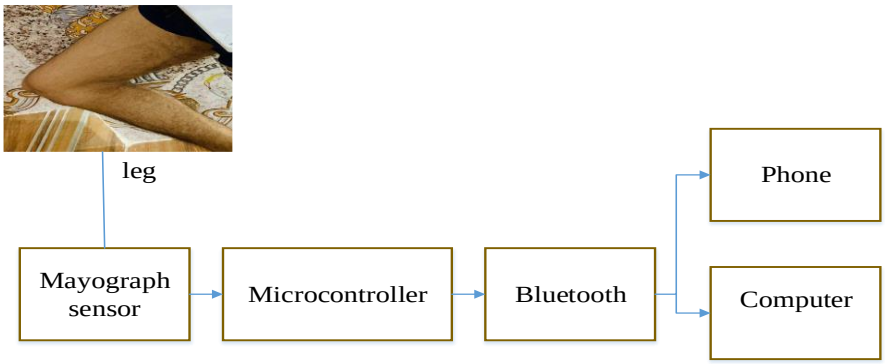


Fig. 1 Block diagram of the system.

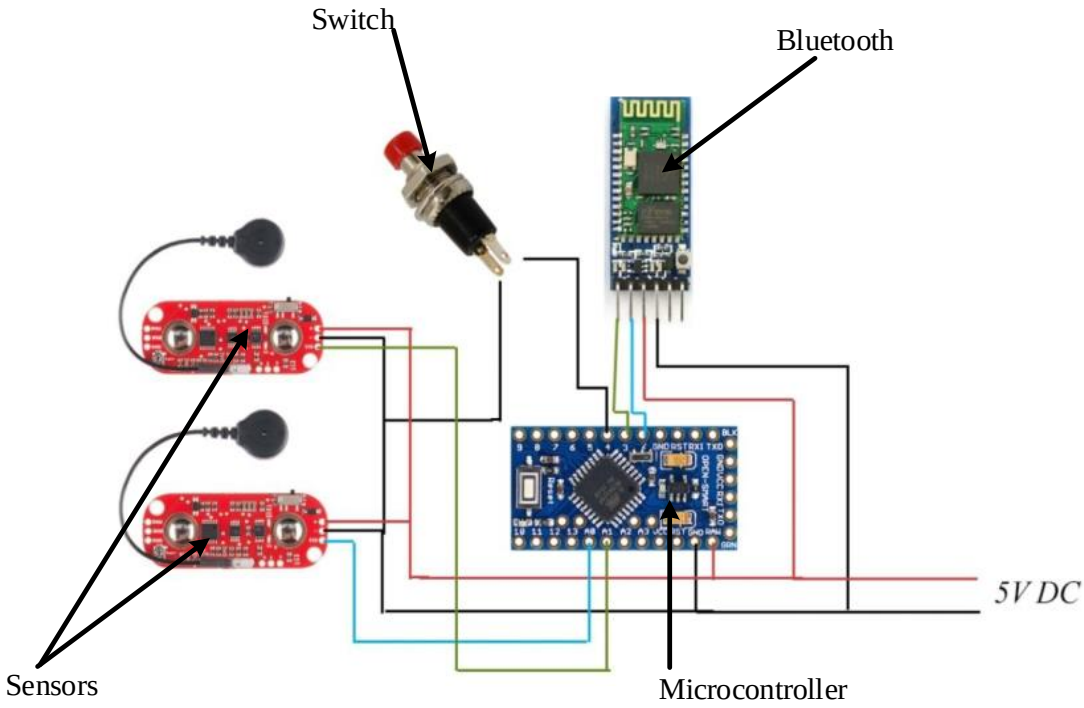


Fig. 2 Schematic and the hardware components of the system.

Table 2 Action of muscles during activities.

Muscle name	Action	Ph. 1	Ph. 2	Ph. 3	Ph. 4	Ph. 5	Ph. 6
Quadriceps	knee extensors helping in control of knee flexion	W.	W.	N.W.	W.	N.W.	N.W.
Gluteus Maximus	Move of the hip and thigh	W.	W.	N.W.	N.W.	N.W.	N.W.
Hamstrings	Extend the hip and flex knee via concentric contraction	W.	N.W.	N.W.	N.W.	N.W.	W.
Iliopsoas	hip flexor and active during the initial and mid-swing phase	N.W.	N.W.	N.W.	W.	W.	N.W.
Tibialis Anterio	During loading response and initial swing and the ankle dorsiflexion during the late swing phase.	W.	W.	N.W.	W.	W.	W.
Triceps	During late mid-stance and terminal stance	N.W.	N.W.	W.	N.W.	N.W.	N.W.

Ph.: phase, W.: work, N.W.: not work,
Ph. 1: heel strike, Ph. 2: foot flat, Ph. 3: Midstance, Ph. 4: Heel off, Ph. 5: Toe release, Ph. 6: Medium swing.

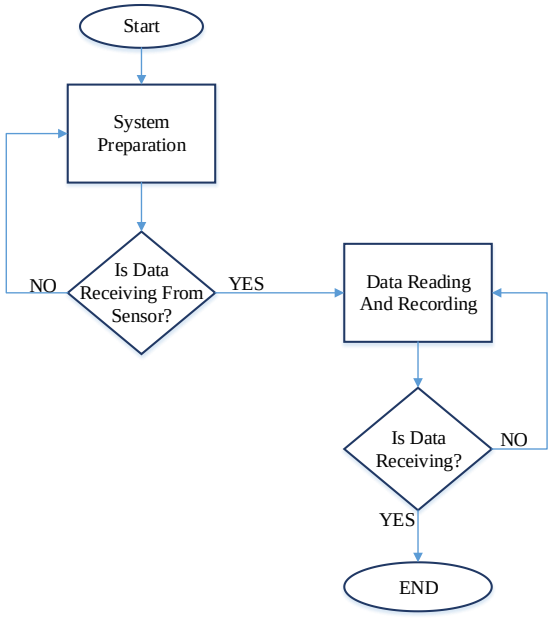


Fig. 3 System flowchart.

Besides, Fig. 2 illustrate the schematic and the hardware components of the system, which comprises an Arduino Pro Mini board [30, 31], two MyoWare muscle sensor module [32], and Bluetooth [33, 34]. The signals from the MyoWare are received by the microcontroller, and the computer or phone serves as an adapter between the microcontroller and the MyoWare. In the Arduino programming, the obtained signals are processed using a specified algorithm that cleared as a flowchart which is depicted in Fig. 3.

3 Data Collection

The position and origin point of the muscles themselves determine the individual body parts responses to a muscle function. To make this procedure simpler, the system will concentrate on the body's skeletal muscles. The mobility of the majority of skeletal muscles is restricted or guided by their attachment to bone, cartilage, or connective tissue. The testing of the data is applied to 28 normal people (17 males and 11 females) aged from 24 to 54 years old. The data for this work has been collected from following:

Part 1: for normal walking with and without weight (5 kg, 10 kg, and 15 kg); for quadriceps as well as hamstring muscles, once for left leg and once for right leg with six phases.

Part 2: for stair clamping with and without weight (5 kg, 10 kg, and 15 kg), for quadriceps as well as hamstring muscles, once for the left leg and once for the right leg, with six phases.

Part 3: six phases for two legs at the same time for normal walking and stair clamping with and without weight (5 kg, 10 kg, and 15 kg) for quadriceps and hamstring muscles.

Part 4: for normal walking with and without weight (5 kg, 10 kg, and 15 kg); for Tibialis and triceps muscles, with six phases, once for left leg and once for right leg.

Part5: for stair clamping with and without weight (5 kg, 10 kg, and 15 kg), for tibialis as well as triceps muscles, once for the left leg and once for the right leg, with six phases.

Part 6: six phases for two legs at the same time for normal walking and stair clamping with and without weight (5 kg, 10 kg, and 15 kg) for Tibialis and triceps muscles.

4 Result and Discussion

For muscle evaluation by observing the user and recording the readings of muscle contraction and relaxation during walking and climbing the stairs for all the parts that were mentioned in the collection of data, it is notice that some muscles strengthen and weaken during the phase that is assigned to them. As illustrated in Table 2, that shows the action of muscles during activities.

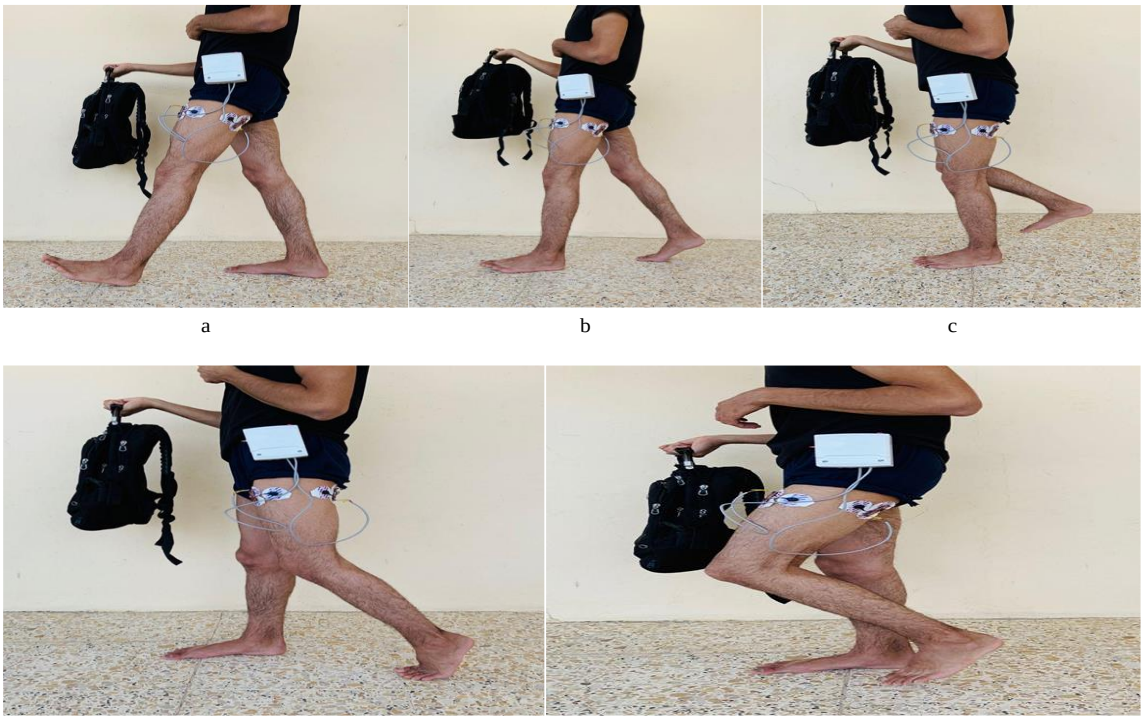
The collected data presented in Table 3 represented the quadriceps and hamstring muscles and the sensor on the left leg (with or without weight). The numbers in the tables are the activity of the muscles as a voltage that was collected from the sensor, which is measured in microvolts, and Fig. 4 shows the phases for each case.

The collected data presented in Table 4 represented the quadriceps and hamstring muscles and the sensor on the left leg (with or without weight). The numbers in the tables are the activity of the muscles as a voltage that was collected from the sensor, which is measured in microvolts, and Fig. 5 shows the phases for each case.

The collected data presented in Table 5 represented the tibialis and triceps muscles and the sensor on the left leg (with or without weight). The numbers in the tables are the activity of the muscles as a voltage that was collected from the sensor, which is measured in microvolts, and Fig. 6 shows the phases for each case.

Table 3 Activity of the quadriceps and hamstring muscles in microvolts (with or without weight).

Muscle name	Heel strike	Foot flat	Midstance	Heel release	Toe release	Medium swing
Gait cycle with normal walk						
Quadriceps	251	212	198	279	328	231
Hamstrings	92	70	56	91	88	57
Normal walk with 5 kg in the left hand						
Quadriceps	88	152	244	221	243	191
Hamstrings	66	171	234	342	355	244
Normal walk with 10 kg left hand						
Quadriceps	297	236	145	163	255	205
Hamstrings	73	87	87	26	65	60
Normal walk with 15 kg left hand						
Quadriceps	317	329	300	314	334	330
Hamstrings	499	455	416	433	412	366
Normal walk with 5 kg in the right hand						
Quadriceps	323	327	322	312	355	368
Hamstrings	315	312	300	307	355	352
Normal walk with 10 kg right hand						
Quadriceps	362	312	308	323	330	333
Hamstrings	448	318	308	397	319	324
Normal walk with 15 kg right hand						
Quadriceps	170	178	129	186	215	134
Hamstrings	174	192	132	152	150	139



a b c d e

Fig. 4 Phases of a) heel strike phase, b) foot flat phase, c) midstance phase, d) heel off phase, e) medium swing phase.

Table 4 Activity of the quadriceps and hamstring muscles in microvolts (with or without weight).

Muscle name	Heel strike	Foot flat	Midstance	Heel release	Toe release	Medium swing
Stair climbing						
Quadriceps	116	224	214	128	146	139
Hamstrings	227	325	238	231	265	390
Stair climbing with 5kg in the left hand						
Quadriceps	195	213	215	171	214	153
Hamstrings	255	291	282	263	253	276
Stair climbing with 10kg left hand						
Quadriceps	151	212	165	191	245	303
Hamstrings	256	281	216	254	291	250
Stair climbing walk with 15kg left hand						
Quadriceps	128	219	231	280	192	244
Hamstrings	312	236	314	285	218	234
Stair climbing with 5kg in the right hand						
Quadriceps	125	237	195	324	142	205
Hamstrings	157	218	253	112	214	176
Stair climbing with 10kg right hand						
Quadriceps	163	512	378	114	221	251
Hamstrings	193	318	200	134	161	250
Stair climbing walk with 15kg right hand						
Quadriceps	192	352	590	408	400	619
Hamstrings	183	272	380	357	215	305

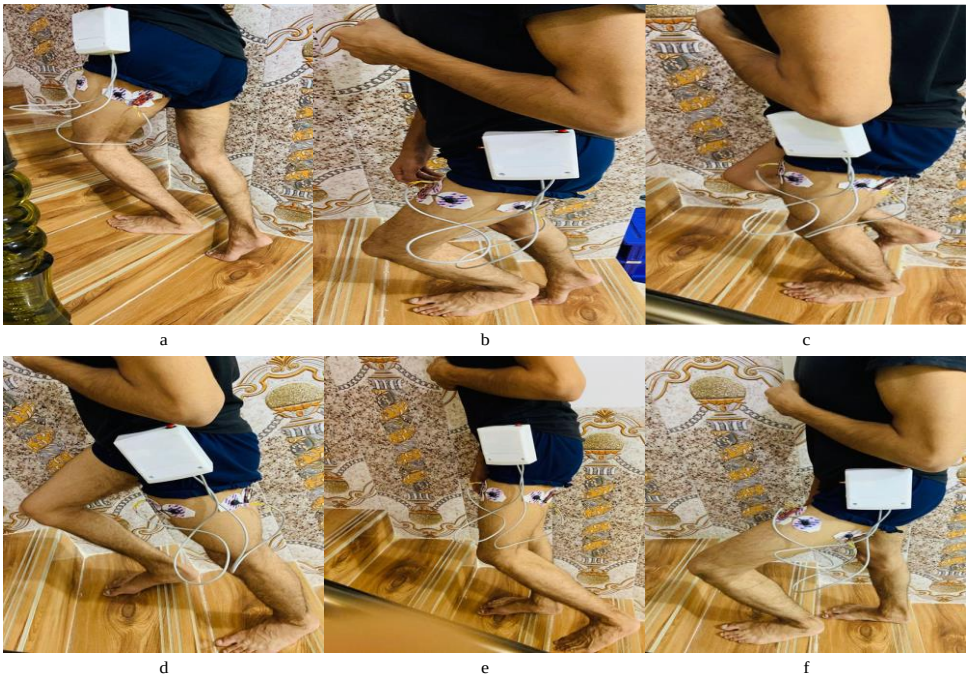
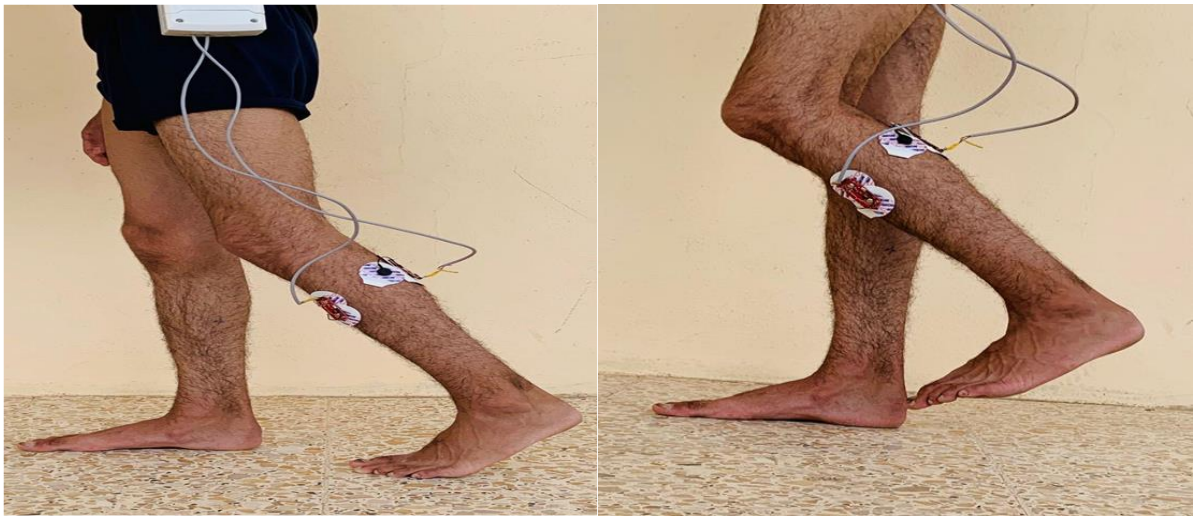


Fig. 5 Phases of a) foot flat phase, b) toe release phase, c) medium swing phase, d) midstance phase, e) midstance phase, f) heel strike phase.

Table 5 Activity of the tibialis and triceps muscles in microvolts (with or without weight).

Muscle name	Heel strike	Foot flat	Midstance	Heel release	Toe release	Medium swing
Stair climbing						
Tibialis	121	221	349	135	128	166
Triceps	94	124	149	121	139	96
Stair climbing with 5 kg in the left hand						
Tibialis	74	225	357	169	134	186
Triceps	98	130	176	132	175	114
Stair climbing with 10 kg left hand						
Tibialis	212	214	394	124	169	102
Triceps	105	102	174	175	168	87
Stair climbing walk with 15kg left hand						
Tibialis	137	246	225	235	195	285
Triceps	114	113	224	318	405	163
Stair climbing with 5kg in the right hand						
Tibialis	266	272	379	228	199	168
Triceps	120	147	173	182	291	158
Stair climbing with 10kg right hand						
Tibialis	121	276	527	287	282	202
Triceps	106	147	183	126	389	246
Stair climbing walk with 15kg right hand						
Tibialis	145	445	286	338	214	209
Triceps	109	122	195	210	187	124



a b

Fig. 6 Phases of a) foot flat phase, b) medium swing phase.

The collected data presented in Table 6 represented the right (R.) triceps and left (L.) triceps muscles and the sensor on the left and right leg (with or without weight). The numbers in the tables are the activity of the muscles as a voltage that was collected from the sensor, which is measured in microvolts, and Fig. 7 shows the phases for each case.

Table 6 Activity of the right (R.) triceps and left (L.) triceps muscles in microvolts (with or without weight).

Muscle name	Heel strike	Foot flat	Midstance	Heel release	Toe release	Medium swing
Normal walk						
R. Triceps	138	141	193	124	120	117
L. Triceps	130	124	127	103	200	190
Normal walk with 5kg in the left hand						
R. Triceps	85	202	145	76	162	188
L. Triceps	167	111	103	105	231	193
Normal walk with 10kg left hand						
R. Triceps	124	80	177	70	160	190
L. Triceps	118	140	121	155	181	204
Normal walk with 15kg left hand						
R. Triceps	88	374	356	98	213	188
L. Triceps	125	160	109	100	165	211
Normal walk with 5kg in the right hand						
R. Triceps	92	208	292	100	122	128
L. Triceps	128	193	124	105	212	231
Normal walk with 10kg right hand						
R. Triceps	106	190	324	80	79	115
L. Triceps	130	163	146	107	228	282
Normal walk with 15kg right hand						
R. Triceps	167	140	355	86	135	127
L. Triceps	110	240	110	100	244	258



a b

Fig. 7 Phases of a) heel strike phase, b) Midstance phase.

From the results, in normal walking with quadriceps muscles, when the weight is in the left hand, the activity increases, and in stair climbing, when the weight is in the left hand, the activity decreases significantly in the first three stages and increases in the other three. Also, in normal walking with tibialis muscle weight in the left hand, the activity increases, and when stair ascending with weight in the left hand, the action is the same as with weight. In addition, in a comparison between the left and right triceps muscles, when the weight is in the left hand, the activity increases in the left muscle more than the right, and when the weight is in the right hand, the activity increases in the right muscle more than the left.

5 Conclusion

In this paper, the activation values of the tibialis, triceps, quadriceps, and hamstring muscles are measured and analyzed in different conditions. The value is found by a wireless system using an Arduino microcontroller and wearable muscle sensors. With the practical experience, which involved the gait cycle at various phases, the biomechanics influence was implemented. On the right, left, and both legs, gait cycles are computed in real-time for heel contact, foot neutrality, oriented practices, heel release, toe-off, and medium swing. The results are found with phases of the gait cycle in normal walking and upstairs, with and without lifting weight. The measurements are applied to 28 individuals (17 males and 11 females) aged 24–54 years old, and the collected data represents the voltage activity of the muscles that can be used for future work to get more equate results to analyze the biomechanical gait cycle at various phases in real time.

Acknowledgements

For their assistance throughout this investigation, the authors gratefully acknowledge the Department of Medical Instrumentation Techniques Engineering, Electrical Engineering Technical College, Middle Technical University.

Disclosures

The authors have no relevant financial interest in this article and no conflict of interest to disclose.

References

1. J. M. Oliva-Lozano, J. M. Muyor, "Core muscle activity during physical fitness exercises: A systematic review," International Journal of Environmental Research and Public Health 17(12), 4306 (2020).
2. A. Fleming, N. Stafford, S. Huang, X. Hu, D. P. Ferris, and H. H. Huang, "Myoelectric control of robotic lower limb prostheses: a review of electromyography interfaces, control paradigms, challenges and future directions," Journal of Neural Engineering 18(4), 041004 (2021).
3. M. Grimmer, J. Zeiss, F. Weigand, G. Zhao, S. Lamm, M. Steil, and A. Heller, "Lower limb joint biomechanics-based identification of gait transitions in between level walking and stair ambulation," Plos One 15(9), e0239148 (2020).
4. F. Lullo, L. Donisi, G. Piscosquito, B. Lanzillo, C. Armando, and G. D'Addio, "Gait analysis: technical notes," Journal of Advanced Health Care 2(1), 67–70 (2020).
5. B. Sanchez, O. G. Martinsen, T. J. Freeborn, and C. M. Furse, "Electrical impedance myography: a critical review and outlook," Clinical Neurophysiology 132(2), 338–344 (2021).
6. J. D. Farah, N. Baddour, and E. D. Lemaire, "Design, development, and evaluation of a local sensor-based gait phase recognition system using a logistic model decision tree for orthosis-control," Journal of NeuroEngineering and Rehabilitation 16(1), 22 (2019).
7. X. Zou, "The Design of the Electromyography Sensor with the Modifying Circuit," Journal of Physics: Conference Series 1693, 012189 (2020).
8. M. A. M. Said, B. E. J. Tubam, N. K. Khamis, and A. Arsad, "A Study of Postural Safety and Low-Cost Electromyography (EMG) Device Towards Grocery Workers in Kota Samarahan, Sarawak," Journal of Engineering and Science Research 4(4), 1–5 (2020).
9. R. Wall, T. Laeubli, R. Seibt, M. A. Rieger, and B. Steinhilber, "Associations between low back muscle activity, pelvic movement and low back discomfort development during prolonged standing–An exploratory laboratory study," International Journal of Industrial Ergonomics 72, 380–389 (2019).
10. R. N. Kumar, A. Saravanan, S. Shankar, R. Nithyaprakash, B. Jaikumar, A. Mohanraj, and K. Mohanprasath, "Investigating the Impact of the Hoe handle Length and Angle on the Shoulder and Arm Muscle Activity during Manual Farming Activities," Journal of the Institution of Engineers (India): Series A 102(4), 1053–1060 (2021).
11. S. Pasinetti, A. Fornaser, M. Lancini, M. De Cecco, and G. Sansoni, "Assisted gait phase estimation through an embedded depth camera using modified random forest algorithm classification," IEEE Sensors Journal 20(6), 3343–3355 (2019).
12. Z. Majid, N. T. Al-Sharify, and Z. T. Al-Sharify, "Measurement of Muscle Activity using Arduino Advanced Software for Sustainable Aid," Journal of Green Engineering 10(9), 4965–4976 (2020).

13. D. Xu, Q. Wu, and Y. Zhu, "Development of a sEMG-based joint torque estimation strategy using Hill-type muscle model and neural network," Journal of Medical and Biological Engineering 41, 34–44 (2021).
14. H. K. Hameed, W. Z. Wan Hasan, S. Shafie, S. A. Ahmad, H. Jaafar, and L. N. Inche Mat, "Investigating the performance of an amplitude-independent algorithm for detecting the hand muscle activity of stroke survivors," Journal of Medical Engineering & Technology 44(3), 139–148 (2020).
15. A. Kochanowicz, B. Niespodzinski, J. Mieszkowski, M. Marina, K. Kochanowicz, and M. Zasada, "Changes in the muscle activity of gymnasts during a handstand on various apparatus," The Journal of Strength & Conditioning Research 33(6), 1609–1618 (2019).
16. A. Prakash, A. K. Sahi, N. Sharma, and S. Sharma, "Force myography controlled multifunctional hand prosthesis for upper-limb amputees," Biomedical Signal Processing and Control 62, 102122 (2020).
17. Y. Cheng, G. Li, J. Li, Y. Sun, G. Jiang, F. Zeng, H. Zhao, and D. Chen, "Visualization of activated muscle area based on sEMG," Journal of Intelligent & Fuzzy Systems 38(3), 2623–2634 (2020).
18. Z. G. Xiao, C. Menon, "An investigation on the sampling frequency of the upper-limb force myographic signals," Sensors 19(11), 2432 (2019).
19. K. Momeni, A. Ramanujam, E. L. Garbarini, and G. F. Forrest, "Multi-muscle electrical stimulation and stand training: effects on standing," The Journal of Spinal Cord Medicine 42(3), 378–386 (2019).
20. M. F. Ribeiro, A. P. Espindula, J. B. Lage, D. E. B. Júnior, L. H. Diniz, E. C. de Mello, A. A. Ferreira, M. L. Fonseca Ferraz, and V. de P. A. Teixeira, "Analysis of the electromiographic activity of lower limb and motor function in hippotherapy practitioners with cerebral palsy," Journal of Bodywork and Movement Therapies 23(1), 39–47 (2019).
21. P. Clos, R. Lepers, "Leg Muscle Activity and Perception of Effort before and after Four Short Sessions of Submaximal Eccentric Cycling," International Journal of Environmental Research and Public Health 17(21), 7702 (2020).
22. G. H. Mirzaie, A. Rahimi, M. Kajbafvala, F. D. Manshadi, K. K. Kalantari, and A. Saidee, "Electromyographic activity of the hip and knee muscles during functional tasks in males with and without patellofemoral pain," Journal of bodywork and movement therapies 23(1), 54–58 (2019).
23. S. Majumder, M. J. Deen, "Wearable IMU-based system for real-time monitoring of lower-limb joints," IEEE Sensors Journal 21(6), 8267–8275 (2020).
24. S. Gong, Z. Wang, W. Ye, and Q. Hua, "Real-time Detection System of Gait Event for Disabled People," Journal of Physics: Conference Series 1650, 032106 (2020).
25. E. Dorschky, M. Nitschke, A.-K. Seifer, A. J. van den Bogert, and B. M. Eskofier, "Estimation of gait kinematics and kinetics from inertial sensor data using optimal control of musculoskeletal models," Journal of Biomechanics 95, 109278 (2019).
26. J. C. Perez-Ibarra, A. A. Siqueira, and H. I. Krebs, "Identification of gait events in healthy and Parkinson's disease subjects using inertial sensors: A supervised learning approach," IEEE Sensors Journal 20(24), 14984–14993 (2020).
27. N. Mani, P. Haridoss, and B. George, "A wearable ultrasonic-based ankle angle and toe clearance sensing system for gait analysis," IEEE Sensors Journal 21(6), 8593–8603 (2020).
28. A. Kumar, A. K. Godiyal, P. Joshi, and D. Joshi, "A new force myography-based approach for continuous estimation of knee joint angle in lower limb amputees and able-bodied subjects," IEEE Journal of Biomedical and Health Informatics 25(3), 701–710 (2020).
29. M. A. B. Silva, A. F. G. Lupianhes, J. B. Lage, L. A. P. Sande, R. C. Rosa, L. A. Lombardi, and A. P. Espindula, "Electromyographic analysis of muscle activation of the trunk and lower limbs during human gait and hippotherapy using different ride mount materials," Journal of Bodywork and Movement Therapies 27, 507–511 (2021).
30. Getting Started with the Arduino Pro Mini (accessed on 17 January 2023). [https://docs.arduino.cc/retired/getting-started-guides/ArduinoProMini].
31. A. B. Fakhri, S. K. Gharghan, S. L. Mohammed, and S. L. Zubaidi, "Measurement Validation of Patient Vital Signs Monitoring System Using Wireless Sensor Network," in 2020 13th International Conference on Developments in eSystems Engineering (DeSE), 423–426 (2020).
32. Myoware-muscle-sensor (accessed on 17 January 2023). [https://www.digikey.com/en/maker/projects/myoware-muscle-sensor-kit/39ecba5502ad4c59ad0f7eca25b6e338].
33. ElectronicWings, Bluetooth Module HC-05 Pinout, AT Commands & Arduino Programming (accessed on 17 January 2023). [https://www.electronicwings.com/sensors-modules/bluetooth-module-hc-05-].
34. A. Q. Baktash, S. L. Mohammed, and H. F. Jameel, "Multi-Sign Language Glove based Hand Talking System," in IOP Conference Series: Materials Science and Engineering 1105, 012078 (2021).

 doi: 10.18287/JBPE23.09.020305

Side-by-Side OCE-Study of Elasticity and SHG-Characterization of Collagen Fibers in Breast Cancer Tissue before and after Chemotherapy

Anton A. Plekhanov[1*], Arseniy L. Potapov[1], Mikhail V. Pavlov[2], Vadim V. Elagin[1], Ekaterina V. Gubarkova[1], Alexander A. Sovetsky[3], Lev A. Matveev[3], Dmitriy A. Vorontsov[2], Alexander L. Matveyev[3], Alexey Y. Vorontsov[2], Sergey V. Gamayunov[2], Elena V. Zagaynova[1], Marina A. Sirotkina[1], Vladimir Y. Zaitsev[3†], and Natalia D. Gladkova[1†]

[1] Privolzhsky Research Medical University, 10/1 Minin and Pozharsky sq., Nizhny Novgorod 603950, Russia
[2] Nizhny Novgorod Regional Oncologic Hospital, 11/1 Delovaya str., Nizhny Novgorod 603093, Russia
[3] Institute of Applied Physics Russian Academy of Sciences, 46 Ulyanova str., Nizhny Novgorod 603950, Russia
[†] These authors contributed equally to this work

***e-mail:** strike_gor@mail.ru

Abstract. In the recent years promising results have been shown by the use of Compression optical coherence elastography (C-OCE) as a new optical biopsy approach to morphological assessment/diagnostics of human breast cancer using differences in elastic properties of morphological components of cancerous tissues. In this study, for the first time, a relationship was established between microstructural organization and biomechanical properties of breast-cancer tissue with pathomorphological changes caused by chemotherapy. To characterize texture of collagen fibers in the microenvironment of breast cancer, high-resolution visualization by Second-harmonic generation (SHG) microscopy was used. A side-by-side C-OCE and SHG imaging of patients' breast cancer tissues before and after chemotherapy was carried out. Regions of the cancer stroma (collagen fibers outside aggregates of cancer cells) were assessed separately from regions of cancer cell clusters penetrated by collagen fibers. For cancer stroma areas after chemotherapy, a statistically significant decrease in stiffness values was found. Simultaneously, parameters of collagen texture in SHG images (mean intensity, "coherency" and "energy") indicated increase in the collagen content, orientational orderliness, and collagen-texture heterogeneity. In contrast, cancer-cell areas post chemotherapy showed a statistically significant increase in stiffness. Analysis of SHG images of these regions indicated decrease in the inter-cellular collagen content and heterogeneity of its texture, whereas its orientational orderliness somewhat increased. The established negative correlation between stiffness and SHG parameters of collagen in cancer stroma indicates the contribution of the increase in orientational orderliness and total collagen content to the reduction in stiffness of breast cancer stroma after chemotherapy. For cancer-cell regions, significantly lower correlation between stiffness and SHG parameters (especially for coherency) was found, indicating stronger role of chemotherapy-induced changes in cancer cells themselves. These results give a deeper insight in the role of collagen texture organization in biomechanics of breast cancer tissues and contribute to a more detailed substantiation of the morphological characterization of breast cancer by C-OCE imaging.
© 2023 Journal of Biomedical Photonics & Engineering.

Keywords: breast cancer; tissue stiffness; morphological assessment; compression optical coherence elastography (C-OCE); second-harmonic generation (SHG).

Paper #8959 received 20 Apr 2023; revised manuscript received 31 May 2023; accepted for publication 2 Jun 2023; published online 15 Jun 2023. doi: 10.18287/JBPE23.09.020305.

1 Introduction

Various optical technologies of bioimaging are being introduced into medical practice in the recent years, which has significantly extended possibilities for studying anatomical/structural features and functional state of patients [1]. In the last decade, a major progress was observed in the development of optical coherence tomography (OCT), where, in addition to unprecedented success of OCT usage in ophthalmic diagnostics, there was a significant advance in the abilities of OCT application for performing *in situ* optical biopsy enabling early cancer diagnosis and a deeper understanding of oncogenesis [2]. In addition to OCT-angiography that is already widely used in ophthalmology [3], other functional extensions of OCT technology are being tested for solving various clinical tasks. Such OCT modalities include, for example, cross-polarization OCT [4], OCT-lymphangiography [5], dynamic contrast OCT [6], or optical coherent elastography [7, 8]. In particular, the use of compression optical coherence elastography (C-OCE) makes it possible to distinguish morphological components of tissue based on mechanical contrast (e.g., in order to identify the location and boundaries of the pathology). Similarly, C-COE-based evaluation of biomechanical properties of morphological tissue components gives a deeper insight in biological mechanisms of the formation and course of a disease) [9]. The C-OCE technology has a resolution of 15–100 μm, which makes possible studying of biological tissue at the level of structural/morphological components or agglomeration of cells [10], which in many cases is quite sufficient, for example, for evaluation of the efficiency of cancer therapy [11, 12].

An important aspect of biomechanical visualization of functional changes occurring in tissues is evaluation and sufficiently ample understanding of contributions of various morphological components to the overall biomechanical properties of the tissue [13]. In this context, the use of C-OCE bodes well for studying biomechanical properties of tissue components in their natural state. During the last decade, C-OCE method has been attracting much attention in studies of elasticity of breast cancer tissues [8]. This is explained by high occurrence of breast cancer which is diagnosed in over 13% of women [14]. The use of C-OCE made it possible to establish characteristic elastic properties for various individual morphological components of breast cancer [15, 16], as well as for different morpho-molecular types of breast cancer [16–18] and formulate the corresponding C-OCE-based criteria of clean resection boundaries during breast-cancer surgery [19, 20]. C-OCE also made it possible to detect changes in elastic properties of cancer components (regions of cancer stroma and cancer cells themselves) after chemotherapy [11, 21]. In those studies, C-OCE revealed a paradoxical effect of increase in stiffness in regions of residual cancer cells after chemotherapy, whereas in histological images of these regions no obvious morphological changes were seen [22]. At the same time it is known that, for tumors demonstrating high resistance and weak response to therapy, specific structural changes are typical of extracellular matrix [23, 24] consisting mostly of type I collagen [25]. Besides, some connection was mentioned between the micro-environment of cancer cells, including specific organization of collagen bundles in cancer stroma, with early metastasis and occurrence of delayed recurrence [26, 27]. Those facts indicate the necessity of revealing the connection between the structure of collagen fibers and biomechanical properties of breast-cancer tissues in order to get a deeper insight in tumor evolution and better understanding of the morphological background of elastographic C-OCE images.

In this regard, in the present study we applied the second-harmonic generation (SHG) microscopy to visualize and quantitatively assess structure (texture) of collagen fibers in breast-cancer tissue before and after chemotherapy using excised tissue samples. Quantitative assessment of SHG images included evaluation of mean density of collagen (characterized by the mean intensity of SHG image), estimation of orientational ordering of collagen-fibers texture (using the parameter usually called “coherency”) and the parameter called “energy” to characterize the degree of heterogeneity of collagen texture. For the first time, we correlated the above-mentioned SHG-based characteristics of collagen-fibers texture in breast-cancer samples with the stiffness (Young’s modulus) of the same regions estimated using C-OCE. SHG microscopy allowed us to detect not only fairly thick collagen bundles (which were visible in histological images), but also isolated collagen fibers. Earlier studies indicated that SHG microscopy made it possible both qualitative and quantitative assessment of microenvironment of breast-cancer cells [28]. In this study we performed targeted analysis of morphologically different regions of cancer [29], namely, regions of cancer stroma sufficiently distant from agglomerates of cancer cells and regions of cancer cells themselves. For the regions of cancer stroma, characteristic range of stiffness was determined using C-OCE and parameters of collagen-fibers texture for these regions were estimated using SHG microscopy. For the regions of cancer cells,

we also determined the characteristic stiffness range using C-OCE, parameters of collagen texture using SHG microscopy. Besides, density of cancer cells was estimated for these regions using histological images.

The goal of this study was to reveal how the so-determined microstructural parameters and stiffness values for cancer stroma and cancer-cell agglomerates are related to pathomorphological changes in breast-cancer tissues caused by chemotherapy. Co-location of the same breast-cancer regions in the C-OCE and SHG-microscopy images made it possible to evaluate the complementary variations in stiffness and parameters of collagen fibers texture. The established correlation between the collagen texture parameters and biomechanical properties cancerous tissues gives a deeper insight in the morphological background of variations in stiffness of the main structural components of breast cancer after chemotherapy.

2 Materials and Methods

2.1 Patients and Therapy

The study complies with international and ethical standards set out in the World Medical Association Declaration of Helsinki "Ethical principles for medical research involving human subjects" [30]. The present study was approved by the Institutional Review Boards of the Nizhny Novgorod Regional Oncologic Hospital (protocol #12 of December 23, 2021). All patients included in the study provided written informed consent prior to enrolment. The patients (the mean age is 62 years; age range 34–76 years) were treated in the Nizhny Novgorod Regional Oncologic Hospital in 2018–2022 and had been morphologically diagnosed with locally advanced breast cancers ($T_{2\text{-}3}N_{0\text{-}1}M_0$ stages). Patients were prescribed courses of neoadjuvant chemotherapy according to the clinical guidelines [31], consisting of 4 cycles of AC (Adriamycin & Cytoxan) given at 3 weekly intervals comprising doxorubicin (60 mg/m^2) and cyclophosphamide (600 mg/m^2), all given by intravenous injection followed by 12 weekly paclitaxel (80 mg/m^2) injections. Following completion of primary chemotherapy before surgical resection, assessments of the responses and tumor bed detection were performed clinically by ultrasound. The surgical procedure (total mastectomy) was carried out between the 2nd and 6th weeks following the completion of chemotherapy. All patients had histologically proven invasive adenocarcinoma (Luminal-B Her2 negative (n = 3) and Triple-negative (n = 7) subtypes) without detectable metastatic disease prior to commencing chemotherapy.

2.2 Study Design

Breast cancer tissues of 10 patients obtained by core needle biopsy (before chemotherapy) and surgical resection (after completion of chemotherapy) were examined (Figs. 1A–B). Two fresh tissue samples per patient were obtained, a core-needle biopsy tissue sample (~1.5 × 0.1 × 0.1 cm) and surgically excised tissue samples (~3.0 × 1.0 × 0.5 cm). Breast cancer tissue samples were delivered within one hour after punctation/resection to the laboratory in 10% solution of bovine serum albumin on ice. At the first stage, C-OCE studies of fresh breast cancer tissues were carried out for 20–25 min (Fig. 1C). During C-OCE visualization, we used a 3D positioning system [32], which enabled both high-precision positioning of the probe in lateral directions (with an accuracy of 10 μm), as well vertical movement of the probe required for performing controlled compression of the studied tissue samples. Immediately after the C-OCE study, samples were subjected to histological preparation (Fig. 1D). At the second stage, a histological examination of the prepared histological slides was carried out for targeted comparison with C-OCE images to evaluate the cancer response to chemotherapy, as well as to assess the cancer-cell density in pre- and post-chemotherapy samples (Fig. 1E). To analyze the organization of collagen fibers, deparaffinized unstained histological sections were studied using SHG microscopy (Fig. 1F).

For subsequent quantitative assessment of cell density (in histological images), stiffness values (in C-OCE images) and collagen fibers texture parameters (in SHG images), two types of breast cancer tissue areas before/after chemotherapy were analyzed: cancer stroma (collagen fibers in the projection of the anatomical tumor bed, but outside cancer-cell regions) and cancer-cell regions themselves (clusters of cancer cells and penetrating collagen fibers in the tumor bulk) (Figs. 1G–I).

2.3 Compression Optical Coherence Elastography (C-OCE)

A custom-made spectral-domain multimodal OCT device (Institute of Applied Physics of Russian Academy of Sciences, Russia) was used [33]. The OCT device had the following characteristics: a central wavelength of 1.3 μm, spectral width of 90 nm, spectral-fringe rate of 20 kHz, radiation power on the sample of 2 mW, axial resolution of 10 μm, lateral resolution of 15 μm, and scanning depth of 2 mm in air.

For characterization of tissue elasticity we use the variant of quantitative C-OCE described in detail in previous works [34–38]. In this C-OCE method, a thin layer of translucent silicone with pre-calibrated Young's modulus is placed onto the surface of the studied tissue. This sandwich structure silicone-tissue is slightly compressed by the output window of the OCT probe and a series of complex-valued OCT scans is acquired during this process. In the course of compression, the tissue and silicone are allowed to freely expand laterally, so that their elastic response is determined by the Young's moduli of the silicone and tissue. It was carefully verified that silicone is a highly elastically linear material, so that its cumulative strain is proportional to the elastic stress applied to the compressed sandwich structure. Consequently, by plotting the cumulative strain in the

silicone against the strain in the tissue beneath one obtains stress-strain curves $\sigma(\varepsilon)$ characterizing the tissue elasticity [37]. These stress-strain curves are pronouncedly nonlinear for the majority of real tissues, so that the local slope $d\sigma / d\varepsilon = E_{tg}$ of such a curve yields the tangent Young's modulus E_{tg} of the tissue. In was shown in previous studies [11, 16, 17, 39] that the tangent Young's modulus in breast-cancer tissue is pronouncedly stress-dependent and may vary several times and even more when the applied stress varies in the range of several kPa. In view of this, for reliable quantitative conclusions, reproducibility and comparison of different measurements, the Young's modulus (stiffness) of the tissue should be estimated for the same pre-chosen stress level [37]. It was experimentally verified that a stress level of 4 kPa is quite a convenient value for measurement procedures and at the same time different morphological components of breast-cancer tissue often demonstrate better contrast in their stiffness than for significantly higher and significantly lower stress [16, 37].

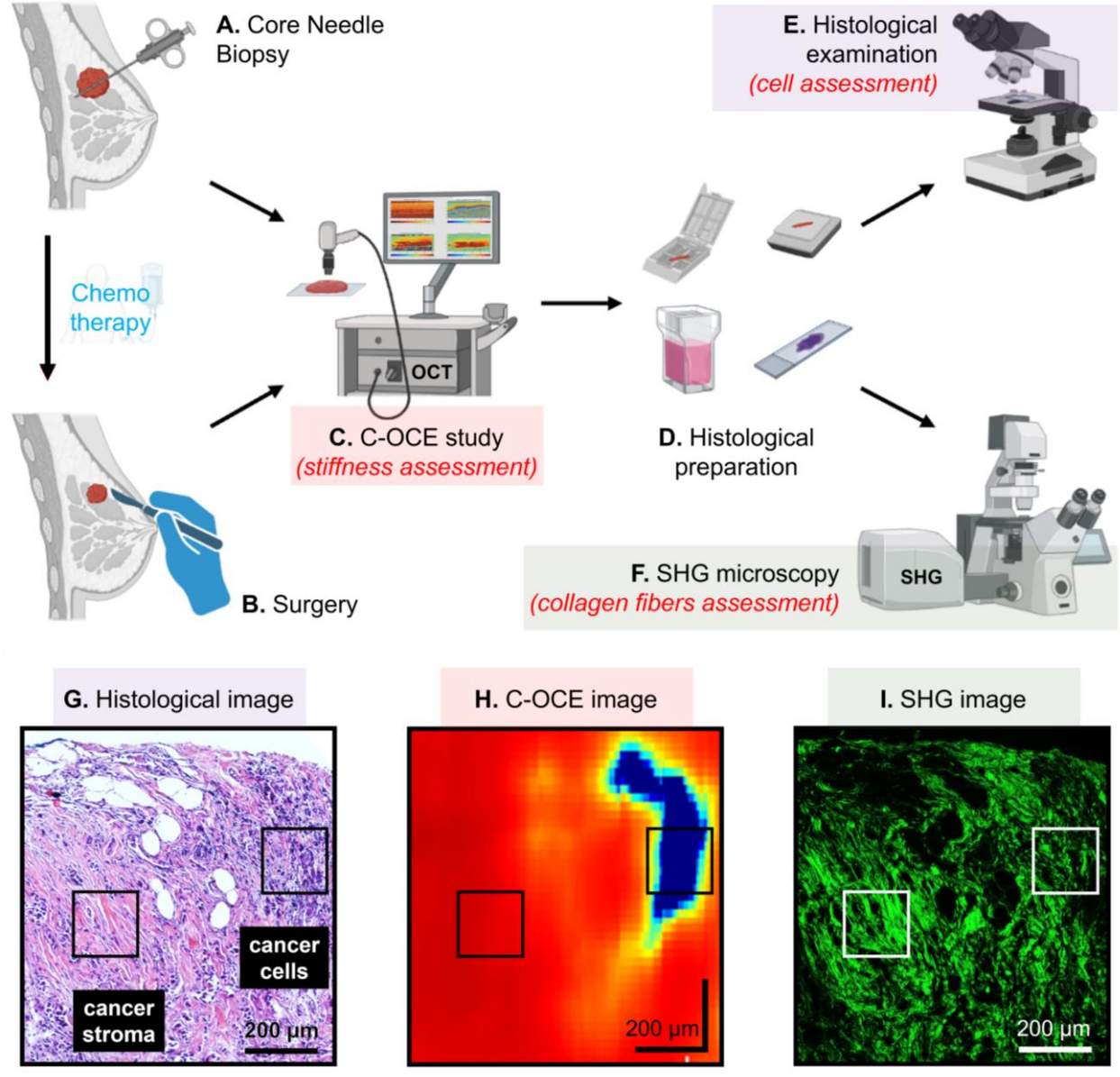


Fig. 1 Schematic of the study design demonstrating all main steps with representative images of various types. (A) harvesting of core needle biopsy samples before chemotherapy and (B) surgical excision of cancer samples after chemotherapy. (C) C-OCE examination of the fresh-tissue followed by histological preparation (D). (E) morphological assessment of the cancer-cell component; (F) SHG-based assessment of collagen fibers texture parameters; representative co-located histological image (G), C-OCE-based stiffness map (H) and SHG image (I). The images demonstrate the possibility of gathering various-type data for the same tissue regions for subsequent quantitative assessment of the corresponding parameters within a standard-size ROI of 180 × 180 μm in size. Two of such ROI are shown in panels (G), (H), and (I) by rectanges, one corresponding to cancer stroma and the other to a cancer cell region.

This fact is important for detection of tumor zones, for which the maximal contrast between the cancer cell areas with high stiffness values and stroma areas with medium/low stiffness values is usually observed at an intermediate (neither very low, no too high) stress level about a few kPa [16]. In this study, we adopted the "standardized" stress level ~ 4kPa. For this stress, it was previously established in Ref. [17] and confirmed in several independent studied [16, 18, 21, 40] on the possibility to differentiate stiffer breast cancer cell areas from the surrounding softer stroma areas that a stiffness of 420 kPa can be taken as the boundary (threshold) value. This conclusion is also true for breast cancer tissue after chemotherapy [21, 22].

2.4 Second-Harmonic Generation (SHG) Microscopy

In this study, we use SHG microscopy as a high-resolution method for visualizing type I collagen fibers, which play a major structural role in the tumorous stroma. The study was carried out on deparaffinized unstained sections 7 μm thick, which were made together with strained sections for histological examination. This allowed identical structures to be observed on both SHG images (Fig. 1I) and histological images (Fig. 1G).

A multiphoton laser scanning microscope LSM 880 (Carl Zeiss, Germany) was used. The images were constructed using an objective with a "C Plan-Apochromat" ×40/1.3 NA oil immersion, the field of view is 212 × 212 μm (image size 1024 × 1024 px). The source of the exciting radiation was Ti:Sapphire femtosecond laser Mai Tai HP (Spectra Physics, USA). The excitation wavelength was 800 nm. The average laser power was maintained at 3 mW. The SHG signal was detected using spectral selection in the wavelength range 370 to 420 nm. The images were detected from the back-scattered SHG signal.

2.5 Histological Examination

Immediately after C-OCE study, for co-location, the positions of the C-OCE scans were marked on the surface of the studied samples using the histological ink (Histo-Line, blue). Samples were fixed in 10% formalin for 48 h and then dehydrated using a gradient ethanol bath, followed by xylene purification and paraffin embedding. Then several (3–6) serial sections with a thickness of 7 μm were made along the direction coinciding with the C-OCE-scan position. Histological sections were stained according to the standard technique with hematoxylin and eosin (H & E), which made it possible to assess the breast cancer tissue structures (cancer cells and stroma) and to carry out an accurately comparison of histological and C-OCE images (Figs. 1G–H), which is described in detail in the papers [11, 17].

According to the results of histological examination, among the ten studied cases of breast cancer, only two showed a pathological complete response to neoadjuvant chemotherapy, which was expressed in the absence of residual cancer cells. For eight other cases, cancer cells areas were identified and analyzed both before and after chemotherapy. Cancer stroma areas were analyzed for all ten cases of breast cancer before and after chemotherapy.

2.6 Quantification of the Examination Results

We emphasize once again that quantitative assessment of histological, C-OCE and SHG images was made for the two types of breast cancer tissue areas, i.e., before and after chemotherapy. We analyzed separately the cancer stroma (collagen fibers in the projection of the anatomical tumor bed, but away from cancer cells) and cancer cells (clusters of cancer cells and collagen fibers in tumor bulk) (Fig. 1G). To analyze the cellular density by histological images of breast cancer, the number of cancer cell nuclei in a region of interest (ROI) of 180 μm^2 was counted (squares in Fig. 1G) and calculated using the multipoint tool in ImageJ 1.8.0 software (NIH, USA). The same size of areas (for cancer stroma and cancer cells) was used for quantitative analysis of parameters in C-OCE and SHG images (Figs. 1H–I). For the statistical calculation of parameters, 30 areas of the cancer stroma and 30 areas of cancer cells (with the exception of two cases of pathologically complete response) were analyzed for each patients' breast cancer tissue both before and after chemotherapy.

As mentioned in Section 2.3, for quantitative assessment of C-OCE data, the analyzed elastographic maps correspond to the stress-standardization level of 4 kPa. The "local" stiffness was estimated as a mean value over a rectangular ROI with a side size 180 μm^2.

In order to quantify the state of type I collagen fibers in the studied ROIs, the methods of first-order statistics (mean signal intensity) and texture analysis (coherency, energy) of SHG images were applied. These methods are able to quantify changes in collagen fibers texture caused by various pathological conditions [41] and are widely used in SHG image analysis [42]. The average intensity of the SHG signal reflects the relative amount of collagen fibers in the ROI [43]. Coherency is directly proportional to the degree of ordering of the packaging of collagen fibers and reflects the degree of alignment (the existence dominant direction) of the fibers [44]. The "energy" parameter characterizes the degree of the texture heterogeneity. High energy values occur when the gray level distribution is characterized by high spatial gradients. In our case, this corresponds to a highly heterogeneous texture of collagen fibers in the ROI. The mean intensity of SHG-signal was calculated using ImageJ's histogram analysis toolbox [45] and "coherency" and "energy" parameters of the SHG-visualized collagen texture were calculated using the OrientationJ plugin [46] (see Appendix section for a more detailed information).

2.7 Statistics

The variable for statistical intergroup (before/after chemotherapy) comparison was the average stiffness (elastic Young's modulus) calculated from the C-OCE images, as well as the indices of the subsequent tissue morphological measuring (cell density, mean signal

intensity, coherency, and energy of collagen fibers) for tissue areas of cancer stroma and cancer cells. For quantitative comparative analysis of these parameters all results are expressed as mean ± SD. Box plots were used for graphical presentation of data and indicate the median, lower/upper quartiles (25th and 75th percentile), and 5th and 95th percentile. The non-parametric Wilcoxon signed-rank test is a were used to detect significant differences in numerical data between related studied groups (from patient before/after chemotherapy). The results were considered statistically significant if the p value was < 0.05. The Spearman's correlation coefficient (r) was calculated to determine the correlation between stiffness values according to the C-OCE data and mean signal intensity, coherency, and energy parameters of collagen fibers according to SHG data or cancer cell density according to histology data.

The calculations were carried out using the GraphPad Prism 8.0 (San Diego, CA, USA) and the Statistical Package for Social Sciences 26.0 (Chicago, IL, USA).

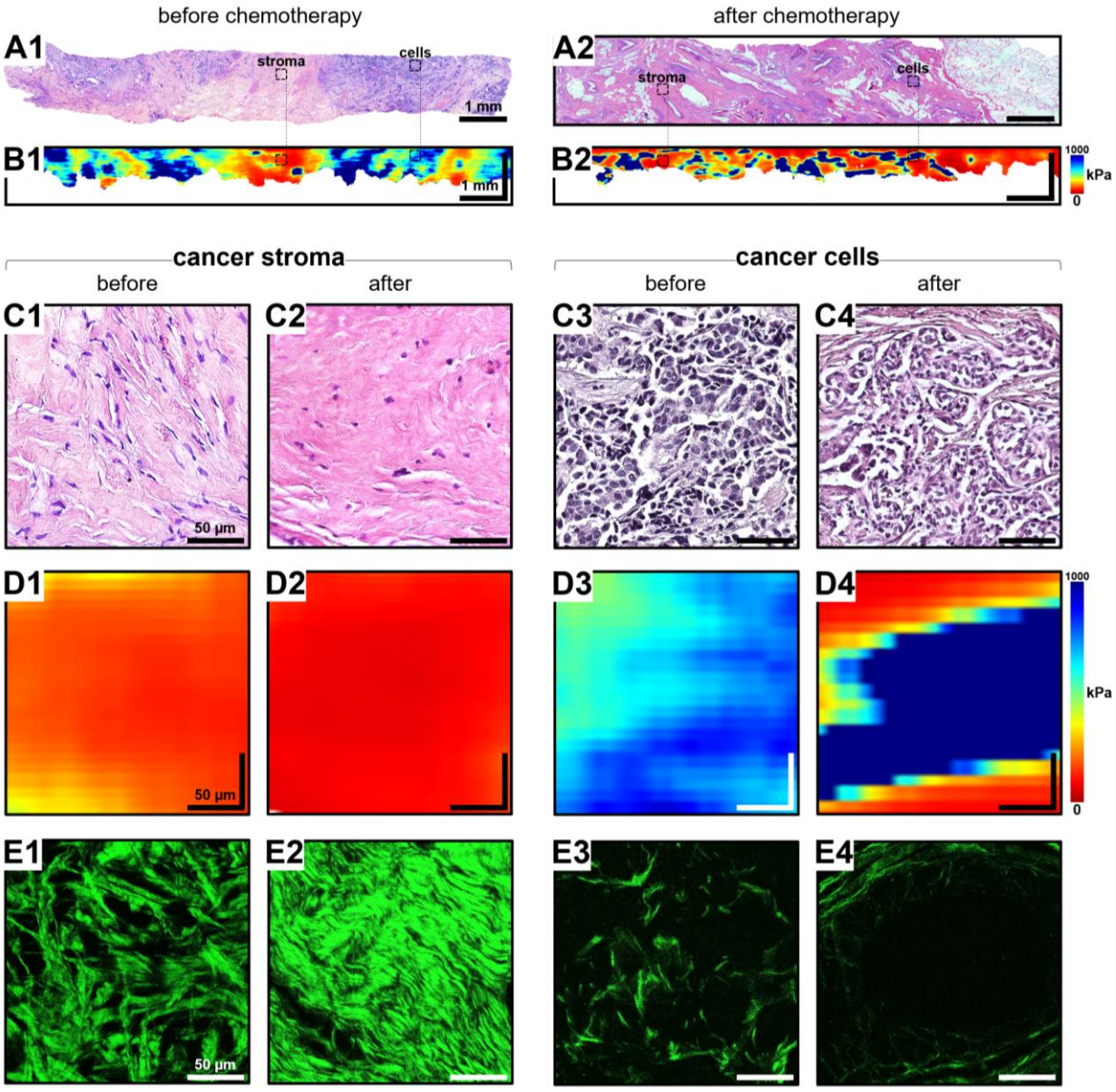


Fig. 2 Representative examples of various images obtained for breast-cancer samples from one patient. Characteristic histological images (A) and C-OCE-based stiffness maps (B) obtained before (A1–B1) and after (A2–B2) chemotherapy. Panels (C)–(E) demonstrate zoomed histological images (C), C-OCE-based stiffness maps (D) and SHG-microscopy images (E) for the analyzed regions of cancer stroma and cancer cells before and after chemotherapy. For cancer stroma images, clear reduction in stiffness is visible in C-OCE images (see D1 and D2), whereas SHG images (E1–E2) demonstrate increase in the collagen content (via increase in the SHG-signal intensity), increase in the orientational ordering (i.e., increase in the coherency parameter) and increase in spatial heterogeneity (expressed via energy parameter of the collagen fibers texture) after chemotherapy. For cancer-cell regions, in contrast to stroma, stiffness increases (D3–D4), collagen content decreases after chemotheraphy. The trends for the coherency and energy of the collagen fibers texture are not visually evident and results of their quantification are shown in Fig. 3.

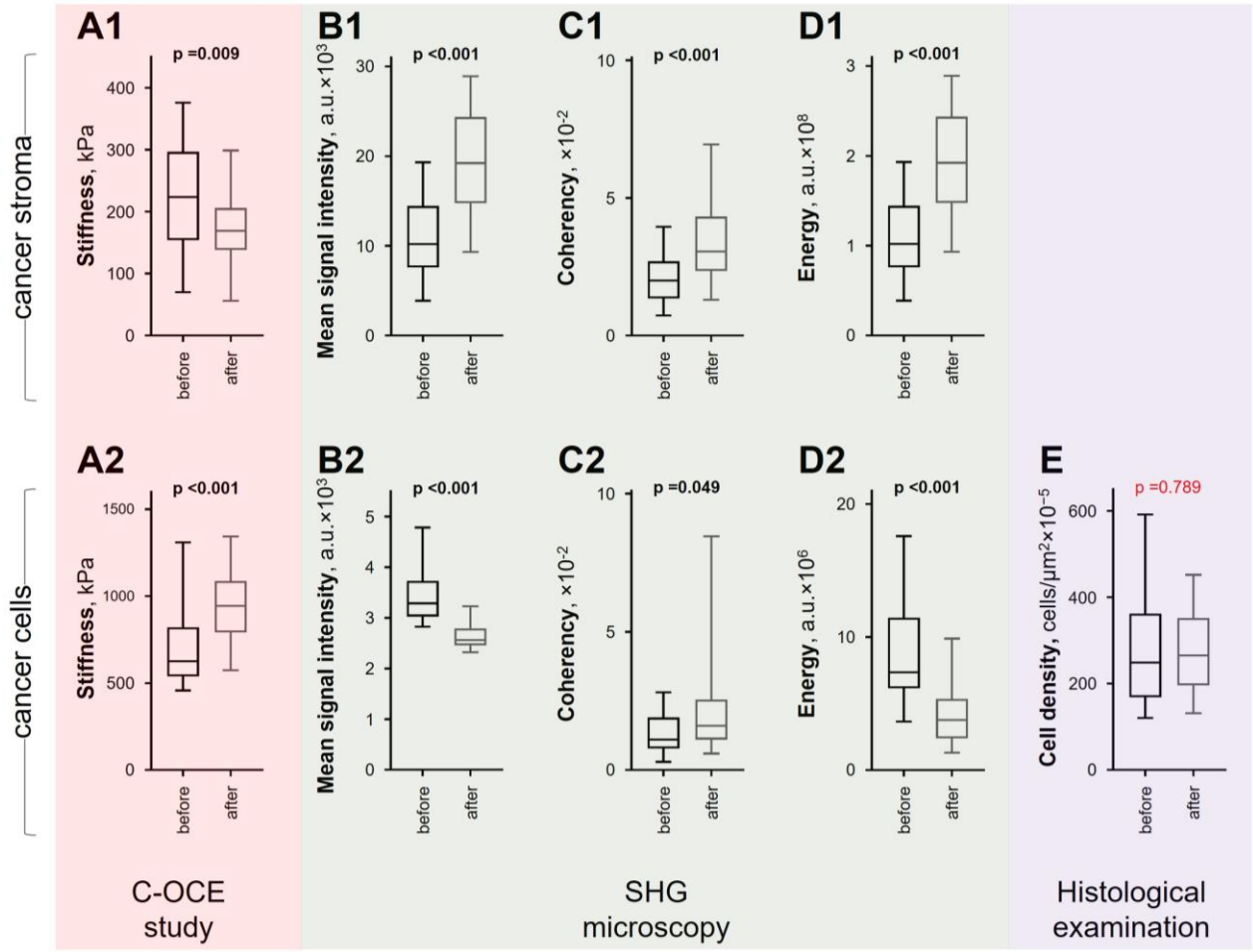


Fig. 3 Quantitative assessment of parameters for cancer stroma areas and cancer cells areas: Stiffness values (A) by C-OCE, Mean signal intensity (B), Coherency (C), and Energy (D) by SHG, and cancer Cell density in standard ROI (E) by histology; for each box plot, the center line represents medians, box plot limits indicate lower/upper quartiles (25th and 75th percentile), whiskers are 5th and 95th percentil; p-values demonstrate statistical significance of the established differences between the corresponding parameters before and after chemotherapy (non-parametric Wilcoxon signed-rank test); a.u. – arbitrary units; the exponential values for arbitrary units are retained in the form given by the ImageJ/OrientationJ software).

3 Results

The obtained histological images (Fig. 2A) from patients before and after the chemotherapy were compared with relevant C-OCE images (Fig. 2B) to determine the stiffness of areas of the cancer stroma and cancer cells. When assessing a full-scale tissue sample, one can note a change in the cellularity of the tumor, which is characteristic of breast cancer tissue after chemotherapy with a pathological partial response [47] – there is a prevalence of fibrosis areas and rare individual clusters of residual cancer cells (Fig. 2A2). When comparing full-scale C-OCE images before and after chemotherapy, there is a decrease in high stiffness values areas (light and dark blue areas in Fig. 2B2) from cancer cells (previously established threshold for detection of cancer cells > 420 kPa [17]) and a predominance of medium and low stiffness values areas (orange and red areas in Fig. 2B2) from cancer stroma after chemotherapy.

In a detailed comparison of histological images of cancer stroma areas and cancer cells areas before and after chemotherapy (Fig. 2C), only thickening of collagen bundles in cancer stroma areas after chemotherapy can be visually noted (Fig. 2C2). There were no visible qualitative features of changes in cancer cells (and in their density positioning relative to each other) or the condition of the collagen fibers after chemotherapy by histology (Fig. 2C4). However, qualitative changes in stiffness before and after chemotherapy were found in C-OCE images: for areas of cancer stroma – a decrease in stiffness was observed (the predominance of orange areas changed to red in Figs. 2D1–D2), and for areas of cancer cells – an increase in stiffness was observed (the predominance of light blue areas changed to dark blue in Figs. 2D3–D4). A detailed visualization of such areas in SHG images shows an expressive change of collagen fibers structure: for areas of cancer stroma – disordered thin collagen fibers are observed before chemotherapy (Fig. 2E1), and an increase in the number of collagen bundles, their orientational ordering and thickening are observed after chemotherapy (Fig. 2E2); within areas of cancer cells randomly oriented isolated collagen fibers are observed

before chemotherapy (Fig. 2E3) and demonstrate almost complete disappearance after chemotherapy (Fig. 2E4).

Then, a quantitative assessment was carried out to determine the significance of differences in the studied parameters before and after chemotherapy. Fig. 3 shows the corresponding results: stiffness values (Fig. 3A) according to C-OCE images, mean SHG-signal intensity (Fig. 3B), parameters of coherency (Fig. 3C) and energy (Fig. 3D) of collagen fibers extracted from SHG images, and the cancer-cell density in a standard ROI (Fig. 3E) extracted from histological images. C-OCE indicated that for *cancer stroma* areas, the stiffness values statistically significantly *decreased* from 224 ± 95 kPa before chemotherapy down to 175 ± 67 kPa after chemotherapy ($p = 0.009$) (Fig. 3A1). However, the analysis of SHG-images of these areas revealed a statistically *significant increase* ($p < 0.001$) in the SHG-based parameters of collagen texture after chemotherapy compared with the pre-chemotherapy values. Namely, mean signal intensity increased from $(11.0 \pm 4.5) \times 10^3$ a.u. to $(19.4 \pm 5.9) \times 10^3$ a.u., coherency increased from $(2.1 \pm 1.0) \times 10^{-2}$ to $(3.5 \pm 1.7) \times 10^{-2}$, and energy increased from $(1.0 \pm 0.5) \times 10^8$ a.u. to $(1.7 \pm 0.6) \times 10^8$ a.u. (see Figs. 3B1–D1). Increase in the mean signal intensity indicates the increase in collagen content in cancer stoma. Increase in the coherency и energy parameters indicate post-chemotherapy increase in orientational ordering accompanied by increase in spatial heterogeneity of the collagen fibers texture.

For *cancer cells* areas, C-OCE, on the contrary to stroma, indicated that stiffness statistically significantly *increased* after chemotherapy from 719 ± 264 kPa to 954 ± 231 kPa ($p < 0.001$) (Fig. 3A2). The SHG analysis of these areas, also in contrast to stroma, revealed a statistically significant post-chemotherapy *decrease* ($p < 0.001$) in the mean signal intensity from $(3.5 \pm 0.6) \times 10^3$ a.u. down to $(2.6 \pm 0.2) \times 10^3$ a.u., as well as in the energy parameter, from $(8.7 \pm 4.1) \times 10^6$ a.u. down to $(4.2 \pm 2.3) \times 10^6$ a.u. (see Figs. 3B2 and 3D2). These results indicate that the content of collagen fibers decreases (the texture visually becomes more rarified). This also led to a decrease in the heterogeneity of the collagen texture reflected in the decrease in the "energy" parameter of the texture. An increase ($p = 0.049$) in the coherency parameter in SHG images of cancer-cell areas after chemotherapy, from $(1.3 \pm 1.0) \times 10^{-2}$ to $(2.7 \pm 3.3) \times 10^{-2}$ (see Fig. 3C2), indicates some increase in the orientational ordering of the collagen fibers residual post therapy.

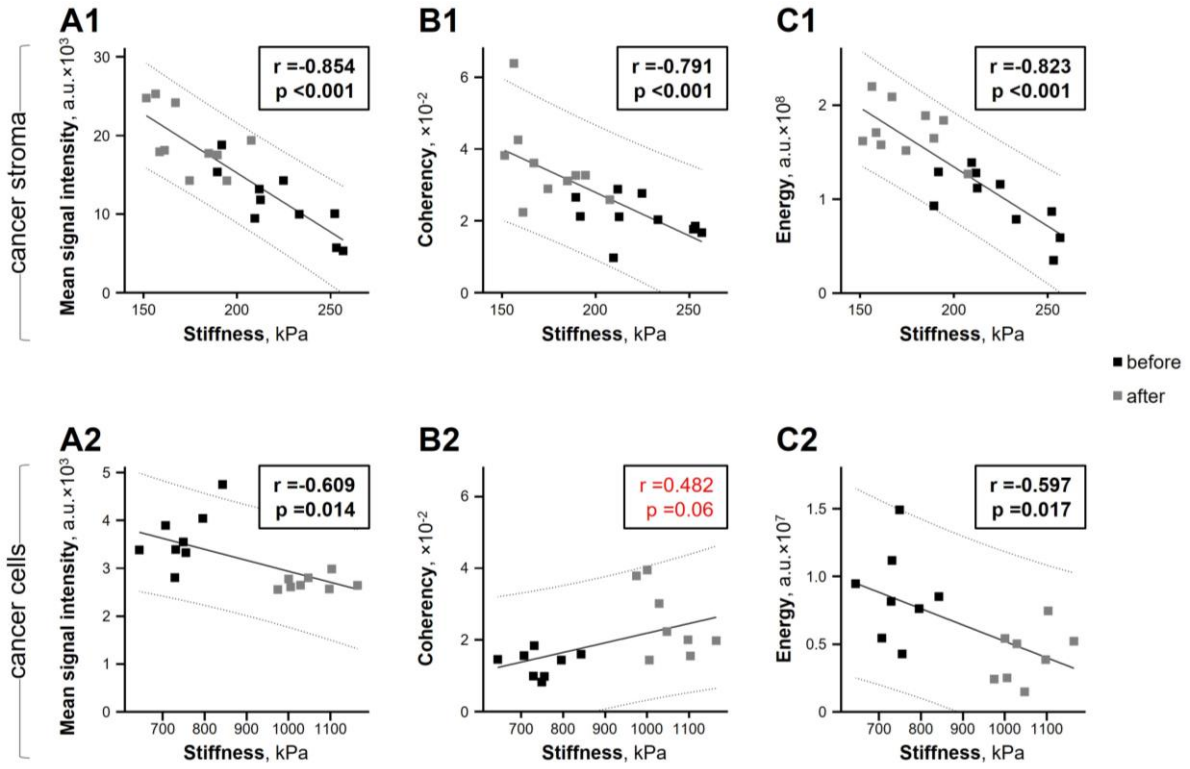


Fig. 4 Relation between stiffness values (according to C-OCE) and values of mean signal intensity, coherency, energy (according to SHG) for areas of cancer stroma (A1–C1) and cancer cells (A2–C2); high inverse significant correlation is demonstrated between stiffness values and mean signal intensity ($r = -0.854$, $p < 0.001$) (A1) / coherency ($r = -0.791$, $p < 0.001$) (B1) / energy ($r = -0.823$, $p < 0.001$) (C1) for cancer stroma areas; lower significant inverse correlation is demonstrated between stiffness values and mean signal intensity ($r = -0.609$, $p = 0.014$) (A2) / energy ($r = -0.597$, $p = 0.017$) (C2) for cancer cells areas; a significant correlation has not been established between stiffness values and coherency ($r = 0.482$, $p = 0.06$) (B2) for cancer cells areas; black squares are values for breast cancer cases before chemotherapy; gray squares are values for breast cancer cases after chemotherapy; the dotted lines show 95% prediction intervals; a.u. – arbitrary units; exponential values for arbitrary units are kept in the form given by the ImageJ/OrientationJ software.

When analyzing the cancer cell density in a standard ROI in histological images (Fig. 3E) before and after chemotherapy (284.9 ± 144.0 cell/$\mu m^2 \times 10^{-5}$ versus 276.8 ± 90.6 cell/$\mu m^2 \times 10^{-5}$), no statistically significant differences were found ($p = 0.789$).

In order to analyze the relation between stiffness values according to C-OCE data and values of mean signal intensity / coherency / energy according to SHG data, or cancer cell density according to histology data the correlation coefficients were calculated separately for areas of cancer stroma (Figs. 4A1, B1, C1) and for cancer cells (Figs. 4A2, B2, C2). There was a high negative (inverse) correlation between the stiffness of cancer stroma areas and their parameters of mean signal intensity ($r = -0.854$, $p < 0.001$), coherency ($r = -0.791$, $p < 0.001$), and energy ($r = -0.823$, $p < 0.001$) (Figs. A1–C1). Also there was an inverse correlation between the stiffness of cancer cells areas and their SHG parameters of mean signal intensity ($r = -0.609$, $p = 0.014$) (Fig. A2), and energy ($r = -0.597$, $p = 0.017$) (Fig. C2). No significant correlation has been established between the stiffness of cancer cells areas and SHG parameter of coherency ($r = 0.482$, $p = 0.06$) (Fig. B2).

4 Discussion

To the best of our knowledge in the reported study for the first time side-by-side high-resolution C-OCE-based characterization of stiffness with SHG-based characterization of collagen texture in patients' breast-cancer tissues before and after chemotherapy. Our earlier study [17] in agreement with other authors [15, 20] already demonstrated the possibility to efficiently characterize various morphological types of breast cancer using C-OCE and even to perform quantitative morphometric analysis of fresh tissue samples using the established differences in stiffness for regions of cancer cells (high stiffness values) and cancer stroma (medium and low stiffness values). Besides, in our recent study related to C-OCE-based evaluation of breast-cancer response to chemotherapy, a certain increase in stiffness of cancer-cell regions post neoadjuvant chemotherapy was revealed [22] in comparison with cancer-cell regions in samples from patients who did not receive chemotherapy before surgery [17]. Furthermore, in the present study elastic properties were studied using needle core biopsy tissue samples (before chemotherapy) and surgery tissue samples (after chemotherapy) taken from the same patients. The obtained results directly confirmed the fact of statistically significant ($p < 0.001$) increase in stiffness of residual cancer-cell regions post chemotherapy (954 ± 231 kPa) in comparison with the stiffness values before chemotherapy (719 ± 264 kPa). It can be noted that the hypothesis that the increase in stiffness of the cancer-cell regions is due to the increase in the density of cancer-cell packing was not confirmed. It was found that the packing density of cancer cells per unit area (counted in histological images over areas $180\ \mu m \times 180\ \mu m$) did not reveal any statistically significantly differences ($p > 0.78$) between the pre-chemotherapy and post-chemotherapy samples: 284.9 ± 144.0 cell/$\mu m^2 \times 10^{-5}$ and 276.8 ± 90.6 cell/$\mu m^2 \times 10^{-5}$, respectively. Penetrating collagen fibers among cancer cells were hardly seen in such regions in histological images. An inverse situation was seen in the regions of cancer stroma, for which the stiffness values statistically significantly decreased post-chemotherapy down to 175 ± 67 kPa from the pre-therapy 224 ± 95 kPa ($p = 0.009$). However, in histological images for these regions, only a certain thickening of collagen bundles was visible. In view of this we tried to obtain a more detailed information about the morphological differences accompanying the stiffness changes in cancer stroma and cancer-cell regions after breast cancer chemotherapy by using SHG microscopy to quantitatively characterize collagen fibers texture.

The importance of studying collagen as the main structural component of breast-tissue stroma is indicated by the known data on the correlation between the density of breast tissue with the risk of breast cancer development [48]. It was also shown that structural features and biomechanical properties of collagenous environment essentially affect the progressive development of cancer, its molecular characteristics and results of therapy [49]. Our previous studies demonstrated the possibility of identification of various morphological subtypes of breast cancer based on SHG-microscopy data on structural/textural features of collagen fibers [28]. In this study the limited amount of samples did not suffice for performing gradation of the revealed textural features of collagen bundles for multiple morpho-molecular subtypes of breast cancer. Nevertheless, the studies 10 cases of breast cancer before and after chemotherapy statistically significantly indicated the fact of therapy-induced variations in the SHG-based parameters of collagen fibers. For the regions of cancer stroma, statistically significant increase in the following SGH-based textural parameters was revealed ($p < 0.001$): mean signal intensity increase from $(11.0 \pm 4.5) \times 10^3$ a. u. to $(19.4 \pm 5.9) \times 10^3$ a. u. after chemotherapy; coherency increased from $(2.1 \pm 1.0) \times 10^{-2}$ to $(3.5 \pm 1.7) \times 10^{-2}$ after chemotherapy; energy increased from $(1.0 \pm 0.5) \times 10^8$ a. u. to $(1.7 \pm 0.6) \times 10^8$ a. u. after chemotherapy. These findings indicate the overall increase in the collagen content accompanied by increase in orientational ordering the collagen bundles and increase in spatial inhomogeneity of the collagen fibers texture after chemotherapy, which is also visually noticeable (Figs. 2E1–E2) and correlates with the results of other authors [50, 51]. Reorganization of collagen bundles and their structuring along a dominant direction may be associated with easier migration of cancer cells along the aligned collagen bundles in cases of weak cancer response to the chemotherapy [52, 53]. In this context, studies [54, 55] can be mentioned, in which differences were found in the SHG-based parameters between cases of pathological complete response of cancer to chemotherapy and cases of partial response. Our plans for future foresee to study a larger amount of cases corresponding to pathological complete and

incomplete responses to chemotherapy for performing side-by-side evaluation of variations in stiffness and SHG-based parameters to reveal differences and determine characteristic values of these parameters for each type of cancer response to the therapy.

For the cancer-cell regions before chemotherapy, in the SHG images thin isolated and randomly directed collagen fibers are fairly well visible (Fig. 2E3), whereas after chemotherapy, collagen fibers among clusters of residual cancer cells visually almost disappear (Fig. 2E4). Statistical analysis of SHG images indicates significant reduction in the following parameters of collagen fibers texture ($p < 0.001$): mean signal intensity – before $(3.5 \pm 0.6) \times 10^3$ a. u and $(2.6 \pm 0.2) \times 10^3$ a. u. after chemotherapy; and energy – before $(8.7 \pm 4.1) \times 10^6$ a. u. and $(4.2 \pm 2.3) \times 10^6$ a. u. after chemotherapy. These variations in the collagen fibers texture parameters well agree with the visually observed reduction in the density of collagen fibers penetrating the cancer cell regions. The observed increase of the coherency parameter in the SGH images $(1.3 \pm 1.0) \times 10^{-2}$ before chemotherapy versus $(2.7 \pm 3.3) \times 10^{-2}$ after it) also well agrees with above-mentioned strong reduction in the density of collagen fibers because residual isolated fibers demonstrate certain "preferential orientation" ($p = 0.049$). Such changes in the texture of breast-cancer collagen fibers after neoadjuvant chemotherapy were also mentioned in study [51]. The observed pathomorphological changes in the breast cancer samples are typical in cases of partial response of tumor to chemotherapy, for which quite typical are clusters of residual cancer cells embedded into overgrown collagenous stroma which substituted the regions of necrotic cancer cells that responded to the chemotherapy [56]. These regions of collagenous stroma prevail over the regions of residual cancer cells survived after chemotherapy, which reduces the overall stiffness of the tumor node detectable by instrumental diagnostic methods [57].

The performed C-OCE study and analysis of the complementary SHG images indicate that the stiffness values of cancer stroma areas demonstrate pronounced negative correlation with the SHG parameters of mean signal intensity ($r = -0.854$, $p < 0.001$), coherency ($r = -0.791$, $p < 0.001$) and energy ($r = -0.823$, $p < 0.001$). The SHG images indicate the increase in the content of collagen fiber, increased orientational ordering (coherency) and increase in the heterogeneity (energy) of the collagen fibers texture. These facts give reasons to assume that it is the change in the structural characteristics of the collagen fibers which give the dominating contribution in the decrease in stiffness of cancer stoma (and overall stiffness reduction of the tumor) after chemotherapy. These conclusions are consistent with the results of our previous C-OCE study [58] of elastic properties of the vaginal wall, in which a high correlation was observed between the wall stiffness and parameters of collagen bundles extracted from quantitative analysis of histological images with Van Gieson staining. It was found that the increase in the vaginal wall stiffness was accompanied by decrease in the coherency (orientational ordering) of collagen bundles, whereas the energy parameter of collagen fibers texture in the histological images increased. Therefore, for the vaginal wall in Ref. [58], the correlation between stiffness and coherency of the collagen fibers texture was also negative like in the present study, whereas for stiffness-energy, the positive sign of correlation in Ref. [58] was opposite to the negative correlation revealed in the present study. In this context it can be pointed out that in Ref. [58] the parameters of collagen bundles texture were estimated using Van-Gieson stained histological images rather that SHG-images used in the present study. Concerning orientation of collagen bundles, these two types of images could give fairly similar results (at least qualitatively), whereas for estimation of texture energy, the results based on stained histological images and SHG-microscopy could differ rather significantly.

For the regions of cancer cells penetrated by collagen fibers, the sign of correlation between stiffness and collagen fibers texture coherency is opposite than for regions of cancer stroma (compare Fig. 4B2 and Fig. 4B1). In contrast, the revealed negative signs of correlation between stiffness and intensity ($r = -0.597$, $p = 0.017$) and between stiffness and collagen fibers texture energy ($r = -0.597$, $p = 0.017$) for cancer-cell regions qualitatively agree with the corresponding correlations found for cancer stroma (see Fig. 4), although the correlation coefficients are somewhat smaller than for stromal regions. The latter fact may be attributed to the stronger contribution of cancer cells themselves to stiffness of cancer-cell regions. In this study we limited ourselves by estimations of densities (concentrations) of the cancer cells before and after chemotherapy putting aside possible structural changes in the individual cancer cells caused by the therapy. Studying of such biomechanical characteristics with a sub-cellular resolution require high-resolution methods such as atomic-force microscopy (AFM) [59]. However, application of this technique for studying intact tissues and, moreover, living tissues is very challenging. Usually, AFM require utilization of either cell-culture samples or tissue slices in the surface layer of which there are very few cells with unperturbed structure [60]. Under such visualization conditions, the influence of mechanical inter-cellular transduction and influence of surrounding cells and extra-cellular matrix may be strongly perturbed [10, 61]. At the same time, it is known (e.g., based on electron-microscopy data [62]) that cell malignization is accompanied by essential disorganization of actin cytoskeleton, which is likely to affect elastic properties of individual cells and may be responsible for the appearance of the so-called higher elasticity peak according to AFM results [59, 63]. However, influence of chemotherapy on the state of cyto-skeleton of residual cancer cell has not yet been studied. Besides, presently there is no sufficient understanding of the contribution of nuclei to the cellular stiffness, although the fact of some increase in the nuclei's sizes

after chemotherapy is known [64]. In view of this only the use of multiparameter analysis of data form various diagnostic techniques may give sufficiently ample understanding of the contributions of various morphological components to the overall stiffness of biological tissues.

5 Conclusion

In this study we performed side-by-side OCE characterization of elasticity collagenous stromal tissue and quantitative characterization of collagen texture using SHG imaging in patients' breast-cancer tissues before and after chemotherapy. The analysis of cancer stromal tissue (i.e. collagen fibers fairly distant from conglomerates of cancer cells) was performed separately from the regions of cancer itself (i.e., clusters of cancer cells penetrated by collagen fibers in the tumor bulk). For the regions of cancer stromal tissue after chemotherapy the performed C-OCE examinations for the first time revealed statistically significant reduction in stiffness ($p = 0.009$). In parallel, the SHG microscopy indicated the statistically significant increase in the amount of collagen bundles accompanied by increase in their coherency and thickening ($p < 0.001$). The revealed high negative correlation ($p < 0.001$) between the stiffness and the SHG-based parameters of collagen texture indicate an important contribution of the collagen organization and collagen-bundle thickening to the reduction of stiffness of the cancer stroma areas after chemotherapy. For the regions of residual cancer cells post chemotherapy, C-OCE for the first time revealed statistically significant opposite trends: increase in stiffness ($p < 0.001$), whereas SHG microscopy indicated statistically significant decrease in the amount of penetrating collagen fibers ($p = 0.014$) and reduction in their thickness ($p = 0.017$). The revealed negative correlation ($p = 0.014$–0.017) between the stiffness of these regions and SHG-based parameters characterizing the amount and uniformity of visualized collagen fibers also indicates the existence of some relationship between the reduction of the collagen-fiber proportion and increase in stiffness of the residual cancer-cell regions after chemotherapy. Further studies will be focused on characterization of post-chemotherapy changes in the cancer cells themselves and clarification of the relationship of these changes with variations in their elastic.

Appendix

This section describes in more detail how the parameters "intensity", "energy" and "coherency" were calculated for the acquired SHG images using the ImageJ / OrientationJ software [44].

Mean signal intensity is a simple first-order moment used to estimate the intensity of the SHG signal, the parameter is calculated over a rectangular processing window by Eq. (1A):

$$< I >= \frac{1}{N^2}\sum_{i=1}^{N}\sum_{j=1}^{N} I(i,j)\,, \qquad (1A)$$

where N is the size of the processing window and $I(i,j)$ is the intensity of a pixel with coordinates (i,j).

The coherency and energy parameters are expressed via spatial derivatives I_x and I_y of the image matrix $I(x,y)$ along the principal directions x and y, respectively, from which a 2×2 symmetric positive matrix J is composed,

$$J = \begin{bmatrix} \langle I_x, I_x \rangle_w & \langle I_x, I_y \rangle_w \\ \langle I_x, I_y \rangle_w & \langle I_y, I_y \rangle_w \end{bmatrix}. \qquad (2A)$$

In Eq. (2A), $<..>_w$ denotes the weighted inner product, which for two quantities is defined as

$$< g,h >_w = \int\int w(x,y)g(x,y)h(x,y)dxdy\,. \qquad (3A)$$

Here, $w(x,y)$ is the Gaussian weighting function that specifies the area of interest. Once the structure tensor in Eq. (2A) is known, the quantities "energy" and "coherency" in the vicinity of each pixel can be calculated [44, 65].

The energy parameter (E) is given by the trace of the tensor matrix:

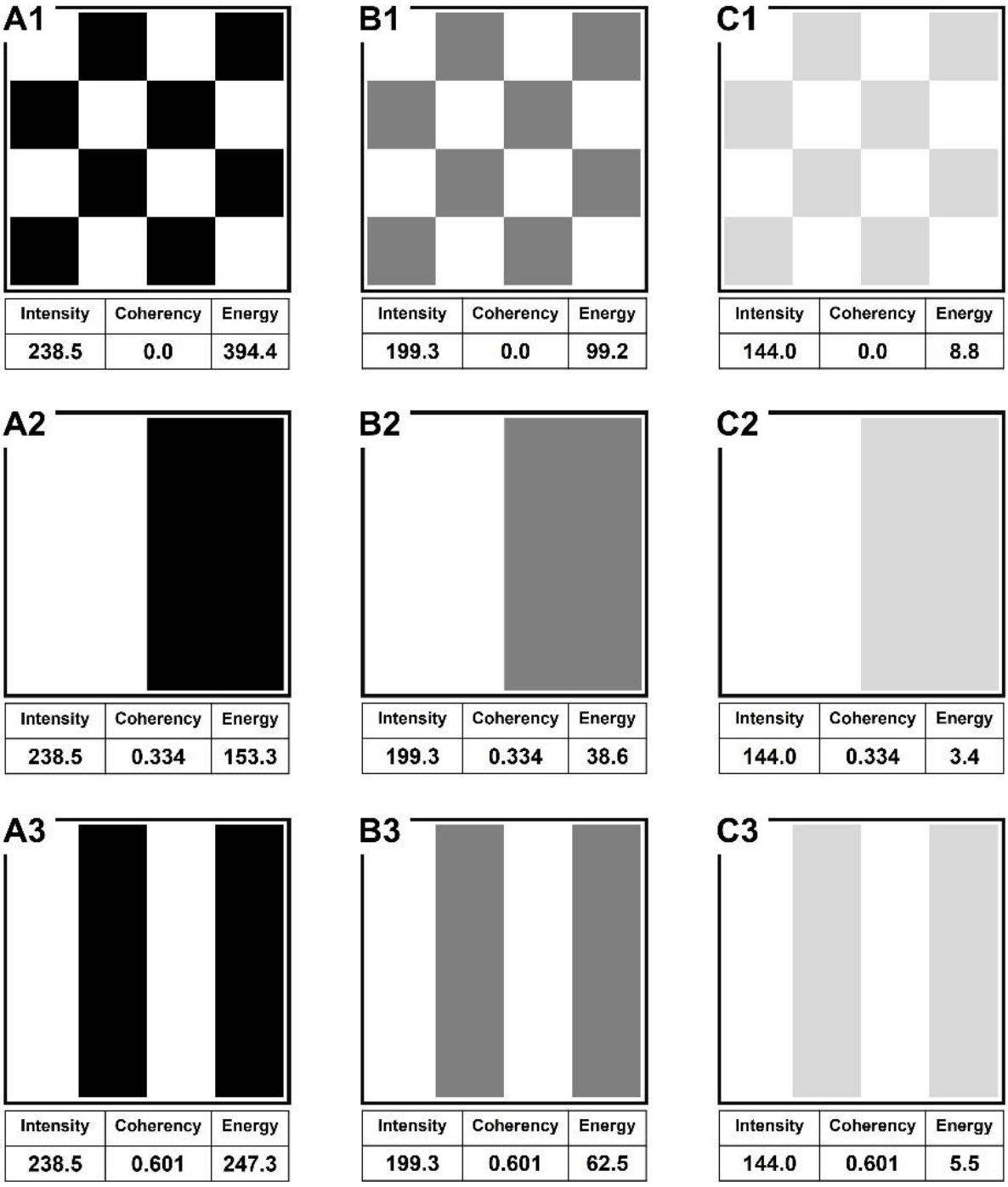
$$E = Trace(J) = \langle I_x, I_x \rangle_\omega + \langle I_y, I_y \rangle_\omega\,. \qquad (4A)$$

The coherency parameter (C) is defined as the ratio of the difference and the sum of the maximal and minimal eigenvalues λ_{max} and λ_{min} of tensor J,

$$C = \frac{\lambda_{max} - \lambda_{min}}{\lambda_{max} + \lambda_{min}} = \frac{\sqrt{(\langle I_y, I_y \rangle_w - \langle I_x, I_x \rangle_w)^2 + 4\langle I_x, I_y \rangle_w}}{\langle I_x, I_x \rangle_w + \langle I_y, I_y \rangle_w}. \qquad (5A)$$

Coherency is bounded between 0 and 1, with 1 indicating highly oriented structures and 0 indicating isotropic regions.

The OrientationJ software realizes calculation of tensor J defined by Eq. (2A) and then the energy and coherency parameters defined by Eqs. (4A) and (5A).



	Intensity	Coherency	Energy
A1	238.5	0.0	394.4
B1	199.3	0.0	99.2
C1	144.0	0.0	8.8
A2	238.5	0.334	153.3
B2	199.3	0.334	38.6
C2	144.0	0.334	3.4
A3	238.5	0.601	247.3
B3	199.3	0.601	62.5
C3	144.0	0.601	5.5

Fig. 1A The test images and the corresponding parameters of mean signal intensity, coherency and energy calculated with the ImageJ/OrientationJ software for each image.

To illustrate the correspondence of these parameters with visually seen image features, we processed a series of simple test images shown in Fig. 1A with the ImageJ/OrientationJ software.

We start from images with a chess-board-like structure, in which dark squares are characterized by various levels of grey color (compare panels A1, B1, C1). The patterns in the upper row have no preferred orientation, so that the coherency parameter is zero, whereas for the invariable pattern geometry, the parameters of intensity and energy monotonically decrease with decreasing contrast of the darker squares.

The 2nd and 3rd rows in Fig. 1A are obtained by reordering the same white and dark squares as in the upper-row images towards more oriented structures with the visually most pronounced pattern orientation in the 3rd row.

The intensity parameter evidently remains insensitive to rearrangement of the squares in each column of Fig. 1A according to the definition given by Eq. (1A). Consequently, the intensity parameter remains invariable

for each column in Fig. 1A (albeit different for different columns).

The energy parameter, for a given grey-color intensity, is maximal for the upper-row images, characterized by the most pronounced spatial heterogeneity and maximal length of boundaries separating white and dark squares, where spatial gradients are localized. Notice that for the same geometrical structure in each row in Fig. 1A, the energy parameter is higher for patterns with higher grey levels.

Finally, the coherency parameter is maximal for the lowest row in Fig. 1A, where the patterns visually demonstrate the most pronounced orientation. Unlike the energy parameter, the coherency parameter is entirely determined by the pattern geometry and is insensitive to the grey level according to the definition given by Eq. (5A). Consequently, the coherency parameter remains invariable for each row in Fig. 1A.

Acknowledgements

The study was funded by the Russian Science Foundation (Grant No. 18-75-10068). The OCT-system adaptation was supported by the contract № 075-15-2022-316 with the Ministry of Science and Higher Education of Russian Federation. The authors thank Maria Karabut and Alexandra Bogomolova (PRMU) for their help in conducting experiments.

Disclosures

The authors declare no conflict of interest.

References

1. H. S. Lahoti, S. D. Jogdand, "Bioimaging: Evolution, Significance, and Deficit," Cureus 14(9), e28923 (2022).
2. R. Leitgeb, F. Placzek, E. Rank, L. Krainz, R. Haindl, Q. Li, M. Liu, M. Andreana, A. Unterhuber, T. Schmoll, and W. Drexler, "Enhanced medical diagnosis for dOCTors: a perspective of optical coherence tomography," Journal of Biomedical Optics 26(10), 100601 (2021).
3. A. H. Kashani, C. L. Chen, J. K. Gahm, F. Zheng, G. M. Richter, P. J. Rosenfeld, Y. Shi, and R. K. Wang, "Optical coherence tomography angiography: A comprehensive review of current methods and clinical applications," Progress in Retinal and Eye Research 60, 66–100 (2017).
4. K. A. Achkasova, A. A. Moiseev, K. S. Yashin, E. B. Kiseleva, E. L. Bederina, M. M. Loginova, I. A. Medyanik, G. V. Gelikonov, E. V. Zagaynova, and N. D. Gladkova, "Nondestructive label-free detection of peritumoral white matter damage using cross-polarization optical coherence tomography," Frontiers in Oncology 13, 1133074 (2023).
5. A. A. Moiseev, M. A. Sirotkina, A. L. Potapov, L. A. Matveev, N. N. Vagapova, I. A. Kuznetsova, and N. D. Gladkova, "Lymph vessels visualization from optical coherence tomography data using depth-resolved attenuation coefficient calculation," Journal of Biophotonics 14(9), e202100055 (2021).
6. H. M. Leung, M. L. Wang, H. Osman, E. Abouei, C. MacAulay, M. Follen, J. A. Gardecki, and G. J. Tearney, "Imaging intracellular motion with dynamic micro-optical coherence tomography," Biomedical Optics Express 11(5), 2768–2778 (2020).
7. S. Wang, K. V. Larin, "Optical coherence elastography for tissue characterization: a review," Journal of Biophotonics 8(4), 279–302 (2015).
8. V. Y. Zaitsev, A. L. Matveyev, L. A. Matveev, A. A. Sovetsky, M. S. Hepburn, A. Mowla, and B. F. Kennedy, "Strain and elasticity imaging in compression optical coherence elastography: The two-decade perspective and recent advances," Journal of Biophotonics 14(2), e202000257 (2021).
9. J. A. Mulligan, G. R. Untracht, S. N. Chandrasekaran, C. N. Brown, and S. G. Adie, "Emerging Approaches for High-Resolution Imaging of Tissue Biomechanics With Optical Coherence Elastography," IEEE Journal of Selected Topics in Quantum Electronics 22(3), 246–265 (2016).
10. B. F. Kennedy, P. Wijesinghe, and D. D. Sampson, "The emergence of optical elastography in biomedicine," Nature Photonics 11(4), 215–221 (2017).
11. A. A. Plekhanov, M. A. Sirotkina, A. A. Sovetsky, E. V. Gubarkova, S. S. Kuznetsov, A. L. Matveyev, L. A. Matveev, E. V. Zagaynova, N. D. Gladkova, and V. Y. Zaitsev, "Histological validation of in vivo assessment of cancer tissue inhomogeneity and automated morphological segmentation enabled by Optical Coherence Elastography," Scientific Reports 10(1), 11781 (2020).
12. M. A. Sirotkina, E. V. Gubarkova, A. A. Plekhanov, A. A. Sovetsky, V. V. Elagin, A. L. Matveyev, L. A. Matveev, S. S. Kuznetsov, E. V. Zagaynova, N. D. Gladkova, and V. Y. Zaitsev, "In vivo assessment of functional and morphological alterations in tumors under treatment using OCT-angiography combined with OCT-elastography," Biomedical Optics Express 11(3), 1365–1382 (2020).
13. P. Wijesinghe, B. F. Kennedy, and D. D. Sampson, "Optical elastography on the microscale," in Tissue Elasticity Imaging, S. K. Alam, B. S. Garra (Eds.), Elsevier, Amsterdam, 185–229 (2020).
14. D. Kashyap, D. Pal, R. Sharma, V. K. Garg, N. Goel, D. Koundal, A. Zaguia, S. Koundal, and A. Belay, "Global Increase in Breast Cancer Incidence: Risk Factors and Preventive Measures," BioMed Research International 2022, 9605439 (2022).

15. B. F. Kennedy, R. A. McLaughlin, K. M. Kennedy, L. Chin, P. Wijesinghe, A. Curatolo, A. Tien, M. Ronald, B. Latham, C. M. Saunders, and D. D. Sampson, "Investigation of Optical Coherence Microelastography as a Method to Visualize Cancers in Human Breast Tissue," Cancer Reseach 75(16), 3236–3245 (2015).
16. E. V. Gubarkova, A. A. Sovetsky, L. A. Matveev, A. L. Matveyev, D. A. Vorontsov, A. A. Plekhanov, S. S. Kuznetsov, S. V. Gamayunov, A. Y. Vorontsov, M. A. Sirotkina, N. D. Gladkova, and V. Y. Zaitsev, "Nonlinear Elasticity Assessment with Optical Coherence Elastography for High-Selectivity Differentiation of Breast Cancer Tissues," Materials 15(9), 3308 (2022).
17. E. V. Gubarkova, A. A. Sovetsky, V. Y. Zaitsev, A. L. Matveyev, D. A. Vorontsov, M. A. Sirotkina, L. A. Matveev, A. A. Plekhanov, N. P. Pavlova, S. S. Kuznetsov, A. Y. Vorontsov, E. V. Zagaynova, and N. D. Gladkova, "OCT-elastography-based optical biopsy for breast cancer delineation and express assessment of morphological/molecular subtypes," Biomedical Optics Express 10(5), 2244–2263 (2019).
18. E. V. Gubarkova, E. B. Kiseleva, M. A. Sirotkina, D. A. Vorontsov, K. A. Achkasova, S. S. Kuznetsov, K. S. Yashin, A. L. Matveyev, A. A. Sovetsky, L. A. Matveev, A. A. Plekhanov, A. Y. Vorontsov, V. Y. Zaitsev, and N. D. Gladkova, "Diagnostic Accuracy of Cross-Polarization OCT and OCT-Elastography for Differentiation of Breast Cancer Subtypes: Comparative Study," Diagnostics 10(12), 994 (2020).
19. D. A. Vorontsov, E. V. Gubarkova, M. A. Sirotkina, A. A. Sovetsky, A. A. Plekhanov, S. S. Kuznetsov, D. A. Davydova, A. Y. Bogomolova, V. Y. Zaitsev, S. V. Gamayunov, A. Y. Vorontsov, V. A. Sobolevskiy, and N. D. Gladkova, "Multimodal Optical Coherence Tomography for Intraoperative Evaluation of Tumor Margins and Surgical Margins in Breast-Conserving Surgery," Sovremennye tehnologii v medicine 14(2), 26–38 (2022).
20. P. Gong, S. L. Chin, W. M. Allen, H. Ballal, J. D. Anstie, L. Chin, H. M. Ismail, R. Zilkens, D. D. Lakhiani, M. McCarthy, Q. Fang, D. Firth, K. Newman, C. Thomas, J. Li, R. W. Sanderson, K. Y. Foo, C. Yeomans, B. F. Dessauvagie, B. Latham, C. M. Saunders, and B. F. Kennedy, "Quantitative Micro-Elastography Enables In Vivo Detection of Residual Cancer in the Surgical Cavity during Breast-Conserving Surgery," Cancer Research 82(21), 4093–4104 (2022).
21. A. Plekhanov, E. Gubarkova, A. Sovetsky, M. Sirotkina, S. Kuznetsov, L. Matveev, D. Vorontsov, A. Matveyev, E. Zagaynova, V. Zaitsev, and N. Gladkova, "Improvement of breast cancer histological examination by means of multimodal OCT," in European Conferences on Biomedical Optics, 20–24 June 2021, Munich, Germany, EW4A.22 (2021).
22. A. A. Plekhanov, E. V. Gubarkova, M. A. Sirotkina, A. A. Sovetsky, D. A. Vorontsov, L. A. Matveev, S. S. Kuznetsov, A. Y. Bogomolova, A. Y. Vorontsov, A. L. Matveyev, S. V. Gamayunov, E. V. Zagaynova, V. Y. Zaitsev, and N. D. Gladkova, "Compression OCT-elastography combined with speckle-contrast analysis as an approach to morphological assessment of breast cancer tissue," Biomedical Optics Express 14(6), 3037–3056 (2023).
23. T. Oskarsson, "Extracellular matrix components in breast cancer progression and metastasis," The Breast 22, S66–S72 (2013).
24. I. Druzhkova, E. Nikonova, N. Ignatova, I. Koryakina, M. Zyuzin, A. Mozherov, D. Kozlov, D. Krylov, D. Kuznetsova, U. Lisitsa, V. Shcheslavskiy, E. A. Shirshin, E. Zagaynova, and M. Shirmanova, "Effect of Collagen Matrix on Doxorubicin Distribution and Cancer Cells' Response to Treatment in 3D Tumor Model," Cancers 14(22), 5487 (2022).
25. P. J. Keely, A. M. Fong, M. M. Zutter, and S. A. Santoro, "Alteration of collagen-dependent adhesion, motility, and morphogenesis by the expression of antisense alpha 2 integrin mRNA in mammary cells," Journal of Cell Science 108(2), 595–607 (1995).
26. D. Chauhan, S. Geetika, S. Kumar, and R. Kumar, "Combined Interaction of Cellular and Extracellular Components Causes Genetic Cascade Activation in Breast Cancer Metastasis," Oncology 100(6), 354–362 (2022).
27. O. Tezcan, A. S. Elshafei, K. Benderski, E. Rama, M. Wagner, D. Moeckel, R. Pola, M. Pechar, T. Etrych, S. von Stillfried, F. Kiessling, R. Weiskirchen, S. Meurer, and T. Lammers, "Effect of Cellular and Microenvironmental Multidrug Resistance on Tumor-Targeted Drug Delivery in Triple-Negative Breast cancer," Journal of Controlled Release 354, 784–793 (2023).
28. E. V. Gubarkova, V. V. Elagin, V. V. Dudenkova, S. S. Kuznetsov, M. M. Karabut, A. L. Potapov, D. A. Vorontsov, A. Y. Vorontsov, M. A. Sirotkina, E. V. Zagaynova, and N. D. Gladkova, "Multiphoton tomography in differentiation of morphological and molecular subtypes of breast cancer: A quantitative analysis," Journal of Biophotonics 14(5), e202000471 (2021).
29. D. Desa, M. Bhanote, R. Hill, J. Majeski, B. Buscaglia, M. D'Aguiar, R. Strawderman, D. Hicks, B. Turner, and E. Brown, "Second-harmonic generation directionality is associated with neoadjuvant chemotherapy response in breast cancer core needle biopsies," Journal of Biomedical Optics 24(8), 086503 (2019).
30. World Medical Association, "Ethical principles for medical research involving human subjects," European Journal of Emergency Medicine: Official Journal of the European Society for Emergency Medicine 8(3), 221–223 (2001).
31. F. Cardoso, S. Kyriakides, S. Ohno, F. Penault-Llorca, P. Poortmans, I. T. Rubio, S. Zackrisson, and E. Senkus, "Early breast cancer: ESMO Clinical Practice Guidelines for diagnosis, treatment and follow-up," Annals of Oncology 30(8), 1194–1220 (2019).

32. A. A. Plekhanov, M. A. Sirotkina, E. V. Gubarkova, E. B. Kiseleva, A. A. Sovetsky, M. M. Karabut, V. E. Zagainov, S. S. Kuznetsov, A. V. Maslennikova, E. V. Zagaynova, V. Y. Zaitsev, and N. D. Gladkova, "Towards targeted colorectal cancer biopsy based on tissue morphology assessment by compression optical coherence elastography," Frontiers in Oncology 13, 1121838 (2023).
33. V. M. Gelikonov, V. N. Romashov, D. V. Shabanov, S. Y. Ksenofontov, D. A. Terpelov, P. A. Shilyagin, G. V. Gelikonov, and I. A. Vitkin, "Cross-Polarization Optical Coherence Tomography with Active Maintenance of the Circular Polarization of a Sounding Wave in a Common Path System," Radiophysics and Quantum Electronics 60, 897–911 (2018).
34. V. Y. Zaitsev, A. L. Matveyev, L. A. Matveev, E. V. Gubarkova, A. A. Sovetsky, M. A. Sirotkina, G. V. Gelikonov, E. V. Zagaynova, N. D. Gladkova, and A. Vitkin, "Practical obstacles and their mitigation strategies in compressional optical coherence elastography of biological tissues," Journal of Innovative Optical Health Sciences 10(06), 1742006 (2017).
35. A. L. Matveyev, L. A. Matveev, A. A. Sovetsky, G. V. Gelikonov, A. A. Moiseev, and V. Y. Zaitsev, "Vector method for strain estimation in phase-sensitive optical coherence elastography," Laser Physics Letters 15(6), 065603 (2018).
36. A. A. Sovetsky, A. L. Matveyev, L. A. Matveev, D. V. Shabanov, and V. Y. Zaitsev, "Manually-operated compressional optical coherence elastography with effective aperiodic averaging: demonstrations for corneal and cartilaginous tissues," Laser Physics Letters 15(8), 085602 (2018).
37. A. A. Sovetsky, A. L. Matveyev, L. A. Matveev, E. V. Gubarkova, A. A. Plekhanov, M. A. Sirotkina, N. D. Gladkova, and V. Y. Zaitsev, "Full-optical method of local stress standardization to exclude nonlinearity-related ambiguity of elasticity estimation in compressional optical coherence elastography," Laser Physics Letters 17, 065601 (2020).
38. A. A. Sovetsky, A. L. Matveyev, L. A. Matveev, G. V. Gelikonov, and V. Y. Zaitsev, "Mapping Large Strains in Phase-Sensitive OCT: Key Role of Supra-Pixel Displacement Tracking in Incremental Strain Evaluation," Journal of Biomedical Photonics & Engineering 8(3), 030304 (2022).
39. E. V. Gubarkova, D. A. Vorontsov, A. A. Sovetsky, E. L. Bederina, M. A. Sirotkina, A. Yu Bogomolova, S. V. Gamayunov, A. Yu Vorontsov, P. V. Krivorotko, V. Y. Zaitsev, and N. D. Gladkova, "Quantification of linear and nonlinear elasticity by compression optical coherence elastography for determining lymph node status in breast cancer," Laser Physics Letters 20(6), 065601 (2023).
40. A. A. Plekhanov, M. A. Sirotkina, V. Y. Zaitsev, E. V. Gubarkova, S. S. Kuznetsov, E. N. Grigoreva, A. A. Sovetsky, L. A. Matveev, A. L. Matveyev, E. V. Zagaynova, and N. D. Gladkova, "Determining morphological structures' stiffness values of tumor tissue by optical coherence elastography," Proceedings of SPIE 11457, 1145707 (2020).
41. L. B. Mostaço-Guidolin, A. C. Ko, F. Wang, B. Xiang, M. Hewko, G. Tian, A. Major, M. Shiomi, and M. G. Sowa, "Collagen morphology and texture analysis: from statistics to classification," Scientific Reports 3(1), 2190 (2013).
42. Z. Nejim, L. Navarro, C. Morin, and P. Badel, "Quantitative analysis of second harmonic generated images of collagen fibers: a review," Research on Biomedical Engineering 39(1), 273–295 (2023).
43. C. B. Raub, V. Suresh, T. Krasieva, J. Lyubovitsky, J. D. Mih, A. J. Putnam, B. J. Tromberg, and S. C. George, "Noninvasive Assessment of Collagen Gel Microstructure and Mechanics Using Multiphoton Microscopy," Biophysical Journal 92(6), 2212–2222 (2007).
44. R. Rezakhaniha, A. Agianniotis, J. T. Schrauwen, A. Griffa, D. Sage, C. V. Bouten, F. N. van de Vosse, M. Unser, and N. Stergiopulos, "Experimental investigation of collagen waviness and orientation in the arterial adventitia using confocal laser scanning microscopy," Biomechanics and Modeling in Mechanobiology 11, 461–473 (2012).
45. J. Schindelin, I. Arganda-Carreras, E. Frise, V. Kaynig, M. Longair, T. Pietzsch, S. Preibisch, C. Rueden, S. Saalfeld, B. Schmid, J. Y. Tinevez, D. J. White, V. Hartenstein, K. Eliceiri, P. Tomancak, and A. Cardona, "Fiji: an open-source platform for biological-image analysis," Nature Methods 9(7), 676–682 (2012).
46. E. Fonck, G. G. Feigl, J. Fasel, D. Sage, M. Unser, D. A. Rüfenacht, and N. Stergiopulos, "Effect of aging on elastin functionality in human cerebral arteries," Stroke 40(7), 2552–2556 (2009).
47. S. C. Hagenaars, S. de Groot, D. Cohen, T. J. A. Dekker, A. Charehbili, E. Meershoek-Klein Kranenbarg, M. Duijm-de Carpentier, H. Pijl, H. Putter, R. Tollenaar, J. R. Kroep, and W. E. Mesker, "Tumor-stroma ratio is associated with Miller-Payne score and pathological response to neoadjuvant chemotherapy in HER2-negative early breast cancer," International Journal of Cancer 149(5), 1181–1188 (2021).
48. N. F. Boyd, Q. Li, O. Melnichouk, E. Huszti, L. J. Martin, A. Gunasekara, G. Mawdsley, M. J. Yaffe, and S. Minkin, "Evidence that breast tissue stiffness is associated with risk of breast cancer," PLoS One 9(7), e100937 (2014).
49. G. J. Yoshida, A. Azuma, Y. Miura, and A. Orimo, "Activated Fibroblast Program Orchestrates Tumor Initiation and Progression; Molecular Mechanisms and the Associated Therapeutic Strategies," International Journal of Molecular Sciences 20(9), 2256 (2019).
50. S. Wu, Y. Huang, Q. Tang, Z. Li, H. Horng, J. Li, Z. Wu, Y. Chen, and H. Li, "Quantitative evaluation of redox ratio and collagen characteristics during breast cancer chemotherapy using two-photon intrinsic imaging," Biomedical Optics Express 9(3), 1375–1388 (2018).
51. L. Li, Z. Han, L. Qiu, D. Kang, Z. Zhan, H. Tu, and J. Chen, "Label-free multiphoton imaging to assess neoadjuvant therapy responses in breast carcinoma," International Journal of Biological Sciences 16(8), 1376–1387 (2020).

52. P. P. Provenzano, K. W. Eliceiri, J. M. Campbell, D. R. Inman, J. G. White, and P. J. Keely, "Collagen reorganization at the tumor-stromal interface facilitates local invasion," BMC Medicine 4(1), 38 (2006).
53. C. D'Alterio, S. Scala, G. Sozzi, L. Roz, and G. Bertolini, "Paradoxical effects of chemotherapy on tumor relapse and metastasis promotion," Seminars in Cancer Biology 60, 351–361 (2020).
54. D. E. Desa, M. Bhanote, R. L. Hill, J. B. Majeski, B. Buscaglia, M. D'Aguiar, R. Strawderman, D. G. Hicks, B. M. Turner, and E. B. Brown, "Second-harmonic generation directionality is associated with neoadjuvant chemotherapy response in breast cancer core needle biopsies," Journal of Biomedical Optics 24(8), 086503 (2019).
55. L. Li, Z. Han, L. Qiu, D. Kang, Z. Zhan, H. Tu, and J. Chen, "Evaluation of breast carcinoma regression after preoperative chemotherapy by label-free multiphoton imaging and image analysis," Journal of Biophotonics 13(1), e201900216 (2020).
56. E. Provenzano, V. Bossuyt, G. Viale, D. Cameron, S. Badve, C. Denkert, G. MacGrogan, F. Penault-Llorca, J. Boughey, G. Curigliano, J. M. Dixon, L. Esserman, G. Fastner, T. Kuehn, F. Peintinger, G. von Minckwitz, J. White, W. Yang, and W. F. Symmans, "Standardization of pathologic evaluation and reporting of postneoadjuvant specimens in clinical trials of breast cancer: recommendations from an international working group," Modern Pathology 28(9), 1185–1201 (2015).
57. Y. Ma, S. Zhang, J. Li, J. Li, Y. Kang, and W. Ren, "Comparison of strain and shear-wave ultrasounic elastography in predicting the pathological response to neoadjuvant chemotherapy in breast cancers," European Radiology 27, 2282–2291 (2017).
58. E. Gubarkova, A. Potapov, D. Krupinova, K. Shatilova, M. Karabut, A. Khlopkov, M. Loginova, A. Sovetsky, V. Zaitsev, S. Radenska-Lopovok, N. Gladkova, G. Grechkanev, and M. Sirotkina, "Compression Optical Coherence Elastography for Assessing Elasticity of the Vaginal Wall under Prolapse after Neodymium Laser Treatment," Photonics 10(1), 6 (2023).
59. M. Plodinec, M. Loparic, C. A. Monnier, E. C. Obermann, R. Zanetti-Dallenbach, P. Oertle, J. T. Hyotyla, U. Aebi, M. Bentires-Alj, R. Y. H. Lim, and C.-A. Schoenenberger, "The nanomechanical signature of breast cancer," Nature Nanotechnology 7(11), 757–765 (2012).
60. F. Xia, K. Youcef-Toumi, "Review: Advanced Atomic Force Microscopy Modes for Biomedical Research," Biosensors 12(12), 1116 (2022).
61. G. Y. H. Lee, C. T. Lim, "Biomechanics approaches to studying human diseases," Trends in Biotechnology 25(3), 111–118 (2007).
62. S. Havaki, M. Kouloukoussa, K. Amawi, Y. Drosos, L. D. Arvanitis, N. Goutas, D. Vlachodimitropoulos, S. D. Vassilaros, E. Z. Katsantoni, I. Voloudakis-Baltatzis, V. Aleporou-Marinou, C. Kittas, and E. Marinos, "Altered expression pattern of integrin alphavbeta3 correlates with actin cytoskeleton in primary cultures of human breast cancer," Cancer Cell International 7, 16 (2007).
63. A. Stylianou, S. V. Kontomaris, C. Grant, and E. Alexandratou, "Atomic Force Microscopy on Biological Materials Related to Pathological Conditions," Scanning 2019, 8452851 (2019).
64. Z. Han, L. Li, D. Kang, Z. Zhan, H. Tu, C. Wang, and J. Chen, "Label-free detection of residual breast cancer after neoadjuvant chemotherapy using biomedical multiphoton microscopy," Lasers in Medical Science 34, 1595–1601 (2019).
65. B. Jähne(Ed.), Spatio-Temporal Image Processing: Theory and Scientific Applications, Lecture Notes in Computer Science No. 751, Springer-Verlag (1993).

Theoretical and Experimental Study of the Hair Bonding by Continuous Laser Radiation with a Wavelength of 980 nm

Andrey V. Belikov, Yulia V. Fyodorova*, and Vladislav M. Ermolaev
ITMO University, 49 Kronverksky pr., Saint Petersburg 197101, Russia

***e-mail:** yvsemyashkina@mail.ru

Abstract. The possibility of hair bonding by continuous laser radiation with a wavelength of 980 nm has been studied. A computer optical model of a laser system for bonding of human hair has been created. Using the Monte Carlo method, the distribution of the power of the absorbed laser radiation in the contact area of two hairs during their laser irradiation was obtained. The power distribution of the absorbed laser radiation obtained in the optical model is used in a computer thermophysical model of the laser bonding of human hair, the calculation in which is carried out by the finite element method. The maximum values of the temperature and the Arrhenius function of a pair of hairs in the area of their contact are calculated for different laser radiation power (1–10 W) and scanning speed of the laser beam along the area of hair contact (1–10 mm/s). It is shown that the temperature slowly decreases with increasing scanning speed, at the same time the Arrhenius function demonstrates a sharp decrease, while the values of both the temperature and the Arrhenius function increase with increasing laser radiation power. The power of laser radiation and the scanning speed at which the temperature of hair denaturation is reached, and the value of the Arrhenius function becomes equal to one were determined. Assuming that for the bonding of hair it is necessary that the temperature in the irradiation area exceeds the temperature of hair denaturation, and the Arrhenius function is less than one, the region of optimal laser radiation powers and scanning speeds is determined. In an *in vitro* experiment, the possibility of hair bonding by radiation from a continuous diode laser with a wavelength of 980 nm was studied and the validity of the optimal parameters of laser exposure selected at the stage of theoretical research was demonstrated. The results of the study can be used to develop a device for laser hair extension. © 2023 Journal of Biomedical Photonics & Engineering.

Keywords: diode laser; power; scanning speed; hair bonding; absorption; heating; temperature; denaturation; Arrhenius function.

Paper #8949 received 3 Apr 2023; accepted for publication 14 Jun 2023; published online 28 Jun 2023. doi: 10.18287/JBPE23.09.020306.

1 Introduction

Currently, laser technologies are increasingly used in dermatology and cosmetology [1–3]. In the field of hair care, laser hair extensions are gaining popularity [4]. Hair extensions are a highly sought-after cosmetic procedure, the essence of which is to attach donor hair (natural or artificial) to human hair in one way or another [5]. Hair extension methods can be divided into two large groups: “hot” and “cold”, that is, with and without heating, respectively [6]. Each of the existing extension methods has its advantages and disadvantages. Thus, “cold” methods allow to connect hair without heating it, however, they are distinguished by a long procedure duration and a limited set of hairstyle options [7]. As for the “hot” methods, the most well-known is capsule

extension, which consists in attaching donor hair with keratin capsules to human hair by melting these capsules using special thermal tongs [7]. This method of extension due to its speed, efficiency and flexibility is the most popular now. However, capsular extensions are not without drawbacks, mainly due to the keratin capsules themselves, which can cause discomfort during the first days after the procedure and require caution when caring for hair, which is associated with the risk of damage to the capsules. Currently, laser hair extension is a variant of the capsular extension technology, only in this case, the capsules are melted not with the help of special thermal tongs, but with the help of laser radiation [7]. The limitations associated with the use of capsules stimulate the search for new laser hair extension technologies without the use of capsules.

The subject of tissue bonding by laser radiation has been actively studied almost from the moment of the discovery of lasers. The mechanisms of laser bonding of biological tissues are considered in sufficient detail in literature [8–10]. Among these mechanisms laser welding and laser soldering are distinguished. In the first case, the bonding is carried out directly by laser radiation, while in the second case, the bonding occurs due to the action on the bonding substance – solder [11]. Thus, the existing technology of laser capsule extension is one of the options for laser soldering. The advantages of using laser soldering to connect biological tissues are, firstly, the reduction of heating and thermal damage to the biological tissue itself and, secondly, the creation of a joint that allows the biological tissue to successfully undergo the healing process [12, 13]. If the first advantage is important for laser hair extension, then the second one is not important, since the hair in the joint area does not regenerate [14]. In this regard, considering the inconvenience associated with the use of keratin capsules, it is of interest to study the possibility of hair extensions by welding them with laser radiation.

The connection of biological tissues is carried out by both continuous and pulsed laser radiation [11–13]. The main idea of using laser pulses is to reduce the thermal load on the biological tissues being joined [15]. The connection of biological tissues is possible both with a stationary laser spot and with a laser spot moving along the connection area. The choice between possible connection options occurs mainly based on the features of a particular procedure. When connecting biological tissues with continuous radiation, the fundamental parameters of laser exposure are the power of laser radiation and the exposure time (with a stationary laser spot) or scanning speed (with a moving laser spot) [16]. The choice of laser wavelength is very important. Hair consists of water, keratin, lipids, and melanin [14]. Hair components have specific absorption spectra [17]. According to Ref. [17], hair absorption in the region >2.7 μm is due to the absorption of water and keratin, while in the region <2.7 μm, it is due to the absorption of melanin. While extending hair, it is important that laser radiation is evenly absorbed throughout the entire volume of hair bundle, the size of which can vary from 50–60 μm (a single hair in a pair of connected hairs) to 1–2 mm or more (hair bundle). In this regard, the light attenuation coefficient at the wavelength of laser radiation should be in the range from 160–200 cm^{-1} (for bonding single hairs) to 5–10 cm^{-1} or less (for bonding hairs in a bundle). The absorption of a hair at a wavelength of 980 nm is 36.6 cm^{-1} [17], which makes it possible to use this radiation for bonding both single hairs and hairs in a bundle. Unfortunately, the hair welding by continuous laser radiation with a wavelength of 980 nm has not been studied.

Based on the foregoing, the main goal of the study was to theoretically and experimentally study the possibility of bonding (extending) human hair by welding them with continuous laser radiation with a wavelength of 980 nm and to determine the optimal combinations of laser radiation power and laser beam scanning speed for this procedure.

2 Materials and Methods

A computer optical model of a laser system for bonding of human hair was created using the TracePro Expert ver. 7.0.1 software package (Lambda Research Corporation, USA). The optical model of the system consisted of a laser radiation source, a lens, an optical fiber, and a sample (Fig. 1a).

The laser radiation source was an emitting area with a diameter of 300 μm. At the output of the source, the laser beam had a numerical aperture NA = 0.22. The spatial distribution in the laser beam was set to Gaussian. The laser radiation power at the output of the source was set equal to 1 W. The design parameters and optical properties of the lens and optical fiber are presented in Table 1.

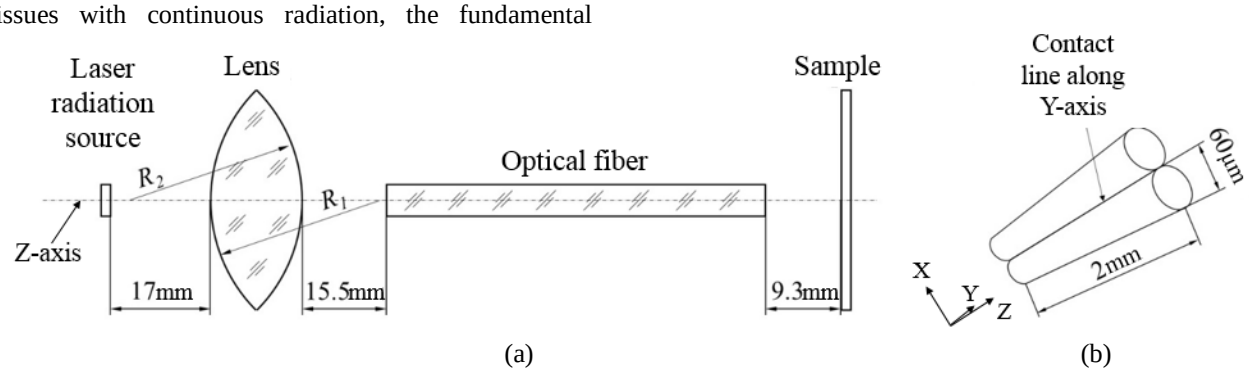


Fig. 1 Scheme of a laser system for bonding of human hair (a) and 3D model of the sample (b).

Table 1 Design parameters and optical properties of lens and optical fiber of a laser system for bonding of human hair [18, 19].

Component of laser system	Design parameters	Optical properties		
		Wavelength, nm	Refractive index	Absorption coefficient, mm^{-1}
Lens	R_1 = 9 mm; R_2 = –9 mm; diameter 5 mm	980	1.5111	2×10^{-4}
Optical fiber	core diameter = 400 μm; cladding diameter = 440 μm; length = 1 m	980	1.457 (core); 1.439 (cladding)	1×10^{-5}

Table 2 Optical properties of human hair [20, 21].

Wavelength, nm	Refractive index	Absorption coefficient, mm^{-1}	Scattering coefficient, mm^{-1}	Anisotropy factor
980	1.55	3.66	1.345	0.79

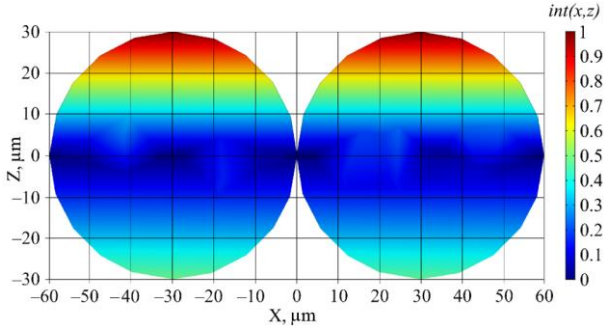


Fig. 2 Spatial power distribution of the absorbed 980 nm laser radiation in the sample (function *int(x, z)* in the X Z plane).

The sample consisted of two cylinders (hairs) with a diameter of 60 μm and a length of 2 mm each located in air, parallel to each other and in perfect contact (Fig. 1b). The components of a laser system for bonding of human hair were located in such a way that the center of the laser spot was on the line of contact of the hair, and its diameter in the plane passing through the axis of symmetry of the hair was 1 mm. Such a construction of the optical scheme was carried out considering the specifics of the experiments (see below), so that it would be possible to adequately compare their results with the results of theoretical simulation. The optical properties of human hair used for modeling are presented in Table 2.

The calculation of the propagation of laser radiation in the optical model of the laser system for bonding of human hair was carried out by the Monte Carlo method [22]. The result of optical modeling was the interpolating function *int(x, y, z)* describing the spatial distribution of the power of the absorbed laser radiation in the sample. When calculating this distribution, the sample was divided into many cubic elements with a side of 4 μm (grid cell size). An example of the spatial power distribution of the absorbed 980 nm laser radiation in the sample in the X Z plane is shown in Fig. 2.

The *int(x, y, z)* was used for subsequent calculations in a computer thermophysical model of laser bonding of human hair.

A computer thermophysical model of laser bonding of human hair was created using the COMSOL Multiphysics ver. 6.0 software package (COMSOL Inc., USA). The geometry of the sample in the computer thermophysical model was the same as in the computer optical model described above. The thermophysical and kinetic properties of human hair used for modeling are presented in Table 3.

The frequency factor A denotes the frequency of molecular collisions [25]. The simulation of the thermal effect of laser radiation was carried out on the basis of the power distribution of the absorbed laser radiation in the sample obtained as a result of optical simulation (see Fig. 2). The computational area was a parallelepiped with sides 120 × 2000 × 120 μm (X, Y, Z). Data on the power distribution of absorbed laser radiation in the sample, presented in tabular form, were linearly interpolated by software tools built into COMSOL Multiphysics ver. 6.0. Based on the obtained interpolating function, according to Ref. [26], an equation was compiled and applied to calculate the distribution of the volumetric power density of heat sources in the sample:

$$Q = int(x, y, z) \times \frac{P}{V}, \quad (1)$$

where Q is the volumetric power density of heat sources, $int(x,y,z)$ is the interpolating power distribution function, P is the power of laser radiation at the output of the source, V is the volume of the grid cell of the calculation.

Here, it should be noted that since the laser power at the output of the source was set equal to 1 W in the optical simulation, the multiplication of the interpolating function by the changing value of the laser power when specifying the heat source made it possible to easily scale the calculation of Q for different values of the laser power.

Table 3 Thermophysical and kinetic properties of human hair [23, 24].

Density ρ, kg/m^3	Coefficient of thermal conductivity k, W/(m·K)	Specific heat c, J/(kg·K)	Frequency factor A, s^{-1}	Activation energy E_a, J/mol
1.31×10^3	0.37	1×10^4	2.49×10^{13}	1.47×10^5

In thermophysical modeling in the COMSOL Multiphysics ver. 6.0, the finite element method [27] was used to solve the standard heat transfer equation for the physical interface "Heat transfer in solids" [28]:

$$\rho c\left(\frac{\partial T}{\partial t}+v\times\nabla T\right)+\nabla\left(q+q_r\right)=Q, \qquad (2)$$

where ρ is the density of the sample, c is the specific heat capacity of the sample, T is the temperature of the sample, t is the time, v is the translational velocity vector of the sample, q is the heat flux density of the heat transfer, q_r is the heat flux density of the radiation, Q is the volumetric power density of heat sources.

To implement the finite element method, the sample was divided into elements. Splitting was done automatically with element size "Finer". With such a division, the side of the element was no more than 16 μm. Trial calculations showed that a decrease in the size of the elements did not lead to a significant change in the results. It is important to note that the translation velocity vector of the sample was responsible for the velocity of the sample, the movement of which simulated the movement of the laser spot along the line of contact of the hair, thus, the calculation was carried out for different values of the scanning speed. For the correct operation of the thermophysical model, the coordinate systems in the optical and thermophysical models were matched. The initial conditions were established: an initial temperature of 298.15 K, a pressure of 101 kPa, and the presence of natural convection of the air surrounding the sample. In the COMSOL Multiphysics ver. 6.0, the convection heat flux in air q_0 for both hairs was calculated as:

$$q_0=h\cdot(T_{ext}-T), \qquad (3)$$

where h is the heat transfer coefficient, T_{ext} is the ambient temperature (air), T is the hair temperature.

The heat transfer coefficient was calculated for the case of a thin cylinder as:

$$h=\frac{k}{H}\left(\frac{4}{3}\left(\frac{7\mathrm{Ra}_H\,\mathrm{Pr}}{5(20+21\,\mathrm{Pr})}\right)^{1/4}+\frac{4(272+315\,\mathrm{Pr})H}{35(64+63\,\mathrm{Pr})D}\right), \qquad (4)$$

where k is the thermal conductivity of air, H is the cylinder (hair) height, Ra_H is the Rayleigh number, Pr is the Prandtl number of air, D is the cylinder (hair) diameter. In this case, the Rayleigh number was given as:

$$\mathrm{Ra}_H=\frac{g\alpha_p\left|T-T_{ext}\right|H^3}{k\mu}, \qquad (5)$$

where g is the acceleration of gravity, α_p is the coefficient of thermal expansion of air, μ is the dynamic viscosity of air [28].

The hairs in the model are in contact along the line of contact (see Fig. 1), no additional boundary conditions have been specified for this area due to the negligible hair contact area. The contribution of boiling and evaporation of water was not considered in the approximation that the water content in dry hair is low (in what follows, dry hair was used in the experiment).

As a result of thermophysical modeling, the maximum values of temperature and the Arrhenius function were calculated at the line of hair contact in the sample. The Arrhenius function is used to assess the degree of thermal damage to a biological tissue (the relative concentration of damaged molecules) and is calculated as [29]:

$$\Omega=\int_0^t Ae^{-\frac{E_a}{RT}}dt, \qquad (6)$$

where Ω is the value of the Arrhenius function, t is time, A is the frequency factor, E_a is the activation energy, R = 8.31 J/(mol·K) is the universal gas constant; T is the temperature.

The degree of thermal damage Λ is calculated as [30]:

$$\Lambda=\frac{C_0-\mathrm{C}(t)}{C_0}=1-\exp(-\Omega), \qquad (7)$$

where C_0 is the initial concentration of molecules or cells, C(t) is the concentration of molecules or cells at a time t.

At Ω = 1, the degree of thermal damage Λ becomes equal to $1-e^{-1}\approx 0.63$, and the temperature reaches a value sufficient for denaturation (irreversible change) of the biological tissue [31].

In the calculations, the laser radiation power was varied from 1 W to 10 W, and the laser spot scanning speed was varied from 1 mm/s to 10 mm/s.

In an *in vitro* experiment, the possibility of bonding two human hairs by welding them with 980 nm continuous laser radiation was studied. Dry dark uncolored hair of one person (volunteer) was used in the study. Before the experiment, a fragment 10–15 cm long was mechanically cut off from a hair 50–60 cm long and stored for 14 days in a dry, dark, unlit, air-conditioned room at a temperature of 23 ± 1 °C. A total of 20 fragments were obtained from 20 neighboring hairs. It

was these hair fragments that were used to create samples for research. The scheme of the experimental setup is shown in Fig. 3. The sample was a pair of hairs 60 ± 10 μm in diameter and 20 ± 2 mm long, fixed in a holder so that their surfaces were in contact with each other along the line of contact parallel to the hair axis. An Alta-ST diode laser (Dental Photonics Inc., USA) with a wavelength of 980 nm operating in a continuous mode was used as a source of laser radiation. Laser radiation was delivered to the sample via an optical fiber, the output end of which moved along the sample fixed in the holder. The movement of the fiber was provided by a scanning system controlled by a computer.

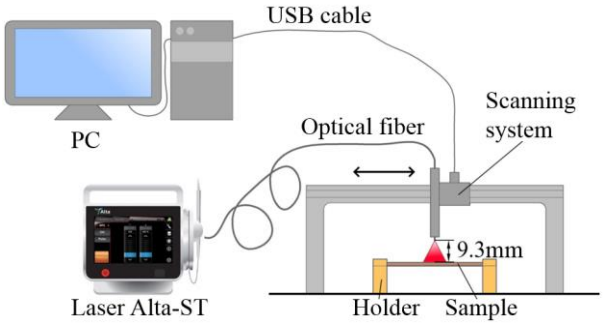


Fig. 3 Scheme of an experimental setup for *in vitro* study of the possibility of bonding two human hairs by welding them with continuous laser radiation at a wavelength of 980 nm.

The design parameters and optical properties of the materials were identical to those used previously in optical modeling. After laser exposure, the samples were photographed using an AxioScope A1 optical microscope (Carl Zeiss, Germany) equipped with an AxioCam camera (Carl Zeiss, Germany) and the appearance of the samples was analyzed for visible changes, bonding (welding) or irreversible thermal damage.

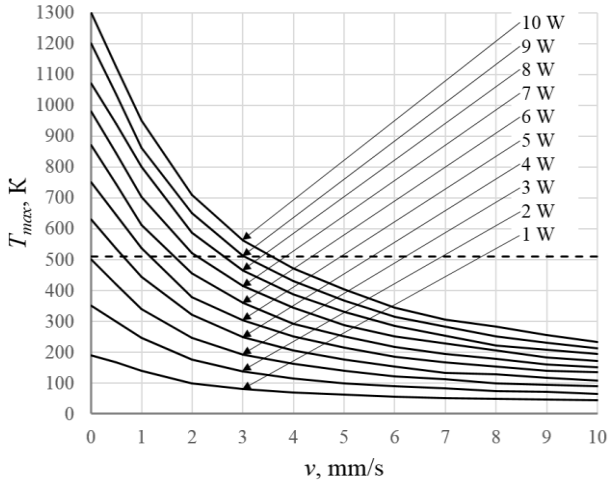
3 Results and Discussion

The dependences of the maximum temperature and the maximum value of the Arrhenius function at the line of contact of the hairs in the sample on the scanning speed obtained as a result of modeling at various values of the laser radiation power are shown in Fig. 4(a) and Fig. 4(b), respectively.

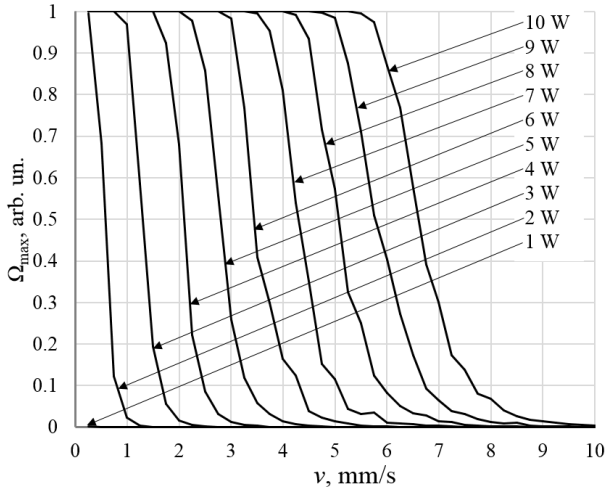
It can be seen that with an increase in the scanning speed at a constant laser radiation power, the maximum temperature at the line of hair contact in the sample decreases. In this case, the higher the laser radiation power, the higher the maximum temperature that can be achieved at a constant scanning speed. The melting point of a Caucasian hair of 508.95 K is not achieved for all combinations of power and speed, which is obviously due to the competition between heating and cooling processes.

It can also be seen that with an increase in the scanning speed at a constant laser power, the maximum value of the Arrhenius function at the line of hair contact in the sample decreases. At the same time, the higher the laser radiation power, the higher the scanning speed at which $\Omega_{max} = 1$. The maximum value $\Omega_{max} = 1$, at which irreversible thermal damage to the hair occurs, is not achieved for all combinations of power and speed, which is due both to the competition between heating and cooling processes and with the contribution of the rate of the denaturation process.

The analysis of the dependences presented in Fig. 4 made it possible to determine the combinations of scanning speed and laser radiation power at which the melting temperature is reached at the hair contact line in the sample and at which $\Omega_{max} = 1$ (see Fig. 5).



(a)



(b)

Fig. 4 Dependence of the maximum temperature T_{max} (a) and the maximum value of the Arrhenius function Ω_{max} (b) at the line of hair contact in the sample on the scanning speed v at different powers of laser radiation at a wavelength of 980 nm (dashed line corresponds to the melting temperature of a Caucasian hair of 508.95 K [32]).

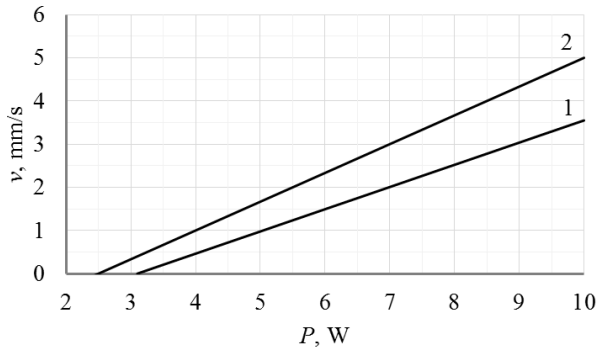


Fig. 5 Dependence of the scanning speed v at which the temperature at the line of hair contact in the sample reaches the melting point of a Caucasian hair of 508.95 K (line 1) and at which $\Omega_{max} = 1$ (line 2) on the power of laser radiation P at a wavelength of 980 nm.

Achieving the melting temperature of the hair at the line of contact of the hair in the sample leads to a reversible thermal change in the hair shell (cuticle), which consists mainly of keratin, and does not affect the hair as a whole. This change makes it possible to connect the hairs to each other. At the same time, reaching the value $\Omega_{max} = 1$ by the Arrhenius function leads to irreversible thermal damage to the hair, which should be avoided.

Thus, based on the simulation, it can be assumed that hair welding can be achieved by heating them to the melting temperature and the optimal combinations of laser radiation power with a wavelength of 980 nm and laser beam scanning speed for bonding (extension, welding) hair lie above line 1 and below line 2 in Fig. 5.

In the *in vitro* experiment, the impact on the sample was carried out at three combinations of the scanning speed of the laser spot and the power of the laser radiation. Combination #1 (P = 3.5 W and v = 4 mm/s) lies above line 1 and line 2 in Fig. 5 and, according to the previously formulated assumption, should not cause melting and irreversible thermal damage to the hair, therefore, should not lead to welding. Combination #2 (P = 5.0 W and v = 1.5 mm/s) lies below line 1 and above line 2 in Fig. 5 and, according to the previously formulated assumption, should lead to welding along the line of hair contact in the sample. Combination #3 (P = 6.5 W and v = 1 mm/s) lies below line 1 and line 2 in Fig. 5 and should lead to irreversible thermal damage to the hair. In total, 10 samples were studied in the experiment for each of the three combinations of the laser spot scanning speed and the laser radiation power. Typical photographs of samples after laser exposure with each of the three combinations are shown in Fig. 6.

It can be seen that laser exposure with Combination #1 did not change the appearance of the hair and did not lead to their bonding. Combination #2 did not change the appearance of the hair and led to their bonding along the line of contact. Combination #3 changed the appearance of the hair (they increased in diameter and collapsed) and did not lead to their bonding along the line of contact.

Thus, the results observed in the experiment confirm the conclusion made on the basis of modeling about the possibility of hair welding and the validity of the recommendations on choosing the optimal combinations of the power of continuous laser radiation with a wavelength of 980 nm and the scanning speed of the laser beam for their bonding (extension).

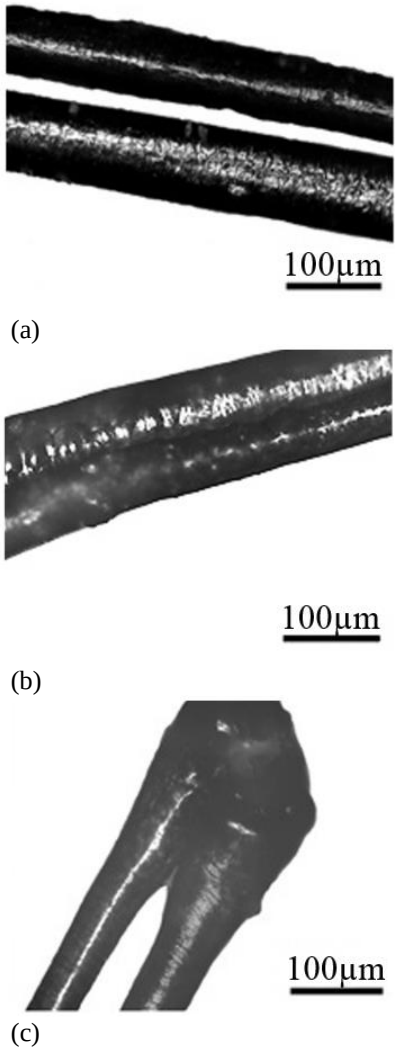


Fig. 6 Typical photographs of samples after exposure to continuous laser radiation with a wavelength of 980 nm: (a) Combination #1, (b) Combination #2, and (c) Combination #3.

4 Conclusion

In the course of the study, a computer optical model of a laser system for bonding of human hair and a computer thermophysical model of laser bonding of human hair were created. As a result of modeling, the dependences of the maximum temperature and the maximum value of the Arrhenius function at the line of contact of hairs in the sample on the scanning speed of the laser beam were obtained at different powers of laser radiation with a wavelength of 980 nm. The optimal combinations of laser radiation power and laser beam scanning speed for bonding (extension) of hair were determined. *In vitro* experiments were carried out on bonding hair with laser

radiation with a wavelength of 980 nm. The results of the experiments confirmed the possibility of bonding (extension) hair by welding with continuous laser radiation with a wavelength of 980 nm and showed a satisfactory agreement with the simulation results.

Disclosures

All authors declare that there is no conflict of interests in this paper.

Acknowledgements

The work was supported by a NIRMA grant from ITMO University and presented at the International Symposium FLAMN-22 (06.22.2022-06.30.2022, St. Petersburg, Russia).

References

1. S. Watanabe, "Basics of laser application to dermatology," Archives of Dermatological Research 300, 21–30 (2008).
2. O. V. Sheptii, L. S. Kruglova, O. V. Zhukova, T. V. Ektova, D. A. Raksha, and A. A. Shmatova, "High-energy laser exposure in dermatology and cosmetology," Russian Journal of Skin and Venereal Diseases 15(6), 39–43 (2012). [in Russian]
3. P. L. Bencini, A. Tourlaki, M. Galimberti, C. Longo, G. Pellacani, V. D. Giorgi, and G. Guerriero, "Nonablative fractional photothermolysis for acne scars: clinical and in vivo microscopic documentation of treatment efficacy," Dermatologic Therapy 25(5), 463–467 (2012).
4. A. Alessandrini, B. M. Piraccini, "Essential of hair care cosmetics," Cosmetics 3(4), 34 (2016).
5. C. Porterfield, The forensic value of processed human hair extensions, Master Of Science In Forensic Science Thesis, University of Central Oklahoma, Edmond (2014).
6. A. Yang, M. Iorizzo, C. Vincenzi, and A. Tosti, "Hair extensions: a concerning cause of hair disorders," British Journal of Dermatology 160(1), 207–209 (2009).
7. A. Tosti, D. Asz-Sigall, and R. Pirmez (Eds.), Hair and Scalp Treatments, Springer, Cham, Switzerland (2019).
8. T. Vo-Dinh, Biomedical Photonics Handbook, CRC Press, Boca Raton, USA (2003). ISBN: 9780429214295.
9. L. Pavesi, P. M. Fauchet (Eds.), Biophotonics, Biological and Medical Physics, Biomedical Engineering, Springer Berlin, Heidelberg (2008). ISBN: 9783540767824.
10. C. Li, K. Wang, "Effect of welding temperature and protein denaturation on strength of laser biological tissues welding," Optics & Laser Techology 138, 106862 (2021).
11. B. Ott, B. J. Züger, D. Erni, A. Banic, T. Schaffner, H. P. Weber, and M. Frenz, "Comparative in vitro study of tissue welding using a 808 nm diode laser and a Ho: YAG laser," Lasers in Medical Science 16(4), 260–266 (2001).
12. H. Ö. Tabakoğlu, M. Gülsoy, "In vivo comparison of near infrared lasers for skin welding," Lasers in Medical Science 25(3), 411–421 (2010).
13. D. R. Pabittei, M. Heger, S. van Tuijl, M. Simonet, W. de Boon, A. C. van der Wal, R. Balm, and B. A. de Mol, "Ex vivo proof-of-concept of end-to-end scaffold-enhanced laser-assisted vascular anastomosis of porcine arteries," Journal of Vascular Surgery 62(1), 200–209 (2015).
14. B. Bhushan, Biophysics of human hair: structural, nanomechanical, and nanotribological studies, Springer Berlin, Heidelberg, Germany (2010). ISBN: 9783642159015.
15. K. Litvinova, M. Chernysheva, B. Stegemann, and F. Leyva, "Autofluorescence guided welding of heart tissue by laser pulse bursts at 1550 nm," Biomedical Optics Express 11(11), 6271–6280 (2020).
16. C. Li, H. Jun, W. Kehong, L. Qimeng, and C. Zibo, "Investigation on thermal damage model of skin tissue in vitro by infrared laser welding," Optics and Lasers in Engineering 124, 105807 (2020).
17. G. B. Altshuler, I. K. Ilyasov, and C. V. Prikhodko, "Optical properties of human hair," Laser Interaction with Hard and Soft Tissue II 2323, 344–350 (1995).
18. M. N. Polyanskiy, Refractive index database, (accessed 25 April 2022). [https://refractiveindex.info].
19. Thorlabs, (accessed 25 April 2022). [https://www.thorlabs.com].
20. C. R. Robbins, Chemical and physical behavior of human hair, Springer, New York (2012). ISBN: 9781475720099.
21. X. Huang, M. D. Protheroe, A. M. Al-Jumaily, S. P. Paul, and A. N. Chalmers, "Review of human hair optical properties in possible relation to melanoma development," Journal of Biomedical Optics 23(5), 050901 (2018).
22. D. P. Kroese, T. Brereton, T. Taimre, and Z. I. Botev, "Why the Monte Carlo method is so important today," Wiley Interdisciplinary Reviews: Computational Statistics 6(6), 386–392 (2014).
23. E. Petrovicova, Y. K. Kamath, "Heat transfer in human hair," International Journal of Cosmetic Science 41(4), 387–390 (2019).
24. F. J. Wortmann, "The toughening transition in hair keratin," Colloid and Polymer Science 271(8), 802–804 (1993).
25. Y. N. Litvishkov, "On the physical meaning of the parameters of the Arrhenius equation," Kimya Problemleri (3), 456–464 (2019). [in Russian]

26. Q. M. Luong, S. D. Dams, "The light distribution in skin of a 976nm laser diode using different parameter sets in Monte Carlo simulations," Philips Research, (2009).
27. K. Shurrab, N. Kochaji, and W. Bachir, "Development of temperature distribution and light propagation model in biological tissue irradiated by 980 nm laser diode and using COMSOL simulation," Journal of Lasers in Medical Sciences 8(3), 118–122 (2017).
28. User's Guide, Heat Transfer Module, COMSOL (2018).
29. K. J. Laidler, "The development of the Arrhenius equation," Journal of Chemical Education 61(6), 494–498 (1984).
30. M. H. Niemz, Laser – Tissue Interactions: Fundamentals and Applications, Springer Berlin, Heidelberg (2007). ISBN: 978-3-540-72192-5.
31. L. G. Astafyeva, G. I. Zheltov, "Temperature field formed inside a blood vessel under the action of pulsed laser radiation," Optics and Spectroscopy 103(4), 665–670 (2007).
32. C. R. R. C. Lima, M. M. de Almeida, M. V. R. Velasco, and J. D. R. Matos "Thermoanalytical characterization study of hair from different ethnicities," Journal of Thermal Analysis and Calorimetry 123, 2321–2328 (2016).

3D Printed Modular Vein Viewing System Based on Differential Light Absorption in the Near Infrared Range

Nikita V. Remizov*, Elena M. Bataeva, Dmitry P. Stramousov, Anastasiya A. Shatskaya, and Dmitry N. Artemyev

Samara National Research University, 34 Moskovskoye shosse, Samara 443086, Russia

***e-mail:** erenv97@yandex.ru

Abstract. There are many cases in the medical laboratory examinations when it is necessary to detect a vein in a patient and the blood vessels are not visible to the naked eye. In such situations, devices for optical vein visualization are required. Nowadays, the technology of optical vein visualization is promising, but it has a number of disadvantages. Moreover, no objective approach has been proposed to estimate visualization quality, which complicates the choice of technical parameters of a vein viewer. For this reason, a prototype of vein viewer with interchangeable and easily replaceable parts was presented in this paper. This prototype allowed to perform experiments changing the optical properties of the vein viewer. A new methodology of visualization quality estimation was developed. This new methodology allows to quantitatively estimate the visualization quality. Proposed technique is also almost independent of the human factor. The research involved 20 volunteers aged 20–24 with Fitzpatrick skin phototype III. Studies were carried out to evaluate the change in the output signal of the prototype under the use of different optical elements for the same object Thus, the influence of absorption long-pass optical filters HWB780 and HWB830 on the contrast of veins in relation to the skin surface when using two different LED illumination sources (850 nm and 940 nm peak wavelengths) was analyzed. The effectiveness of lenses with focal lengths of 3.6 mm, 16 mm, and 25 mm was observed. © 2023 Journal of Biomedical Photonics & Engineering.

Keywords: vein viewer; differential absorption; light source; objective lens; absorption long-pass optical filters; optical diffuser; contrast estimation.

Paper #8941 received 14 Mar 2023; revised manuscript received 3 Jun 2023; accepted for publication 5 Jun 2023; published online 29 Jun 2023. doi: 10.18287/JBPE23.09.020307.

1 Introduction

Medical laboratory examination is one of the most common diagnostic methods in medicine. A number of diseases (including most of the infectious diseases, endocrine pathologies, and genetic disorders) can be detected exclusively by laboratory means. One of the main methods of laboratory examinations is a blood test. Blood can be drawn from a capillary in a finger or from a vein. Drawing blood from a vein requires detection of a vein of the patient, which can be difficult in cases when veins are not visible to the naked eye [1, 2]. Vein viewers are used to highlight an invisible vein and thus quickly locate it in order to prevent preanalytical errors and to avoid patient pain caused by unnecessary punctures in search of a vein [1–4].

The vein viewer is a non-invasive device that provides a map of the patient's veins, including those invisible to the naked eye. The main principle of the device is the different absorption of light by blood hemoglobin and the surrounding tissues. The device emits light in the range of 750–950 nm to a part of a patient's body and registers the light reflected from the surrounding tissues with a camera. The resulting image is displayed on the device screen or optionally projected onto the patient using a pico projector.

A vein viewer has a wide range of applications. For example, it can be used during sclerotherapy or

This paper was presented on the Biophotonics Workshop of the XX All-Russian Youth Conference-Contest on Optics and Laser Physics, Dedicated to the 100th Anniversary of N.G. Basov, Samara, Russia, November 8–12, 2022.

phlebectomy to remove invisible varicose veins provoking growth of new formations [1]. It may also be suitable for intravenous injections, blood sampling, catheter placement [2–4]. There are also non-medical applications, such as identification of a person by the vein pattern in the biometrics [5].

Many researchers note a number of disadvantages of optical vein visualization technology: poor vein visibility in the presence of skin defects (stretch marks, scars, pigment spots), poor vein visibility for dark-skinned patients, for patients with excessive body weight, low visualization depth, within 3–5 mm [1–3].

Nevertheless, this technology is very promising. Improvement and active implementation of vein viewers would simplify a number of medical procedures, such as injections and blood sampling, which is necessary to improve patient comfort and treatment quality. Researchers consider the possibility of using polychromatic sources, multispectral imaging and hyperspectral imaging to improve the technology [6–8]. It should be noted that the visible light range is rarely used as a source for vein visualization because the light in the range below 400–700 nm has a low penetration depth into the biological tissue, less than 2–4 mm, compared to the light in the range of 750–950 nm, which can reach a penetration depth of 5 mm [1, 2]. In such devices, the visible range is usually employed only to project a vein map onto a part of the patient's body.

In addition, many studies have no evaluation of the obtained results. In the papers where the results have been evaluated [2, 6], the evaluation is performed roughly, visually, and highly dependent on the human factor. For example, in the research [2] the evaluation of the results is performed visually, i.e., the researcher assigns a class to each digital photo obtained with the vein viewer: "Veins are perfectly visible", "Veins are visible" or "Veins are not visible". The results provide statistics on the number of subjects assigned to each class. Similarly, the research [6] divides the pictures into 2 classes: "Veins are visible" and "Veins are invisible". Then the success rate is calculated, i.e. the ratio of the number of subjects whose forearm photos belong to the "Veins are visible" class to the total number of subjects. This approach makes it difficult to select optimal, according to the criterion of maximum vein contrast with respect to the skin surface, vein viewer parameters.

Thus, there is the challenge of developing a device for troublesome vein visualization patients that provides maximum contrast of veins with respect to the skin surface with an affordable price. To develop such a device, it is necessary to carry out a number of experiments to select light sources, objective lenses and filters. In this paper, a prototype of vein viewer experimental stand is proposed and researches on selection of objective lenses, filters and light sources are carried out.

A novel approach to the evaluation of visualization quality, which has not been found in previous studies, has been developed. The novel approach allows to quantitatively compare vein visualization results while using different long-pass optical filters, objective lenses, and light sources.

2 Basic Principles of Vein Viewers Design

Currently, many ways of vein viewers design are proposed. Basically, vein viewer construction includes an LED light source which emits in the near infrared range, a compact camera sensitive to the infrared range, and a long-pass optical filter attached to the objective lens of the camera. The spectrum of the LED source emission is usually located between 750 and 950 nm, at the researcher's discretion [1]. Different implementations of optical filters are used: simple and inexpensive options, for example, floppy disk substrates or negative photographic film, or factory-produced long-pass optical filters [1].

Mark D. Francisco et al. (2021) proposed a low-cost vein viewer design [2]. The emitting part of the proposed device consists of three LEDs with a peak wavelength of 960 nm. The reflected light is recorded using a 1920 × 1080 UXGA (1080P) CMOS camera, with a long-pass IR filter attached to the lens. The characteristics of the filter are not specified. The filter cut off the visible range and passes light in the 960 nm range. Authors also applied digital image processing techniques to obtained images.

Marathe et al. (2014) suggested the design of a wireless vein viewer with the ability to transmit the image via XBee to an image processing unit (personal computer) [3]. The researchers use an LED matrix consisting of 25 LEDs with a peak wavelength of 940 nm and CCD camera module. To block visible light, a long-pass IR filter, the parameters of which are not specified, is attached to the camera objective lens. Data transfer via XBee and digital image processing is performed using MATLAB.

Tran and Pham (2020) developed a vein viewer with computer image processing and vein map back projection [4]. A LED ring containing 6 LEDs with a peak wavelength of 850 nm is used as a light source. A NoIR Camera Board connected to a Raspberry Pi 3 Model B is used to capture the image. The data is transmitted to a personal computer, where image processing and filtering is performed, as well as an output to the display. In addition, the image is projected onto the patient's arm using a Texas Instruments DLPDLCR2010EVM DLP-projector. MATLAB environment is used for image processing.

Dhakshayani and Yasin (2015) presented a vein viewer with a polychromatic source [6]. The light source is a LED ring, which contains 24 LEDs: 6 for each wavelength (740, 765, 770, 780 nm). The IR detector is based on a CMOS webcam. A Kodak wratten 87 IR filter is attached to the camera in combination with an IR photo film, which allows to detect light in the 740–790 nm range. The control device is a Raspberry Pi board. The resulting image then outputs to the display.

In addition, consider the relevance of using LED source as part of a vein viewer. In medical facilities, gas-

discharge lamps are often used as a light source. Such lamps contain spectral components in the near infrared range, which may give the impression that there is no need to use an additional source of light for vein visualization. However, such lamps have unpredictable spectral characteristics and optical power. In addition, in this case, the patient must be positioned in close proximity to the light source, due to the low power of infrared light, which is often impossible.

The LED source as a part of the vein viewer has more stable parameters, and is designed specifically for the task of vein visualization, which provides stability and reproducibility of the results. Furthermore, such sources are quite small and affordable, which makes it unreasonable to refuse using an additional source as part of the vein viewer. Thus, LED source is a necessary part of vein viewer.

3 Materials and Methods

3.1 Experimental Stand

The prototype of vein viewer experimental stand was developed within the scope of the given task on the basis of the reviewed principles (Fig.1). The prototype is connected to the PC via the USB interface. There is a ring board with IR LEDs and a camera with an IR filter attached to it for image registration in a 3D printed plastic body. The design also includes a 0.6 mm thick 3D printed optical diffuser, which allows for relatively uniform illumination from the LED ring with reduced optical power. A 12 V 500 mA DC power supply is connected to the ring board. The camera is connected to the PC via USB and displays the image on the screen of the PC. The body is placed on a tripod. The disassembled experimental stand is shown in Fig. 2. The developed design of the body allows easy and quick replacement of elements, which helps to carry out experiments with different components.

The body model was developed in the OpenSCAD environment. PETG plastic was used for 3D printing of the bodies and diffusers.

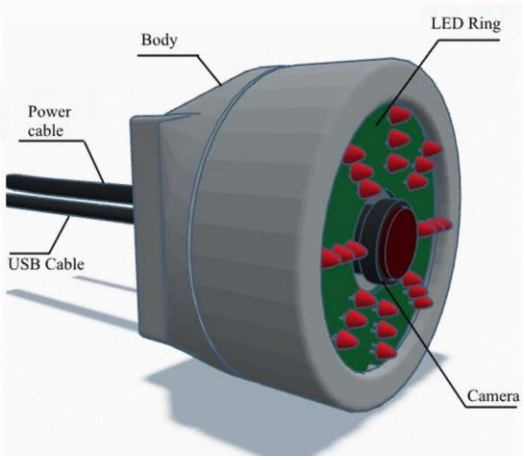


Fig. 1 3D model of the vein viewer experimental stand.

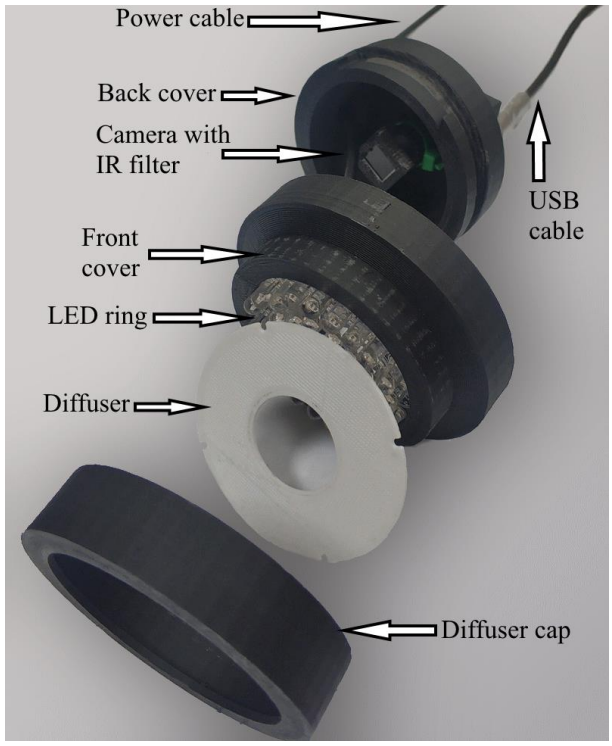


Fig. 2 Disassembled experimental stand of vein viewer.

Two LED rings were used as a light source during the experiment. The first had LEDs with a peak wavelength of 850 nm, the second – LEDs with a peak wavelength of 940 nm. Similar parameters were used by most of the researchers, because the 750–950 nm light is known to be characterized by the greatest depth of penetration into the biological tissue [1–4]. Both rings were assembled according to the circuit diagram shown in Fig. 3. The LED rings were built on the basis of KR142EN12A (DA1) chips connected according to the current source circuit, and 5-mm Chanzon brand LEDs (HL1–HL24) with peak wavelengths at 850 and 940 nm. The optical power of one LED was 14 mW.

As a result, two lighting units designed as a ring of LEDs with central wavelengths of 850 nm and 940 nm, having the same connection circuit, were produced. Characteristics of the blocks: 24 LEDs, the scattering angle of the LEDs is 90º. Optical power of each block is 336 mW.

The camera module based on a Sony IMX335 CMOS sensor was used for image capture. This module allowed to reduce the device size, as well as to ensure low power consumption and affordable cost.

The main specifications of IMX335:

- Max resolution: 5 MP / 2592 × 1944 px,
- Bit rate: 10/12 bit,
- Image Rate: 60 FPS,
- Chromaticity: color, mono.
- PC interface: USB 2.0.

Spectral sensitivity plots of IMX335 are shown in Fig. 4.

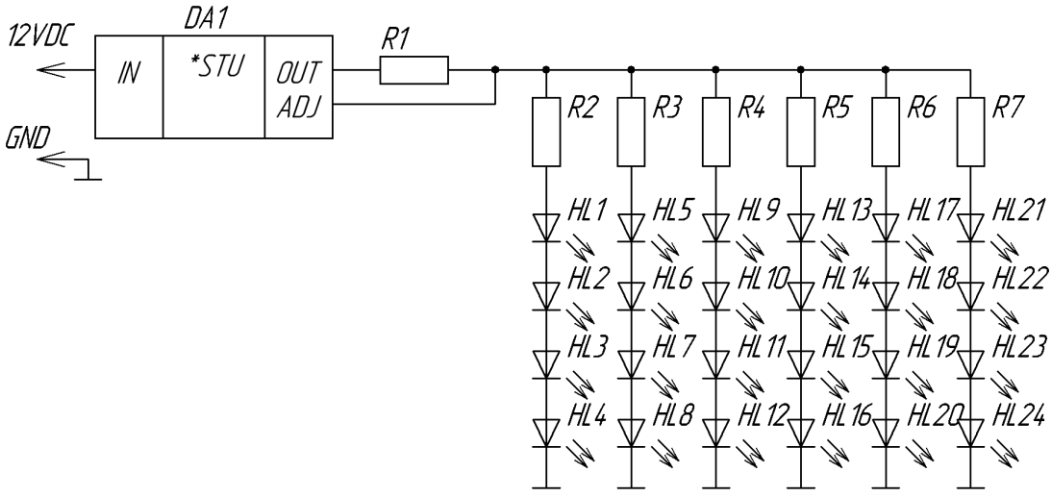
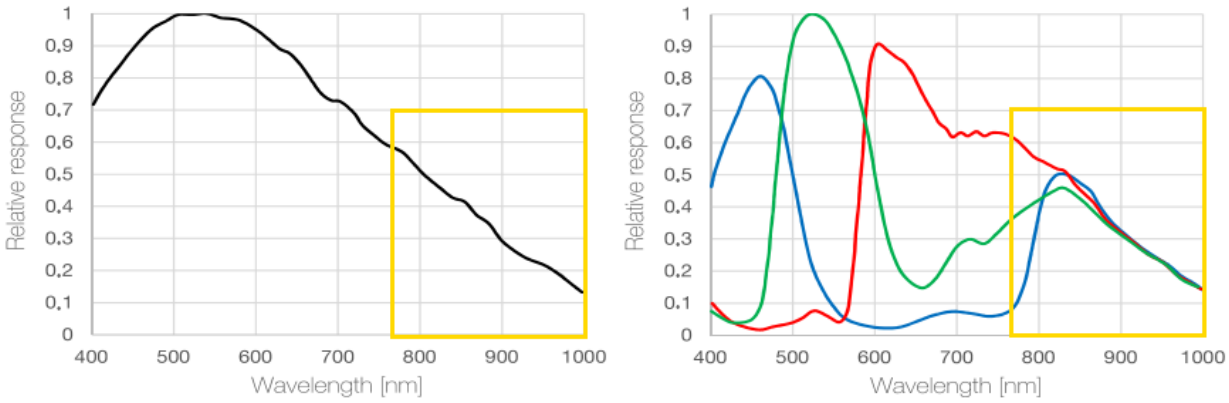


Fig. 3 Circuit diagram of the lighting unit.



(a) (b)

Fig. 4 Spectral sensitivity plots of the IMX335 module: (a) chromaticity: monochrome, (b) chromaticity: color. Rectangle highlights the area used for experimental research.

3.2 Methodology

The research was carried out with 20 volunteers aged 20–24 years old with Fitzpatrick Skin Phototype III. The experiments were completely safe for the eyes and the skin. According to the method of estimation of eye-hazardous exposure to infrared radiation given in IEC 62471 : 2006 [9], eye exposure to infrared light for both LED rings did not exceed 40 $W \cdot m^{-2}$, which was significantly lower than the established limit, even for exposure over 1000 s, which was 100 $W \cdot m^{-2}$. Similarly, in accordance with the methodology for assessing the limit of thermal exposure hazard for the skin [9], provided the exposure time is 20 min, the skin exposure is limited to a value of 50000 $J \cdot m^{-2}$ or less, with an estimated limit of 117713 $J \cdot m^{-2}$.

The contrast of veins in relation to the skin surface was estimated using different camera objective lenses and cut-off filters.

The test subject placed his hand under the vein viewer stand mounted on a tripod at a distance of about 30 cm. Images of the hand were captured using the camera with the IR source turned on with different objective lenses and cut-off filters. No additional digital image processing was performed. Unlighted hand images were taken with a smartphone camera. A fixed exposure time of 7.7 ms was used to capture images. Exposure time was chosen empirically.

The contrast of the obtained photos was evaluated as follows. The images were converted from color to black-and-white and then converted from integer data type to a scale from 0 to 1. Then, similar areas with a resolution of at least 200 × 200 pixels were selected. For these areas the root-mean-square value (RMS) of contrast was estimated according as follows:

$$C_{RMS} = \sqrt{\frac{1}{n-1}\sum_{i=1}^{n}(x_i - \bar{x})^2}, \qquad (1)$$

where x_i is the normalized brightness value of the i-th gray pixel, $0 \le x_i \le 1$, n is the total number of pixels in the image, $\bar{x}$ is the mean normalized gray level, which is estimated as follows:

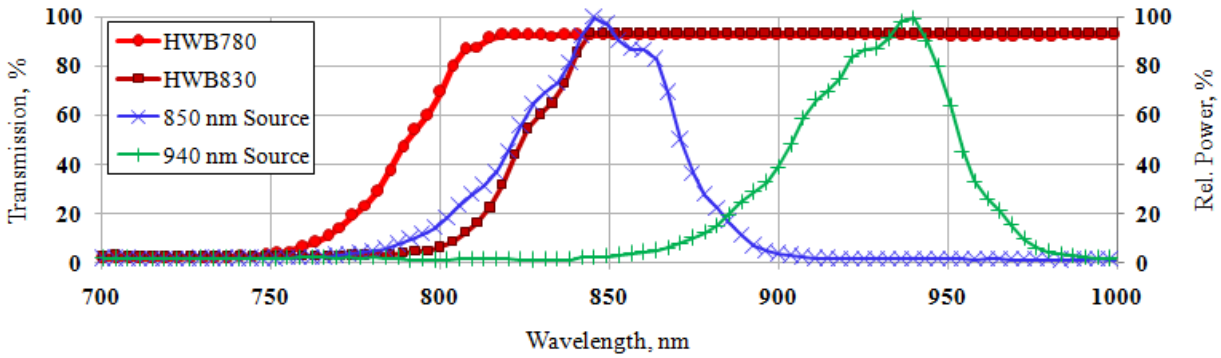
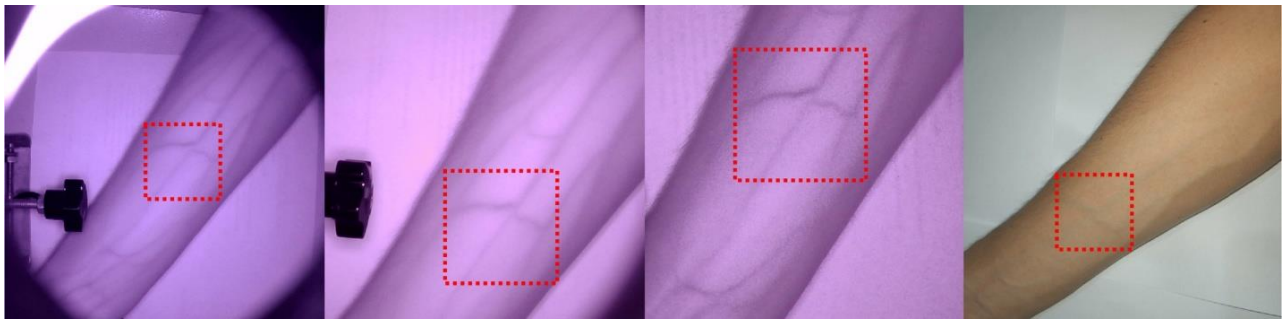
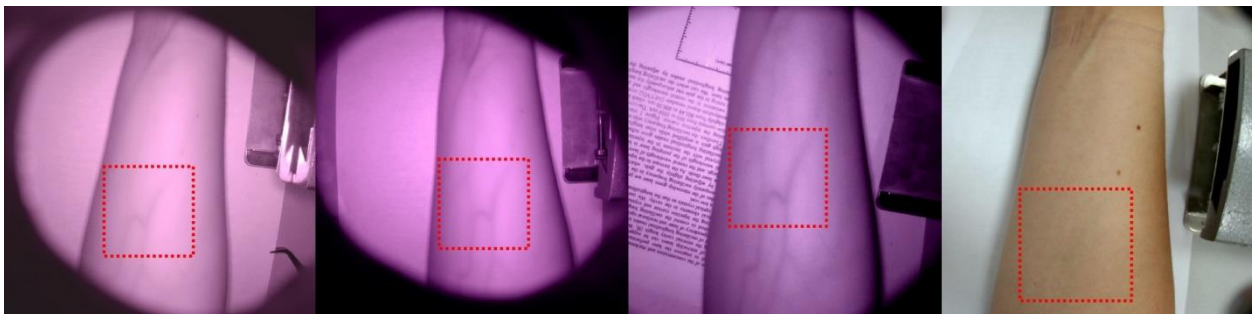


Fig. 5 LED rings spectrum overlap with HWB780 and HWB830 filter transmission bandwidths.



(a) (b) (c) (d)

Fig. 6 Digital images of a volunteer's forearm with the vein viewer prototype with LED highlighting at 850 nm: (a) HWB830, 3.6 mm objective focal length, (b) HWB830, 16 mm objective lens focal length, (c) HWB830, 25 mm objective lens focal length, and (d) digital image from a smartphone.



(a) (b) (c) (d)

Fig. 7 Digital images of a volunteer's forearm with the vein viewer prototype with LED highlighting at 850 nm: (a) without filter, objective lens focal length 3.6 mm, (b) HWB780, objective lens focal length 3.6 mm, (c) HWB830, objective lens focal length 3.6 mm, and (d) digital image from a smartphone.

$$\bar{x} = \frac{1}{n}\sum_{i=1}^{n} x_i. \qquad (2)$$

This estimation technique is suitable for comparing the contrast of different images [10].

The parameters of HWB780 (780 nm) and HWB830 (830 nm) long-pass optical filters were compared. Focal lengths of the lenses: 3.6 mm, 16 mm, and 25 mm.

The plot in Fig. 5 shows the overlap of the LED ring spectrum with the transmission bandwidth of the HWB780 and HWB830 filters.

As the Fig. 5 shows, the light from the source with a peak wavelength of 940 nm completely overlaps with the passband of the filters, while the light from the 850 nm source is slightly attenuated.

4 Results

The following results were obtained during the experiment and estimation. Fig. 6 shows examples of digital images of the hand of one of the subjects, obtained with the smartphone (d) and with the vein viewer prototype with different lenses using theHWB830filter (a, b, c). Fig. 7 shows examples of digital images of another subject obtained with a smartphone (d), without filter and with highlighting (a), using differentfilters (b, c), for an objective lens with a focal length of 3.6 mm.

Table 1. RMS contrast values for the 850 nm source.

Subject №	No highlight	3.6 mm lens		16 mm lens		25 mm lens	
		HWB780	HWB830	HWB780	HWB830	HWB780	HWB830
1	0.049	0.058	0.064	0.056	0.065	0.055	0.062
2	0.044	0.072	0.091	0.076	0.089	0.071	0.091
3	0.056	0.105	**0.122**	0.109	**0.120**	0.101	**0.122**
4	0.046	0.081	0.108	0.079	0.102	0.081	0.098
5	0.068	0.090	0.102	0.095	0.104	0.092	0.101
6	0.048	0.057	0.063	0.055	0.064	0.052	0.061
7	0.066	0.088	0.099	0.091	0.102	0.089	0.099
8	0.054	0.101	**0.118**	0.107	**0.115**	0.102	**0.119**
9	0.043	0.071	0.089	0.073	0.084	0.069	0.089
10	0.061	0.075	0.085	0.082	0.091	0.084	0.088
11	0.058	0.109	**0.127**	0.115	**0.126**	0.107	**0.128**
12	0.049	0.055	0.069	0.053	0.064	0.053	0.063
13	0.053	0.102	**0.117**	0.105	**0.113**	0.099	**0.118**
14	0.051	0.099	0.109	0.104	0.109	0.087	0.115
15	0.044	0.069	0.094	0.072	0.091	0.071	0.092
16	0.048	0.078	0.099	0.084	0.095	0.079	0.094
17	0.061	0.084	0.094	0.088	0.098	0.087	0.095
18	0.055	0.101	**0.119**	0.109	**0.117**	0.114	**0.120**
19	0.067	0.090	0.101	0.095	0.102	0.091	0.100
20	0.062	0.088	0.098	0.086	0.099	0.089	0.096

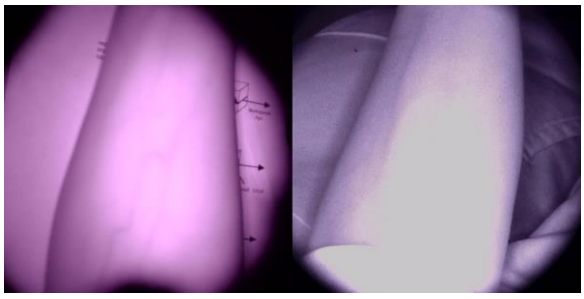


Fig. 8 Digital images obtained with the vein viewer without diffuser.

Figs. 6 and 7 show that in the images obtained with the vein viewer prototype, the vessels are much more recognizable than those in the digital photos from a smartphone. The areas used in contrast estimation are highlighted with a rectangle. It is not evident that the lens has a significant effect on the vein contrast (Fig. 6). It is noticeable that in the presence of a long-pass optical filter, veins become more recognizable (Fig. 7).

Furthermore, several images were obtained from a vein viewer with highlighting, but without the diffuser. In this case, the images were overexposed, resulting in a contrast estimation tending to zero (Fig. 8).

Table 1 shows the contrast estimation values for 20 subjects when the highlighting in 850 nm range.

As shown in Table 1, the influence of highlighting on the RMS contrast of veins is obvious. It can be noticed in all cases, that the use of the vein viewer provided an increase in contrast in comparison with the image from the smartphone camera. In addition, in all cases, the HWB830 filter, with a transmission bandwidth starting at 830 nm, produced higher vein contrast than the HWB780, with a transmission bandwidth starting at 780 nm. The contrast enhancement in percentage when using the HWB830 filter is shown in Fig. 9.

Fig. 9 shows that the choice of objective lens has no influence on the contrast. Slight changes in the RMS contrast with lens change are noticeable, but they have no regularity and most probably are associated with manual cropping of images and the unavoidable slight change in the hand position of the test subject when capturing a new photo after changing the objective on the prototype.

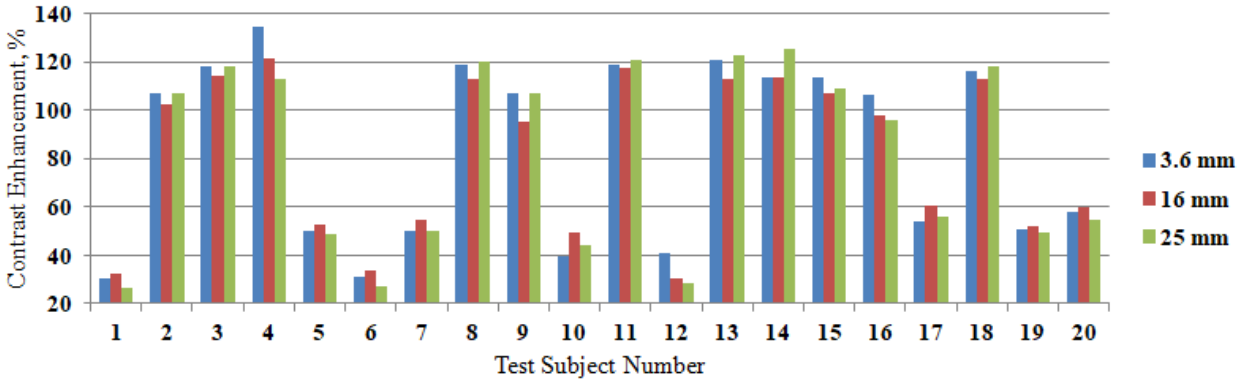
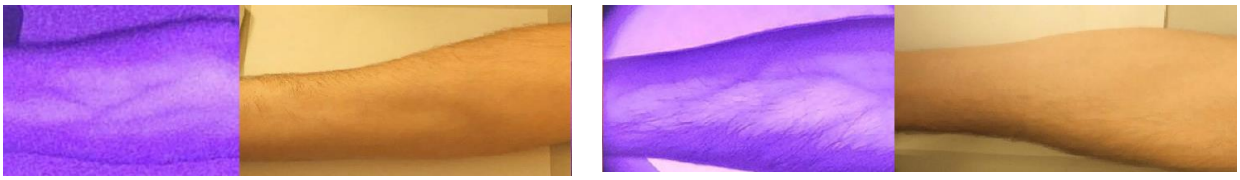


Fig. 9 Contrast enhancement percentages when using the vein viewer with the HWB830 filter for image capture compared to using a smartphone. Results are shown for the three lenses used at focal lengths of 3.6 mm, 16 mm, and 25 mm.



(a) (b)

Fig. 10 Examples of digital photos of subjects with low RMS contrast enhancement: (a) subject №1, (b) subject №6.

It is important to note that in 11 cases the contrast enhancement was 90% and higher, while in the remaining 9 cases the enhancement did not exceed 60%. Low contrast enhancement in such cases is explained by different skin composition and greater vein depth. Examples of digital photos of such subjects are shown in Fig. 10.

Fig. 10 shows that vein contrast is improved, although mathematically the RMS contrast enhancement is insignificant.

To be compared with the previous studies [2, 6], a visual qualitative estimation of the results was performed. In 16 cases, vein visibility was strongly improved, including invisible veins, in 4 cases veins became more recognizable.

Mark D. Francisco et al. assessed their results of vein visualization on the forearms as follows: in 110 cases veins were well visible, in 118 cases veins became visible, in 14 cases visualization results were unsatisfactory [2].

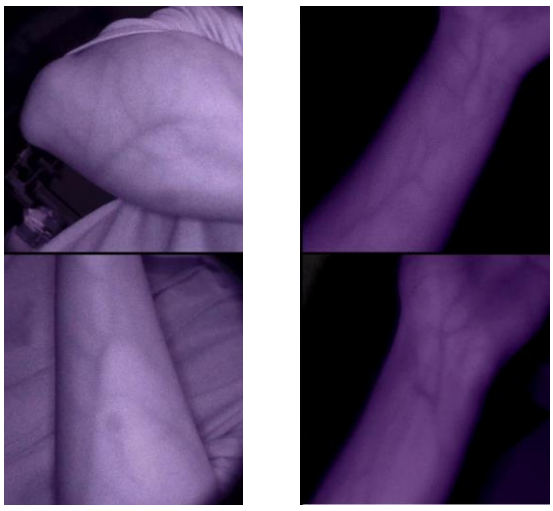
Dpakshayani and Yacin estimated their results as follows: in 90% of the cases, the visualization was satisfactory. The number of subjects was 100 [6].

It should be noted that an adequate comparison of results in the present case is impossible, because other studies involve significantly more subjects, as well as “problematic” subjects: the elderly, overweight, different skin types, etc.

In addition, an experiment was performed using 8 subjects from the original population with similar conditions using a LED ring with a peak wavelength of 940 nm (Fig. 11). Only one lens with a focal length of 16 mm was used.

Fig. 11 illustrates that the veins of the subjects are well recognizable in general.

Table 2 shows the results of this experiment in comparison with the 850 nm source experiment. According to the Table 2, the contrast increased in 4 cases and decreased in 4 cases. Possibly, this difference is caused by the individual characteristics of particular subjects. Therefore, it is concluded that the preference should be given to the possibility of switching the light range by the operator and using several ranges simultaneously, so that the device can be adjusted for each individual patient. Previously, the use of a polychromatic source with LEDs with peak wavelengths of 740, 765, 770, and 780 nm as a light source was proposed by Dhakshayani and Yacin [6].



(a) (b)

Fig. 11 Digital photos of forearms of volunteers obtained using the prototype of vein viewer with LED highlighting at 940 nm range: (a) with HWB780 filter, (b) with HWB830 filter.

Table 2 Comparison of RMS contrast for 850 nm and 940 nm sources.

Subject №	No highlighting	850 nm LED ring		940 nm LED ring	
		HWB780	HWB830	HWB780	HWB830
1	0.049	0.056	0.065	0.071	0.084
2	0.044	0.076	0.089	0.078	0.099
6	0.048	0.055	0.064	0.063	0.077
7	0.066	0.091	0.102	0.077	0.085
10	0.061	0.082	0.091	0.074	0.081
11	0.058	0.115	0.126	0.092	0.111
18	0.055	0.109	0.117	0.121	0.133
20	0.062	0.086	0.099	0.075	0.089

5 Conclusion

In this paper the vein viewer prototype and the technique for estimating the quality of visualization were proposed. The prototype was used to obtain images of the subjects' forearms using two different LED light sources: with peak wavelength of 850 nm and 940 nm, and different absorption long-pass optical filters (HWB780 and HWB830) and objective lenses with different focal lengths (3.6 mm, 16 mm, and 25 mm). The RMS contrast of the images was evaluated with the GNU Octave environment. The results show that the presence of highlighting increases the RMS contrast of the image, i.e., simplifies the detection of the subject's veins. As can be seen from the results, the contrast enhancement was 100% or more in most cases. Visual estimation shows that vein recognition was improved in all cases, and in 16 out of 20 cases, visibility was sufficiently improved, i.e., deep invisible veins became recognizable. It was noted that the HWB830 long-pass optical filter, with a transmission bandwidth starting at 830 nm, provided greater contrast of veins relative to the skin surface in all cases. On the other hand, the choice of objective lens does not affect the contrast. The objective lens only affects the focus and hand grip area.

Disclosures

The authors have no relevant financial interest in this article and no conflict of interest to disclose.

References

1. C.-T. Pan, M. D. Francisco, C. K. Yen, S. Y. Wang, and Y. L. Shiue, "Vein Pattern Locating Technology for Cannulation: A Review of the Low-Cost Vein Finder Prototypes Utilizing near Infrared (NIR) Light to Improve Peripheral Subcutaneous Vein Selection for Phlebotomy," Sensors 19(16), 3573 (2019).
2. M. D. Francisco, W.-F. Chen, C.-T. Pan, M.-C. Lin, Z.-H. Wen, C.-F. Liao, and Y.-L. Shiue, "Competitive Real-Time Near Infrared (NIR) Vein Finder Imaging Device to Improve Peripheral Subcutaneous Vein Selection in Venipuncture for Clinical Laboratory Testing," Micromachines 12(4), 373 (2021).
3. M. Marathe, N. S. Bhatt, and R. Sundararajan, "A novel wireless vein finder," International Conference on Circuits, Communication, Control and Computing, 277–280 (2014).
4. L. T. Tran, H. T. T. Pham, "Designing and Building the Vein Finder System Utilizing Near-Infrared Technique," In 7th International Conference on the Development of Biomedical Engineering in Vietnam (BME7) Translational Health Science and Technology for Developing Countries 69, 383–387 (2019).
5. C. Kauba, B. Prommegger, and A. Uhl, "OpenVein – An Open-Source Modular Multipurpose Finger Vein Scanner Design," Chapter in Handbook of Vascular Biometrics. Advances in Computer Vision and Pattern Recognition, A. Uhl, C. Busch, S. Marcel, and R. Veldhuis (Eds.), Springer, Cham, 77–111 (2019).
6. M. Dhakshayani, S. Yacin, "Economically Affordable and Clinically Reliable Vein Finder," Proceedings of the 30th Indian Engineering Congress, the 21st Century Engineering: The Make in India Pathway, 63–69 (2015).
7. F. Wang, A. Behrooz, and M. Morris, "High-contrast subcutaneous vein detection and localization using multispectral imaging," Journal of Biomedical Optics 18(5), 050504 (2013).
8. N. Sharma M. Hafeeda, "Hyperspectral Reconstruction from RGB Images for Vein Visualization," Proceedings of the 11th ACM Multimedia Systems Conference, 77–87 (2020).
9. Europen standard, Photobiological safety of lamps and lamp systems (IEC 62471:2006, modified), Brussels (2008).
10. E. Peli, "Contrast in complex images," Journal of the Optical Society of America A 7(10), 2032–2040 (1990).

Mathematical Analysis of Raman Spectra Data Arrays Using Machine Learning Algorithms

Yana A. Byuchkova*, Andrey Y. Zyubin, Vladimir V. Rafalskiy, Ekaterina M. Moiseeva, and Ilia G. Samusev

Immanuel Kant Baltic Federal University, 14 Alexander Nevsky str., Kaliningrad 236016, Russian Federation

***e-mail:** 18377@mail.ru

Abstract. This paper is devoted to the application of mathematical methods of classification and differentiation of low-resolution spectral data arrays of Raman light scattering for complex biological compounds as human platelets. Spectral data arrays consisted of 1266 spectra from 4 groups of patients, totaling 152 people were analyzed. A random forest algorithm was used. Potential biomarkers of differences between patient groups were identified, on which the given algorithms were tested. Using the random forest algorithm for classification of spectra of healthy patients without therapy and patients with cardiovascular pathologies without therapy, we have achieved the accuracy of 83.4%. Classification of the healthy patients on and off therapy shows the accuracy of 76.26% and classification of the patients with cardiovascular pathologies shows 70% accuracy. © 2023 Journal of Biomedical Photonics & Engineering.

Keywords: spectroscopy; surface-enhanced Raman scattering; cardiovascular disease; machine learning; random forest algorithm.

Paper #8684 received 5 Mar 2023; revised manuscript received 13 Jun 2023; accepted for publication 16 Jun 2023; published online 29 Jun 2023. doi: 10.18287/JBPE23.09.020308.

1 Introduction

Cardiovascular diseases (CVDs) are the leading cause of death worldwide and in the Russian Federation. An estimated 17.9 million people died of cardiovascular disease in 2016, accounting for 31% of all deaths worldwide. Eighty five percent of these deaths were caused by heart attack and stroke [1]. Cardiovascular disease is the most frequent cause of hospitalization and disability among the population of the Russian Federation. At the same time, about 40% of people in Russia die at an active working age (25–64 years) [2].

The development of new methods for diagnosing and detecting the risks of such diseases can significantly increase the efficiency and accuracy of preventing these diseases. The application of machine learning algorithms for blood Raman spectra analysis is a relatively novel method for detecting cardiovascular diseases.

Research into the application of machine learning to the processing of Raman spectra for the diagnosis of cardiovascular diseases is at an early stage of development. For example, machine learning has been applied to early warning of heart attacks using surface-enhanced Raman spectroscopy [3].

A random forest algorithm was chosen to classify Raman spectra by patient groups and select the most significant spectral shifts [4–7]. This choice is due to the ability of this method to classify, the ability to select the most significant features and to deal with large amounts of data. It is also effective and relatively fast, which is important for the analysis of large amounts of data in a short time. The originality of the approach lies in the first application of machine learning to the processing of a spectral array of complex Raman light scattering spectra of human platelets.

The purpose of this paper is to develop a solution for an important problem of differentiation of Raman spectra [8–11] in patients with and without cardiovascular pathologies, detection of spectral markers of platelet changes in pathologies and due to medication.

This article describes the results of applying a machine learning algorithm to the processing of spectral data arrays for different groups of patients: healthy patients, patients with pathologies of cardiovascular disease, healthy patients receiving therapy, and patients with pathologies of cardiovascular disease receiving

This paper was presented on the Biophotonics Workshop of the XX All-Russian Youth Conference-Contest on Optics and Laser Physics, Dedicated to the 100th Anniversary of N.G. Basov, Samara, Russia, November 8–12, 2022.

therapy. The applicability of the random forest algorithm is shown.

2 Materials and Methods

2.1 SERS Experiment

For the platelet study using SERS, fresh venous blood samples were collected from healthy volunteers and patients with CVD in a vacuum tube containing EDTA (BD Vacutainer®). The samples were then centrifuged at 60 g for 15 min to separate platelet-rich plasma, and then it was centrifuged again with 60 g for 15 min to precipitate leukocytes and erythrocytes. In the last step, platelets were precipitated by centrifugation of the supernatant at 1500 g for 15 min. All centrifugation steps were performed at 4 °C.

Fresh venous blood samples for SERS were taken in a vacuum tube containing sodium citrate (Vacutainer 4.5 ml with 3.2%® sodium citrate). SERS spectra were obtained on a Centaur U HR Raman spectrometer (NanoScanTechnology LTD, Russia) using a Cobolt Samba diode-pumped solid-state laser with a photoexcitation wavelength of $\lambda = 532$ nm and a power per sample of 45 mW. The optical scheme included an Olympus BX 41 microscope with a 100X objective (NA 0.9). The spectrometer monochromator (ZAO Solar LS, Belarus) had a focal distance of 284 mm with a diffraction grating of 1200 gr/mm and was equipped with a IDus 401 CCD camera (Andor, UK). The resolution of camera was 1024 × 256 pixels. The spectrometer had a spectral resolution of 2.5 cm^{-1}. A 1 × 25 μm laser spot was positioned manually on the platelet mass. Rayleigh scattering was eliminated with a reflector filter. A drop of 5 μl of platelet-rich plasma was applied to a previously created titanium-based nanostructured surface, a detailed methodology of production of which is described in Ref. [12] substrate, dried for 5 min at room temperature, and then placed in a microscope rack. For each sample, spectra averaged three times from ten different drop locations were collected. The exposure time for the CCD camera was set as 70 s. Each time before the experiment, the spectrometer was calibrated for silicon by a static spectrum centered at a spectral shift frequency of 520.1 cm^{-1} for 1 s. After registration, the spectra were saved in .txt format and in a special format (.ngs) on a PC connected to the Raman spectrometer. Due to the possibility of plasmon resonance generation, roughened titanium surfaces with spherical gold nanoparticles were used to amplify the Raman signal. The plasmon absorption maxima were $\lambda = 530$ nm and $\lambda = 570$ nm for gold nanoparticles and the rough Ti surface, respectively. For such structures, the spectral signal amplification was recorded up to orders of 103 times.

The study focused on the Raman spectra of the following groups of patients:

- healthy without therapy (group 1),
- healthy on therapy (aspirin, clopidogrel) (group 2),
- patients with cardiovascular disease without therapy (group 3),
- patients with cardiovascular disease on therapy (group 4).

The total number of study participants was 152. Subjects were divided into 4 groups: healthy volunteers not receiving AT (group 1) and receiving acetylsalicylic acid (ASA), group 2; patients with cardiovascular disease (CVD) without AT (group 3) and receiving AT (group 4). Aggregometry and SERS spectra of platelets were performed in all subjects. An original optical sensor based on gold particle-modified nanostructured titanium surface was developed to obtain SERS spectra of platelets.

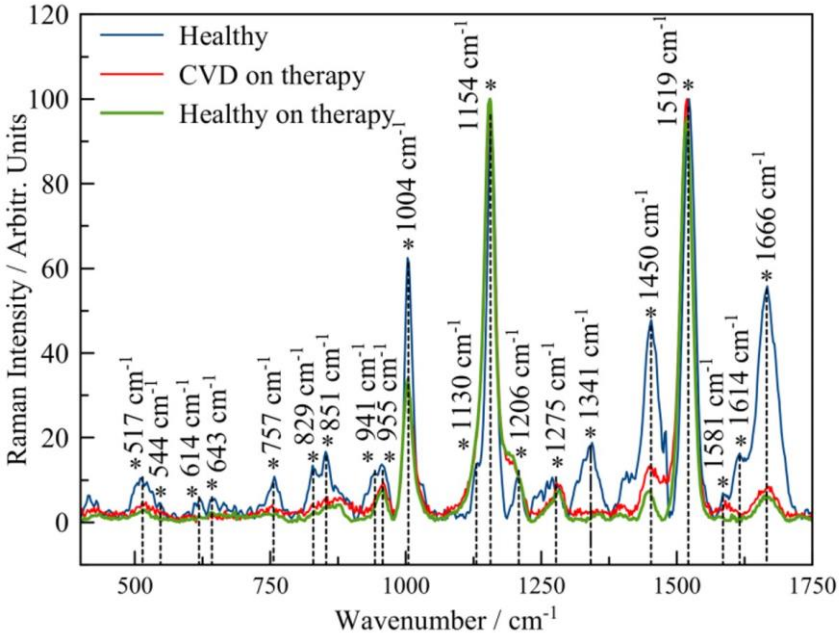


Fig. 1 Example of Raman spectra for healthy patients (blue line), patients with CVD on therapy (red line), group of healthy patients on therapy (green line) [12].

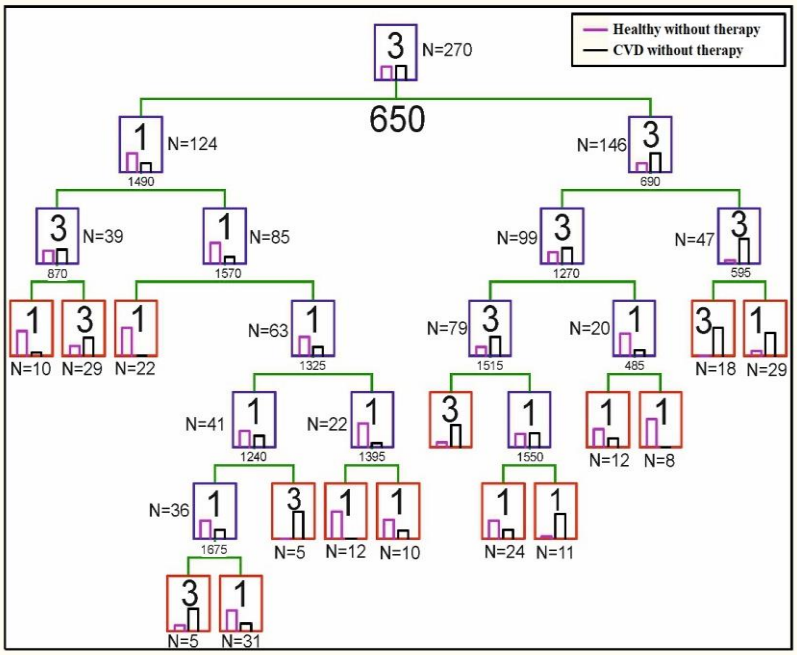


Fig. 2 Decision tree in the classification of spectra by groups of healthy patients without therapy (group 1) and patients with cardiovascular disease pathologies without therapy (group 3).

Spectrum data were read from the instrument and entered into .txt and .csv files. For the following study, spectral data were brought to uniformity by classifying a single frequency grid using the Parcer program. Uniform group tables were created and a unified frequency grid of 5 cm^{-1} spacing was generated. Thus, the developed program automatically converted files and formed an array of data. This program was written in C++ and arranged the spectrum by grid cells in the range from 400 cm^{-1} to 1800 cm^{-1} in 5 cm^{-1} increments. Thus, all spectral fluctuations were correlated with the designated grid.

2.2 Spectral Data Processing with Machine Learning

The Statistica 13 Random Forest module, which is an implementation of the random forest classifiers developed by Breiman [13], whose algorithm is also applicable to regression tasks, was chosen to process spectral data.

To implement the random forest classification tasks, a group column was added to the data table, which included the name of the patient group of the selected observation. The dependent variable was the group distribution of patients according to their condition and medication intake. And spectral shift values between 400 cm^{-1} and 1800 cm^{-1} were taken as continuous predictors. Next, a test sample of spectral observations was allocated using the additional option of selecting the proportion of test and training samples. In our study, the test sample represents 30% of all observations. The random forest method in Statistica 13 defines a boundary function that measures the extent to which the mean number of votes for the correct class exceeds the mean number of votes for any other class present in the dependent variable. This measure provides us not only with a convenient way to make predictions, but also a way to relate the validity score to those predictions. The accuracy of the classifier was determined by the ratio of the number of correct responses to the total number of responses.

3 Results and Discussions

An array of spectral data from four groups of patients was accumulated based on the results of spectral imaging. An example of the obtained spectra is shown in Fig. 1.

Table 1 Classification matrix for separating healthy patients without therapy from CVD patients without therapy.

	Predicted healthy without therapy	**Predicted CVDs without therapy**
True healthy without therapy	37.5%	10.07%
True CVD without therapy	6.53%	45.9%

Note: The number of correctly classified spectral data by patient group is highlighted in green. The number of misclassified spectral data is highlighted in red.

Table 2 The most important spectral shifts and their interpretation for the classification of healthy patients without therapy from CVD patients without therapy.

Spectral shift, cm^{-1}	Significance of the trait, relative units	Interpretation	Reference
1305	0.00803	$\tau(CH_2)$ (lipids)	[14]
1485	0.00782	1485 planar variations (adenine/guanine)	[15]
1155	0.00678	C–C valence oscillations (v) in proteins	[16–17]
1395	0.00671	Amid	[18]
890	0.00621	CH_3 bend in Tricaprylin	[14]

Table 3 Classification matrix to separate healthy patients without therapy from healthy patients on therapy.

	Predicted healthy without therapy	Predicted CVDs without therapy
True healthy without therapy	69.38%	11.88%
True healthy on the therapy	11.88%	6.88%

Note: The number of correctly classified spectral data by patient group is highlighted in green. The number of misclassified spectral data is highlighted in red.

Table 4 The most important spectral shifts and their interpretation for the classification of healthy patients without and on therapy.

Spectral shift, cm^{-1}	Significance of the trait, relative units	Interpretation	Reference
1040	0.00714	Unsaturated fatty acids	[14]
1035	0.00707	β(CH) in lipids	[14]
1685	0.00607	Protein beta sheet and polyproline helix	[19]
980	0.00571	β(CH) in lipids	[14]
1165	0.005	ν(C-C) in lipids	[14]
1305	0.005	$\tau(CH_2)$, δ(=CH) in lipids	[14]

3.1 Spectral Data Processing with Machine Learning

The data were classified into patient groups using a random forest algorithm. Let us first consider differentiation of spectra by groups of healthy patients without therapy (group 1) and patients with cardiovascular pathologies without therapy (group 3). Fig. 2 shows one of the decision trees, which shows the most informative spectral lines.

Most of the data were correctly identified using the random forest algorithm. The correctness of the algorithm for classifying the observations into groups of healthy patients without therapy and patients with cardiovascular pathology without therapy was 83.4%, as shown in Table 1.

In carrying out this classification, the most significant spectral shifts in separating the observations into groups were highlighted, as presented in Table 2.

Table 5 Classification matrix for separating non-therapy CVD patients from therapy naive CVD patients.

	Predicted CVDs without therapy	**Predicted CVDs on therapy**
True CVD without therapy	59.5%	3.0%
True CVD on therapy	27.0%	10.5%

Note: The number of correctly classified spectral data by patient group is highlighted in green. The number of misclassified spectral data is highlighted in red.

Table 6 The most important spectral shifts and their interpretation for the classification of CVD patients without and on therapy.

Spectral shift, cm^{-1}	**Significance of the trait, relative units**	**Interpretation**	**Reference**
1565	0.00662	C–N stretching	[20]
1425	0.00655	The band at ~1420 cm^{-1} observed for saturated and Z-unsaturated FAs is hardly seen in the spectra of the unsaturated compounds and presumably accounts for the shoulder at approximately 1422 cm^{-1}	[21]
1055	0.00615	Lipid hydrocarbon chain	[14]
1440	0.00602	CH_2 bend (lipids)	[16–17]
1385	0.00582	Hydrogen bonding in protein	[22]
1125	0.00576	V($C_ß$-methyl)	[23]

Also, a random forest algorithm was used to classify healthy patients on and off therapy with an accuracy of 76.26%, as can be seen in Table 3.

The most significant spectral shifts and their interpretation for the classification of healthy patients without and on therapy were highlighted, shown in Table 4.

When the patients with cardiovascular pathologies on and off therapy were classified, 70% accuracy was achieved, as shown in Table 5.

Table 6 highlights the most important spectral shifts and their interpretation for the classification of patients with cardiovascular pathologies without and on therapy.

4 Conclusions

As a result of this research, the initial results on the development of machine learning methods for the differentiation of Raman spectra in patients with and without cardiovascular disease pathologies were demonstrated.

Approaches were applied to process spectral data arrays consisting of 1266 spectra for different groups of patients: healthy patients, patients with pathologies of cardiovascular diseases, healthy patients receiving therapy and patients with pathologies of cardiovascular diseases receiving therapy. The applicability of the random forest algorithm was shown. Potential biomarkers of differences between patient groups on which the given algorithms were tested were identified. The achieved accuracy of classification using the random forest algorithm of spectra across the groups of healthy patients without therapy and patients with cardiovascular pathologies without therapy was 83.4%. Classification of the healthy patients on and off therapy shows the accuracy of 76.26% and classification of the patients with cardiovascular pathologies shows 70% accuracy.

Acknowledgements

This research was supported from the Russian Federal Academic Leadership Program Priority 2030 at the Immanuel Kant Baltic Federal University.

Disclosures

The authors have no conflict of interest to disclose.

References

1. World Health Organization, Cardiovascular Diseases (CVDs), (accessed 6 May 2023). [https://www.who.int/news-room/fact-sheets/detail/cardiovascular-diseases-(cvds)].
2. N. N. Pribylova, O. A. Osipova, M. A. Vlasenko, O. A. Vlasenko, and A. Y. Chetverikova, "Diagnostic aspects of definition of operational damage of a myocardium at a coronary revascularization," Challenges in Modern Medicine 18(10), 17–23 (2012). [in Russian]
3. Z. Liu, D. Meng,G. Su, P. Hu, B. Song, Y. Wang, W. Junhan,Y. Hao, Y. Tianyi, C. Buyun, O. Tse-Hsien, H. Sushmit, M. Matthew, L. Fanxin, and W. Wu, "Ultrafast Early Warning of Heart Attacks through Plasmon-Enhanced Raman Spectroscopy using Collapsible Nanofingers and Machine Learning," Small 19(2), 2204719 (2023).
4. F. B. de Santana, W. B. Neto, and R. J. Poppi, "Random forest as one-class classifier and infrared spectroscopy for food adulteration detection," Food Chemistry 293, 323–332 (2019).
5. B. P. Lovatti, M. H. Nascimento, K. P. Rainha, E. C. Oliveira, Á. C. Neto, E. V. Castro, and P. R. Filgueiras, "Different strategies for the use of random forest in NMR spectra," Journal of Chemometrics 34(12), e3231 (2020).
6. A. Wójtowicz, J. Piekarczyk, B. Czernecki, and H. Ratajkiewicz, "A random forest model for the classification of wheat and rye leaf rust symptoms based on pure spectra at leaf scale," Journal of Photochemistry and Photobiology B: Biology 223, 112278 (2021).
7. S. Khan, R. Ullah, A. Khan, A. Sohail, N. Wahab, M. Bilal, and M. Ahmed,"Random forest-based evaluation of Raman spectroscopy for dengue fever analysis," Applied Spectroscopy 71(9), 2111–2117 (2017).
8. G. Li, D. Wang, J. Zhao, M. Zhou, K. Wang, S. Wu, and L. Lin, "Improve the precision of platelet spectrum quantitative analysis based on "M+N" theory," Spectrochimica Acta Part A: Molecular and Biomolecular Spectroscopy 264, 120291 (2022).
9. L. Hu, C. Yin, S. Ma, and Z. Liu, "Rapid detection of three quality parameters and classification of wine based on Vis-NIR spectroscopy with wavelength selection by ACO and CARS algorithms," Spectrochimica Acta Part A: Molecular and Biomolecular Spectroscopy 205, 574–581 (2018).
10. T. Chen, Q. Chang, J. G. P. W. Clevers, and L. Kooistra, "Rapid identification of soil cadmium pollution risk at regional scale based on visible and near-infrared spectroscopy," Environmental Pollution 206, 217–226 (2015).
11. R. K. Douglas, S. Nawar, M. C. Alamar, A. M. Mouazen, and F. Coulon, "Rapid prediction of total petroleum hydrocarbons concentration in contaminated soil using vis-NIR spectroscopy and regression techniques" Science of the Total Environment 616, 147–155 (2018).
12. A. Zyubin, V. Rafalskiy, A. Tcibulnikova, E. Moiseeva, K. Matveeva, A. Tsapkova, I. Lyatun, P. Medvedskaya, I. Samusev, and M. Demin, "Surface-enhanced Raman spectroscopy for antiplatelet therapy effectiveness assessment," Laser Physics Letters 17(4), 045601 (2020).
13. L. Breiman, "Random forests,"Machine Learning 45, 5–32 (2001).
14. K. Czamara, K. Majzner, M. Z. Pacia, K. Kochan, A. Kaczor, and M. Baranska, "Raman spectroscopy of lipids: a review," Journal of Raman Spectroscopy 46(1), 4–20 (2015).
15. A. J. Hobro, M. Rouhi, E. W. Blanch, and G. L. Conn, "Raman and Raman optical activity (ROA) analysis of RNA structural motifs in Domain I of the EMCV IRES," Nucleic Acids Research 35(4), 1169–1177 (2007).
16. D. Garc´ıa-Rubio, B. de la Mora, I. Badillo-Ram´ırez, D. Cerecedo, J. Saniger, J. Ben´ıtez-Ben´ıtez, and M. Villagr´an-Muniz, "Analysis of platelets in hypertensive and normotensive individuals using Raman and Fourier transform infrared-attenuated total reflectance spectroscopies," Journal of Raman Spectroscopy 50(4), 509–521 (2019).
17. J. Depciuch, E. Kaznowska, I. Zawlik, R. Wojnarowska, M. Cholewa, P. Heraud, and J. Cebulski, "Application of Raman spectroscopy and infrared spectroscopy in the identification of breast cancer," Applied Spectroscopy 70(2), 251–263 (2016).
18. E. M. Jones, G. Balakrishnan, T. C. Squier, and T. G. Spiro, "Distinguishing unfolding and functional conformational transitions of calmodulin using ultraviolet resonance R aman spectroscopy," Protein Science 23(8), 1094–1101 (2014).
19. N. C. Maiti, M. M. Apetri, M. G. Zagorski, P. R. Carey, and V. E. Anderson, "Raman spectroscopic characterization of secondary structure in natively unfolded proteins: α-synuclein," Journal of the American Chemical Society 126(8), 2399–2408 (2004).
20. P. Schellenberg, E. Johnson, A. P. Esposito, P. J. Reid, and W. W. Parson, "Resonance Raman scattering by the green fluorescent protein and an analogue of its chromophore," The Journal of Physical Chemistry B 105(22), 5316–5322 (2001).
21. W. Curatolo, S. P. Verma, J. D. Sakura, D. M. Small, G. G. Shipley, and D. F. H. Wallach, "Structural effects of myelin proteolipid apoprotein on phospholipids: a Raman spectroscopic study," Biochemistry 17(9), 1802–1807 (1978).
22. H. Takeuchi, "Raman structural markers of tryptophan and histidine side chains in proteins," Biopolymers: Original Research on Biomolecules 72(5), 305–317 (2003).
23. B. R. Wood, P. Caspers, G. J. Puppels, S. Pandiancherri, and D. McNaughton, "Resonance Raman spectroscopy of red blood cells using near-infrared laser excitation," Analytical and Bioanalytical Chemistry 387, 1691–1703 (2007).